ON-ORBIT SPATIAL IMAGE CHARACTERISATION AND RESTORATION BASED ON STOCHASTIC CHARACTERISTIC TARGETS

WONG SOO MEE

FACULTY OF COMPUTER SCIENCE AND INFORMATION TECHNOLOGY
UNIVERSITY OF MALAYA
KUALA LUMPUR

2021

ON-ORBIT SPATIAL IMAGE CHARACTERISATION AND RESTORATION BASED ON STOCHASTIC CHARACTERISTIC TARGETS

WONG SOO MEE

THESIS SUBMITTED IN FULFILMENT OF THE REQUIREMENTS FOR THE DEGREE OF DOCTOR OF PHILOSOPHY

FACULTY COMPUTER SCIENCE AND
INFORMATION TECHNOLOGY
UNIVERSITY OF MALAYA
KUALA LUMPUR

2021

UNIVERSITY OF MALAYA

ORIGINAL LITERARY WORK DECLARATION

Name of Candidate: WONG SOO MEE

Matric No: 17005067/1 (WHA130053)

Name of Degree: DOCTOR OF PHILOSOPHY

Title of ~~Project Paper/Research Report/Dissertation~~/Thesis ("this Work"):

ON-ORBIT SPATIAL IMAGE CHARACTERISATION AND RESTORATION BASED ON STOCHASTIC CHARACTERISTIC TARGETS

Field of Study: IMAGE PROCESSING

I do solemnly and sincerely declare that:

(1) I am the sole author/writer of this Work;
(2) This Work is original;
(3) Any use of any work in which copyright exists was done by way of fair dealing and for permitted purposes and any excerpt or extract from, or reference to or reproduction of any copyright work has been disclosed expressly and sufficiently and the title of the Work and its authorship have been acknowledged in this Work;
(4) I do not have any actual knowledge nor do I ought reasonably to know that the making of this work constitutes an infringement of any copyright work;
(5) I hereby assign all and every rights in the copyright to this Work to the University of Malaya ("UM"), who henceforth shall be the owner of the copyright in this Work and that any reproduction or use in any form or by any means whatsoever is prohibited without the written consent of UM having been first had and obtained;
(6) I am fully aware that if in the course of making this Work I have infringed any copyright whether intentionally or otherwise, I may be subject to legal action or any other action as may be determined by UM.

Candidate's Signature Date: 25 May 2021

Subscribed and solemnly declared before,

Witness's Signature Date: 25 May 2021

Name:

Designation:

ON-ORBIT SPATIAL IMAGE CHARACTERISATION AND RESTORATION BASED ON STOCHASTIC CHARACTERISTIC TARGETS

ABSTRACT

While the qualities associated with the radiometric and geometric resolution are a major concern in earth observation satellite (EOS) imaging sensors calibration and validation, spatial resolution quality is an important parameter that is essentially needed for on-orbit spatial EOS imaging performance assessment. Moreover, its calibration results can be applied to an image restoration problem, to improve the spatial quality of the EOS data. A practical way to characterize the on-orbit spatial quality performance of an EOS imaging sensor is to determine the modulation transfer function (MTF) from its remotely sensed images on the ground. However, existing approaches and techniques for spatial characterisation are highly reliant on the presence and manual identification of a well-separated characteristics target. These approaches and techniques impose stringent criteria and temporal sampling issues. In spatial image restoration, even with the perfect estimation of degradation function, restoring coherent high-frequency image details can still be very difficult.

This thesis presents two frameworks; the first one is for on-orbit spatial characterisation, whereas the second is for optical satellite image restoration. In the first framework, this thesis introduces an insight to effectively measure the MTF by analyzing the stochastic characteristics in the observed image. In particular, first, it proposes a segmentation method to select the ideal candidates for MTF Measurement. Second, it develops an adaptive structure selection method that removes detrimental structures and selects only useful information for point spread function (PSF) estimation. Finally, it introduces a spatial prior that can simultaneously suppress noises while preserving the sparsity and continuity of data to obtain high fidelity two-dimensional PSF model for MTF measurement. The experimental results demonstrate that the proposed framework is practical and effective, with < 2.3% of relative error at the Nyquist frequency as compared to the well-established edge method.

In continuation of the first framework, the proposed MTF measurement algorithms are evaluated experimentally as a blur kernel estimation method for spatially varying and invariant blur removal. Furthermore, this thesis presents a comparative study on blur estimation methods that utilize the principle of sparse representation to gain an insight into image priors type that appropriate for blur removal in blind optical satellite images. Given the fact that the heavy-tailed properties of MTF typically introduce noise and an unacceptable aliasing effect. Therefore, in the second framework, this thesis exploits the image properties and shows that only one image property used in a regularization-based framework is insufficient to obtain satisfying restoration results. Hence, this thesis presents a strategy for high-fidelity MTF compensation by characterizing both the local smooth and nonlocal self-similarity properties of images in the hybrid domain. To minimize computational complexity, it establishes a simple joint statistical model in the Curvelet domain to combine these image properties and employ the multi-objective bilevel optimization approach to efficiently solve the severely ill-posed inverse problem of MTFC. The experimental results show that the proposed methods achieve significant performance in preserving high fidelity images with feature similarity (FSIM) index value as high as 0.99876 and minimum computational complexity.

Keywords: Modulation Transfer Function, Remotely-sensed imagery, Sparsity priors, Regularized-based Joint Statistical Model, Image Fidelity.

PENCIRIAN DAN PEMULIHAN IMEJ SPATIAL DI-ORBIT BERDASARKAN TARGET CIRIAN STOKASTIK

ABSTRAK

Walaupun kualiti yang berkaitan dengan resolusi radiometrik dan geometri adalah keutamaan dalam Kalibrasi dan Validasi sensor pengimejan bagi satelit pencerapan bumi (EOS), kualiti resolusi spatial adalah parameter penting yang pada asasnya diperlukan untuk penilaian prestasi pengimejan EOS dari segi spatial yang berada di orbit. Selain itu, hasil penentukurannya juga dapat membantu dalam masalah pemulihan imej bagi meningkatkan kualiti spatial data EOS. Satu cara praktikal untuk mencirikan prestasi spatial bagi sensor pengimejan EOS yang berada di orbit adalah dengan menentukan fungsi pemindahan modulasi (MTF) dari imejnya yang dicerap melalui penderia jauh. Pendekatan dan teknik pencirian spatial yang sedia ada amat bergantung pada kewujudan target dengan cirian yang jelas terpisah dan memerlukan pengenalpastian secara manual. Perkara ini mengenakan pematuhan kriteria dan masalah persampelan temporal yang tidak fleksibel. Dalam usaha pemulihan imej spatial, walaupun dengan anggaran fungsi degradasi yang sempurna, memulihkan perincian imej berfrekuensi tinggi yang koheren masih boleh menjadi sangat sukar.

Tesis ini membentangkan dua rangka kerja; Yang pertama adalah untuk pencirian spatial pengimejan EOS yang berada di orbit, manakala kedua adalah untuk pemulihan imej satelit. Dalam rangka pertama, tesis ini memperkenalkan saranan baru untuk menganggarkan MTF secara berkesan dengan menganalisis ciri-ciri stokastik pada imej yang diteliti. Untuk merealisasikan matlamat rangka kerja ini; Pertama, tesis ini mencadangkan kaedah segmentasi untuk memilih calon pinggir yang sesuai dari imej untuk anggaran MTF. Kedua, kita membangunkan kaedah pemilihan struktur boleh-suai yang dapat menghindarkan struktur imej yang tidak sesuai dan hanya memilih maklumat struktur yang berguna untuk perkiraan fungsi sebaran titik (PSF). Akhir sekali, tesis ini

mengemukakan kaedah anggaran yang mantap dengan memperkenalkan “spatial prior” yang dapat menyekat hingar, dan memelihara kejelasan dan kesinambungan kernel PSF pada masa yang serentak untuk peroleh model PSF dua dimensi berfideliti tinggi untuk kiraan MTF. Hasil eksperimen menunjukkan bahawa rangka kerja yang dicadangkan adalah praktikal dan berkesan Hasil eksperimen menunjukkan bahawa kerangka kerja yang dicadangkan adalah praktikal dan berkesan, dengan <2.3% ralat relatif pada frekuensi Nyquist berbanding dengan kaedah sedia ada yang mapan.

Dalam kesinambungan rangka kerja pertama, tesis ini menilai algoritma pengukuran MTF yang dicadangkan secara eksperimen sebagai kaedah anggaran kernel kabur untuk penyingkiran kabur. Selanjutnya, tesis ini membentangkan kajian perbandingan mengenai kaedah anggaran kabur yang menggunakan prinsip perwakilan jarang untuk mendalami pemahaman dalam “image prior’ yang sesuai untuk penyingkiran kabur dalam imej satelit optik. Pada hakikatnya, ciri-ciri MTF biasanya memperkenalkan hingar dan kesan alias yang tidak disenangi dalam usaha MTFC yang sedia ada. Maka, dalam rangka kerja kedua, tesis ini mengeksploitasi ciri-ciri tersebut dan menunjukkan bahawa kerangka kerja berdasarkan ‘regularisation’ yang hanya bergantung pada satu sifat imej sahaja adalah tidak memadai untuk mendapatkan hasil pemulihan imej yang memuaskan. Dengan itu, tesis ini membentangkan strategi untuk menghasilkan kaedah pempampasan MTF berfideliti tinggi dengan mencirikan sifat-sifat “local smooth” dan “nonlocal self-similarity” pada imej dalam domain ruang dan frekuensi secara hibrid. Untuk mengurangkan kerumitan komputasi, tesis ini membangunkan satu model statistik cantuman yang mudah dalam domain Curvelet untuk menggabungkan sifat-sifat imej ini. Bagi membolehkan kaedah ‘regularised-based’ pempampasan MTFC ini mudah dikawal dan lebih mantap, tesis ini menggunakan pendekatan “multi-objective bilevel optimization” untuk menyelesaikan masalah MTFC yang pada dasarnya adalah “ill-posed inverse problem”. Hasil eksperimen pada kedua kerangka ini menunjukkan bahawa kaedah yang dicadangkan dapat mencapai prestasi yang signifikan dalam memelihara imej berfideliti ttinggi dengan nilai "Feature similarity (FSIM) index" setinggi 0.99876 berserta dengan kerumitan komputasi yang minimum.

Kata Kunci: Fungsi pemindahan modulasi, Imej penderiaan jarak jauh, "Sparsity priors", Model statistik cantuman berdasarkan "regularization", Fideliti imej.

ACKNOWLEDGEMENTS

Although this Work has been a great personal endeavor over the past several years, there are many people who have been influential in helping me reach this point. I would like to begin by thanking my supervisors, Assoc. Prof. Dr. Chan Chee Seng and Dr. Ong Simying, for their guidance, encouragement, and advice in this Work — and of course their unique ability for tangential thinking that no doubt helped open my mind and formulate new ideas along the way.

During the last year of my Ph.D., I was fortunate enough to spend a few minutes chat over the internet with a friend, whom I haven't keep in touch for more than four years. She is Elena Woo Lai Leng, who reminds me of the virtue of "perseverance". It is a virtue that I was once told is one of my strengths. I wish to express my deepest gratitude to her for the encouraging word, it was a wake-up call that prompts me to continue this Ph.D.

I am grateful to colleagues and friends at the Malaysian Space Agency (MYSA) who provided support, both in terms of providing advice or listening ear, and those who lighten my burden at the workplace. In particular, I would like to mention Wayne Ng Su Wai, Abadi Azhar, Mohd Khairul Hisham Ismail, Asmaliza Zulkifli, Adhwa Amir Tan, and Sharizal Fadlie Sabri who have provided encouragement and necessary distraction and helped to shape my thoughts over these years.

Finally, closer to home, this thesis would not have been possible without my husband, Lee Kong Weng, my special thanks for his constant love, patience, and support throughout the years required to complete my Ph.D. Last but not least, my deepest gratitude to my family for supporting me in every way possible during my studies.

TABLE OF CONTENTS

LIST OF FIGURES

LIST OF TABLES

LIST OF ABBREVIATIONS

1-D	:	One-dimensional
2-D	:	Two-dimensional
BID	:	Blind Image Deconvolution
BC	:	Boundary Condition
CEOS	:	Committee On Earth Observing Satellites
CS	:	Compressed Sensing
CG	:	Conjugate Gradient
CLS	:	Constrained Least-Square
EOS	:	Earth Observation Satellite
ESF	:	Edge Spread Function
FFT	:	Fast Fourier Transform
FSIM	:	Feature-Similarity Index Metric
FIR	:	Finite Impulse Response
FWHM	:	Full Width Half Maximum
GM	:	Gradient Magnitude
GSP	:	Graph Signal Processing
HPID	:	Hyper-Laplacian Prior Image Deconvolution
IQA	:	IMAGE QUALITY ASSESSMENT
ISNR	:	Improvement Of Signal To Noise Ratio
IRLS	:	Iterative Reweighed Least Square
JPG-SR	:	Joint Patch-Group Based Sparse Representation
LIDQA	:	Landsat Image Data Quality Analysis
LPA	:	Local Polynomial Approximation
LRMA	:	Low-Rank Matrix Approximation
LSF	:	Line Spread Function
MAP	:	Maximum A Posteriori
MLD	:	Maximum Likelihood Deconvolution
MTF	:	Modulation Transfer Function
MTFC	:	Modulation Transfer Function Compensation
MBP	:	Multi-Objective Bilevel Programming
MSS	:	Multispectral Scanner System
NLM	:	nonlocal means
NP	:	Nondeterministic Polynomial Time
NNM	:	Nuclear Norm Minimization
OSUT	:	Optical System Under Test
OTF	:	Optical Transfer Function
PSNR	:	Peak Signal-To-Noise Ratio
PC	:	Phase Congruency
PSD	:	Positive Semi-Definite
PSF	:	Point Spread Function
PWS	:	Piecewise Smooth
RER	:	Relative Edge Response
RGTV	:	Reweighted Graph Total Variation

RMSE	:	Root Mean Square Error
SNR	:	Signal To Noise Ratio
SVD	:	Singular Value Decomposition
SVT	:	Singular Value Thresholding
SPID	:	Sparse Prior Image Deconvolution
SD	:	Standard Deviation
SSIM	:	Structural Similarity Index Metric
TM	:	Thematic Mapper
TV	:	Total Variation
WGCV	:	Working Group On Calibration And Validation

LIST OF SYMBOLS

#	:	Number of pixels per pattern
$\overline{\mathcal{F}(.)}$	:	The complex conjugate operator
$\mathcal{F}^{-1}(.)$	:	Inverse FFT
$\ddot{G}$	:	Weighted directed graph
N_j	:	Number of scales
V_z	:	Computes an orthonormal basis $V_z = [v_{1,} v_2, \dots, v_n]$ of
$\hat{X}$	:	Latent low-rank matrix
f_L	:	Lower-level decision,
f_U	:	Upper-level decision
$\tilde{g}, \acute{g}$	:	Sub-image
(u, v)	:	Spatial frequency coordinates
(x, y)	:	Image plane coordinates
$\lvert\xi\rvert$	:	A corona of frequencies
σ^2	:	The variance values
τ	:	Weights
$\otimes$	:	2-D convolution operator
$\circ$	:	Element-wise multiplication operator.
∇	:	Gradient vectors
μ	:	Adjustable parameter
a	:	Along-track direction
c	:	Cross-track direction
$C(f, h)$	:	Cost function
Ƒ	:	Fourier transforms
$\mathcal{F}(.)$	:	FFT
$H(u, v)$	:	Optical transfer function
h	:	Point spread function
j	:	Curvelet scale
K	:	A set of PSF estimate
L	:	Width of the bar pattern
$\boldsymbol{L}$	:	A combinatorial graph Laplacian matrix
$m \times n$	:	The size of an image
$N(u, v)$	:	Noise spectrum
Θ	:	Orientation angle
$\ddot{p}$	:	Total number of potential candidates from sub-images
$P(.)$	:	New spatial function
px	:	Pixel pitch in the image plane
R	:	The radius of the siemens star
$r(x)$	:	*R*-map
S	:	Structure elements
T	:	Texture details
U	:	An orthogonal matrix

β	:	Step size.
γ, α	:	Shape parameters of Generalised Gaussian distribution (GGD)
$\mathbf{\Lambda}$	:	A diagonal matrix
λ	:	Regularization parameter.
$\Pi(.)$	:	Heaviside step function,
F	:	Original image spectrum
G	:	Degraded observed image spectrum
$R(.)$	:	Regularization function denoting image prior
b	:	The observed blurry image in the vector-matrix form of the image degradation model
f	:	Latent image
g	:	Degraded observed in the spatial domain
k	:	Blur kernel in the vector-matrix form of the image degradation model
l	:	Latent sharp image
$\Phi(.)$	:	Data-fidelity function
$\Psi(.)$	:	Regularization function
∇s	:	Final selected salient structures
η	:	Unknown noise in the spatial domain
σ	:	Standard derivation of Gaussian blur
$\ddot{s}$	:	Level of Significance

LIST OF APPENDICES

CHAPTER 1: INTRODUCTION

1.1 Research Overview

Over the decades, remote sensing technology guided by satellite imagery has been a prevailing technique for exploring and obtaining meteorological, geophysical, and biophysical information about the earth, and the effects that human activities have had upon them. With the advancement of technology, more sophisticated passive remote sensing sensors systems are developed to provide high-resolution optical satellite images. This advancement has opened fields of exploration and application, which demand the ever-increasing quality for remotely sensed imageries; solely because detection and quantification of objects, and monitoring of environmental trends require high quality and long term stability of earth observations. Therefore, it is important to have quality assurance in Earth Observation Satellite (EOS) data processing in place to ensure users that the remotely sensed imageries are reliable and suitable for operational use or research. Specifically, in other words, they must ensure the "fitness for purpose" of the delivered EOS data product (Fox, 2010a; WGCV, 2019). Since it is a data product, hence it consists of measurements that require characterisation (WGCV, 2019).

For remote sensing quality assurance to be optimal and widely applicable operationally, it should include the fundamental steps of calibration and validation (Cal/Val) (Teillet, Horler, & O'Neill, 1997; QA4EO, 2010; WGCV, 2019). In the passive imaging (i.e., optical) remote sensing platform Cal/Val initiative, before an EOS is launched into orbit, pre-flight calibration should be conducted to characterize the radiometric and geometric performance of the satellite's imaging sensors. Once the satellite is in orbit, in-flight calibration (also known as post-launch calibration) should be carried out to validate the performance of the satellite's imaging sensors and the quality of the remotely sensed data (Chen, 1996; Fox, 2010b; WGCV, 2019).

The spatial characterisation is one of the key parts of Cal/Val for post-launch optical EOS sensor calibration (Viallefont-robinet et al., 2018). The quantitative information from the spatial characterisation is essential to (1) evaluate the usefulness of delivered EOS data products for image analysis, (2) understand what data level of spatial processing is available from passive remote sensing imaging, (3) evaluate the performance of the in-flight EOS spatial imaging, and (4) determine the stability of delivered EOS data products during commissioning and continuing throughout the mission life of the EOS program (Ryan et al., 2003; WGCV, 2019).

Generally, the characterisation of spatial resolution in most of the passive remote sensing imaging systems is described by the sensor modulation transfer function (MTF) and ground sampling distance (GSD) (Holst, 2017). This is to say, it can be characterized by estimating the MTF value of the system at Nyquist spatial frequency, where its sampling frequency is equal to the inverse of GSD. Here, MTF is defined as the normalized magnitude of the Fourier Transform (FT) for the imaging system's point spread function (PSF). Knowledge of the MTF for a given image acquisition system is fundamentally important since it enables an objective assessment of the imaging performance. Furthermore, the MTF can be utilized through image restoration techniques as an image degradation function to undo the spatial image degradation effect.

Spatial image degradation in remotely sensed imagery could happen while launching into orbit (Haghshenas, 2017), during image acquisition and data transmission, or even throughout its mission time in the orbit. The degradation in sensor performance with time in orbit is generally attributed to material deposition on the sensor optics caused by outgassing from the system in the vacuum condition of space (Rao & Chen, 1994; Loew, 2017; Saiga et al., 2018). For remote sensing optical satellite imaging, image acquisition occurs while orbiting the earth. Because of the satellite's attitude control for maneuvering, the instantaneous field of view (IFOV) of the imaging system can be greater or lesser than the nominal resolution during image capturing. This results in MTF degradation proportional to the ratio of IFOV and GSD during image acquisition (Schott, 2007). Besides, during image acquisition, the imaging system could cause a blurring due to the cumulative (e.g., diffraction, aberrations, focusing errors) effects of the instrumental optics and environmental factors. Moreover, regardless of how well an imaging system is fabricated, it will inevitably suffer from some degree of blur due to uncertainties in fabrication. Blurred images inherently have less information than sharp images, which leads to difficulty when performing image analysis. These types of degradations, therefore, need to be compensated, and they can be compensated using the MTF as a degradation function for that image restoration.

This Work explores solutions from the ill-posed problem of image restoration area to address the current challenges of (1) low precision and temporal sampling frequencies in the existing MTF measurement approach for spatial characterisation and assessment of on-orbit optical satellite imaging and its data products; and (2) the adverse effects (i.e., noise amplification and aliasing) of MTF compensation to improve the spatial quality of delivered optical EOS data products. The contribution of this thesis is threefold; first is the development of a new on-orbit spatial characterisation framework based on stochastic characteristics in the observed image; second is the development of an MTF compensation method for spatial image restoration that exploits the local smooth and nonlocal self-similarity of image properties; third is an insightful study about the usefulness of image priors for spatially varying and invariant blur in optical satellite images.

This chapter gives a brief overview of the research work as above. In the following sections, the research problems motivated by the current challenges, including the objectives, the scope, and the significance of this research will be explained. The correlation among the articles (i.e., Chapter 4 to Chapter 6) in this thesis is organized in Section 1.7, where a brief description of the proposed solution in the respective article is included for an overview.

1.2 Research Motivation

In the year 2009, the second EOS of Malaysia, RazakSAT™, was launched into a near-equatorial orbit to offer imaging opportunities in the equatorial region (SpaceX Successfully Launches Satellite Into Earth Orbit, 2009). Unfortunately, it ceased operation after one year of operation (Subari, 2014). During its mission life, on-orbit spatial quality assessment has been conducted using natural characteristic targets from the nominal image scene as artificial targets are not available for imaging (Wong, 2012). It was reported in (Wong, 2012) that one of the challenges of the work is the difficulty to find suitable edge features due to the condition of the images (i.e., cloud cover, saturation due to high gain setting and low contrast image); only 23 out of 256 datasets were found useful for further analysis. These issues provide a rationale for research to explore alternative or new methods for on-orbit spatial image quality assessment and improvement. In the following subsections, the challenges of the research focus area will be described in greater detail.

1.2.1 On-orbit Spatial Characterisation

Derivation of MTF from remotely sensed imagery for on-orbit spatial characterisation requires the use of specific artificial (i.e., man-made target) or natural targets on the surface of the earth. On-orbit MTF measurement methods are mainly based on artificial targets such as sharp edge (Viallefont-robinet et al., 2018; Pagnutti et al., 2017; Kohm 2004), pulse target (Ryan, 2003; Helder et al., 2006), or bar target (Kaftandjian et al., 1996; Reulke et al., 2006) with different spatial frequencies, and also point target (Helder et al., 2004) were developed and successfully applied to evaluate the spatial qualities of IKONOS (Ryan et al., 2003; Helder et al., 2006), Quickbird (Helder et al., 2004; Helder et al., 2006), OrbView-3 (Kohm 2004), Landsat (Rauchmiller & Schowengerdt, 1988; Schowengerdt et al., 1985; Storey, 2001; Stensaas, 2014; Dennis, 2015; Wenny et al., 2015), SPOT (Viallefont-Robinet & Léger, 2010), KOMPSAT (Lee et al, 2008; Seo et al., 2015; Lee at al., 2016), etc. Figure 1.1 shows a test site with artificial targets situated in the Finnish Geodetic Institute. Note that these targets are engineered with different shapes and sizes, and they are either permanent or portable targets.

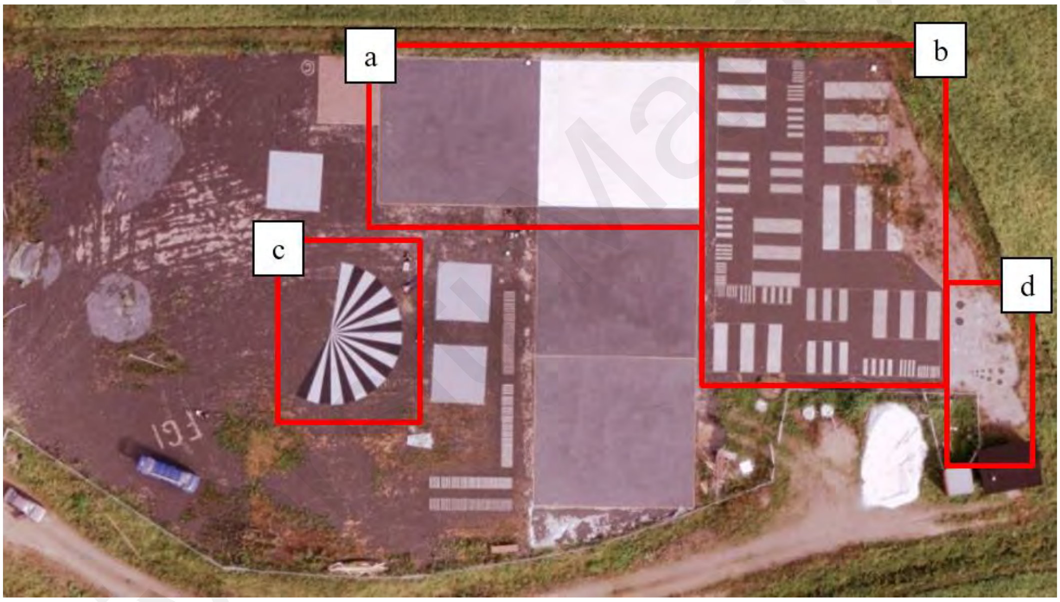

Figure 1.1: The Sjökulla Site at Finnish Geodetic Institute; the artificial target highlighted in the red box is (a) portable edge target, (b) permanent sparse resolution bar target, (c) portable Siemens star target, and (d) permanent point targets.

1.2.1.1 Challenges from measurement target data

Although utilization of the artificial targets in the test site for MTF measurement has been shown to produce quality results, there are not always available or convenient, because their access to the targets is limited. While building own test site can be the solution to access issues, establishing a test site can impose many challenges. This is because building a test site not only requires an amount of cost but finding a suitable site is a non-trivial task. As it must meet selection criteria, such as surface properties of the site (e.g. reflectance factor, etc.), horizontal land, size of land (i.e. the size of the surface area to be sampled is selected depending on the imaging sensor resolution), and altitude of the site location (Berthelot et al., 2008; Santer et al., 2013). The site should be located at a high altitude, far from the ocean, urban and industrial areas, and have easy access. One important criterion that is difficult to meet by equatorial region countries, such as Malaysia, is that the site should have cloud-free and low precipitation characteristics. This is important because the low probability of cloud coverage increases the probability of the EOS imaging the test site at the time of overpass. Since the measurement is strictly depending on the imaged targets that are not guaranteed by weather conditions, this ultimately leads to another challenge, which is the temporal sampling (i.e., how frequently is the area of interest is being imaging.) issue, where measurement data may not always be available.

With the aforementioned limitations, alternatively, one can exploit and use the natural characteristic target found in nominal scenes. For example, as shown in Figure 1.2, one can use the street centerline or bridge in the nominal scene in a pulse target method to estimate its MTF value.

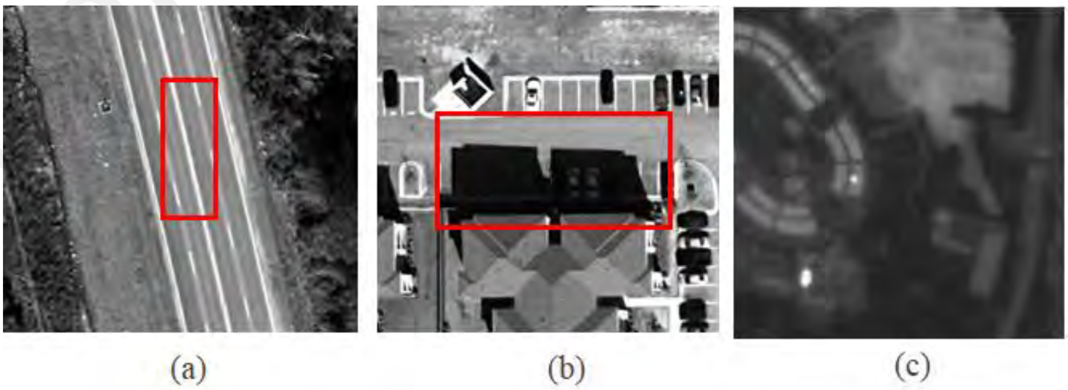

Figure 1.2: In-scene natural targets: (a) a high-resolution sensor image, the street center-line highlighted in the red box can be utilized as a pulse target, (b) a high-resolution sensor image, building shadows highlighted in the red box can be utilized as edge target, and (c) a low-resolution sensor image without an ideal target.

This type of target allows many other measurement opportunities. However, a major concern of using the natural characteristic targets is that they must meet certain criteria such as magnitude, length, noise, and contrast level (Helder et al., 2004, Blanc, 2009; Pagnutti et.al., 2010). Therefore, they are generally required to be manually selected. Most of the time, the manual selected targets may not be ideal, or, in some cases, they are simply not available. Moreover, some optical satellite images are low in spatial resolution, and this resulted in even limited well-separately characteristic targets in these images. Because of this, the MTF measurement methods based on fixed characteristic target is not very suitable for some of the passive remote sensing imaging systems. Due to the constraints imposed by the fixed characteristic issues, there is a need to find an alternative to fixed characteristic targets for MTF measurement, thus, this becomes one of the motivations of this thesis.

1.2.1.2 Challenges from the measurement methods

In general, there are two image-based methods to measure the MTF of passive remote sensing imaging systems. One method is based on fixed characteristic targets as stated previously and the other method is based on random targets.

A long list of literature has been published on MTF measurement based on the fixed characteristic target. For notable representative works, consider those from Ryan et al. (2003), Kohm (2004), Helder et al. (2004), Wenny et al. (2015), Wang et al. (2017), Pagnutti et al. (2017), and Viallefont-Robinet (2018). Contrary to the fixed characteristic target, very little MTF measurement methods based on random targets were found in the literature. Besides, most of the literature proposed random target-based methods (Daniels et al., 1995; Xie, Hwang & Zhang, 2015; Saiga et al., 2018; Kang, Hao & Cheng, 2015; Backman, 2004) are conducted in laboratories and applied to medical and natural (i.e., consumer photography) imaging. Throughout this thesis, the terms ‘natural images’ or ‘natural imaging’ will refer to consumer photography.

Up to now, there have been no detailed studies of the usability of random target on-orbit spatial characterisation. Therefore, this thesis explores a stochastic target-based MTF measurement method, to determine whether it is practical and effective to use for on-orbit spatial characterisation. Note that the term "stochastic" is used instead of "random" because it would be a deterministic process, no random phenomena are involved.

1.2.2 Spatial Image Restoration

As was stated in the research overview, knowledge of the MTF not only provides a quantitative measurement for on-orbit spatial characterisation, but it enables a means to compensate the degradation for spatial image quality improvement. In this context, if one can measure the MTF which represents the degradation function that compromises the sharpness of the remotely sensed images, then the MTF can be utilized to 'undo', or at least reduce the degenerative effects to find the best estimate of an ideal remotely-sensed image. MTF compensation (MTFC) has its root in the image restoration problem (Schowengerdt, 2007), as the name implies, it works by using the measured MTF to compensate (i.e., inverse) for the system impulse response, to amplify the attenuated spatial frequencies for visual enhancement.

1.2.2.1 Challenges in existing Modulation Transfer Function Compensation

The existing MTFC is capable of enhancing the fine spatial detail of an image. However, as MTF exhibits a heavy-tailed distribution, division by the singularities value of MTF will amplify noise at those generally high frequencies. Thus, it introduces noise and unacceptable aliasing in the restored image (Holst, 2017). These degenerative effects compromise the signal-to-noise ratio (SNR) of the image because noise can corrupt the image signal and causes difficulty in image analysis (Stensaas, 2014, Lee et al, 2016).

Figure 1.3 illustrates an example of satellite images before and after preprocessing using the existing MTFC.

(a) (b)

Figure 1.3: Example of satellite images (a) before and (b) after preprocessing using the existing MTFC. It can be noticed that after MTFC, the image shows enhancement. However, it also results in a grainy appearance.

Due to this problem, when acquiring remote sensing datasets, the end-users and data providers need to evaluate the relative importance of image sharpness versus SNR in their application, to decide whether to have a processed dataset with MTFC or without MTFC (Schott, 2007; Stensaas, 2014; Kang, Chung & Kim, 2015). Due to this shortcoming, users usually apply image enhancement techniques to improve the quality of the acquired image for image analysis. Over the years, many research (e.g., Suresh et al., 2018; Kumari et al., 2017; Sajid & Khurshid, 2015; Li, Si, & Jia, 2017) in remote sensing data processing mostly revolved around the enhancement of contrast or removal of noise. These attempts can cause loss of significant information, which affects the remote sensing data comprehensibility and clarity (Suresh et al., 2018, Liang, Li, & Wang, 2012). Image enhancement is mainly concerned with the modification of images to optimize their appearance to the visual system, making it a subjective process (Gonzalez and Woods, 2017). As pointed out by Liang et al. (2012), this process can artificially alter the radiometric properties (such as atmospheric conditions, sun angles, shadows, etc) that characterize the environmental conditions captured in the remotely sensed imageries. Therefore, it is not viable to use image enhancement techniques to improve image quality for assisting scene interpretation tasks before quantitatively estimating the biophysical variables[1] of the image. In this regard, it is worth noting that just how important image restoration is for assuring quality in the remote sensing data processing.

Image restoration, unlike image enhancement, is an objective process where its goal is to reconstruct the original image spectrum from its degraded observed version using prior knowledge of the degradation phenomenon. Despite the importance of image restoration, there remains a paucity of research for MTFC improvement. MTFC is an inverse problem, therefore it is inherently an ill-posed problem, which requires a priori knowledge about the ideal image to alleviate its ill-posedness and stabilize the solution. However, for an application like remote sensing, it is difficult to statistically model the original image or obtain prior information about scenes never imaged before. Therefore, designing effective regularization terms to reflect the image priors for remotely sensed image restoration is one of the challenges to address in this research.

There exist many blind image restoration methods for restoring natural images in the literature, many have demonstrated successful results (e.g., Ren et al., 2016; Zhang, J. et al., 2014b; Schonfeld & Wang, 2019). However, they require a heavy mathematical model to carry out the task effectively and consequently suffer from the complexity of computation. Moreover, the studies are mostly using a priori blur estimation methods, thus they focused on developing a blur kernel estimation method to restore a latent sharp

[1] Biophysical variables in scene interpretation task using remote sensing technology are referring to planimetric location, topographic-bathymetric elevation, color and the spectral signature of features, vegetation chlorophyll absorption characteristics, vegetation biomass, vegetation moisture content, soil moisture content, surface temperature, and texture or surface roughness (Jensen, 1983; Laing et al. 2012).

image. Relatively to blind image restoration methods, little research has been carried out on non-blind image restoration methods. In practice, even if the degradation function (i.e., blur kernel) from a blurry image in the blind image restoration problem could be perfectly estimated, restoring coherent and high-frequency image details can still be very difficult. Hence, the development of an MTFC that exhibits the most appropriate compromise among computational complexity, reliability, and robustness to noise is motivated in this research.

1.2.2.2 Challenges in spatial deblurring problem

The satellite imaging system is typically designed to be a linear spatially-invariant system (Holst, 2017); hence it is natural to assume the blur that occurred in the observed image would be spatially invariant. However, in a practical situation of passive remote sensing imaging, many factors can extrinsically or intrinsically cause image blur (Haghshenas, 2017). Any of these factors could make motion blur spatially varying which makes its estimation and removal highly difficult. Figure 1.4 shows an example of a satellite image that is degraded by spatially varying blurs.

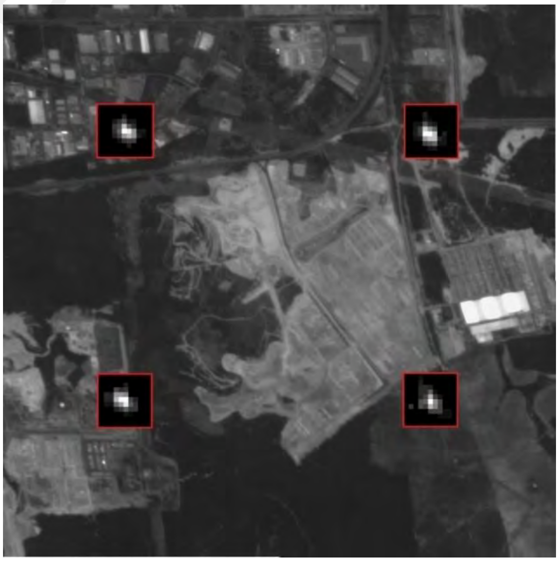

Figure 1.4: Example of a satellite image with a spatially varying blur; The red boxes emphasize the close-up view of the spatial varying blur kernel of the satellite image.

So far, however, there has been too little attention has been paid to the study that includes spatially varying blur estimation methods for optical satellite image processing.

The success of Fergus et al., (2006) in single-blind image deblurring that stemmed from the use of various sparse priors has inspired much research in blur kernel estimation for spatial deblurring. Each of the research has shown its importance and usefulness in several domains, and their goal is always to lead to better results than existing ones. Nevertheless, all those techniques (e.g., Ma, Xu, & Zeng, 2017; Zha et al., 2018; Gong et al. 2018) implicate complicated mathematical problems solving strategies, consequently, more complex formulas are developed. To address this challenge, this thesis examines various image priors to study their significance in both spatially-invariant and varying blur removal, and to examine the fact that complex formulations are generally assumed to produce restoration results more effectively.

1.3 Statement of Problem

The existing MTF measurement approach for on-orbit spatial imaging performance evaluation highly relies on the presence and manual identification of a well-separated fixed characteristics target, which confined with stringent criteria and temporal sampling issue to provide accurate measurements (Pagnutti et al., 2010; Lee et al., 2016; Viallefont-Robinet et al., 2018). Besides, it is not suitable for low spatial resolution EOS (Xie et al., 2015). These drawbacks make it a non-versatile approach. Therefore, there is a need to explore an alternative to fixed characteristic target for a versatile and robust MTF measurement approach (i.e. suitable for high, medium, and low spatial resolution optical EOS) in the field of EOS data Cal/Val.

Due to the ill-posedness of MTFC, in practice, restoring a high-quality image from a degraded image is non-trivial, even when using a perfectly estimated MTF, unpleasant artifacts can still appear in the restored image. Consequently, the estimated MTF from the on-orbit spatial characterisation effort has become an optional process in operational use (Albert, 2015; Lee et al., 2016). Many natural image restoration algorithms exist and demonstrate successful results at the price of additional complexity (e.g, Ren et al., 2016; Zha et al., 2018). These shortcomings demand a need for an improved MTFC. Hence, studies to develop an MTFC method that can find a compromise between solution accuracy (i.e., high fidelity data) and computational efficiency are a recognized need for low-level vision processing. In the context of image processing, high fidelity is about the reproduction of an effect (i.e., image) that is very faithful (i.e., as similar as possible) to the original image. An image with high fidelity is an image without adverse artifacts (e.g., noise, aliasing, etc), with rich contrast edges and details as illustrated in Figure 1.5 (f). Figures 1.5 (a) to 1.5(e) depict examples of low fidelity images.

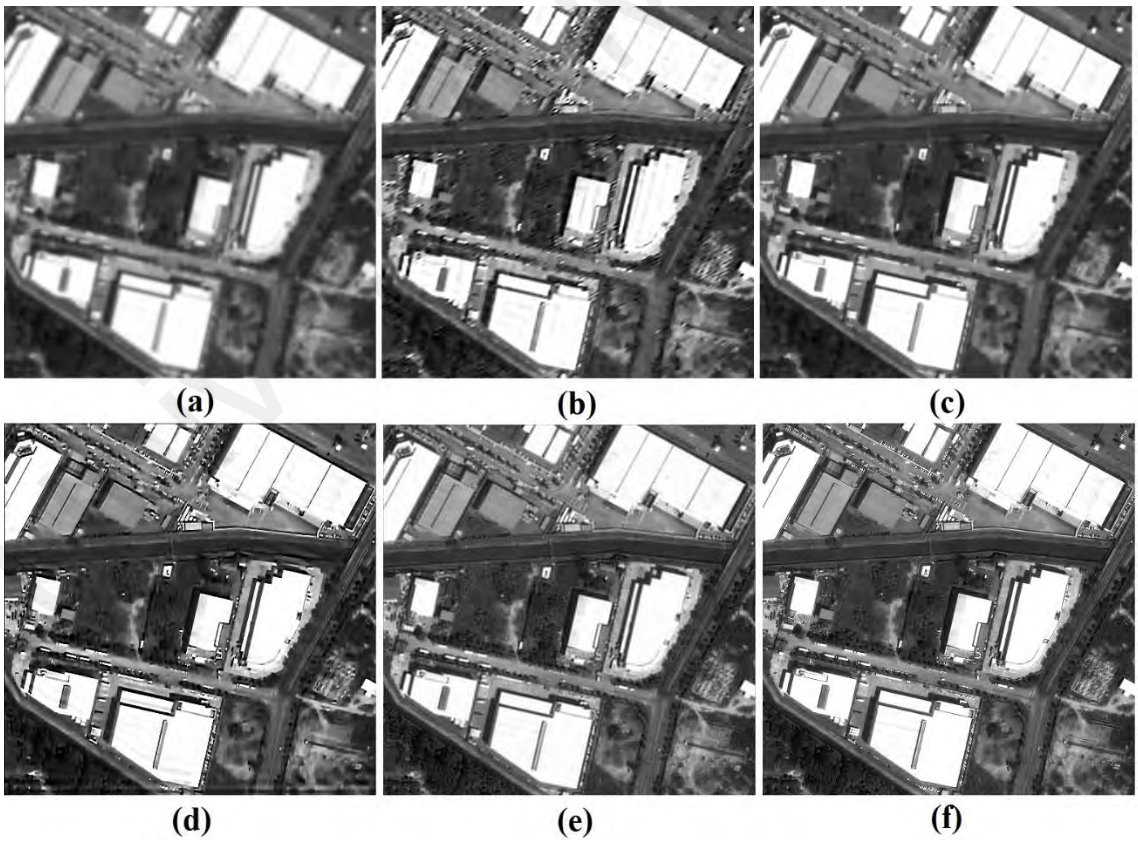

Figure 1.5: Examples of low and high fidelity images; (a) Blur and noisy image, (b) Image with motion blur, (c) Image with over smooth effects (d) Image with aliasing, holo effect, and boundary condition issue, (e) Image with visible noise and aliasing effect, (f) A high fidelity image with rich contrast edges and details.

Furthermore, passive remote sensing imaging, just as any other observation process is never perfect because of the uncertainties caused by extrinsic and intrinsic factors in the imaging chain. The uncertainties could cause defocus and motion blur spatially varying which makes its estimation and removal highly difficult. To date, there is a notable paucity of studies investigating this type of blur in optical satellite image restoration. Therefore, there is a need to conduct a comparative study to gain further understanding of image priors by developing new prior that can adequately handle complex constraints in the solution space.

1.4 Statement of Objectives

This research aims to develop the consolidated framework that encompasses on-orbit spatial image characterisation and restoration methods, to facilitate spatial quality assurance of optical EOS data product processing in a reliable, efficient, and expedient manner that is commensurate with the needs of the users (i.e., data processors, data providers, and end-users).

More specifically, the objectives of this research are as follow:

1) To propose a stochastic target-based MTF measurement framework for a reliable[2] and expedient[3] approach to conducting on-orbit spatial characterisation.

[2] reliable defines dependable to produce accurate and precision measurement (Squara et al., 2020; JCGM 2012); In this framework, relative error and relative standard deviation are used for measurement accuracy and precision, respectively.

[3] In this study, expedient describes a means for attaining an end with flexibility and convenient. For this study, it will be considered flexible and convenient when it is able to overcome the hassle of manual identification and dependency on the presence of a well-separated characteristic target. In another words, it can be conducted without the needs of test site and an automatic method.

2) To evaluate the effectiveness and practicality of using stochastic characteristics targets for On-orbit spatial characterisation.
3) To develop a low[4] computational regularized-based MTFC method that executes an optimal trade-off between noise regularization and detail preservation for high fidelity low-level vision processing of optical EOS data product.
4) To conduct a comparative study on the characteristic of image priors in order to gain further understanding of image priors that appropriate for spatial blur removal in optical satellite images.

1.5 Significance of Research

This research is conducted to provide an insight to estimate the on-orbit MTF conveniently and effectively by measuring the degradation function of the observed image solely based on the properties (i.e., nonlocal self-similarity characteristic) of the observed image, regardless of its features (e.g., straight line, edge, or round). The proposed framework offers an automated approach for spatial characterisation, thus overcomes the constraints in the manual identification process and dependence on the presence of a well-separated characteristic target in the image. In addition, it enables an improvement of spatial image quality through regularized-based MTF compensation.

On-orbit spatial characterisation through the MTF measurement method as proposed above could be used by the engineer or researcher from the satellite development program as a validation process in assessing the quality of the acquired EOS data to ensure its "fitness for purpose" before data dissemination. Furthermore, this method could be used

[4] This work targets on a low computational cost algorithm, which is the processing time to produce the final output. For the purpose of this study, the algorithm is considered low when its processing time is at least tenfold faster than the competing method.

to monitor the quality degradation of the EOS imaging system during commissioning and continuing throughout the life of the EOS program. Furthermore, the proposed techniques in the framework aim to estimate an accurate degradation function in the image restoration model. These techniques, therefore, could be adopted by the researcher and practitioners in the image processing discipline to restore degraded images. The usefulness of these studies is not limited to remote sensing applications, but also other applications such as consumer photography, microscopy, medical, astronomy imaging, etc.

1.6 Scope of the Research

The focus area of this research is the optical EOS data Cal/Val. There are five responsivity domains to be addressed in the Cal/Val process for ensuring EOS delivered product data quality, namely Spatial, Radiometric, Spectral, Temporal, and Polarization (Tansock et al., 2015). This research is focused on spatial responsivity to determine the image sensor performance and EOS data product quality in terms of spatial resolution. The test data used for this research are remotely-sensed images from the optical satellite, a passive remote sensing sensor that measures naturally occurring energy. These images comprise the level 2A product of IKONOS (Dial et al., 2003) and the level-0 product of RazakSAT (ATSB, 2010).

As a measure of the geospatial quality of imagery, the MTF of the system is often used along with the SNR. Of particular interest here are image quality criteria related to spatial resolution performance. Hence, this thesis focuses on the measurement of MTF for on-orbit spatial characterisation. This thesis proposes an on-orbit spatial characterisation based on nonlocal self-similarity of an image, where it employs the two system quality metric as follows: Full-Width Half Maximum of the one dimensional (1-D) PSF and MTF at Nyquist frequency.

Degradation comes in many forms such as blurring, noise, and distortion. However, this research concentrates on compensation for the degradation of spatial image properties caused by blurring only.

1.7 Organization of the Thesis

The remainder of the thesis is organized as follow:

Chapter 2 presents some theoretical knowledge and past studies of **spatial image characterisation and image restoration** that form an important background of the research problem. The purpose of this chapter is to detail the literature work related to the research topic in order to identify and justify the research problem. This chapter starts the discussion by describing the rationale for on-orbit spatial characterisation and its important aspects, including the definition of spatial resolution and its relationship to image sharpness, and the performance quality metric. This chapter describes and critically reviews the relevant method available for spatial image characterisation and image restoration for optical satellite images. After that, this chapter categorizes all available methods and discusses their merits and drawbacks in detail. Finally, to justify the research problems and move on to Chapter 3 to find solutions to the ill-posed problem of image restoration.

Chapter 3 provides a critical review of the **ill-posed problem of blind image deblurring**. This chapter outlines the key ideas and theories from the existing nature image restoration that applicable in solving the research problem. This chapter starts by describing why blind image restoration is a difficult task, due to it being an ill-posed problem. This chapter then discusses how good image prior modeling via the regularization method can create a well-posed image restoration problem. This chapter explores various image deblurring methods, of particular importance, are the structure-texture image decomposition method variational method. The practical issues in an image deblurring design and image quality assessment metric used in the proposed methods are also presented in this chapter. Finally, this chapter concludes the literature review for this thesis.

Chapter 4 present the first framework of this Work which is the **on-orbit spatial characterisation based on stochastic characteristics** of optical satellite images. This chapter introduces a framework that aims to achieve the first and second objectives presented in Section 1.4 of this chapter. For this framework, selection and extraction of reliable structures (i.e., the nonlocal self-similarity properties), and computation costs are critical to ensure accurate MTF measurement. To this end, three strategies are being established in this work: First, to reduce the computation complexity, an effective segmentation method to select the ideal candidates that wholly represent the data is formulated. Second, to remove detrimental structures and obtain useful information for the MTF measurement, this work develops an effective adaptive structure selection method. Third, to preserve the sparsity and continuity of the PSF kernels, this work proposes a robust kernel estimation method by introducing a new total variation (TV) spatial prior to finally obtain a two-dimensional PSF for MTF measurement. For a comprehensive analysis and experimental to evaluate the effectiveness and practicality of the proposed framework, a wide range of real satellite images are being considered.

Chapter 5 presents another research work on the **restoration of spatially blurred optical satellite images**. This research work aims to achieve the fourth objective of this thesis. It is organized in Chapter 5 instead of Chapter 6, since it is an extension of the first framework, which continue to evaluate the effectiveness of the proposed MTF measurement algorithms experimentally as a blur kernel estimation method for image restoration using three different blur groups (i.e., Defocus, Gaussian, and motion blur). Moreover, this work also studies the significance of the two most recent use priors that utilize the principle of sparse representation, namely the graph-based prior by Bai, Cheung, Liu, & Gao, (2019) and enhanced low-rank prior by Ren et al., (2016). Based on the experimental evaluation of the three methods, a comparative study to gain further understanding of image priors that appropriate for blur removal in optical satellite images (i.e., the fourth objective of this thesis) is conducted in this chapter.

Chapter 6 presents the second framework of this Work, which is the **regularization-based MTFC for spatial image quality improvement** using a joint statistical model in the curvelet domain**.** The purpose of this chapter is to propose a solution to achieve the third objective outlined in this thesis. In this framework, this work designs two regularization terms; one that exploits Gaussian priors and hyper-laplacian priors in the hybrid spatial and frequency domain, whereas the other one exploits Laplacian prior in the frequency domain. Later, a simple joint statistical model in the Curvelet domain to combine the two regularization terms is established in this work. In order to have a tractable and robust regularization-based MTFC method, a bilevel optimization approach for MTFC is developed to efficiently solve the underdetermined inverse problem for spatial image quality improvement.

Chapter 7 summarizes the research presented in this thesis. In particular, it concludes the significance of this Work and the limitation of the proposed framework in the field of EOS data Cal/Val. Future research direction is also recommended.

CHAPTER 2: SPATIAL IMAGE CHARACTERISATION AND RESTORATION

This chapter presents extensive background studies of spatial image characterisation and image restoration for optical satellite imageries, and the current knowledge pertaining to the research topic. The purposes of this chapter are to detail the literature related to the research domain and to identify the potential research problems in the field of EOS data calibration and validation, specifically in spatial image characterisation and restoration. This chapter also provides the basic knowledge of the technical elements found in the thesis, including spatial resolution definition, spatial quality measurement metrics, and electro-optical satellite imaging concept.

In section 2.1, this chapter describes the initiative of on-orbit spatial calibration and validation for the EOS mission. In particular, it explains what defines a spatial resolution and its importance. Furthermore, it describes the quality metrics related to on-orbit spatial characterisation and reviews its application to the assessment of EOS imaging system performance. Section 2.2 presents approaches to on-orbit spatial characterisation. In this section, this chapter explains and reviews the generic MTF measurement methods that have been used operationally in the past and current EOS program, and outlined their advantages and disadvantages. In section 2.3, this chapter discusses the spatial image restoration methods for optical satellite images. The discussion is organized from two aspects. Firstly, the introduction of the degradation models, where it briefly explains the sources of degradation and its model. Secondly, the related works and limitations of the generic spatial image restoration methods that have been used for optical satellite image spatial quality improvement in real operation. Finally, section 2.4 lists the identified current research issues in the on-orbit spatial characterisation and image restoration and provides the concluding remarks.

2.1 On-orbit Spatial Calibration and Validation

The first launched of Landsat Multispectral Scanner System (MSS) sensor in the year 1972 initiated the modern era of earth observation from space when it provides a systematic set of synoptic, high resolution remotely sensed imagery of the earth's surface to the world scientific community (Schowengerdt & Slater, 1972). Since then, there have been series of EOS, dedicated to applications that cover various domains, from meteorology to surveillance and mapping, disseminating images with spatial resolution ranging from several kilometers to several tens of centimeters.

With the continuing advancement, expertise in the exploitation and processing of such images is also increasing, which triggers a growing need for assessing the performance of the imaging system. As such, in 1984, the Working Group on Calibration and Validation (WGCV) under the Committee on Earth Observing Satellites (CEOS) was established. The mission of WGCV is to ensure long-term confidence in the quality of EOS delivered product data (WGCV, 2019). There are five responsivity domains to be addressed in the Cal/Val process for ensuring the delivered EOS product data quality. One of these is spatial responsivity (Tansock, Thurgood & Larsen, 2003; Morain & Budge, 2004).

This section presents the post-launch EOS spatial Cal/Val criteria related to spatial responsivity. The spatial responsivity domain includes calibration parameters that quantify spatial figures of merit for an optical sensor. The spatial resolution is one of the optical sensor parameters often mentioned, nevertheless, also one that is least understood. Hence, this section provides some basic knowledge and principles about spatial resolution and its relationship with image quality in the following subsections.

2.1.1 Defining Spatial Resolution

Spatial resolution is often used to describe the smallest discernable object within an image. But, is the spatial resolution the smallest object that can be discerned in the imagery? As it is well known that an optical remote sensing sensor is possible to detect considerably smaller objects than the ground instantaneous field of view (GIFOV[5]) if there is adequate contrast compared to the surrounding background (Schowengerdt, 2007, Reulke & Eckardt, 2013). Even though such objects may be detectable, they are not necessarily recognizable, except by the general context of the image (e.g., the object detected in the observed scene may be known as a traffic path but cannot be recognized whether a road or bridge.) The Innovative Imaging and Research Corporation (I2R), therefore under the request of the United States Geological Survey (USGS) has prepared a guide called *Guide to Digital Imagery Spatial Resolution* to help the remote sensing community to understand how certain image specification parameters affect spatial resolution (I2R, 2018). According to the Guide by I2R (2018), "Spatial resolution determines the smallest discernable feature within an image (Holst, 2017). Often, the spatial resolution of remotely sensed imagery is described only in terms of pixel spacing, or GSD" (p.2).

GSD is an image quality measurement involving the pixel size, focal length, and altitude (i.e., the flight height of a satellite imaging system to imaged object), as illustrated in Figure 2.1. In remote sensing, image sampling refers to the conversion of an observed continuous spatial signal into a discrete and digitized image. The sampling rate is controlled by the size of the sensor's detectors and optics. The GSD is determined by the distance between the sensor and the object being imaged, and the focal length of the

[5] GIFOV can be defined as the geometric size of the image projected by the detector on the ground through the optical system (Schott, 2007).

sensor; it is the distance between two consecutive pixels centered measured on the ground (Holst, 2017). As explained by Slater (1980) in Schowengerdt (2007), the digitized image is comprising of a grid of pixels that is achieved by a combination of sensor platform scanning direction in the cross-track direction and along-track direction.

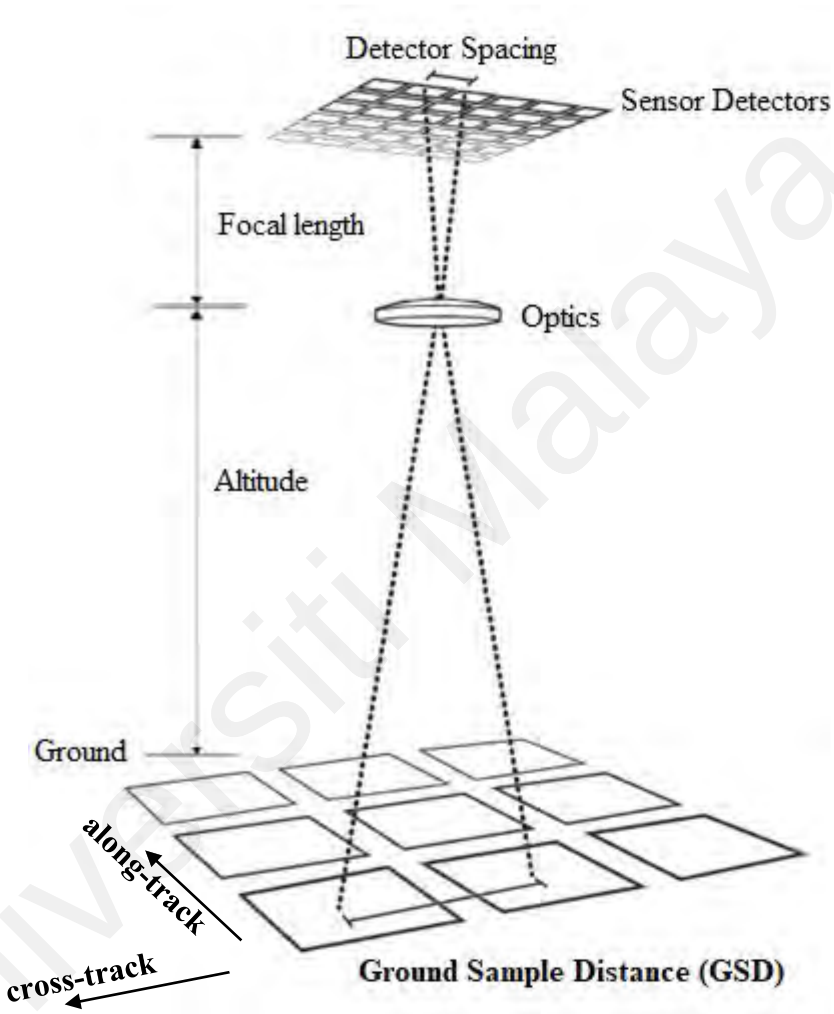

Figure 2.1: Illustration of Ground Sample Distance.

While GSD is significant, it only represents a single aspect of spatial resolution. There are other important features that affect image resolution quality and interpretability. One of them is image sharpness. Image sharpness can be defined in several different ways. Before further discussion, it is better to understand what happens when a passive remote sensing imager acquires an image.

Passive remote sensing imaging is a process that converts solar radiance that either reflected or emitted from the scene into an image of radiance spatial distribution. When an electro-optical imaging system measures the reflected or scattered light from a single point, or point source, the light is not acquired by a single detector. Rather the light is spread over and measured by several detectors (See Figure 2.1). This point source system response is the impulse response resulted from the measurement system (i.e. detectors and optics) of an electro-optical imaging system (Scott, 2007; Holst 2017). The impulse response is called PSF.

The PSF can accurately describe the spatial responsivity of the sensor by measuring how sharp an imaging system can acquire imagery. Hence, it should be noted that the spatial resolution information cannot be fully captured by only using GSD; it also depends on how well an imaging system is focused during image capturing. Figure 2.2 illustrates the effect of the imaging system with a response to various image sharpness. Based on the visual inspection, these two images can have the same GSD, but with different levels of image sharpness, they can look very different.

(a) (b)

Figure 2.2: Two images with the same GSD of 15m but different levels of image sharpness; (a) Image is in focus, (b) Image is blurry, it has a poorer image sharpness compared to (a).

It is important to appreciate the spatial characteristics of an image, particularly if the data is to be used for image analysis. A more detailed account of why the spatial resolution is important will be explained in the next subsection.

2.1.2 Importance of Spatial Resolution

Spatial resolution can influence the usefulness of a delivered product dataset for different applications of remote sensing technology (Irons et al. 1985; Schowengerdt, 2007; Lisani, Michel, Morel, Petro, & Sbert, 2016). For example, in meteorology, this application may require a relatively low spatial resolution, as it focuses on features that cover a large area, while others like environmental assessment and mapping applications may require the highest possible spatial resolution because they involve the identification of small features in a particular area.

It is important to understand the technical characteristics of image data before initializing an image analysis. Understanding can help a person's ability to extract useful information from imagery. Furthermore, it can help in optimizing the amount of data needed, ensuring image quality assurance, and even driving camera design (Reulke & Eckardt, 2013).

An understanding of the effects of GSD and image sharpness can help EOS imager developers and EOS data end-users in different ways. For EOS developers, it can guide data acquisition parameters, such as acquisition height or image stabilization requirements to improve the development of the next EOS program. For example, they can develop image sensors with improved optics. For EOS data providers and end-users, this knowledge can help to decide whether to trade GSD for image sharpness when acquiring datasets. Such circumstances occurred when the spatial quality of the acquired data is compromised by generative effects such as blur. There exist image sharpening algorithms that reduce blur for spatial quality improvement. However, a sharper image is not always a better image. Datasets with limited detector sensors or inherently limited detection sensitivity can be over-sharpened and will appear pixelated, or aliased. Aliasing causes fringing patterns, such as Moiré patterns. These artifacts will appear in an image even though they are not physically present in a scene. Typically, a blurrier dataset that has a smaller GSD could provide the same level of detail as a sharpened, slightly aliased dataset that has a larger GSD (Reulke & Eckardt, 2013). In such cases, end-users may prefer datasets with larger GSD because it covers a larger area of interest, despite the noise.

In addition, spatial resolution is an important component in the National Imagery Interpretability Rating Scale (NIIRS) (Leachtenauer, 1996; Colburn et al, 1996) that is used by the National Geospatial-Intelligence Agency to assess image utility (Pike, 2019). The NIIRS concept provides a means to directly quantify the interpretability and the usefulness of remote sensing imagery for scene interpretation tasks (Pike, 2019).

While image sharpness is an important feature that affects spatial image quality for scene interpretability, it is a subjective parameter for imaging system performance measures. Hence, the next subsection will present the key calibration parameters in spatial responsivity that characterize the spatial resolution objectively.

2.1.3 Quantifying Spatial Resolution

Spatial resolution can be quantified using either spatial data or spatial frequency data. If the assessment is conducted using spatial data, then it is in the spatial domain, where the data is measured as a function of x and y in a spatial coordinate plane. Alternatively, if the assessment is conducted using spatial frequency data, then it is in the frequency domain using Fourier analysis, where the data is measured as a function of u and v in spatial frequency coordinate. Among others, Full Width Half Maximum (FWHM) of the one dimensional (1-D) PSF and Relative Edge Response (RER) are the most widely used electro-optical remote sensing system quality metric in the spatial domain, whereas the MTF at Nyquist frequency is the most commonly used in the frequency domain (Pagnutti et al., 2017; I2R, 2018; Viallefont-robinet et al., 2018). These quality metrics form the basis for defining the sharpness of an image. They have been used in real satellite operation to evaluate the imaging system performance of satellite such as IKONOS (Ryan et al., 2003; Xu & Schowengerdt, 2003; Helder et al., 2004), SPOT 5 (Léger, Viallefont, Hillairet, & Meygret, 2003), QuickBird (Blonski, 2004; Helder et al., 2004), OrbView (Kohm, 2004) and Landsat (Schowengerdt et al., 1985; Storey, 2001). To date, they are still being used by the recent satellites, such as Landsat 8 (Wenny et al., 2015), KOMPSAT-3A (Lee et al., 2016), MODIS (Choi, Xiong, & Wang, 2014; Wang, Xiong, & Choi, 2014), Sentinel-2 (Francesconi, Lonjou, & Lafrance, 2017), THEOS (Khetkeeree & Liangrocapart, 2018), and SPOT 7 (Wu, Luo, Zhang, Guo, & He, 2018). The following subsections will first explain the spatial domain measures and are followed by frequency domain measures.

2.1.3.1 Spatial domain measures

Imaging systems are sensitive to changes at all spatial frequencies. Hence, the inevitably imperfect imaging behavior of an optical system can produce blurred (or spread out) function depending on the input signal source of the original imaged scene (Holst, 2017). In optical imaging, when the source of the input signal is a single point source, the image is scanned to produce the PSF in two-dimensional (2-D). Whereas, when the source of the input signal is from a collection of point sources that formed a line or an edge, the image is scanned to produce Line Spread Function (LSF) or Edge Spread Function (ESF) in 1-D. Figure 2.3 illustrates the variation of the spread function of a point, line, and edge.

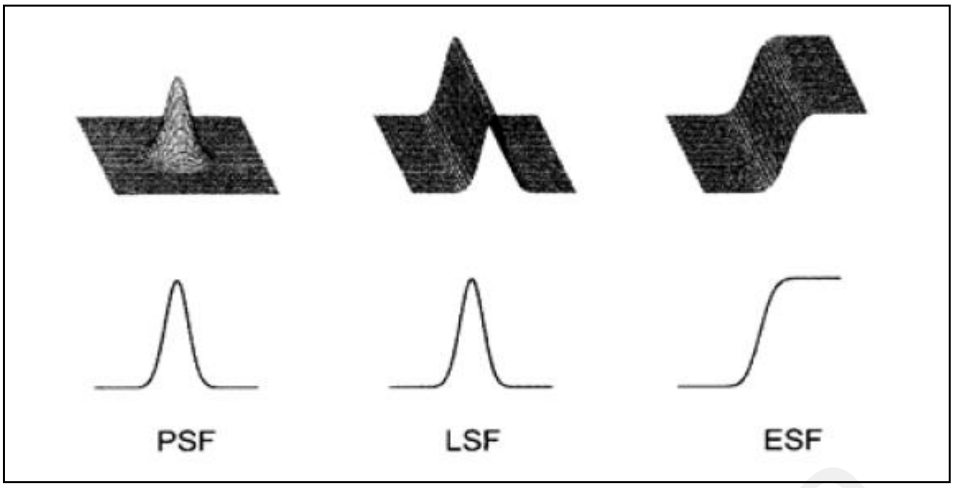

Figure 2.3: Variation of spread function (Boreman, 2001)

In practice, due to SNR and sampling considerations, it is very difficult to directly measure the 2-D PSF of an imaging system (Park, Schowengerdt, & Kaczynski, 1984; Helder et al., 2004). Compare to a point source in 2-D PSF, the light source level of LSF and ESF in the image are greater, therefore, they are often much easier to measure. Nevertheless, they must be measured in multiple directions to determine whether there is an asymmetry in the PSF (Schowengerdt, 2007). Before proceeding to describe the FWHM of 1-D PS, this subsection will first describe the RER of ESF, because the derivation of a 1-D PSF requires the introduction of ESF.

Relative Edge Response (RER): An edge in an image excites imaging response systems and results in an edge response, this edge response is called edge spread function (ESF). This process is mathematically equivalent to convolving the system impulse response with the edge (Gaskill 1978; Goodman 2008; Boreman, 2011). A common spatial performance metric based on the ESF is the Relative Edge Response (RER). The RER is defined as the slope (steepness) of the normalized ESF evaluated at ± 0.5 pixels of the nominal edge location (Schott, 2007). It represents how an imaging system responds to a change in contrast over one pixel. A steeper edge slope produces higher

RER indicates a sharper image, whereas lower RER values indicate a blurrier image. Figure 2.4 illustrates the measurement of RER from a normalized ESF.

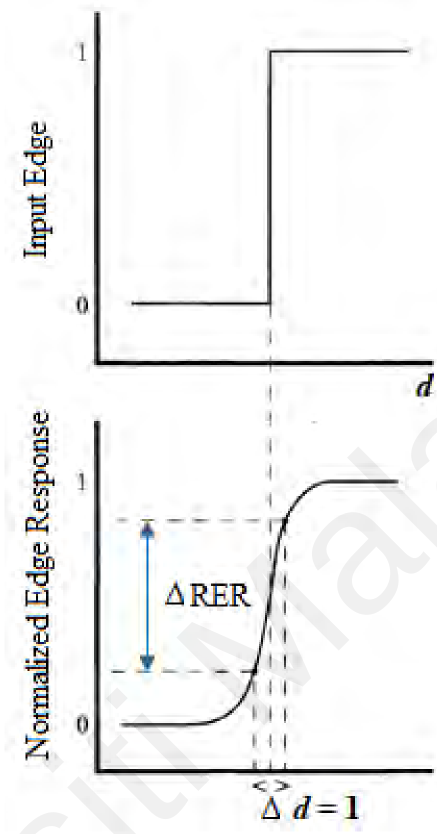

Figure 2.4: Illustration of RER. Δ RER is the region where the slope of normalized edge response is calculated at ± 0.5 pixels (i.e. within Δ *d* = 1) of the nominal edge location.

Full-Width Half Maximum (FWHM) of one-dimensional (1-D) PSF: As explained in subsection 2.1.3.1, it is difficult to directly measure the 2-D PSF. Nevertheless, it can be measured via its 1-D representation. In the optical image formation theory, a 1-D LSF is a projection of the 2-D PSF along the edge. Since the satellite imaging system is typically an anisotropic PSF system; hence a single LSF can represent the 1-D PSF itself. The LSF can be calculated by taking the derivative of normalized ESF (Gaskill, 1978; Boreman, 2001). The width of the LSF at half the height (the 50% point) is called the Full-Width Half Maximum (FWHM). The FWHM of the LSF represents the width of the integral of the system PSF in one direction as illustrated in Figure 2.5. The width is the spatial measure of image sharpness that quantifies the spatial image quality.

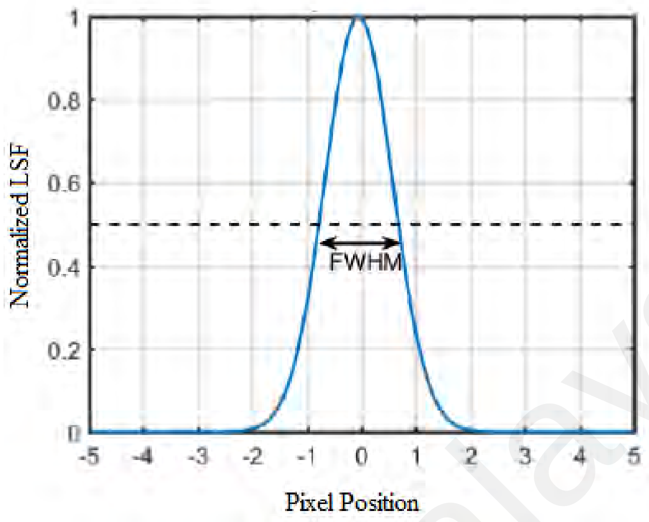

Figure 2.5: Illustration of FWHM of 1-D PSF.

In addition to LSF and ESF, there is another representation of the spatial response that is calculated via the Fourier transform (FT) of a PSF. The detailed description is described in the next subsection.

2.1.3.2 Frequency domain measure

Spatial performance can be quantified in the frequency domain using the MTF (Gaskill, 1978; Boreman, 2001; Goodman, 2008; Holst, 2017). The MTF measures the change in contrast, or modulation, of an optical system's response at each spatial frequency. It is defined as the normalized magnitude of the FT for the imaging system's PSF (Gaskill, 1978). If the PSF is circularly symmetric, then its frequency response will also be circularly symmetric. By applying the FT to a radial slice of the PSF, a 1-D MTF (Boreman 2001, Schott, 2007) can be obtained.

MTF at Nyquist Frequency: The MTF value at the Nyquist frequency is a common measure of image sharpness (Boreman 2011). This value provides a measure of resolvable contrast at the highest 'alias-free' spatial frequency. Figure 2.6 illustrates a sample of an MTF curve with highlighted Nyquist Frequency.

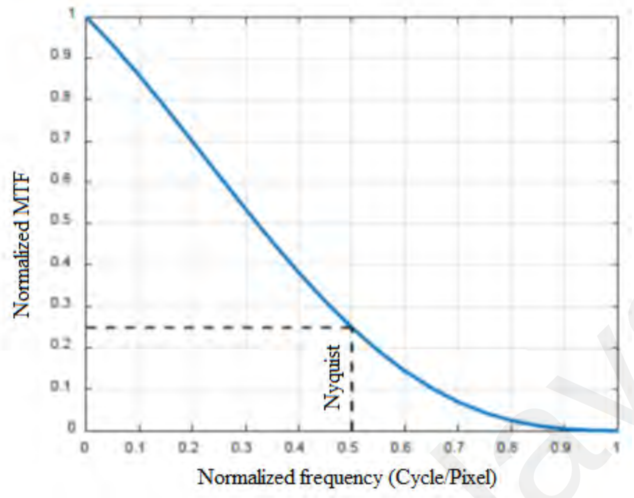

Figure 2.6: Illustration of the MTF curve showing Nyquist frequency.

The Nyquist frequency in Figure 2.6 is defined as half the sampling rate of the frequency, which is 0.5 cycle/pixel, and the sampling frequency is equal to the inverse of GSD. The following table summarized the spatial resolution metrics in both domains:

Table 2.1: Summary of spatial resolution metrics

Domain	Parameter	Description	Shortcomings	Measurements
Spatial	FWHM of the 1-D PSF / LSF	▪ A measure of sharpness	▪ Only one measurement.	Direct measure from 2-D PSF; or derived from a line source or derivative of edge response. <u>Common units:</u> meters or pixels
	Relative Edge Response (RER)	▪ A measure of contrast change over one pixel on a normalized edge response. ▪ A measure of sharpness. ▪ Varies with the inverse of LSF FWHM	▪ Only one measurement typically at the mid-frequency range.	Derived from edge response within ±0.5 pixels. <u>Common units:</u> dimensionless

Table 2.1, Continued.

Domain	Parameter	Description	Shortcomings	Measurements
Frequency	MTF at Nyquist frequency	▪ Measure the MTF value at Nyquist Frequency ▪ A measure of sharpness and aliasing	▪ Only one parameter. ▪ Does not describe the MTF at midrange and lower spatial frequencies.	Normalized MTF value at Nyquist frequency. <u>Common units:</u> dimensionless

Based on the description of spatial and frequency domain measures in this subsection, it is obvious that these quality metric terms are related to each other mathematically. Hence, moving on, the relation among these quality metrics will be outlined.

2.1.4 Image Sharpness Measure Relationships

As pointed by Schowengerdt (2007), an important assumption in remote sensing electro-optical imaging is that the net 2-D sensor PSF_{net} at the image plane coordinates (x, y) is given by a product of two 1-D PSFs in the cross-track, and along-track directions

$$PSF_{net}(x, y) = PSF_c(x)PSF_a(y). \quad (2.1)$$

where c and a are the cross-track and along-track direction as illustrated in Figure 2.1. PSF_{net} consists of several components. First, the optical PSF, which is induced by the optics. Then, the image formed by the optics on the detectors may in some cases move during the integration time for each pixel; this introduces an image motion PSF. After that, the detector adds additional blurring due to the detector PSF. Last, the detected signal is further degraded by the electronics PSF (Schowengerdt, 2007; Schott, 2007). For simplicity, throughout this thesis, PSF will be used instead of PSF_{net}.

As explained in subsection 2.1.3.1., the LSF is the derivative of the ESF, both being a 1-D function, which reveals that 1-D LSF is a projection of the 2-D PSF along the edge. Hence, the LSF in two orthogonal directions in terms of the PSF can be written as follows,

$$LSF_c(x) = \int_{-\infty}^{\infty} PSF(x,y)dy, \quad LSF_a(y) = \int_{-\infty}^{\infty} PSF(x,y)dx. \tag{2.2}$$

Furthermore, the ESF in terms of the LSF can be written as follows,

$$ESF_c(x) = \int_{-\infty}^{x} LSF_c(\alpha)d\alpha, \quad ESF_a(y) = \int_{-\infty}^{y} LSF_a(\alpha)d\alpha. \tag{2.3}$$

Taking the derivation of Equation 2.3, an expression for the LSF can be obtained as follows

$$LSF_c(x) = \frac{d}{dx}ESF_c\,(x), \quad LSF_i(y) = \frac{d}{dy}ESF_a(y). \tag{2.4}$$

The FT of the LSF in Equation 2.4 is the MTF, which can be defined as

$$MTF(u) = \int_{-\infty}^{\infty} LSF(x).e^{-i2\pi vx}dx, \;\; MTF(v) = \int_{-\infty}^{\infty} LSF(y).e^{-i2\pi vy}dy. \tag{2.5}$$

where i is a complex number, u and v are the spatial frequency coordinates.

Figure 2.7 shows several terms from both spatial and frequency domain measures, and generally outlines how they relate to each other mathematically. Note the reduction of the 2-D PSF to the 1-D ESF or LSF is irreversible, which means it is not possible to recover the PSF from the ESF or LSF. Thus, the latter is often measured in at least two directions (i.e., cross-track and along-track direction) to establish any asymmetry. In practice, the line or edge response is usually measured rather than the point response. The mathematical relations among these spread functions established the baseline knowledge for spatial characterisation, they have been used to assess the spatial performance of the EOS imaging system in real operation of the satellite over the decades.

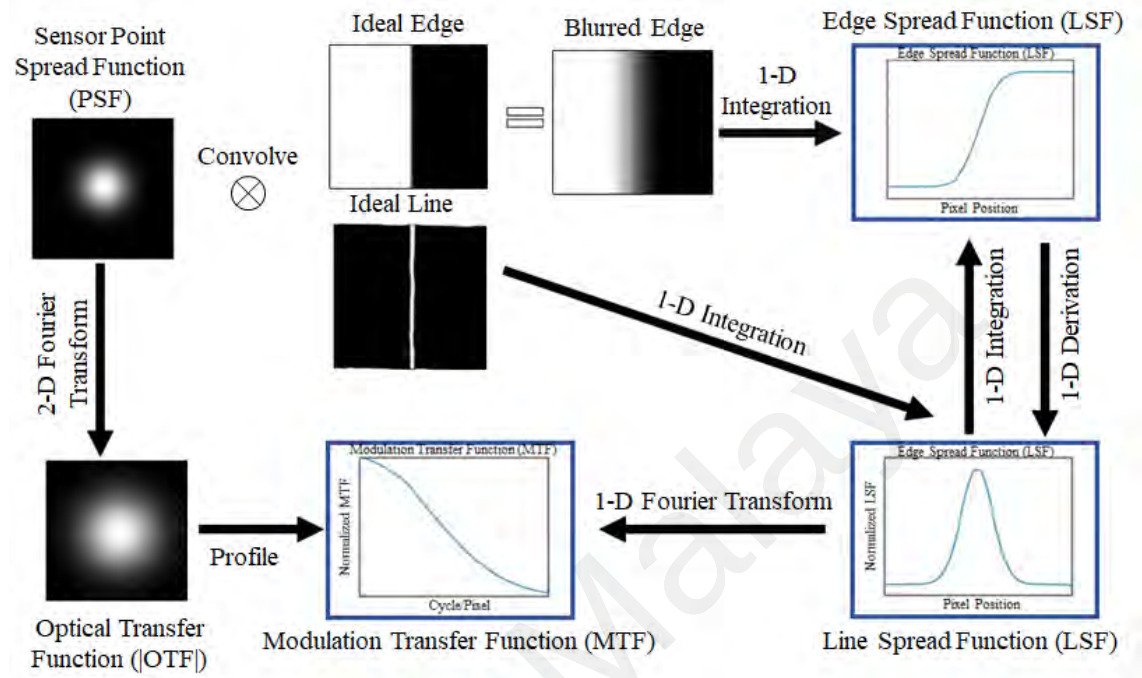

Figure 2.7: The mathematical relations among various representations of optical spatial data and spatial frequency response.

This section has explained and reviewed the key aspects of on-orbit spatial calibration and validation. The section that follows will move on to describe the philosophy of approaches used for on-orbit spatial characterisation as well as their related work.

2.2 Approaches to On-orbit Spatial Characterisation

In order to meet the goal of post-launch calibration and validation, some sensor designs incorporate onboard calibration instruments to facilitate on-orbit calibration. From the literature, only a very limited number of past and current sensors (Tansock, 2015) have an onboard calibration instrument that designed with the SNR assessment capability; and Based on the current literature, none of them has capabilities for on-orbit spatial assessment Onboard calibrators can provide good temporal sampling with high precision for sensor responses temporal trends (Thenkabail, 2015). However, they add significantly to the system complexity and cost of a satellite mission. Moreover, they are susceptible to degradation (i.e., system performance) over time. Fortunately, an alternative called the vicarious calibration technique is made possible by taking in-situ measurements on the ground during satellite overpasses (Thome, 2004). Most often, the vicarious technique is employed based on the earth-viewing approach using an image, or a combination of images. These images are selected when the imaged landscape offers certain properties, such as, well-marked contrast or on the contrary, spatial homogeneity, whose knowledge or modeling permits the assessment of these parameters.

Vicarious calibration, according to WGCV of CEOS (Vicarious calibration, 2013) is referred to as "techniques that make use of natural or artificial targets on the surface of the Earth for the post-launch calibration of sensors. Usually, these targets are imaged in near-coincident fashion by the sensor to be calibrated and by one or more well-calibrated sensors from satellite or aircraft platforms or on the ground".

Vicarious techniques are useful for on-orbit calibration because they are independent of pre-flight calibration and onboard calibrators. However, these techniques also have some drawbacks, where they tend to yield lower precision for high accuracy methods measurement and have lower temporal sampling frequencies (Tansock et al., 2015; Thenkabail, 2015). Despite those drawbacks, over the last 10-20 years, vicarious calibration has become widely adopted as the means to provide independent quality assurance of remotely sensed data from spaceborne sensors. There is a long list of on-orbit spatial characterisation that utilized the vicarious techniques, some notable work from the literature are those from Rauchmille & Schowengerdt (1988), Storey (2001), Helder et al. (2004), Pagnutii et al. (2010), Lee et al. (2016), Qian et al. (2017), and Viallefont-robinet et al. (2018).

The predominant vicarious approach is with regards to the measurement, on satellite overpass days, of pertinent surface and atmospheric optical properties at terrestrial sites with suitable characteristics to estimate (Thome, 2004). Terrestrial sites such as lakebeds with the bridge are most used as vicarious calibration targets for MTF measurement (Blanc, 2009; Calibration Test Sites Selection and Characterisation, 2019), for example, the Chesapeake Bay Bridge-Tunnel, San Mateo Bridge, and Lake Pontchartrain Causeway in the USA. Other terrestrial surfaces from a different country that have been used for this purpose include Jiaozhou Bay Bridge in Shandong Province, China. An alternative to natural targets for vicarious calibration is artificial targets. Usually, these are man-made targets such as point light sources, edges, or rectangular pulses that are fixed and deployable on the ground. Some of the popular artificial targets are summarized in Table 2.2. Figure 2.2 illustrates the example of natural targets and artificial targets.

Table 2.2: Artificial Targets

Target Name, Location	Corresponding MTF Cal/Val Mission	Appropriate GSD
Stennis Spatial Targets, Mississippi, USA	QuickBird, OrbView	GSD < 2.5 – 5 meters
Baotou, Inner Mongolia, China	Landsat 8	GSD < 50 meters
Big Spring, Texas, USA	IKONOS	GSD < 5 – 10 meters
Sjökulla site, Sjökulla, Finland	HR/EHR spaceborne system	GSD from 3 cm to 50 cm
Fort Huachuca, Arizona, USA	SPOT 5	10-15 cm < GSD < 1 - 3 m
Salon de Provence, France	ALOS PRISM, SPOT 5	GSD < 5 – 10 meters
Peng-Hu, Pescadores Islands, Taiwan	FORMOSAT	GSD < 2.5 – 5 meters

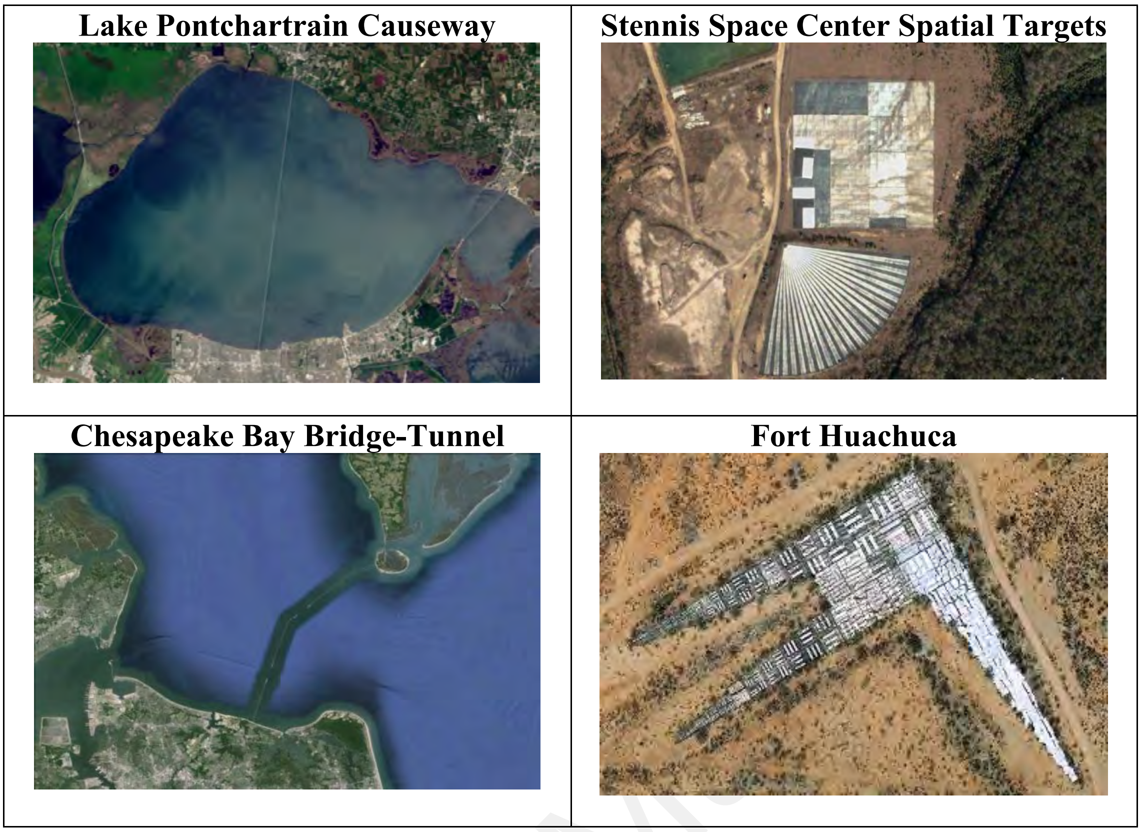

(a) Natural Target (b) Artificial Target

Figure 2.8: Examples of natural targets and artificial targets. Column (a) shows two natural targets; The Lake Pontchartrain Causeway (Top) in Louisiana, USA has been used in the Cal/Val mission of the Landsat series program for decades; whereas the Chesapeake Bay Bridge-Tunnel (Bottom) is used for the Landsat-7 program. Column (b) shows two artificial targets, one at the Stennis Space Center (Top), these targets have been used for QuickBird and Orbview Cal/Val Mission. The other one (Bottom) is at Fort Huachuca, this target was used in the SPOT 5 Cal/Val mission.

Spatial resolution measures related to the MTF are gaining widespread acceptance in the electro-optical instrumentation community for outer space programs since the year 1980s (United Nations Digitally Library, 1980). Since then, its measurement approach has been used for numerous space sensors (as mentioned in subsection 2.1.3), and to date, this approach is still considered the best approach to quantify the spatial image quality of a passive remote sensing imaging system (Viallefont-robinet et al., 2018). The philosophy of this measurement approach in the following subsections.

2.2.1 MTF Measurement Methods

There are many known methods that can be used for measuring the MTF of an imaging system. One example, the Sinusoidal Input method by Coltman (1954) of which is a typical approach that has been to obtain MTF. However, for an EOS that is already launched to the orbit, the Sinusoidal Input method and few of the known methods (Masaoka et al., 2014; Kuhls-Gilcris, Bednarek & Rudin, 2010; Anam et al., 2019) are not applicable.

As the EOS imaging system that is to be evaluated is already on the orbit, therefore, the appropriate and practical way to measure its MTF for spatial quality evaluation is by vicarious approach, where the MTF is determined from the remotely sensed images using specific artificial or natural targets on the ground (i.e. earth surface). These targets have been briefly described in the introduction of this section.

In general, there are two image-based methods to measure the MTF of EOS imaging systems. One method is based on fixed characteristic targets and the other method is based on stochastic targets. The artificial and natural targets are typically fixed-characteristic targets. Based on the literature review, the fixed-characteristic targets are the more commonly used target for MTF measurement as compared to the stochastic targets. The subsections that follow will provide and review the related works that use these targets for MTF measurement and their methods.

2.2.1.1 Fixed-characteristics target-based

There is an extensive work in MTF measurement based on fixed-characteristic dated since the 1980s when the National Aeronautics and Space Administration (NASA) conducted the Landsat Image Data Quality Analysis (LIDQA) program to quantify the performance of the Thematic Mapper (TM) on Landsat-4 (McGillem et al., 1983). The fixed-characteristics targets are ground targets with well-separated characteristics such as imaging points, lines, and edges. Derivation of MTF from these well-separated characteristics is as explained in subsection 2.1.4. Depending on the spatial resolution of the imaging systems, the types of useful targets range from engineered fixed and deployable targets to natural targets such as agricultural and urban features. As presented in the introduction of this section, there are a few independent, comprehensive MTF evaluation sites that are currently available in countries such as the USA, China, etc.

As proposed by Léger et al. (2004), measurement targets for MTF assessment can be categorized into four types: the edge targets, the impulse targets, the pulse targets, and the periodic targets, which use edge input, line input, point source input, and bar input method, respectively.

(a) Edge input method

The Edge input method, also known as the knife-edge method, or the slanted-edge method. This method is widely used for laboratory measurements and may be implemented in various manners. For on-orbit MTF assessment, it requires a slanted edge as illustrated in Figure 2.9.

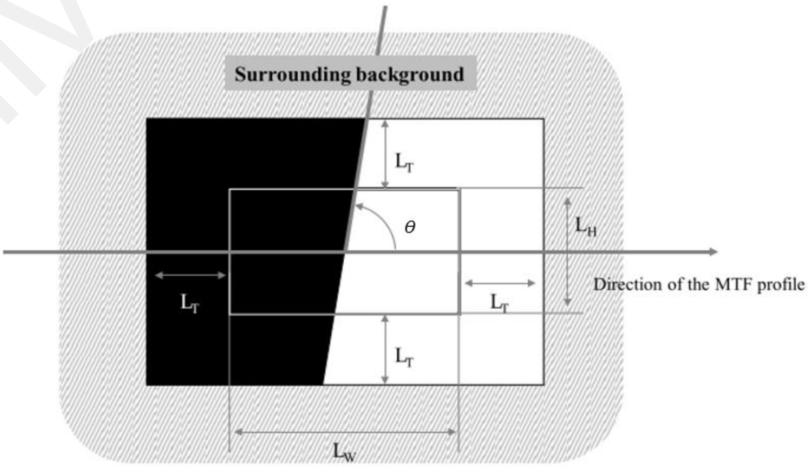

Figure 2.9: Schematic edge targets (Blanc, 2009). The width of the target in the direction of the MTF profile is noted as L_W; The height L_H of the target in the direction normal to the MTF profile, and Θ is the orientation angle with respect to the direction of the MTF profile. The transition distance L_T of the selected target to the surrounding background.

Over the years, it has been widely used in real satellite operations by researchers from many organizations, including the National Institution for space research, the space agency, the Orbital sciences corporation, etc. To name a few, consider those summarized in Table 2.3. This method is favorable to many researchers and scholars because edges are particularly useful since all the appropriate information can be derived from a high quality (i.e., high SNR) edge response without incurring sampling issues. Besides, they can be easily found in an image as they occur naturally throughout many urban and agricultural scenes.

Table 2.3: Some of the operational work published on MTF assessment using Edge Input Method

Authors	Organization	Satellite
Ryan et al. 2003	NASA Stennis Space Center	IKONOS
Helder et al., 2004	South Dakota State University and collaboration with NASA Stennis Space Center	Quickbird
Kohm, 2004	Orbital Imaging Corporation	OrbView-3
Nutpramoon, Weerawong, & Apaphant, 2007	Geo-Informatics and Space Technology Development Agency (GISTDA), Thailand	THEOS (**Th**ailand **E**arth **O**bservation **S**atellite).
Bensebaa, Banon, Fonseca, & Erthal, 2007	National Institute for Space Research (INPE), Brazil	CBERS-2 (**C**hina-**B**razil **E**arth **R**esources **S**atellite-2)
Lee et al. 2008	Korea Aerospace Research Institute (KARI)	KOMPSAT-2 (**Ko**rea **M**ulti-**P**urpose **SAT**ellite-2)
Viallefont-Robinet & Léger, 2010	The French Aerospace Lab in the Department of Optics and Associated Techniques (DOTA)	SPOT-5(**S**atellite **P**our l'**O**bservation de la **T**erre-5)
Wenny et al, 2015	NASA Goddard Space Flight Center	Landsat 8
Min et al. 2016	Environmental Satellites, National Satellite Meteorological Center	FengYun-3C/MERSI
Lee et al. 2016	Korea Aerospace Research Institute (KARI)	KOMPSAT-3 (**Ko**rea **M**ulti-**P**urpose **SAT**ellite-3)
Pagnutti et al, 2017	NASA Stennis Space Center	DLR DESIS (DLR Earth Sensing Imaging Spectrometer)
Gascon et al., 2017	Airbus Defense and Space	Sentinel-2A
Park et al., 2018	Korea Aerospace Research Institute (KARI)	KOMPSAT-3 (**Ko**rea **M**ulti-**P**urpose **SAT**ellite-3)
Kim et al., 2020	Korea Aerospace Research Institute (KARI)	KOMPSAT-3A (**Ko**rean **M**ulti-**P**urpose **SAT**ellite-3A)

A requirement to determine MTF from the edges is to have a high-fidelity representation of the ESF. In particular, a sharp, straight, and slanted-edged target is required to measure the phase change of the edge across the sampling grid to create a "super-resolved" ESF (Kohm, 2004; Wang, Choi & Xiong, 2011; Wang & Xiong, 2013). The edge method usually requires the utilization of both parametric and nonparametric fitting techniques throughout the process to properly calculate an accurate MTF ((Ryan et al., 2003; Kohm, 2003. Helder et al., 2004), which include the Gaussian function fit, sigmoid function fit, modified Savitzky–Golay (SG) filtering (Helder et al., 2004), and Locally Estimated Weighted Scatterplot Smoothing (LOESS) (Cleveland, 1985) curving fitting.

As illustrated in Figure 2.9, an edge target corresponds to a high contrast Heaviside edge. This type of target can be artificially constructed using level smooth surfaces painted with highly reflective (white) paint and dark (black) paint, or specific dark and bright tarps spread out on the ground. The basic idea of the edge method is to find a regularly observed object with high-contrast edges to construct a fine sampled ESF based on the system's response to a step function. Among others, the edge input method by Helder et al. (2004) and Kohm (2004) are the most widely adopted. These authors give some rules of thumb for an "appropriate" edge target dedicated to acquiring a high-fidelity representation of the ESF for an accurate MTF measurement as presented in Table 2.4. The differences between Helder et. al. (2004) and Kohm (2004) are the type of edge detection and curve fitting technique used in their method for ESF construction. For example, Kohm (2003) uses a Sobel edge detection operator followed by thresholding and binary morphological processing to identify suitable edges in the nominal scene for ESF construction. Then he used the LOESS curve fitting techniques to resample the ESF data to uniformly spaced points to obtain the ESF. Whereas Helder et al. (2004) estimate the edge location by fitting the Fermi function (Fermi & Enrico, 1926) to the data and uniformly spaced the samples using a non-linear modified filter based on Savitzky-Golay filter (Savitzky, 1964) to obtain the ESF.

Table 2.4: Edge targets selection criteria

Key Parameters	Criterion	Rationale
The differential radiance between the dark and bright part of the target;	The dark and bright difference divided by the standard deviation (SD) of the noise should be greater than 50.	To produce accurate and consistent results.
The orientation angle α with respect to the direction of the MTF profile;	6 to 8 degrees	To get a uniformly distributed sub-pixel edge location for suitable ESF construction.
The width L_W of the target in the direction of the MTF profile;	6 to 10 GSD	To span enough image rows and columns to increase sampling frequency and improve the SNR budget.
the height L_H of the target in the direction normal to the MTF profile; and	20 GSD	
The transition distance L_T of the edge target to the surrounding background.	3 to 5 GSD	To reduce sampling bias and improve the SNR budget.

In addition to the ground target images, the high-contrast edge of the Moon can also serve as the edge target for the MTF characterisation of remote sensing instruments that has a lunar observation capability (Choi, Xiong & Wang, 2014; Wang et al. 2014; Keller, Chang & Xiong, 2017; Wang, Choi & Xiong, 2011; Wang & Xiong, 2013). NASA's MODerate resolution Imaging Spectroradiometer (MODIS) (Choi et al., 2014; Wang et al. 2014) onboard the Terra and Aqua satellites is an example of this capability. In this case, the curved edge will play the same role as the slanted edge. Due to the curvature of the Moon, the distances between the image grids and the actual edge positions at different lines are different at a subpixel level. Therefore, this method requires sufficient samples (lines) of lunar edges near the lunar equator to construct a high-fidelity representation of the ESF. Choi et al. (2014) adopted the same ESF construction proposed by Helder et al. (2004) to achieve a high-fidelity representation of ESF for MTF measurement.

Based on the literature, a few researchers (Hwang, 2008; Estribeau & Magnan,2004) adapted ISO 12333 standard slanted-edge method proposed by Burns (2002) for on-orbit MTF measurement. Nevertheless, according to a stability and repeatability study performed by Roland (2015), the ISO 12233 slanted-edge MTF measurement method is not robust against noise. This is because it takes the derivative of each data line in the edge-angle estimation. Errors in the estimation introduce negative bias to MTF computation, resulting in underestimation for the actual MTF measurement.

(b) ***Point input method***

The work by Rauchmiller & Schowengerdt (1988) is one of the earliest attempts to measure the 2-D PSF of Landsat TM using an array of black squares on a white-sand surface as a Point input method. Later, this method has been improved to use an impulse target that corresponds to a point source or a set of point sources. Impulse target is a type of artificial target that is generally categorized as a "passive" mirror type reflective point source target or "active" Xenon lamp source target. These point sources reflect the sunlight to the sensor. The light is seen by the sensor as a point source on the ground, where the amount of degradation measured from that point source image signifies a direct measure of the PSF for that system.

The test site of National d'Etudes et de Recherches Aérospatiales (ONERA) used at least two 3 kW Xenon spotlights that can be aimed at EOS imagery systems. These artificial impulse targets have been used to assess the absolute MTF of SPOT-3 (Léger et al., 1994) and SPOT-5 (Léger et al., 2004). Rangaswamy (2003) has tested 1.2 m convex mirrors to create an array of artificial passive point sources. This array of point source targets has been used to assess the MTF of Quickbird II and IKONOS. Figure 2.10

presents the impulse target using a convex mirror (Rangaswamy 2003) and the Xenon spotlight (Léger et al., 2004).

(a) (b) (C)

Figure 2.10: Impulse target set up. (a) An artificial target site (in Stennis Space Center) using an array of convex mirrors as point sources (Rangaswamy 2003). (b)-(c) Impulse target by (Léger et al., 2004); (b) Impulse target set up using Xenon spotlights (b) Image captured by SPOT-3 during Cal/Val mission.

One of the drawbacks of the Point input method is that the 2-D impulse responses acquired during the satellite overpass were always too noisy to fit a surface Gaussian function properly. This technique has been improved in recent research by Schiller, Silny, & Taylor, (2012). The authors proposed a method called the Specular Array Calibration (SPARC) method, which is an adaptable ground-based system that uses convex mirrors to create small reference targets. It used a grid of spherical reflectors to create point source images at different pixel phasing. As a result, the oversampled PSF can be generated from a single image of a mirror array or multiple images of the array for better sampling statistics. This method has been used to assess the MTF of IKONOS (Schiller et al., 2017). One of the disadvantages of this method is its dependence on pre-flight calibration data, where it required the knowledge of the sensor PSF, to accurately extract the integrated signal. The pre-flight calibration data is not always available since some small satellite industries may choose to minimize pre-flight requirements due to cost and time constraints.

Most recently, Li, Zhang, Zhang, & Yu, (2018) employed the point source target method of Rangaswamy (2003) and developed a large area greyscale target to measure 2-D PSF for MTF assessment of Chinese surveying and mapping satellite Tianhui-1. The contribution of their work is an automatic recognition and positioning method to detect point source images for geometric calibration.

Similar to the Edge input method, besides the utilization of ground target images, with agile maneuvering satellite platforms, stars can be excellent natural impulse targets for on-orbit MTF assessment. Several scans of stars have been performed the same manner as the planetary scans with the Advanced Land Imager (ALI) of The Earth Observing-1 (E0-1) for this purpose (Hearn, 2002). According to the analysis from Hearn (2002), stars in the Pleiades constellation and the star Vega in the Lyrae constellation were found to be excellent natural impulse targets in terms of radiance contrast, which is useful for MTF assessment. A notable recent satellite that is equipped with star observation capability is the KOMPSAT-3 (Lee et al., 2014; Kang, Chung & Kim, 2015).

(c) ***Line input method***

Due to surrounding background noise in the image and sampling considerations, instead of using the point target method, various techniques have been developed to estimate a 1-D PSF, known as LSF (as explained in Section 2.1.3.1), where the Line input method (Ryan et al., 2003; Helder et al., 2006), is one of the methods. In real satellite operation, the Line input method is commonly known as the Pulse input method.

The Pulse input method is similar to the Edge input method except that the input to the imaging system was a pulse. If a natural target is used, the pulse input is usually based on an image with a jetty or centerline of an airport runaway. A pulse target consists of a bright region surrounded by dark regions as illustrated in Figure 2.11. To achieve good performance, these measurement techniques typically require a specific size (i.e., width and height) and orientation of targets based on the GSD, as well as scanning the sensor direction if it is equipped with a scan mirror (Helder et al. 2004). The width of the input pulse is critical because of the zero-crossing point of the Sinc function. It is important, therefore, that the width of the input pulse must be appropriately sized. In summary, the key parameters and their importance are the same as for the edge target presented in Table 2.4 of the topic (i) Edge input Method in this subsection.

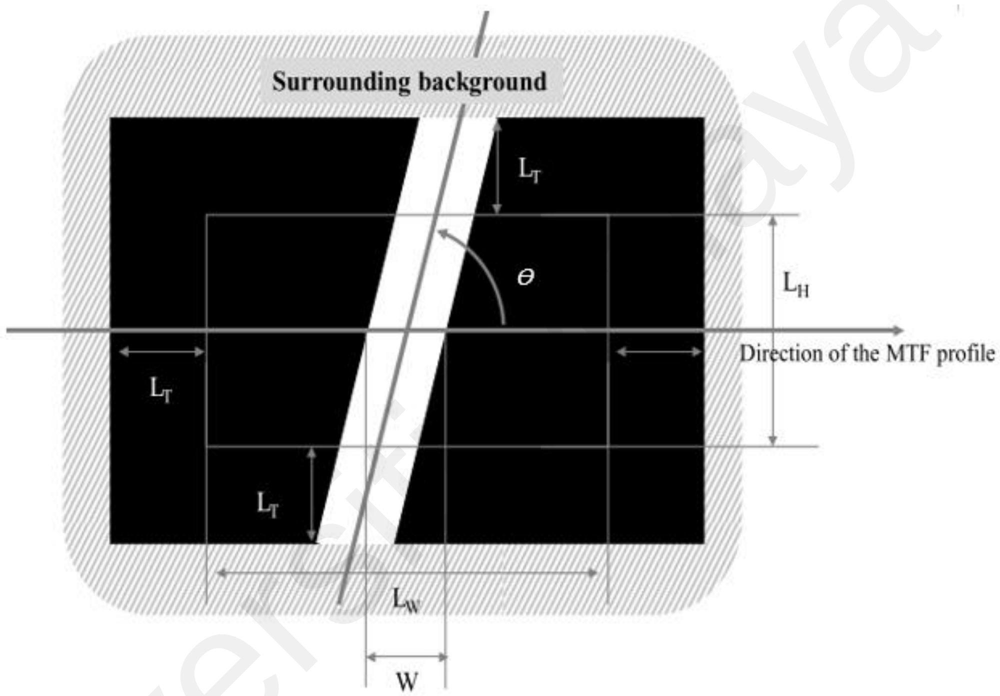

Figure 2.11: Schematic pulse targets (Blanc, 2009). The width of the target in the direction of the MTF profile is noted as W; The width of the pulse L_W on the target in the direction of the MTF profile; The height L_H of the target in the direction normal to the MTF profile, and Θ is the orientation angle with respect to the direction of the MTF profile. The transition distance L_T of the selected target to the surrounding background.

(d) Bars input method

The bars input method is solely artificial targets. In contrast to the aforementioned targets, there is very little published information on this type of target (Léger, Chung & Li, 2003, Xu et al., 2014). A periodic target consists of specific patterns that are periodized, where the pattern can comprise edges, pulses, or impulses (Blanc, 2008). Examples of those periodic patterns are the standard USAF (U.S. Air Force MIL-STD

150A standard) three-bar pattern or the Siemens radial stars pattern (Reulke et al., 2006) both depicted in Figure 2.12.

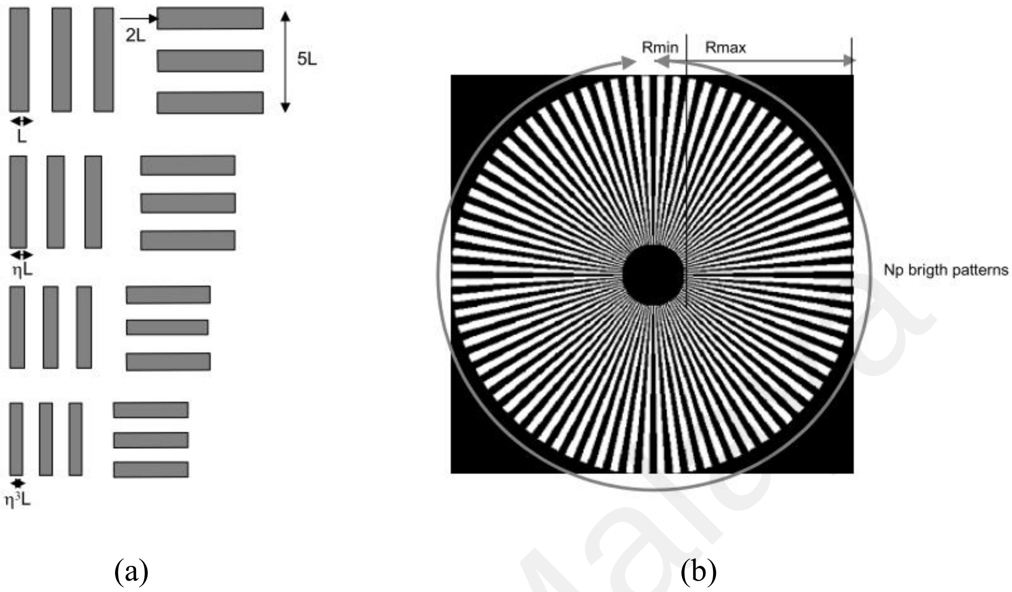

Figure 2.12: Example of periodic targets (Blanc, 2009). (a) Three-bar pattern. (b) Siemens-star pattern.

In Figure 2.12(a), the width L is typically appropriate for GSD, whereby the $\eta = \frac{1}{\sqrt[6]{2}}$. For the Siemens-star pattern in Figure 2.12(b), if it has $\#px$ bright patterns and a radius varying between R_{min} and R_{max}, the appropriate GSD is as follows

$$\frac{\pi R_{min}}{2\#px} < GSD < \frac{\pi R_{max}}{2\#px} \quad (2.6)$$

where px is the pixel pitch in the image plane, # is the number of pixels per pattern, and R is the radius of siemens star.

Even though it is possible to use both targets (i.e., Three-bar and Siemens-star pattern) for MTF assessment, they are usually used to provide a direct and quick visual assessment of the resolving power of the imaging system (Léger, 2004). The edge, pulse, or impulse target method is preferable compared with the periodic target method for numerical on-orbit MTF assessment.

This subsection has described and reviewed the MTF measurement method using fixed-characteristic targets. In the following subsection, the potential use of stochastic characteristic targets for on-orbit MTF measurement will be discussed.

2.2.2 Stochastic Characteristic Target

The stochastic characteristic target, which is also known as the random target, is another type of target that can be employed in image-based MTF assessment (Xie et al., 2015). The fractal properties of an image are a type of stochastic characteristics. Compared to fixed-characteristic targets, very few studies have explored this type of target, particularly for on-orbit MTF assessment.

For optic laboratory MTF assessment, the MTF measurement method based on random target was first proposed by (Daniels et al., 1995), in which a random transparency target is used as the template, and then it is imaged on a charge-coupled device (CCD) by the optical system under test (OSUT). By using the power spectral density values of the image captured by a CCD, the optical system's MTF can be obtained with Fourier spectral analysis. This test method is convenient because the random image has the characteristic of shift-invariance and can easily achieve automatic measurement.

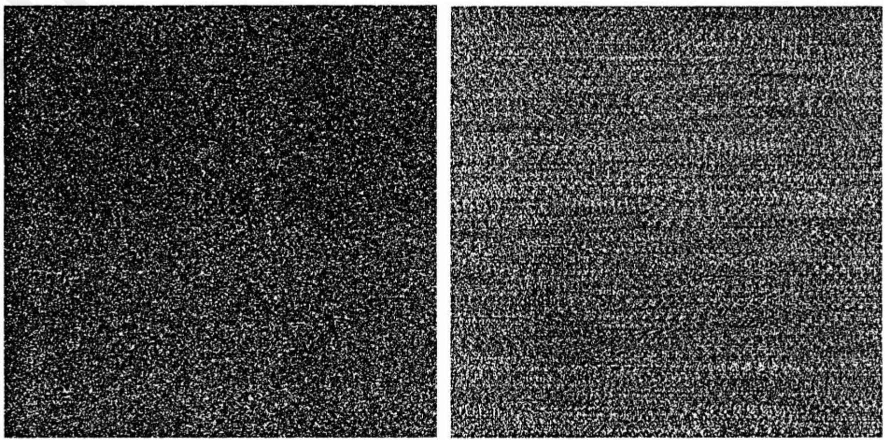

(a) (b)

Figure 2.13: Example of random transparency targets. (a) A bandlimited white-noise random image. (b) A discrete narrowband random image.

Figure 2.13 shows the example of random transparency targets used in Daniels et al. (1995). The MTF measured using the random target of Figure 2.13(a) is to create the 'continuous' MTF that provides a continuous curve for all spatial frequencies of interest. Whereas the random target of Figure 2.13(b) is to create the 'discrete' MTF to measure it at a number of discrete spatial frequencies.

Levy et al. (1999) adopted the same principle as Daniels et al. (1995) for lens measurements, but instead of using random transparency target, they used a random test target generated on a computer screen. As none of the authors have considered speed issues, Backman & Makynen (2004) proposed a different type of random target method for fast MTF inspection. The previous works focus mostly on the 1-D MTF test. The random image can also be used as a 2-D target since its image brightness changes in two orthogonal directions and is available for measuring 2-D MTF. Hence, Evtikhiev et al. (2013) proposed another type of random target to reduce the noise impact for the 2-D MTF measurement. In 2014, Kang et al., (2014) proposed another random target-based 2-D MTF to improve the work of Evtikhiev et al. (2013).

Whilst several studies of optic laboratory MTF assessment based on stochastic targets have shown acceptable results, there is very little research that uses the stochastic target as an input target for on-orbit MTF measurement. Moreover, none of them was used operationally. One of the related works found in the literature is that of Xie et al. (2015). Due to the difficulty in obtaining suitable target images, the authors proposed an MTF measurement method based on natural image power spectrum statistical characteristics. In their work, they constructed a model that combines a fractal Brownian motion model that utilizes natural images with stochastic fractal characteristics, with an inverse Fourier transform of an ideal optical satellite image amplitude spectrum. The model is used to decouple the blurring effect of an ideal natural image. For MTF measurement, they built another statistical model based on the SD of the image sequence amplitude spectrum and estimated the model parameters using the ergodicity assumption of an optical satellite image sequence. The experimental results demonstrate that the method is practical and effective, but it suffers from high computational complexity. Another notable work is from Saiga et al. (2018). The authors proposed an alternative way of estimating MTF using a random target, regardless of the image type or the use of imaging modality. In their work, they estimated MTF by using the Fourier transform a logarithmic plot of the image. One of the limitations of the proposed method is that it has a strict prerequisite because the MTF of the target image must be approximated with a Gaussian. If the linear correlation of the Gaussian is not identified in the logarithmic plot of the image, then the PSF cannot be extracted. Consequently, the MTF will not be estimated from the target image too. In addition, it is not robust in handling sparse images. As stated in Mizutani (2016), a sparse image results in a noise profile that dominates the entire logarithmic plot after the application of the Fourier transform. Thus, this makes it difficult to identify the linear correlation at the left end of the logarithmic plot.

This chapter has discussed two image-based MTF measurement methods, where one method is based on fixed characteristic targets and the other method is based on stochastic targets. For the fixed-characteristic target, none of the studies that have been reviewed so far were using an automatic technique to select input targets. The next subsection will discuss this type of technique.

2.2.3 Automatic MTF Measurement Techniques

From the literature search, there are only a few works that research on MTF measurement using an automatic approach. In Wang, Li & Li (2009), an automatic onboard MTF measurement approach based on the detection of straight lines with Hough transforms was proposed. In this case, a set of conditions are formulated to choose these qualified lines. Once the qualified lines are obtained, MTF will be estimated using a step edge method. Although Hough Transform is robust to noise, it is slow and sensitive to the quantization of parameters. Besides, due to its sensitivity to quantization, for those detected lines, it requires several orthogonal visits in equal intervals along the line to reduce the errors of observed ESF. The authors suggested that a more efficient variant of Hough Transform can be utilized to reduce the computational complexity and enhance the line detection accuracy.

Recently, Li et al. (2015) proposed an automatic method that used an image motion velocity model (Zhong et al., 2009) to extract the edge of the sub-frame images. After the edge extraction, they applied mathematical morphology and correlation–homomorphic filter algorithms to eliminate noise and enhance the sub-frame images. They use the image partial differentiation technique (Helder et al., 2004) to determine the position of edge points and later construct the ESF based on the optical transfer function of the camera. Finally, MTF is calculated by the derivation of ESF and Fourier transform.

Most recently, Pagnutti et al. (2017) developed an automated algorithm to estimate RER. In their work, they exploited the edge features in a nominal scene for on-orbit characterisation of the German Aerospace Center's Earth Sensing Imaging Spectrometer (DESIS) Sensor on the International Space Station. Similar to Kohm's MTF measurement method (2003), it requires the use of an edge detection technique, and an edge screening to find the ideal edges for RER and MTF measurements. According to the paper, the automated algorithm can produce comparable results against the traditional methods (i.e., edge or point input method on natural targets) of Landsat 8 Operational Land Imager.

So far, this chapter has discussed all the key aspects of on-orbit spatial characterisation. The next part of the chapter will provide extensive literature relating to on-orbit spatial image restoration.

2.3 Spatial Image Restoration in Optical Satellite Images

Returning briefly to the optical satellite image formation and its effect on image sharpness. Remotely sensed images inevitably suffer from a series of degradation processes in the imaging chain. The degradations could happen due to extrinsic or intrinsic factors as follow (Schowengerdt, 2007; Schott, 2007; Blanc, 2009): (1) Launching into the orbit, such as launch vibrations, transitions from air to vacuum, or thermal state (Rodin et al., 2019); (2) Image acquisition; Degradation occurs due environmental factors, such as atmospheric turbulence, attenuation, and scattering of aerosols; or due to physical limitation of the imaging system as no instrument (remote-sensing systems included) can measure a physical signal with infinite precision (Schowengerdt, 2007). Disturbance such as diffraction limit, optical aberration, out of focus, image motion, and camera motion (Nan et al., 2015); and (3) Data Transmission; Interference of electronic components, analog to digital transformation, etc.

Generally, an imperfect imaging behavior of the imaging sensors (i.e., detector, optics, and electronics) degrades the spatial properties of remotely sensed imageries in two ways: (1) distortion; and (2) blurring. This thesis focuses on the latter. The blur as described in subsection 2.1.3.1 is the spread function characterized by the PSF. By definition, the MTF is the modulus of the FT of the PSF (Boreman 2001). Knowing that the "sensor" transfer function blurs the image, it is thus natural to consider how to remove, or at least reduce its effect. It can be done using a filter that amplifies (i.e., "boosts") the higher frequencies to compensate for the blurring in the imaging process that has reduced the high-frequency content in the image (Schowengerdt, 2007). This approach is an old topic in image processing, known as image restoration (Andrews & Hunt, 1977).

Image restoration has matured since its inception in space exploration in the 1960s. The great cost and effort required to launch a human into space made any images that were captured on missions extremely valuable to scientists. Consequently, research into image restoration methods grew rapidly and soon spread to other imaging areas. Numerous techniques can be found in the literature (for recent reviews, refer to Lai et al., 2016). These techniques differ primarily in the prior information about the image they incorporate to perform the restoration task.

2.3.1 Image Degradation Model

Image restoration in remote sensing is concerned with the correction and calibration of images that aim to achieve a high fidelity representation of the earth's surface (Liang, Li & Wang, 2012). In other words, it is an objective process where its goal is to reconstruct the original image spectrum $F(u,v)$ from its degraded observed version $G(u,v)$ using a priori knowledge of the degradation phenomenon $H(u,v)$ and $N(u,v)$. The degradation model in the frequency domain can be described as

$$G(u,v) = H(u,v) \circ F(u,v) + N(u,v) \tag{2.7}$$

where $N(u,v)$ denotes the random noise spectrum and H denotes the optical transfer function, which amplitude spectrum is the MTF. The symbol $\circ$ denotes an element-wise multiplication operator.

Using the familiar notation for convolution, if H is a linear, spatially-invariant process, the degraded image $g(x,y)$ corresponds to the expression of Equation (2.7) in the spatial domain is formulated as

$$g(x,y) = f(x,y) \otimes h(x,y) + \eta(x,y) \tag{2.8}$$

where $f(x,y), h(x,y)$ and $\eta(x,y)$ represent a latent image, PSF, and unknown noise respectively; the symbol $\otimes$ denotes 2-D convolution operator; x and y are the continuous variables in x and y plane, respectively. Based on Equation (2.8), the fundamental task of image restoration is to deconvolve the degraded image with the PSF that exactly describes the blurriness. Deconvolution is the process of reversing the effect of convolution.

2.3.1.1 Blur models

The deterministic component of the degradations, called blur, is modeled by a mapping $f(x, y; s(\tilde{x}, \tilde{y}))$ of the scene $s(\tilde{x}, \tilde{y})$ to the image plane coordinates (x, y). In general, this mapping is non-linear and spatially varying; however, in most work, it is assumed that the observed image is the output of a linear spatially-invariant system, representing convolution of the image and blur, to which is also subject to statistical degradations noise, commonly called noise (Schowengerdt, 2007).

(a) ***Linear spatially-invariant blur Models***

The mapping $f(x, y; s(\tilde{x}, \tilde{y}))$ becomes the PSF if $s(\tilde{x}, \tilde{y})$ is substituted by the unit impulse $\delta(\tilde{x}, \tilde{y})$ indicating a point source for the scene. Assuming a *linear* degradation system in the limit of scene representation, with a spatial distribution of an infinite number of point sources; by the rule of superposition, the resulting image plane intensity distribution yields the expression

$$g(x, y) = \sum_{(u,v)\in\Psi} h(x, y; \tilde{x}, \tilde{y}) f(\tilde{x}, \tilde{y}), \tag{2.9}$$

where $h(x, y; \tilde{x}, \tilde{y})$ is the PSF and Ψ denotes the PSF support.

If the blur is considered as spatially-invariant, then (2.9) becomes a discrete convolution summation as follows:

$$g(x, y) = \sum_{(k,l)\in\Psi} h(k, l) s(x - k, y - l), \tag{2.10}$$

where $h(k, l) = h(x - \tilde{x}, y - \tilde{y})$.

Generally, almost all realistic blurs are modeled with non-causal PSFs, the blurring PSF is modeled as an $(\mathrm{M} \times \mathrm{M})^{\mathbf{th}}$ order finite impulse response (FIR) filter (Holst, 2017). The conservation of energy assumption implies that a point source of light should result in no loss of energy as

$$\sum_{(k,l)\in\Psi} h(k,l) = 1. \tag{2.11}$$

(b) ***Spatially variant blur Models***

The most general case of space-variant blurs is modeled by Equation (2.9). However, under some assumptions, it is possible to approximate the space-variant blur model with a piecewise space-invariant PSF. In other words, the space-variant blur can be presumably represented by a collection of $PSF_s \mapsto (PSF_0, PSF_1 \dots, PSF_n,\ s = 0, 1..n)$ where n is a predetermined number, such that at each pixel one of the PSF_s can be matched to the observed data. Then Equation (2.9) is simplified to:

$$g(x,y) = \sum_{(k,l)\in\Psi} h(k,l)(\theta(x,y)s(x-k, y-l), \tag{2.12}$$

where $\theta(x,y)$ is a random variable that indicates the blur model acting at (x,y). The space-variant blur identification problem then reduces to a detection problem, at each pixel, over a finite-population set of possible PSF_s.

2.3.1.2 Sources of blur

Blurring in an image occurs because of a localized averaging of pixels, which results in the smoothing of image content. As expressed in Equation (2.8), it is usually modeled as a convolution of the latent sharp image with the PSF. In a simple description, if the PSF is the same for all image pixels, the blur is termed spatially-invariant. If the PSF changes throughout the image, the blur is termed spatially variant. According to its sources, typically, image blur can be generally categorized into three groups: motion blur, out-of-focus blur, and environmental blur.

Motion blur. The motion blur is fundamentally arising from mismatching between photoinduced charge transfer and optical image movements during the exposure period. Ideally, if the scene is static with uniform depth and if the imaging system motion is 2-D translational, then the motion blur can be viewed as spatially-invariant. This degradation could be estimated and removed through a blind deconvolution procedure (Quan & Zhang et al., 2011). However, in a practical situation of passive remote sensing imaging, imaging system motion includes more complex motion due to satellites' orbit maneuvering. Objects inside the imaged scene can also be moving during the time it takes to integrate the signal for a pixel. Besides, the focal depth of the imaging system is probably spatially changing. Any of these factors could make motion blur spatially varying (see example in Figure 2.14(a)), which makes its estimation and removal highly difficult (Bhaskar et al., 1994, Shi et al., 2015).

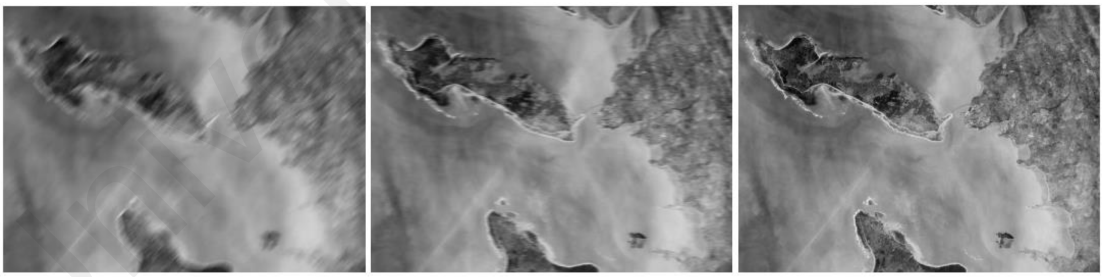

(a) (b) (c)

2.14: Examples of different types of blur. (a) Motion blur, (b) Out-of-focus blur, and (c) Environmental blur.

Out-of-focus blur. Incorrect lens setting or limited depth of field would produce a defocus blur (see example in Figure 2.14(b)), which is an important type of lens blur. Besides, even if the scene is perfectly in focus and no matter how well the lens is corrected, in most optical imaging systems there always exists a fundamental resolution limit due to diffraction, which is called diffraction-limited blur (Holst, 2017). Generally, diffraction-limited blur can be approximately viewed as spatially-invariant, while the spatial variance of defocus blur depends on both the depth of field of the lens and depth of the scene (Liu et al., 2010; Jiang, Chen & Yu, 2012; Li et al., 2013). Typically, a crude approximation of a defocus blur is made as a uniform circular model (Gonzalez & Wood, 2017).

Environmental blur. Environmental factors also cause blurring. As light passes through mediums with different refractive indexes, bending, diffraction, and scattering will occur. Figure 2.14(c) shows an example of an environmental blur.

For remote sensing imaging, atmospheric turbulence, which generates a variation of refractive index along the optical transmission path and distorts the light wavefront, can give rise to attenuation of the irradiance of the propagating image, thus reducing the contrast of the imaged scene. Removing such effects is very important for many applications and meanwhile, it is quite challenging. Some notable works to remove atmospheric blur are those from (Dherete & Rouge, 2003; Ma & Le Dimet, 2009; Semenov et al., 2011; Moshkov et al., 2013; Aouinti et al., 2016). A common generic model of an environmental blur for a measured optical PSF in passive remote sensing is the 2-D Gaussian function (Athanasiou et al., 2017).

2.3.1.3 Blur estimation

Given the fact that the degradation phenomenon is unknown, thus image restoration of optical satellite images is a blind image deconvolution (BID) problem. For a survey on the extensive background literature in this area, readers may refer to (Kundur & Hatzinakos, 1996). The BID estimates the blur, either in preprocessing or simultaneously during restoration. This is to say, the BID approaches can be classified into two categories according to what stage of the blur is identified: a priori or jointly with the image.

A priori blur estimation methods: With this approach, the PSF is identified separately from the original image as a preprocessing step, and later used in combination with one of the classical image restoration (e.g., Modified inverse filter, Wiener filter) algorithms in order to restore the original image. A parametric blur model may be used, for example, one of the general models described in then the objective is to identify the most likely blur parameters *h* from the observation. (e.g., Zhang et al., 2014, Chen et al., 2010; Lee et al., 2008; Mittal & Garg 2013; Li et al., 2017)

Joint estimation methods: Most existing methods fall into this class, where the image and blur are identified simultaneously. However, in practice, many methods in this category use an alternating approach to estimate *f* and *h* rather than truly finding the joint solution. Prior knowledge about the image and blur is typically incorporated in the form of models. Parameters describing such models are also required to be estimated from the available data; often this is performed before image and blur identification, although simultaneous identification is possible (see e.g., Papa et al., 2006; Shen et al., 2012; Liu & Eom 2013; Zhi et al., 2014)).

2.3.2 Approaches to Optical Satellite Image Restoration

This section will discuss and review the studies on optical satellite image restoration under two topics: the first topic discusses the filter-based MTF compensation techniques that have been used operationally by most of the satellite operators. Whereas the second topic presents some notable research works on optical satellite image restoration.

2.3.2.1 Filter-based MTF Compensation techniques

Satellite image restoration based on the compensation of MTF dates to the mid-1980s by Wood et al. (1986) but was not commonly available as a production processing option until about the year 2000 (Schowengerdt, 2007). The restoration kernel is commonly referred to as MTFC. MTFC-based image filtering techniques are commonly adopted by past and current satellites such as IKONOS (Cook et al. 2003; Ryan et al., 2003), OrbView-3 (Kohm, 2004), Landsat (Wu & Schowengerdt, 1993; Storey, 2007; Wenny et al., 2015), QuickBird (Helder et al. 2006), WorldView-2 (Poil et al. 2014) and SPOT (Ruiz & Lopez, 2002, Viallefont-Robinet and Léger, 2010).

The MTFC process involves two steps. First, The MTF is derived from the degraded image by measuring fixed-characteristic targets as described in section 2.2.; second, using the measured MTF, a filter-based method is applied for compensating the MTF to restore the degraded image. Based on these steps, the MTFC thus can be deemed as a deconvolution problem; It estimates blur (i.e., the PSF) in preprocessing. There are several deconvolution techniques available for image restoration. Among others, the Wiener filter (Wiener, 1964) and regularized Inverse filter (Gonzalez & Woods, 2017) are the popular choices and have been operational to restore optical satellite images. These filters are the obvious choice because they are closed-form solutions that could be solved efficiently in the Fourier spatial frequency domain (Fonseca, Prasad, & Mascarenhas, 1993; Bretschneider, 2002; Schowengerdt, 2007; Li et al. 2013; Lee et al., 2016). Specifically, the following subsection will describe these filters and reviews their related works.

(a) ***Inverse filter***

Given $G(u,v)$ which denotes the degraded observed version of the original image spectrum $F(u,v)$ as described in Equation (2.7). In sensor MTF compensation, the attempt is to undo the blurring effects of imaging sensor $H(u,v)$ by dividing both sides of Equation (2.7) to find the best estimate of the restored image $\ddot{F}(u,v)$

$$\ddot{F}(u,v) = \frac{G(u,v)}{H(u,v)} = F(v,\omega) + \frac{N(u,v)}{H(u,v)} \tag{2.13}$$

The spatial domain representation of the restored image $\ddot{F}(u,v)$ is determined by taking the inverse Fourier transform F^{-1} of Equation (2.9) and convolution theorem to yield:

$$\ddot{F}(u,v) = \mathrm{F}^{-1}\left(\frac{G(u,v)}{H(u,v)}\right) = \mathrm{F}^{-1}\left(F(u,v) + \frac{N(u,v)}{H(u,v)}\right) \tag{2.14}$$

When there is no noise in the degraded image, Equation (2.14) produces perfect restoration. However, in practice, there will always be noise in the degraded image, and singular values in $H(u,v)$ cause this noise to be amplified at the output. To avoid noise amplification, usually, a threshold is applied to regulate the modulation boosting of the inverse filter at higher frequencies. This attempt is thus become a modified inverse filter (MIF).

The MIF by Fonseca et al. (1993) is one of the earliest attempts. In their work, they combine the restoration process with an interpolation process to generate images with better resolution over a finer grid than the original sampling grid. The combined interpolation-restoration process is performed through a 2-D, separable, Finite Impulse Response (FIR) filter that has input signals with different sampling rates. The ideal low pass FIR filter for interpolation (Crochiere & Rabiner, 1983) is modified to account for the restoration process. The proposed method is applied to the interpolation-restoration of Landsat-5 TM data. The restoration process amplifies the high-frequency components of the image, therefore an image with sharper transitions is obtained. However, the enhancement of the aliasing effect is also more evident in the restored image.

Boggione and Fonseca (2003) proposed a Modified Inverse Filtering (MIF) to improve the work of Fonseca et al. (1993) by applying a cut off frequency value of $\frac{G(u,v)}{H(u,v)}$outside a predefined radius of the filter. The cut off value acts as a low pass filter on $G(v,\omega)$ to obtains the restored image based on the low pass filtered $\ddot{F}(u,v)$. This filter has been used to restore satellite images of Landsat-7. This method significantly deblurs the image, however, it is still cannot escape from the amplification of noise.

A more recent work of MIF is proposed by Li et al. (2013) to restore the images of the Huanjing 1A satellite (HJ-1A). The MTFC filter for the HJ-1A CCD camera was developed based on the MIF presented by Fonseca et.al. (1993). To overcome the fluctuation of the MTFC filter of Fonseca et al. (1993), instead of using the parametric cubic convolution interpolation approach, the authors adopted the interpolation approach of Gu et al. (2005). The proposed MTFC is effective for sensors characterized by low MTFs.

When the image is degraded by a known blur, it is possible to recover the image by inverse filtering or generalized inverse filtering. However, Inverse filtering is very sensitive to additive noise. To overcome the problems with inverse filtering, a method that can obtain a meaningful approximation solution with some additional constraints is required, and the Wiener filter is one of the most common early methods. Related works that used Wiener Filter for satellite image restoration will be presented in the next subsection.

(b) ***Wiener filter***

The Wiener filter seeks an estimate of an ideal image that minimizes statistical error in the degraded image using a linear filter operation. The aim of the process is to have a minimum mean square error, which is the difference between the original signal and the estimated signal should be as little as possible. Derivation of the Wiener filter is not included in this subsection, details can be found in Gonzalez & Woods (2017).

In the frequency domain, the Wiener Filter is expressed as

$$\ddot{F}(u,v) = \digamma^{-1}\left(\frac{1}{H(u,v)}\right)\left[\frac{|H(u,v)|^2}{|H(u,v)|^2 + \frac{S_n(u,v)}{S_f(u,v)}}\right] \tag{2.15}$$

One of the major difficulties in using the Wiener filter is that the power spectral densities of signal, $S_n(u,v)$ and noise$S_f(u,v)$ are not always known a priori. Therefore, the ratio $\frac{S_n(u,v)}{S_f(u,v)}$ is typically approximated empirically by a constant, K_w (Gonzalez and Woods, 2017), thus become

$$\ddot{F}(u,v) = \digamma^{-1}\left(\frac{1}{H(u,v)}\right)\left[\frac{|H(u,v)|^2}{|H(u,v)|^2 + K_w}\right] \tag{2.16}$$

This type of filter given in Equation (2.16) was also used in the MTFC work of Fonseca et al. (1993). In the same year, Wu and Schowengerdt (1993) also use the same filter to restore Landsat TM imagery.

McNeill and Pairman (1998) proposed to use the Wiener filter to estimate the PSF of SPOT satellite images. According to the authors, the main disadvantage of this method is that it cannot incorporate the constraint limits into the restoration procedure. To overcome this, Bretschneider (2002) suggested an iterative version of deconvolution, which is the Maximum Likelihood Estimation (Pratt, Edgeworth, & Fisher, 1976) to estimate the $H(v,\omega)$. As the Wiener filter has a low-pass characteristic, the extent of the PSF estimated by the iterative Wiener filter is larger than the maximum likelihood estimation. Even though, it can be partly compensated by superimposing a finite extent on the intermediate results. However, this attempt introduced high-frequency components in the restored image. Nevertheless, the Wiener filter is still a favorable MTFC because of its statically optimal behavior, which allows it to execute an optimal tradeoff between inverse filtering and noise smoothing (Wong, 2010, Li et al., 2015).

In (Lee *et al.*, 2008), the authors proposed a deconvolution filter by inversely transforming the Wiener filter to a spatial domain for MTF compensation of KOMPSAT-2 satellite images. The size of the inversely transformed filter for the MTF kernel is 13 × 13. Generally, this filter was able to produce a sharper feature than unprocessed images; however, it is still compromised with ringing and aliasing effect on the restored image. Hence, MTFC becomes an optional process in operational use. Despite this shortcoming, this filter was used in the subsequent KOMPSAT program, namely the KOMPSAT-3 (Lee et al., 2016).

Wiener filter is originally a kind of non-iterative deconvolution filter. Wang and Geng (2008) utilized the classical Wiener filter and modified it into an iterative method to improve the restoration results of CBERS-02 images. This filter contributes to an improved restoration technique, but it requires a *priori* knowledge about the images and availability of the blur factor based on the *in-situ* meteorological parameter. This prior information is important to update the iterative process to ensure the correct and quick iteration procedure. Such a requirement somehow becomes the shortcoming of this method.

Another work of MTFC is proposed by Zhang, Wang, & Pan, (2013), where the author proposed an image restoration approach based on the Kalman filter to generate LSF for MTF measurement. Again, in this work, the Wiener filter is chosen to be the restoration filter. The test data used for this study are the images from satellite CBERS-2. The authors compared their experiments in terms of edge energy and texture contrast with the traditional MTFC. According to the authors, the proposed algorithm can restore more texture information for the restored image as compared to the traditional MTFC. More recently, the Wiener Filter is used as an MTFC kernel by Oh et al. (2014) to restore Geostationary Ocean Color Imager (GOCI) images.

The Wiener Filter is possible to achieve excellent results using the approximation given in Equation 2.11. However, the constant K_w, which is the estimate of the ratio of power spectra is not always a suitable solution (Gonzalez &Woods, 2017).

Most recently, Aouinti et al., (2016) applied the genetic algorithm to the Wiener filter to optimize the regularization parameter in the deconvolution process. Numerical evaluation using SNR demonstrates the improvement of image quality through the elevation of SNR.

Murthy, Kurian, & Guruprasad (2015) conducted a performance evaluation on the Wiener filter, Constrained Lease Square filter, Richardson–Lucy deconvolution, and Blind deconvolution methods in the presence of different artifacts. According to the authors, the Constrained Least Square (CLS) filter is restoring better than other filters. Thus, the CLS filter filtering and its related works will be briefly described in the following subsection.

(c) ***Constrained least square filter***

CLS filter filtering can be considered a type of regularized filtering. It attempts to make the image restoration problem well-posed by introducing information about the original image using the mean and variance of the noise from the degraded image (Gonzalenz & Woods, 2017). This attempt posed an important advantage as it does not rely on prior information of the original image. By the definition of 2-D convolution and lexicographically ordering of the image data, Equation (2.8) in vector-matrix form can be expressed as follows

$$g = Hf + \eta \tag{2.17}$$

Thus, the frequency-domain solution to a constrained least-square optimization problem is given by the expression

$$\ddot{F}(v,\omega) = \mathfrak{F}^{-1}\left(\frac{1}{H(v,\omega)}\right)\left[\frac{|H(v,\omega)|^2}{|H(v,\omega)|^2 + \gamma|P(v,\omega)|^2}\right] \tag{2.18}$$

Subject to the constraint

$$\left\|g - H\hat{f}\right\|^2 = \|\eta\|^2 \tag{2.19}$$

where γ is an adjustable parameter so that constraints in Equation (2.18) is satisfied, and $P(v,\omega)$ is the FT of the Laplacian operator

$$p(x,y) = \begin{bmatrix} 0 & -1 & 0 \\ -1 & 4 & -1 \\ 0 & -1 & 0 \end{bmatrix} \tag{2.20}$$

Detail derivation of this filter can be found in Gonzalenz & Woods (2017). In contrast to the Wiener filter, there is a notable paucity of MTFC that employ CLS. One notable work is from Mu et al. (2013); the authors obtained the *H (v, ω)* by direct laboratory measurements and then used the CLS filter to compensate the MTF.

This subsection has discussed and reviewed the commonly used Filter-based MTFC. In the next subsection, notable works of image restoration for optical satellite images based on the concept of MTFC will be presented.

2.3.2.2 Non-Filter-based MTF Compensation Techniques

The early MTFC approaches that utilized the Wiener filter and Modified Inverse filter, sought to solve the degradation (i.e., the blur) problem by applying inverse filtering to boost the attenuated higher spatial frequencies data of the degraded image. However, such approaches eventually lead to noise amplification and aliasing in the restored image. Hence, researchers have sought solutions from the more advanced blind image deconvolution methods. The blind restoration problem of optical satellite images has been solved using Bayesian analysis (Chen et al. 2010; Shen et al. 2012), nonlinear penalty functions that utilize TV (Li et al. 2017; Liu & Eom, 2013; Jidesh & Shivarama, 2018) or sparsity-based models (Rasti et al. 2014; Mittal & Garg, 2013). A more detailed study of TV and sparsity-based regularizers will be provided in Chapter 3. For example, in the attempts to restore the degraded SPOT-5 image, Chen et al. (2010) proposed a non-iterative blind image-restoration algorithm in the redundant wavelet domain, which included the MTF measurement step and MTF compensation step. In the MTF measurement phase, they used the surface fitting technique (Balaras & Jeter, 1990) to fit the surface of the normalized logarithmic amplitude spectrum of the degraded image to a known parametric MTF model. And later, in the MTF compensation phase, with the MTF, they developed a maximum a posteriori (MAP)-based image-restoration algorithm which required the use of a multivariate statistical model (Tan & Jiao, 2007), Landweber iteration, and Multishrinkage denoising (Sendur & Selesnick, 2002). The restoration results show that the proposed method can significantly retrieve some lost detail information in the degraded SPOT-5 image. However, it imposed computational demand due to the complexity of the algorithm.

Another example of MAP-based satellite image restoration is proposed by Shen et al. (2012). In contrast to Chen et al. (2010), instead of treating the PSF in preprocessing, these authors estimate the PSF simultaneously during restoration. To narrow the solution space for the best possible definition, the author employed the Huber–Markov random field prior model to regularize the constraint in the solution. According to the authors, experimental results on CBERS-2B imageries showed that these methods perform quite well in terms of both visual inspection and quantitative evaluation. However, because of the employment of a complicated prior model, it compromised with computational complexity. For example, the proposed method is up to ten times slower than the iterative Blind Deconvolution (Ayers & Dainty, 1988) method and maximum likelihood deconvolution (MLD) (Lagendijk et al., 1990) methods.

Liu & Eom (2013) developed a hybrid algorithm based on the discrete TV regularization algorithm (Vogel & Oman, 1998) using an auxiliary image from another multispectral satellite imaging sensor as a prior image for restoration. Similar to Shen et al. (2012), the authors estimate the PSF simultaneously during the restoration process. In their approach, the amount of prior information from the auxiliary image to be used in the hybrid algorithm is determined based on the similarity between the auxiliary image and the degraded image. In order to estimate the amount of required prior information, the authors developed an algorithm based on normalized local mutual information. The proposed algorithm is applied to both simulated and real multispectral images from DMC+4 satellite, and the performance of the proposed algorithm is compared with the fixed-point total variation (FP-TV) method (Vogel & Oman, 1998), the shape adaptive discrete cosine transform (SA-DCT) method (Oliveira & Figueiredo, 2009), and the major-maximum total variation (MM-TV) approach (Foi et al., 2007). In both quantitative and qualitative comparisons for effectiveness, the proposed algorithm performed better than other algorithms. No analysis and experimental results on computation time and convergence analysis were reported in this paper.

Recently, Li et al. (2017) proposed an MTFC method that utilizes a regularization TV energy function model to compensate for the MTF using a partial derivative iteration algorithm. This method has been tested on the Space Smart Optical Orbiting Payload Integrated with Attitude and Position (SSPIAP) of China. According to the authors, the compensated MTF can be used to improve the imaging performance of onboard remote sensors and provide a reference for the onboard MTF compensation of space CCD cameras in the future.

One example of the sparsity-based blind satellite deconvolution method is the work of Mittal & Garg (2013). In their work, the authors made a small modification of the existing Local polynomial approximation-intersection of confidence interval (LPA-ICI) algorithm by using a different wavelet technique (Immerkaer-Daubechies) for the restoration of optical satellite images. Unlike existing multi-channel blind restoration methods that require spatially aligned images and correct veneration of blur size and shape (Sroubek & Flusser, 2005). According to the authors, the significant advantage of the proposed algorithm is that it can be applied to images of arbitrary sizes, The authors were inspired by Katkovnik et al. (2006) on their work in contributing a novel nonparametric regression method for deblurring noisy images based on the LPA of the image and the paradigm of ICI that is applied to define the adaptive varying scales (window sizes) of the LPA estimators. According to Katkovnik et al. (2005), the actual filtering for restoration is performed in the signal domain while frequency domain Fourier transform operations are applied only for the calculation of convolutions.

In (Shen et al. 2014), another blind satellite deconvolution method was developed. The authors employed an alternating minimization (AM) framework to simultaneously estimate the PSF and restore the degraded image. In their work, an automatic knife-edge detection method is used to obtain a good initial PSF for the AM framework. Besides, an adaptive-norm prior based on the structure tensor (Zhang, L. et al., 2011) is utilized in the AM framework to guarantee the global performance of the restoration. Preconditioned conjugate gradient (PCG) (Lin et al. 2005) optimization is also implemented to ensure the rapid iteration of the algorithm. Results in both simulated and real data experiments from Zi Yuan 3 (ZY-3) cartographic satellite indicate that the proposed image restoration method is robust, converges quickly, and can stop automatically to obtain satisfactory results. However, the proposed method imposes specific priors over the PSF according to the remote sensing degradation characteristics. In addition, the initial PSF estimation also relies on the existence of knife-edge features, which may not exist in some natural images.

Zhi et al. (2014) proposed to solve the problem of image restoration of high-resolution TDICCD camera due to satellite vibrations, which considers image blur and irregular sampling geometric quality degradation simultaneously. the vibration simulation model is established, and the irregular sampling degradation process of geometric quality is mathematically modeled using bicubic Hermite interpolation. Subsequently, a full image degradation model is developed combined with a blurred and noisy degradation process. Experimental results indicate that the proposed method performs well, and the Structural Similarity between the restored and ideal images is greater than 0.9 in the case of seriously blurred, irregularly sampled, and noisy images. The proposed method can be applied to restore high-resolution on-orbit satellite images effectively.

2.4 Summary

This chapter has reviewed the past and recent studies of two major topics of this thesis, namely (1) The on-orbit spatial characterisation, and (2) The spatial restoration of optical satellite images. Based on the studies, the challenges and problems of these topics have been identified.

In the topic of on-orbit spatial characterisation, much of the literature on EOS Cal/Val was found extensive and focuses particularly on the use of fixed-characteristic targets to measure and assess the on-orbit MTF of EOS. On the contrary, very few published studies have explored the use of stochastic-characteristic targets for on-orbit spatial characterisation. The MTF measurements based on fixed characteristic targets are highly dependent on a well-separated characteristic such as edges, lines, points, or bars in the remotely sensed imagery. The utilization of these well-separated characteristic targets is confined to stringent criteria and temporal issues, which make it a non-versatile approach. While stochastics characteristic targets do not restrict by these issues, but its feasibility and reliability for on-orbit spatial characterisation are still arguable.

For the topic of the spatial restoration of optical satellite images, the early MTFC which has been used operationally in most of the satellites has become an optional process because of its side effect (i.e., noise amplification and aliasing) in the restored images. These side effects are inherently an ill-posed inverse problem. The problem has received a considerable amount of research attention in recent years, yet no method has been proposed that can conclusively claim to have solved it. Besides, one of the most significant problems to the existing methods is that they usually incur computational complexity. Also based on the review, it can be concluded that the majority of advanced MTFC methods utilize nonlinear TV or sparsity-based regularizers. Furthermore, the quality of the restored image depends heavily on accurately estimating the model parameters (i.e., regularization parameters and prior information of an ideal image). Methods that utilize variational methods or nonlinear constrained optimization objectives, currently provide the best method for prior information and parameters modeling to estimate PSF and restore the image.

In Chapter 3, the variational modeling will be further reviewed and analyze, in particular, the TV, and the nonlinear constrained optimization. Furthermore, the ill-posed problem of image restoration will be studied to find a solution to solve the identified research problem.

CHAPTER 3: ILL-POSED PROBLEM OF BLIND IMAGE RESTORATION

This chapter reviews and analyzes the existing image deblurring methods by various researchers in the field of image restoration. The purposes of this chapter are to study the literature work related to the identified problem in Chapter 2 in order to propose solutions towards the identified problem. This chapter also discusses the practical issue of designing an image deblurring method. Furthermore, the performance evaluation measures for the proposed methods are determined and presented in this chapter.

In section 3.1, this thesis explains the ill-posed problems in blind image restoration in general and detailed the solutions for these problems. In this thesis, the image deblurring method is recognized as the potential solution to the identified research problem. Subsequently, the challenges in the estimation of an accurate blur kernel for successful image restoration will be addressed in section 3.2. The crucial aspects of how to find good region priors are also included in this section. Section 3.3 provides a review of three classes of modeling methods for image deblurring. In particular, it provides a critical and comprehensive review of the selected variational method. Section 3.4 identified and discusses the two common issues that are usually encountered in designing deblurring methods. The image quality assessment metrics used to evaluate the performance of the characterisation and restoration of the spatial images are introduced in section 3.5. Finally, section 3.6 provides a summary of this chapter.

3.1 Solutions to Ill-posed Image Restoration Problem

Recall that the field of image restoration is concerned with the estimation of uncorrupted images $f(x,y)$, from noisy, blurred ones $g(x,y)$ as follow:

$$g(x,y) = f(x,y) \otimes h(x,y) + \eta(x,y). \tag{3.1}$$

where $h(x, y)$ and $\eta(x, y)$ represent a PSF and unknown noise respectively; the symbol $\otimes$ denotes 2-D convolution operator; x and y are the continuous variables in x and y coordinate plane, respectively.

By considering a whole image, equation (3.1) is often represented as a matrix-vector form as

$$\boldsymbol{g} = \boldsymbol{H}\boldsymbol{f} + \boldsymbol{n}. \tag{3.2}$$

where g, f, and n are lexicographically ordered column vectors representing $g(x, y), f(x, y)$ and $\eta(x, y)$, respectively. $\boldsymbol{H}$ is a Block Toeplitz with Toeplitz Blocks (BTTB) matrix derived from $h(x, y)$.

Depending on the $\boldsymbol{H}$ operator in Equation (3.1), the image restoration problem can be classified into (1) image deblurring (Pan et al., 2017; Choi & Lee, 2009; Ren et. al, 2016); when $\boldsymbol{H}$ is a blur operator; (2) image Denoising (Dabov et al., 2007; Chen & Liu, 2013; dai et al., 2013), when $\boldsymbol{H}$ is identity; (3) image inpainting (Takeda et al., 2007; Zhai & Yang, 2012; Zhang, J. et al., 2014) when $\boldsymbol{H}$ is a mask, that is, $\boldsymbol{H}$ is a diagonal matrix whose diagonal entries are either 1 or 0, keeping or eliminating the corresponding pixels; and (4) compressing sensing (Zhang et al., 2012; Zhang, J. et al., 2013), when $\boldsymbol{H}$ is a set of random projections.

Mathematically, the image restoration problem, described by Equation (3.1), requires solving an ill-posed problem (Kundur & Hatzinakos, 1996) because (1) there might be many different sets of $\boldsymbol{H}$ and $\boldsymbol{f}$ corresponding to the same observed image $\boldsymbol{g}$, and (2) the inverse problem to estimate $\boldsymbol{f}$ from $\boldsymbol{g}$ often involves some numerical singularities.

According to the sense of Hadamard (1952), a problem is well-posed if the following three properties hold true: (1) Existence: For all suitable data, a solution exists, (2) Uniqueness: For the suitable data, the solution is unique, and (3) Stability: The solution depends continuously on the data.

Given a degradation model in vector-matrix form as expressed in Equation (3.2). To satisfy the first condition, the restoration problem must account for noise, because in practical imaging situations, additive noise is not negligible. For example, equality $\boldsymbol{g} = \boldsymbol{Hf}$ will not always have a solution because it does not account for the noise term $\mathbf{n}$. For the second condition, if only partial information about the imaging process is used to formulate an optimality criterion, this may yield a large number of possible solutions; Hence, to have a unique solution, proper initialization of algorithm or additional assumption on the imaging system is needed to choose the appropriate solution. Finally, the solution must depend continuously on the data, because discontinuities cause instability in many algorithms.

Based on the above deliberation, hence, to create a well-posed problem, it is essential to incorporate a priori information about an ideal image via regularization (Mesarovi et al., 1995). This section will provide a detailed review of the keys to the solution to the ill-posed inverse problem, namely the priori information of an image, and regularization.

3.1.1 Priori Information of an Image

In the image deblurring literature (e.g., Levin et al. 2007, Krishnan & Fergus, 2009, Cao et al., 2015; Dong, W. et al., 2013; Pan et al., 2017; Bai et al., 2019), two types of additional information that often used to create the well-posed problem are (1) image priors, and (2) additional image observations (e.g., image properties). The following subsections will review the relevant additional information about an ideal image that can potentially solve the ill-posed problem.

3.1.1.1 Image properties

In recent years, the nonlocal self-similarity characteristic revealed by natural images has possibly become the most significant nonlocal statistics in image processing (Wu et al., 2019). The nonlocal self-similarity describes the repetitiveness of higher-level patterns (e.g., textures and structures) embodied by the natural images within the nonlocal area (Bahadir & Xin, 2012). State-of-the-art algorithms for various image restoration tasks often rely on the assumption that natural images contain many mutually similar patches at different locations, which describes the prior information of the image. Typically, the patch similarity is assessed through the Euclidean distance of the pixel intensities (Buades, Coll & Morel, 2005).

Inspired by the success of nonlocal means (NLM) denoising filter by Buades et al. (2005), a series of nonlocal regularization functions for inverse problems exploiting nonlocal self-similarity property of natural images have emerged (Kindermann et al., 2005; Gilboa & Osher, 2007; Elmoataz et al., 2008; Peyré, 2008; Dong, W. et al., 2011, Zhang, J. et al., 2014; Jung et al.,2011). Utilization of nonlocal self-similarity as a regularization function in the literature is usually conducted in pixel-level (i.e from one pixel to another) (e.g., Gilboa & Osher, 2007; Zhang, T. et al., 2010) or block-level (e.g., Protter et. al. 2009; Dong, W. et al., 2011).

Apart from nonlocal self-similarity, local smoothness is another significant property in natural images. It characterizes the closeness of neighboring pixels in the two-dimensional space domain of images within the local region. Recently, Zhang, J. et al. (2014) proposed a joint statistical model that combines these two properties as regularization priors to solve the ill-posed inverse problem of image restoration. Figure 3.1 illustrates the local smoothness and nonlocal self-similarity of a natural image.

3.1: Illustrations for local smoothness and nonlocal self-similarity of natural images (adapted from Zhang et al. 2014).

To create a well-posed problem of image restoration, besides the image properties, the characteristics of an image are also significant. As pointed out by Cho et al. (2010), even different textures within the same image also can have a distinct profile of characteristics; thus, it requires further investigation. The next subsection will study these characteristics.

3.1.1.2 Image characteristics

Over the years, besides the aforementioned image properties, many studies also suggest that priors based on natural image statistics can regularize deblurring problems to yield better results (e.g., Levin, 2006; Cho et al., 2010; W. Dong et al., 2013; Zhang et al., 2014; Liu et al., 2016; Bai et al., 2019). Moreover, prior studies have also shown that the marginal distributions of image statistics are non-Gaussian and have significantly heavier tails than a Laplacian, that well modeled by the hyper-Laplacian (Levin et al. 2007, Krishnan & Fergus, 2009). The distribution of gradients of hyper-laplacian (Field, 1994) has most of its mass on small values but gives significantly more probability to large values than a Gaussian distribution. Figure 3.2 illustrates the empirical distribution of gradient with respect to a scene (Krishan & Fergus, 2009). It can be noticed that the hyper-Laplacian (i.e., Green) fits the empirical distribution (i.e., Blue) closely, particularly in the tails.

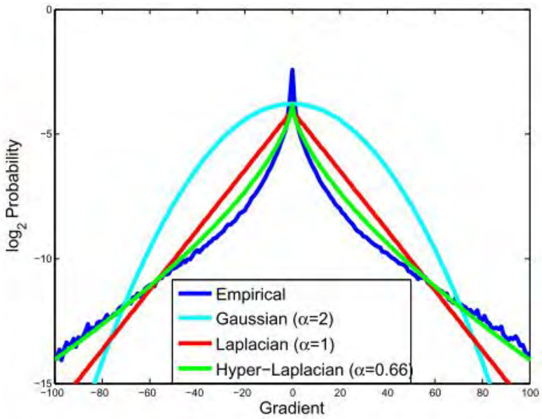

(a) (b)

Figure 3.2: A hyper-Laplacian with exponent α = 2/3 is a better model of image gradients than a Laplacian or a Gaussian (Krishan & Fergus, 2009). (a) A typical real-world scene. (b) The empirical distribution of gradients in the scene (blue), along with a Gaussian fit (cyan), a Laplacian fit (red), and a hyper- Laplacian with α = 2/3 (green).

The marginal statistics of images are usually modeled by Generalised Gaussian distribution (GGD) (Mallat, 1989), the simplified form of GGD is defined as

$$\rho_{GGD}(f) \propto e^{-\gamma|\nabla f|^{\alpha}}, \tag{3.3}$$

where $\nabla f = (\partial_x f, \partial_y f)^T$ is the gradient of the image f, γ, and α are the shape parameters. The distribution $\rho_{GGD}(f)$ is a Gaussian distribution function if $p = 2$, and a Laplacian distribution function if $p = 1$. If $0 < p < 1$, then $\rho_{GGD}(f)$ is named as hyper-Laplacian distribution. In sparse coding, it is as known as L_p-seminorm, which is typically a non-convex problem. More discussion about the value p can be found in the paper by Krishnan and Fergus (2009). The authors have done impressive work in proposing a fast deconvolution method using hyper-Laplacian priors, as such their works have received considerable scholarly attention in recent years. Based on their work, Chang and Wu (2015), and Xu et al. (2013) introduced the hyper-Laplacian priors to handling outliers in the image deblurring process. Furthermore, Liu et al., (2016) fitted the hyper-Laplacian function to high resolution Passive millimeter-wave images as a regularization function to create a well-posed image restoration model. Most recently, Cheng et al. (2019)

proposed a nonconvex variational model for Retinex where they utilized the hyper-Laplacian priors to characterizing the gradients of reflectance in the Retinex model.

So far, this chapter has described the image properties and image characteristics. The following part of this section moves on to provide brief literature on image priors.

3.1.1.3 Image priors

Image priors, also known as the "prior information" of an image (Roth & Black, 2005) play an important role in the development of algorithms to treat the ill-posedness of the image restoration problem. The characteristics and properties of images as explained in the previous subsections are the "prior information" that formed data-authentic (i.e., true, quantitative, or qualitative information, acquired from real-life phenomena) priors of an image (Roth & Black, 2005). With this knowledge, many priors have been proposed based on different principles. The variety range from priors on derivative (e.g., Rudin et al., 1992, Levin, 2006), multiscale image transform coefficient (e.g., Donoho, 1995; Portilla et al., 2003), filter responses (e.g., Zhu & Mumford, 1997; Roth & Black, 2005) and patches (e.g., Buades et al., 2005).

The Image priors can be obtained by either model-based or learning-based approaches depending on the availability of the training data (Wu et al. 2018). With the limitation of training data, in this context, this thesis focuses on a model-based approach (readers may refer to Gong et al. (2018) for more detailed learning-based approaches).

In Model-based approaches, image priors are obtained by mathematical construction of a penalty functional and its parameters must be intrinsically estimated from the observation. Among others, sparse coding and its variations are seemly the most studied in the literature (Dabov et al. 2007; Dong, W. et al., 2011; Dong, W. et al., 2013, Mairal et al., 2009, Wu et al., 2016, Sha et al., 2019; Liu & Osher, 2019). Early studies in sparse coding mostly concentrated on the characterisation of localized structures or transient events in natural images. A sparse coding model with good localization properties in both spatial and frequency domains can be constructed through mathematical design (e.g., wavelet (Mallat, 1996)) or learn them from training data (e.g., dictionary learning (Mairal et al., 2009a)). In the signal frequency domain, the sparse model assumes that natural images will be sparsely distributed in some transformed domain; whereas in the spatial domain, the sparse model assumes each patch of an image can be accurately represented by a few elements from a basis set called a dictionary, which is learned from natural images (Aharon et al. 2006). According to Mairal et al. (2009a), dictionary learning can give sparser solutions as compared to predefined transform matrices, because it is more adaptable to image local structures.

Dabov et al. (2007) proposed a patch-based procedure that exploits image self-similarities and gives state-of-the-art results. Owing to their work, the importance of exploiting nonlocal self-similarity properties in natural images was recognized in simultaneous sparse coding works and nonlocal sparsity-based image restoration. The nonlocal self-similarity property is among the most effective image priors to the constraint solution space effectively. In recent works, studies found that the combination of the sparsity and the self-similarity properties of natural images are usually achieved better performance. Some of the notable works are those from (Mairal et al. 2009b, Zhang, J. et al., 2014; Dong, W. et al., 2013).

Most recently, Dong, W. et al. (2015) proposed an image model named SSC-GSM that combined the Gaussian scale mixture (GSM) (Portilla et al., 2003) with simultaneous sparse coding (SSC) leading to state-of-the-art performance in image restoration. The authors point out that their work clearly has shown the importance of spatial adaptation regardless the underlying image model is local or nonlocal; during the image modeling, it is crucial to take both local variations and nonlocal invariance into account.

In this section, it has been explained that the characteristics and properties of the image are essential to designing image priors. Image priors knowledge plays a critical role in the performance of image restoration algorithms by solving the ill-posed inverse problem, therefore, designing effective regularization functions to reflect the image priors is at the core of image restoration.

3.1.2 Regularization

The success in solving the ill-posed problem of image restoration depends on how accurately the regularizer models priori information of the original image (Kundur & Dimitrios 1996).

In general, the regularization solution that copes with the ill-posed nature of image restoration can be described in the following minimization problem as

$$\min_{f} \frac{1}{2} \|f \otimes \boldsymbol{H} - g\|_2^2 + \lambda \Psi(f), \tag{3.4}$$

where $\frac{1}{2}\|f \oplus H - g\|_2^2$ *is* the ℓ_2-norm data-fidelity function, $\Psi(f)$ is called the regularization function denoting image prior and λ is the regularization parameter.

Traditionally, the regularization function would be defined using the ℓ_2-norm and a simple variational operator Ψ, such as the Laplacian (Gonzalez & Woods, 2017). This could potentially create a well-posed problem by introducing a smoothness constraint that penalizes variations caused by amplified noise. Nevertheless, since images are piecewise smooth, traditional regularizers may adversely affect the restoration of sharp edges, often producing images that are over-smoothed. More advanced regularizers, such as the TV norm, use nonlinear penalty functions to model the characteristics of the original image, which generally produce a better restoration result. A more detailed study of the regularization methods will be discussed in Section 3.3. In this subsection, the optimization approaches for image regularization will be reviewed.

There are various optimization approaches for a regularized-based image restoration problem. Based on the literature review, these approaches can be grouped into four: (1) Pixel-based Regularization Methods, (2) Sparsity-based Regularization Methods, (3) Patch-based Regularization Methods, and (4) Group-based Regularization Methods. The subsections that follow will review each group in detail.

3.1.2.1 Pixel-based regularization methods

Classical regularization functions, such as half quadrature formulation (Geman & Reynolds, 1992), *Mumford-Shah* (MS) model (Mumford & Shah, 1989), and TV models (Rudin et al., 1992), utilize local structural patterns with the underlying assumption that neighboring are locally smooth except at edges.

There is a large number of pixel-based regularization functions (Carter, 2001; Chambolle, 2004; Beck & Teboulle, 2009; Babacan et al, 2008; Chantas et al., 2010; Sánchez et al.,2013; Liu & Huang, 2014; Ma et al., 2017) built on the TV model (Rudin et al., 1992) demonstrate high effectiveness in preserving edges and recovering smooth regions. One representative work from the literature that uses the TV energy model as MTFC for optical satellite images is Li et al (2017). TV regularizer prefers boundaries with limited curvature (Bellettini et al., 2002), therefore, they usually smear out image details and cannot deal well with fine structures.

3.1.2.2 Sparsity-based regularization methods

In the survey by Amudha et al. (2012), the authors stated that sparsity-based restoration methods are emerging methods that perform better deblurring in the presence of noise.

This statement is well supported by many (Zhang et al., 2015; Liu et al., 2016; Wu et al., 2016) because the sparsity-based regularizers force the transform domain coefficients of the restored images to be sparse, thus, it generally reduces noise without adversely affecting the restoration of edges. To take advantage of the multi-scale properties of images, many sparsity-based regularization algorithms (e.g., Figueiredo & Nowak 2003; Figueiredo et al. 2007; Argenti et al. 2008; Dupe et al., 2009; Chan & Zhou, 2007; Cai et al, 2011; Tao 2010; Xu et al. 2013) based on wavelet (Mallat, 1989), curvelet (Candès & Donoho, 2000), and contourlet (Do & Vetterli, 2005) are proposed.

According to Ma et al., (2017), in most cases, the sparsity-based regularization methods (e.g., wavelet) can achieve better quality than the pixel-based regularization method (e.g., TV). However, both regularization methods do not thoroughly make use of all properties of the images. This makes sense because the pixel-based regularization methods cannot characterize the multi-scale properties and multi-level structures of an image. The sparsity-based regularization methods using the transform domain coefficient, even though can characterize both properties, but not capable of characterizing the nonlocal self-similarity of an image.

3.1.2.3 Patch-based regularization methods

Recently, inspired by the success of nonlocal means (NLM) denoising filter by Buades et al. (2005) that exploits nonlocal self-similarity property of natural images, a series of patch-based regularization algorithms have emerged (Jung et al., 2011; Li et al., 2014, Zoran & Weiss, 2011; Zhang, J., et al.,2014a; Gu, Liu & Hu, 2015; Zha et al., 2017). Due to the utilization of self-similarity prior, this type of regularization function has been shown to produce superior results over the pixel-based regularizers, with sharper image edges and more image details (e.g., Zhang, J., et al., 2014a). Since pixel-based regularizers are a type of 1-D feature extraction, therefore they cannot capture the redundancy of small patches inside the same image. The basic idea of regularization using the image patch is to approximate a pixel value using the weighted mean of the other pixels which have similar structures to that of the current one. The patch-based regularizers have sparsity properties because the patch is modeled by a sparse linear combination of learnable basis elements. These elements, called atoms, compose a dictionary (Aharon et al., 2006).

There exist two main problems in the current patch-based sparse representation model (Zhang, J., et al., 2014a; Liu & Hu, 2015; Zha et al., 2017). First, it often requires high computational complexity. This is because dictionary learning is a large-scale and highly non-convex problem (Aharon et al., 2006; Engan, Aase & Hakon-husoy, 1999). Second, a patch is the unit of sparse representation, and each patch is usually considered independently in dictionary learning and sparse coding, which disregard the relationships of self-similarity among patches. In addition, with the learned dictionary, the actual sparse coding process is always calculated with relatively expensive nonlinear estimations, such as match pursuits (Chen, Donoho & Saunders, 2001; Tropp & Gilbert, 2007); This condition also may be unstable and imprecise due to the coherence of the dictionary (Mallat & Yu, 2010).

3.1.2.4 Group-based regularization methods

Most recently, instead of a single image patch, a group of similar patches (i.e., patch group) is used as a basic unit of sparse coding (Xu et al., 2015, Zhang, J., et al., 2014b). In other words, the patch group is representative of a set of sparse codes in the group domain. Similar to patch-based, each group can also be precisely represented by a sparse linear combination of basic elements of the dictionary (Mairal et al., 2009). This type of representation achieves better performance with lower computational complexity than patch-based algorithms since it is designed with self-adaptive dictionary learning for each group. It is different compared with a single patch that utilizes dictionary learning independently from sparse representation modeling of natural images.

Zha et al. (2018, citing Li et al., 2016) point out that the group-based regularization method (Zhang, J., et al., 2014b), even though has shown great successes in various image processing tasks, may suffer an over-smooth effect in the restored image. Hence, the authors proposed a new sparse representation model, so-called dubbed joint patch-group based sparse representation (JPG-SR). Compared with the work of Zhang, J. et al., (2014a) for image inpainting, the proposed JPG-SR achieved a better performance in functions of Peak Signal to noise ratio.

The section that follows moves on to review the blur estimation in image deblurring problem and describe the utilization of image priors to greater detail.

3.2 Addressing Blur Estimation in Blind Image Deblurring

Based on Equation (3.1), the fundamental task of deblurring is to deconvolve the blurred image (i.e., degraded image, g) with the PSF that exactly describes the distortion. Image deblurring has been studied extensively with a rich literature. Early approaches used parameterized forms for blur kernels and imposed constraints on the blur kernels with a single image (Chen et al. 1996; Chan and Wong 1998; Yitzhaky et al. 1998) or multiple images (Rav-Acha & Peleg 2005). However, as demonstrated in Fergus et al. (2006), the real kernel caused by motion blur is complex, beyond a simple parametric form. In the image deblurring process, Fergus et al. (2006) point out, image deblurring task has been shown to render favorable results if it is solved in two steps: (1) blur kernel estimation and (2) non-blind deconvolution. If the blur kernel can be accurately estimated, then the blurred image can be restored with non-blind deconvolution algorithms using the estimated blur kernel. This type of approach is referred to as the a-priori blur identification method (as described in section 2.3 of Chapter 2). Image deblurring is a low-level task aiming to produce high quality images for the subsequent high-level vision tasks.

The success of early single-image deblurring methods (e.g., Fergus et al., 2006; Shan, Jia & Agarwala, 2008) partly stems from the use of various sparse priors in either the blur kernel estimation phase or the restoration phase of the latent sharp image. The primarily used of sparse priors is to avoid possibly results in a dense kernel that causes unwanted artifacts and local minimum problem in an iterative kernel estimation. However, there is a direct consequence, because minimizing a non-convex energy function with the kernel-sparsity prior is usually computationally expensive.

Apart from using the sparse priors, there is another group of methods that use the Gaussian kernel priors (Joshi, Szeliski & Kriegman, 2008; Cho & Lee, 2009). Using the Gaussian kernel priors, thus it reduces to a convex optimization problem that can be solved efficiently using Fourier Transform (FT). This approach greatly shortens the computation time, but the Gaussian priors tend to produce overly smooth images. Furthermore, although the FT can solve the deconvolution problem efficiently, it produces periodic boundary artifacts. This happens because convolution operation in the frequency domain is assumed to be fully cyclic, however, this assumption is wrong along image boundaries (Levin et al., 2007).

Regardless of the limitation of both approaches (i.e., using sparse or Gaussian priors) in the tradeoff of efficiency and effective issues, their success has been an inspiration to many. Such that there is a growing body of literature that recognizes the challenges in the field of single-blind image blind deblurring. The significant progress in this field can be attributed to the advancement of efficient inference algorithms (Levin et al., 2009; Xu & Jia, 2010), various natural image priors (Krishnan & Fergus, 2011; Sun et al, 2013; Pan et al., 2014; Liu et al., 2016; Ma et al, 2017; Bail et al., 2018), and more general motion blur models (Whyte et. al, 2012; Gupta et al, 2010; Hu et al., 2014).

As mentioned in the steps single bling image deblurring proses, estimation of the accurate kernel is one of the keys for successful image deblurring results. Hence, the following subsection reviews the two most important aspects that attribute to an accurate blur kernel estimation, namely image priors, and image structure.

3.2.1 Exploiting Image Priors

From the literature, many blur kernel estimation methods have exploited various constraints to model the characteristics of blur and utilize different natural image priors to regularize the solution space. Based on the principle, this thesis divides these image priors into four types: Gradient-based, Intensities-based, low rank-based, and graph-based. The success of most existing algorithms can be attributed to the use of a wide range of parametric image priors. These constraints are used to avoid local minima, dense kernels, and visual artifacts in the restored image.

3.2.1.1 Gradient-based image priors

Gradient-based image priors are among the earliest priors used to estimate blur kernels from a single blurred image. In (Fergus et al. 2006), the authors proposed to use the Gaussian mixture model (GMM) of that having finite mixture numbers to fit the gradient magnitudes distribution of the natural image to obtain the blur kernel by adopting a Bayesian approach. Chakrabarti et al (2010) extended the GMM to the Gaussian scale mixture (GSM) which is a mixture of infinite Gaussian models with a continuous range of variances. A critical issue of this model is that the infinite selection of Gaussian distribution standard deviation, which makes it computationally expensive. Additionally, for computation efficiency, a generalized Gaussian model is used by Levin et al. (2007)

in their design of an optimal aperture filter, and a Gaussian prior is imposed on the gradient patches instead of gradient pixels by Hu et al (2012).

Shan et al. (2008) introduce a local prior by concatenating two piece-wise continuous functions to fit the logarithmic gradient distribution of natural images. In (Levin et al., 2011), the authors model the sparse priors as a mixture of Gaussian (MOG) and employed an expectation-maximization (EM) approximation method to estimate blur kernels. As pointed out by Levin et al. (2009), sparse priors used in image deblurring favor blurry images rather than clear images. In order to over this problem, the normalized sparsity prior (Krishnan, Tay & Fergus, 2011) and patch recurrence prior (Michaeli & Irani, 2014) have been proposed. While these priors have been demonstrated satisfactory results for image deblurring, they are computationally expensive due to their highly non-convex nature. Other methods have been applied to reduce the computational load. For example, Krishan and Fergus (2009) proposed fast hyper-laplacian priors using a lookup table (LUT) and an analytic approach for image deblurring; the work has gained widespread acceptance. Besides that, in (Cho & Lee 2009; Xu & Jia, 2010), the authors used a Gaussian prior on the latent sharp images that can be computed efficiently by Fast FT. Moreover, they also introduced an edge selection step to select useful edges for kernel estimation. However, as the edge selection step is developed based on heuristic filters, therefore, the assumption that there exist strong edges in the latent sharp images may not always hold. In order to better reconstruct sharp edges for kernel estimation, exemplar-based methods (Sun et al., 2014; Pan et al., 2014; Hacohen, Shechtman & Lischinski, 2013) have been proposed to exploit the priori information contained both in a blurry input and example images. The drawback of this method is that the query in the external dataset is computationally expensive.

In addition to generic priors for natural image deblurring, the authors of (Pan et al., 2014a; Pan et al. 2014b; Cho, Wang & Lee, 2012) also exploited statistics for specific classes of objects (e.g., text and faces) for different application to solve its deblurring problem.

3.2.1.2 Intensities-based image priors

Besides the priors on image gradients, the knowledge of image intensities is extremely helpful in specific applications. For example, in (Chen et al. 2011), the authors developed a content-aware prior based on image intensities to computing the histogram of the whole image for document image deblurring.

Recently, sparse representations have been used to model image priors, their sparsity properties can be comprised of a direct measure of image intensities or a transform coefficient. In Hu et al. (2010), the authors learn an over-complete dictionary directly from a blurry image, and later use the sparsity constraints to iteratively recover the latent sharp image. In the application of face recognition, Zhang, H., et al. (2011) proposed a sparse representation algorithm to deblur and recognize face images in a unified manner. Additionally, Cai, et al., (2012) utilized the multi-scale properties of wavelet to enforcing sparsity constraints on both the sharp image and blur kernel for image deblurring.

Another notable work of sparse representation is from W. Dong et al. (2011), where the authors combined the merit of sparsity and the self-similarity of natural images to achieve a better performance of image deblurring results. In their subsequent work, Dong, W., et al., (2013) developed a method called nonlocally centralized sparse representation (NCSR) to model image patches that exploit image nonlocal self-similarity for deblurring.

In (Couzinie-Devy et al., 2011), the authors model the clear image patches and blurry ones with a linear mapping function and employed the learning dictionary to recover sharp details, More recently, Cao et al. (2015) used several multi-scale dictionaries to describe and deblur text images. As pointed out by Ren et al. (2016), although these dictionary-based methods may restore some high-textured regions, they usually fail to preserve substantially useful information for kernel estimation. Hence, it often generates hallucinated high-frequency contents, which complicate the subsequent kernel estimation steps.

3.2.1.3 Low-rank priors

Apart from employing the aforementioned sparsity priors, the low-rank model has also been proposed to exploit the sparsity (i.e., low-rankness) of the image vector-matrix. In the recent year, low-rank matrix approximation (LRMA) that aims to recover the underlying low-rank matrix from its degraded observation has been employed and successfully applied to image restoration (e.g., Wang et al., 2013; Zhang, H., et al., 2014; Xu et al, 2018). Among which, the nuclear norm minimization (NNM) approach for LRMA has been successfully employed in various application such as matrix denoising (Donoho, Gavish & Montanari), low-level vision tasks (Oh et al., 2013), and face shadow removal(Mu et al, 2011; Kang, Peng & Cheng, 2015). A comparative study for the NNM methods can be found in the work by Zha et al. (2019).

When dealing with the single image denoising problem using the LRMA, authors in (Dong. W., 2013b; Lu et al., 2014, Jia et al., 2016) exploit the nonlocal self-similarity on the patch level. Though LRMA takes full advantage of nonlocal self-similarity on patch level, it usually produces over-smooth estimates.

Recently, to generate a good low-rank estimation from patch groups, Gu et al. (2014) propose a weighted nuclear norm minimization (WNNM) model to adaptively regularize the singular value of the matrix, for which it facilitates more flexible and robust results in image denoising. Inspired by WNNM, Xie et al. (2014) extend the 2-D low-rank matrix model to a higher dimension tensor model for multispectral image denoising tasks. Later, a multi-channel WNNM model is proposed by Xu et al. (2018) to address the real color image denoising problem, which enables a different color to have different noise levels.

The LRMA has also been applied to the non-blind image deblurring problem. A low-rank based nonlocal spectral prior is exploited by W. Wang et al. (2013) for non-blind image deblurring.

In contrast to the WNNM method (Gu et al. 2014) that uses a weighting scheme for denoising, Ren et al. (2016) employed the low rank prior to generating clean intermediate images for kernel estimation. The WNNM was employed by Ma et al. (2017), in the TV regularization framework to solve the deblurring problem.

Similar to W. Dong et al. (2013), Wen, Li & Bresler (2017) also take full advantage of both the local sparsity and nonlocal self-similarity in natural images to propose a model co-called STROLLER (Sparsifying TRansfOrm Learning and Low-Rank) to combine the adaptive transform sparsity of image patches and the low-rankness of data matrices formed by Block Matching (BM) for deblurring.

3.2.1.4 Graph-based Image Priors

With the advance of Graph signal processing (GSP) (Shuman et al., 2013), a new type of image priors has emerged. GSP is an emerging field to study signals on irregular data kernels described by graphs. The GSP models the pixels as nodes with weighted edges that reflect inter-pixel similarities and interprets the images (or image patches) as graph signals (Shuman et al., 2013). This type of priors has been designed for different image applications (Hu, Cheung & Kazui, 2016; Pang & Cheung, 2017; Kheradmand & Milanfar, 2014; Liu et al., 2017; Bai et al. 2019).

Based on the literature review, generally, there are two types of graph-based image priors, namely graph Laplacian regularizer (Pang et al. (2017) and GTV (Graph Total Variation) (Elmoataz, Lezoray & Bougleux, 2008; Hidane, Lzoray & Elmoataz, 2013; Couprie et al., 2013; Berger et al., 2017) have been designed for different inverse problems.

(a) ***Graph laplacian prior***

In (Hu, Cheung & Kazui, 2016), the authors designed a dequantization (i.e., soft-decoded JPEG- compressed) scheme specifically for piecewise smooth (PWS) images (i.e., images with sharp object boundaries and smooth interior surfaces) using the quantization bin boundaries as constraints to optimize the desired graph-signal and the similarity graph in a unified framework. In Liu et al. (2017), another type of soft-decoded JPEG- compressed) scheme for natural images was developed using a combination of three priors. The three priors are comprised of a new graph smoothness prior called Left Eigenvectors of Random walk Graph Laplacian (LERaG), a compact dictionary trained by sparse representation, and Laplacian distribution of discrete cosine transform coefficients. In (Pang et al. 2017), an image denoising method was developed using a graph Laplacian regularization in the continuous domain, whereas in (Kheradmand & Milanfar, 2014), a non-blind image deblurring method was developed using a doubly-stochastic graph Laplacian.

(b) ***Graph total variation prior***

Elmoataz et al. (2008) analyzed the discrete *p-Dirichlet* energy in image and manifold processing. The p-Dirichlet energy prior is also known as GTV is the type of prior that favors the piecewise smooth preserving properties and convexity. In (Couprie et al., 2013), the author proposed a dual constrained GTV regularization on graphs. Hidane et al. (2013) employed the GTV for a non-linear multi-layered representation of graph signals., whereas Berger et al. (2017) employed the GTV for recovering a smooth graph signal from noisy samples taken on a subset of graph nodes. Most recently, Bai et al. (2019) proposed a reweighted graph total variation (RGTV) prior to promoting a bi-modal weight distribution to reconstruct a skeleton patch from a blurry observation for blur kernel estimation. of a blurry image patch to solve the blind image deblurring problem.

From the literature review, numerous studies were found to focus on exploiting additional information (i.e., image priors) for blur kernel estimation to facilitate blind single image deblurring. However, considerably less attention has been paid to exploit image structure for kernel estimation and deblurring. Hence, the following subsection will discuss this topic.

3.2.2 Exploiting image structure

In signal processing, an edge in an image excites imaging response systems and results in an edge response, which derivative is the degradation function that describes the blur in an image. In the sense of single-blind image deblurring, extraction of salient edges from reliable image structure is crucial for an accurate blur kernel estimation. Thus, it leads to a question on "What kind of image feature or structure of a blurred image is considered reliable to help in kernel estimation, and how to extract these features from a blurred image?".

3.2.2.1 Selection of good regions

For the single-blind image deblurring problem (e.g., Fergus et al., 2008; Shan et al., 2008; Zhang, X. et al. 2016, Zhu & Sim, 2011; Zhang, C. et al., 2018), intuitively, it is usually beneficial to make full use of the input blurred image. However, not all pixels of the input blurred image are informative. Smooth regions, for example, not only do not contribute much to estimating the blur kernel but can cost the kernel estimation if containing random noise. Therefore, it is important to detect reliable image features for blur kernel estimation (Zhang, J., et al., 2014), so that the accurately estimated blur kernel can then be used to recover a latent sharp image with high visual quality.

Alternatively, another group of works (Cho, S. & Lee, 2009; Joshi et al., 2008; Cho, T. et al., 2011; Smith 2012) focuses on the use of sharp edges in the image for blur kernel estimation. For example, Cho, T. et al. (2011) employed an explicated edge prediction step that uses the Radon Transform (Deans, 1992) for blur kernel estimation. However, this method has difficulty in dealing with a large blur. Generally, sharp edges can be very useful under proper assumptions. According to Smith (2012), the underlying assumption for effective use of sharp edges is that high contrast regions in the original image can maintain informative structure even after the motion blur. However, Xu & Jia (2010) argues that sharp edges do not always effective for kernel refinement in the estimation process, but instead in some circumstances greatly increase the estimation ambiguity. For example, when detected edges are smaller than the size of the blur kernel. Consequently, they proposed new metric co-called edge maps to measure the usefulness of the image edges. Recently, many existing algorithms (e.g., Pan et al., 2013; Hu & Yang, 2015) have adopted edge maps for kernel estimation.

This subsection has discussed the type of image feature or structure in a blurred image that can be utilized in kernel estimation. The next subsection will move on to review the methods used for structure extraction, particularly in the structure-texture image decomposition approach.

3.2.2.2 Structure-texture image decomposition

Texture, according to Wei et al. (2009) usually refers to surface patterns that are similar in appearance and local statistics, whereas structure is a cohesive whole built up of distinct parts.

In general, the structure-texture decomposition problem is formulated as finding an appropriate (or latent) structure by suppressing texture details in the input image. Hence, given an image I, in structure-texture decomposition, an image is decomposed as

$$I = S + T \tag{3.5}$$

where S and T represent the structure elements and texture details, respectively.

The structure-texture decomposition problem has been used in a broad range of image processing applications, such as image denoising (Rudin et al., 1992; Aujol et al, 2005; Gilles, 2007), image composition (Xu et al., 2012; Gastal & Oliveira, 2011), image smoothing (Perona & Malik, 1998), etc. Due to its importance, several methods have been proposed over the years, which in general can be divided into two categories: (1) filtering-based approaches (Cho, Lee, Kang, & Lee, 2014; Paris, Hasinoff & Kautz, 2011; Karacan, Erdem & Erdem, 2013; Zhang, Q., Xu & Jia, 2014; Lee et al., 2017) and (2) optimization-based (Rudin et al., 1992; Hua et al., 2014; Weiss, 2006; Xu et al, 2011; Xu et al., 2012).

(a) ***Filtering-based approaches***

Among the filtering-based approaches, the bilateral filter (Tomasi & Manduchi, 1998) is the widely used kernel-based edge-preserving filter. It works by weight averaging the colors of neighbor pixels based on their distances in space and range. Due to its simplicity and effectiveness, bilateral filtering has been successfully applied to several computational image applications (Fattal et al, 2007; Winnemoller et al. 2006). Many works have been built on the bilateral filter (e.g., Durand & Dorsey, 2002; Porikli, 2008; Yang et al., 2009). However, all these methods usually lead to runtime and/or memory cost problems, due to the complexity of algorithms.

In (He, Sun & Tang, 2010), another filter-based approach, so-called the guided filter was developed to perform local linear transforms of a guidance image using a strategy that does not lead to gradient distortions near edges.

To remove strong textures within images, several methods have been proposed such as the histogram filter (Kass & Solomon, 2010), median filter (Weiss, 2006; Ma et al., 2013; Zhang, Q., 2014), and diffusion-based approaches (Weickert, 1998; Vanhamel, Pratikakis, & Sahli, 2003). These methods are capable of filtering textures to some extent unless the textures contain large oscillating signals. In (Subr, Soler & Durand, 2009), the authors remove the strong textures within the image using computed envelopes defined from local extrema and smoothed out texture oscillations by averaging the envelopes.

The domain transform method by Gastal and Oliveira (2011) delivers a significantly reduce computational cost in 2-D filtering by reducing the dimensionality to 1-D filtering operation. These methods can produce high-quality edge-preserving smoothing results while preserving strong textures. One limitation of this filter is not it is not rotationally invariant (i.e., filtering a rotated image and rotating a filtered image may produce different results).

Cho et al. (2014) extend the bilateral filter to be a bilateral texture filter that uses joint bilateral filtering with a guidance image. The guidance image is generated via a patch shift mechanism. Similar to Cho et al. (2014), the rolling guidance filter (Zhang, Q., 2014) also uses a guidance image in joint bilateral filtering. The guidance image is based on a Gaussian-blurred image, it is used to eliminate only the image structures that are smaller than a specific scale.

Most recently, Lee, H. et al., (2017) proposed a new gradient operator, the interval gradient method that adaptively smooths image gradients to filter out textures from images. Using interval gradients, textures can be distinguished from structure edges and smoothly varying shadings.

*(b) **Optimization-based approaches***

The TV method was originally proposed by Rudin et al. (1992). It is a renowned denoising algorithm that effectively suppresses textures of arbitrary shapes by enforcing TV regularization constraints on the image to preserve large-scale edges. This approach has been analyzed in Meyer's (2001) and Aujol et al. (2006). It is the inspiration source of many works (Vese & Osher, 2003; Aujol & Chambolle, 2005; Aubert & Aujol, 2005; Aujol et al, 2005; Osher et al., 2003, Xu & Jia, 2010; Pan et al., 2013). The detailed mathematical study of work by Rudin et al. (1992) can be found in the work by Chambolle & Lions,(1997).

According to Farbman et al. (2008), structure-texture decomposition methods based on the bilateral filter (e.g, Durand & Dorsey, 2002; Paris, 2007) are limited in their ability to extract detail at arbitrary scales, which results in halo artifacts. Instead, the authors introduced the weighted least squares (WLS) method in their framework to overcome some of these problems. It works by controlling the level of smoothing, and by forcing the filtered image to be smooth except at regions having large gradient values, thus becomes a multi-scale image decomposition method. Later, Paris et al. (2011) demonstrated that multi-scale detail manipulation can be achieved using a modified Laplacian pyramid with coefficient classification.

In (Xu et al, 2011), L_0 gradient minimization was introduced to globally optimize the quality of filtering by controlling the number of non-zero gradients in the image. With this control, it can remove low-amplitude structures and globally preserve and enhance salient edges, even if they are boundaries of very narrow objects.

As compared to filtering-based approaches, optimization-based techniques (Farbman, 2008; Paris, 2011) are able to produce high quality results; however, their computation costs are higher in general. In addition, these methods cannot satisfyingly distinguish texture from the main structures. In their subsequent work (Xu et al. 2012), the authors introduced relative total variation (RTV) which allows accurate identification and removal of texture regions. One limitation as reported by Xu et al. (2012) is that it cannot distinguish between texture and structure that are similar in scales or are close with respect to the new variation measures. This is because their method assumes neither the specific type of texture nor the latent main structure arrangement.

Except for (Xu et al., 2012), all the aforementioned studies aim at extracting structure from noise with edge-preserving capabilities. However, only a few of them have a specific goal of extracting structure from the texture. Hence, Karacan et al. (2013) proposed a patch-based texture removal algorithm that uses similarity measures based on region covariances (i.e., the covariance matrices of image features).

This section has extensively reviewed both approaches for structure-texture image decomposition. Based on the review, it can be concluded that the optimization-based approaches (e.g., Xu et al., 2011; Xu et al., 2012; Hua et al., 2014) globally suppress the oscillating patterns induced from texture $\boldsymbol{T}$ while guessing the structure image $\boldsymbol{S}$ as similar as possible to the input image I. Although they obtain high-quality results, these methods are comparably complex and cannot easily be parallelized, thus not allowing the algorithm to handle large images and used in interactive applications. Whereby, the filtering-based algorithms (e.g., Cho et al, 2014; Karacan, Erdem & Erdem, 2013; Zhang, Q., Xu & Jia, 2014) try to design effective filter kernels to suppress texture T. Previous filtering approaches, however, often fail to accurately detect structure S for structure edges and corners.

This section has attempted to provide a summary of the past and current literature relating to kernel blur estimation for blind image deblurring. The next section will discuss and review, the literature that employed regularized-based approaches to solving blind image restoration problems.

3.3 Reviewing Blind Image Restoration Methods

As a fundamental problem in the field of image processing, image restoration has been the subject of intensive research among scholars and researchers over the decades. The recent reviews of this problem can be found in the work by Lai et al. (2016).

Recovering an ideal image $f(x,y)$ from degraded image $g(x,y)$ of Equation (3.1) can be formulated as the minimization problem

$$\min_{f(x,y)} \sum_{x,y} |h(x,y) \otimes f(x,y) - g(x,y)|^2. \tag{3.6}$$

As mentioned in Section 3.1, to obtain a good restoration result, prior knowledge of the image must be incorporated in solving Equation (3.4). This leads to the question of choosing regularization functions for Equation (3.4), or equivalently the priors of $f(x,y)$. However, the difficulty is that computationally efficient priors are not necessarily effective (e.g., Tikhonov-Millar regularization) whereas effective priors may not be efficient (e.g., TV regularization). Therefore, seeking a good prior to developing an algorithm becomes the basis of image restoration.

There is a diverse variety of image restoration methods that have been studied in many articles and books (Kundur & Hatzinakos, 1996; Banham & Katsaggelos, 1997; Hansen, Nagy & O'Leary, 2006; Bovik, 2009; Gonzalez & Woods, 2017; Campisi & Egiazarian, 2017). From the viewpoint of how to handle the ill-posedness in image deblurring tasks, existing methods can be grouped into five categories: **variational methods** (e.g., Jordan et al., 1999; Krishan et al., 2011; Papafitsoros & Schonlieb, 2014; Bruckstein, Donoho,

& Elad, 2017; Li et al., 2018; Cheng et al., 2019). **Bayesian inference framework** (e.g., Richardson 1972; Fergus et al., 2006; Levin et al., 2011; Zhang et al., 2014; Bigdeli et al., 2017; Cao et al., 2018), **sparse representation-based methods** (e.g., Chen et al., 1998; Elad & Aharon, 2006; Dong et al., 2013; Dong et al.,2015; Tang et al, 2018; Yu et al., 2019), **homography-based modeling** (Whyte et al., 2010; Joshi et al., 2010; Cho et al., 2012; Zheng et al., 2013; La Camera et al., 2015), and **region-based methods** (e.g., Levin 2006; Hirsch et al., 2010; Xu & Jia, 2012; Kim et al., 2013; Hu & Yang, 2015; Zhi et al, 2017). However, this section will only focus on those that are related to the research problem of this Work, namely the TV regularization in variational methods and alternating minimization in variational Bayesian methods.

3.3.1 Variational Methods

Variational methods are typically used to convert an ill-posed problem into a well-posed problem which is characterized by exploring additional information or constraints to reduce the size of the solution space of the unknown variables (Jordan et al., 1999). These types of methods stem from the calculus of variations. To approximate the problem, it typically involved the extremum (i.e., maximum or minimum) functional setting that comprises a function and the associated constraints:

$$\min_{A} \Phi(A;B) + \lambda\Psi(A), \tag{3.7}$$

where A is the undetermined variables and B is the observations. In variational principle, $\Phi(A;B)$ is called the data-fidelity function, $\Psi(A)$ is the regularization function, and λ denotes the regularization parameter. Under this formulation, the non-blind image deblurring problem can be expressed as

$$\min_{f} \Phi(f;g,h) + \lambda_f\Psi_f(f), \tag{3.8}$$

while the blind case is

$$\min_{f,h} \Phi(f; h, g) + \lambda_f \Psi_f(f) + \lambda_h \Psi_h(h), \tag{3.9}$$

The term Φ is determined according to the noise assumptions, such as Gaussian noise, Poisson noise, or impulse noise. Generally, this section assumes the Gaussian noise model, and the corresponding is given by

$$\Phi = \|g - f \otimes h\|_2^2. \tag{3.10}$$

Here, this thesis will discuss the variational methods from the regularization aspect only.

The Tikhonov-Miller regularizer (Tikhonov 1963) is the earliest regularization term that was used as a variational operator. Traditionally, to stabilize the deblurring result, the solution is expected to have a small norm. Therefore, the Tikhonov-Miller regularizer (Tikhonov 1963) is imposed on the sharp image as

$$\Psi_f(f) = \|f\|^2. \tag{3.11}$$

The drawback of the Tikhonov-Miller regularizer is that it will adversely over-smoothed edges in the deblurred image, therefore, it is rarely used in the current deblurring tasks. In contrast, the development of first-order regularizers which can preserve more significant details is more frequently adopted. One renowned example is the ROF model by Rudin et al (1992). Since the introduction of ROF in 1992, the TV problem has been a popular research problem for more than a decade. Minimizing the TV within an image has the effect of penalizing oscillations and noise, while still allowing sharp discontinuities such as edges. The TV is a norm defined as

$$TV_i(f) = \left\| \sqrt{|\nabla_h f|^2 + |\nabla_v f|^2} \right\|_1, \tag{3.12}$$

where the subscript *i* means it is the isotropic version. Complementarily, anisotropic TV is

$$TV_a(f) = \| |\nabla_h f| + |\nabla_v f| \|_1. \tag{3.13}$$

Both TV_i and TV_a norm is effective in enhancing the edge visualization in the restored image. The main difference between TV_i and TV_a is regarding their sensitivity to edge directions. From Equations (3.12) and (3.13), it can be observed that TV_i enforces the same strength on the edges with different directions, whereas TV_a favors certain directions. Both methods have proven to be useful in numerous applications, such as image denoising, decomposition, super-resolution, inpainting, and non-blind deblurring (Bioucas-Dias, Figueiredo & Oliveira, 2006; Babacan et al., 2008; Amizic, et al., 2010; Afonso, Bioucas-Dias & 2010). Nevertheless, when applied to blind deblurring problems, some failures occur depending on the type of norm (Perrone, 2014).

TV is intrinsically an ℓ_1-norm of the image gradients and thus induces sparsity over image gradients. However, it is not a direct choice for regularization in the image deblurring problem. The reason is that, for a sharp image of natural scenes, the gradient magnitude is typically sparse, meaning that most values are either zero or very small, but may occasionally be large. If a blur kernel is operated on this image, the high-frequency bands will be attenuated, leading to the magnitudes being not sparse. Consequently, minimizing the ℓ_1-norm on the high frequencies of the image will result in a blurry image. Alternatively, to preserve the original sparsity, the ℓ_0-norm that has the intrinsic property of being scale-invariance is a natural choice. Minimizing ℓ_0 will only lead to a sparse effect, without destroying the magnitudes of large values, thus preserving the energy of original gradients. As a regularization term, nevertheless, ℓ_0 is difficult to optimize because of the lack of derivative properties, so typically the ℓ_1 will be utilized as an alternative to approximate ℓ_0. Unfortunately, the blurring process reduces the ℓ_1-norm of the gradients. Minimizing ℓ_1 fails to preserve or recover the energy of the original gradients. Additionally, the scale variant property makes ℓ_1 sensitive to the setting of the regularization parameter λ. Due to these difficulties, various methods of approximating the ℓ_0-norm while maintaining the scale-invariance property are proposed.

One notable example of the approximation is the unnatural ℓ_0 regularizer which is proposed by Xu et al (2013). The idea of unnaturalness stems from the observation that found the intermediate image results in most iterative regularized-base deblurring methods, only contain high-contrast and step-like structures while suppressing others. These images are different from natural scenes, and hence the term 'unnatural' is exploited. To incorporate the step-edge properties in an unnatural representation, the authors utilized the unnatural ℓ_0 scheme to preserve the salient changes (i.e., the gradients) in the image. Given an input image$f$, it regularizes the high-frequency part by manipulating gradient vectors$\nabla_* f$, where $* \in \{h, v\}$ denoting two directions, for each pixel i. The unnatural $\ell_{0\text{-norm}}$ regularization function is defined as

$$\Psi_f(\nabla_* f) = \sum_i \psi(\nabla_* f_i), \tag{3.14}$$

where

$$\varphi(\nabla_* f) = \begin{cases} \frac{1}{\epsilon^2} |\nabla_* f|^2, if\ |\nabla_* f| \leq \epsilon, \\ 1, \quad otherwise. \end{cases} \tag{3.15}$$

Depending on the formulation, the gradient magnitudes smaller than ϵ are penalized by $(\cdot)$ while the larger values result in a constant 1 in the objective function. Minimizing this regularizer will remove fine structures and keep useful salient details in the result. Figures 3.3(a)-3.3(c) illustrate three plots under different values ofϵ. When ϵ approaches zero, this regularizer can be fitted perfectly to the ℓ_0 -norm. Another property ensuring the unnatural ℓ_0 superior to ℓ_1 is its scale invariance property, as previously stated. By using this regularization technique in the estimation of blur kernels, the deblurring performance has been notably improved.

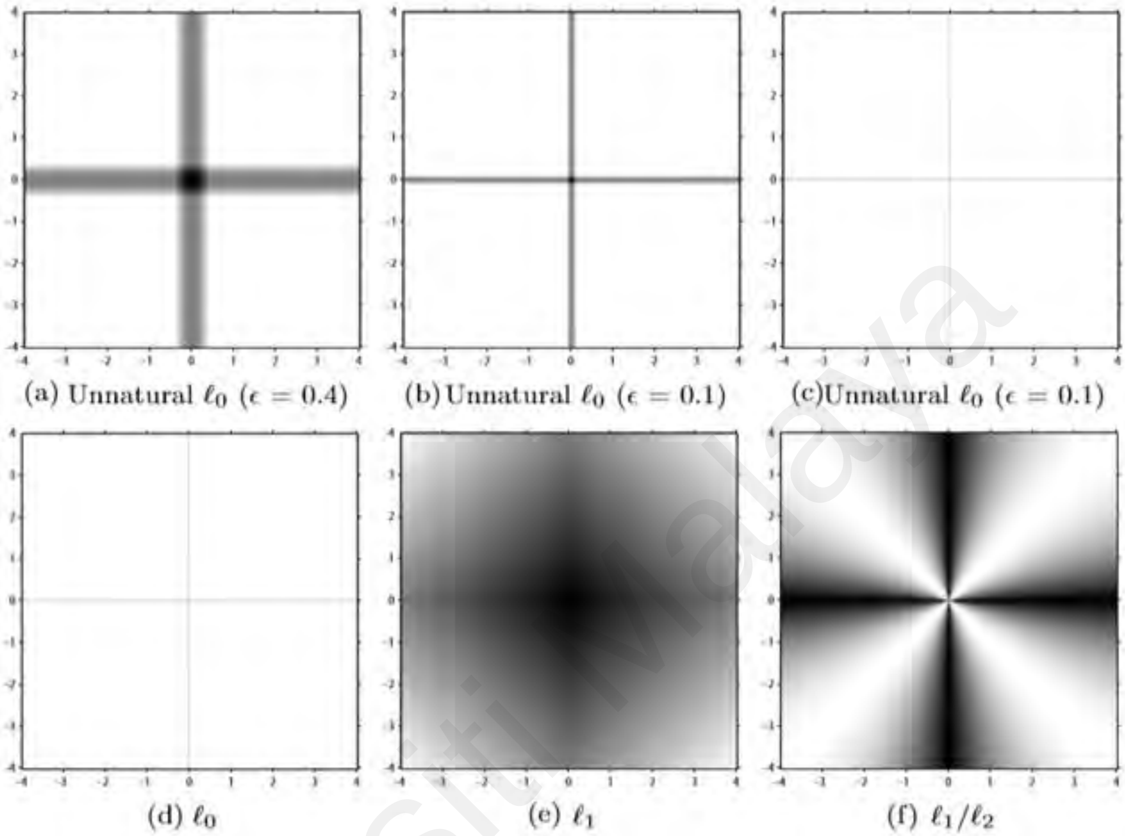

Figure 3.3: Visualization of different measures

Another recent example of the approximation that works on ℓ_0-norm is Pan et al., (2017), where the authors exploited both gradient and intensity prior as the regularization function for text image deblurring.

Besides working on the improvement of ℓ_0-norm approximation, some have attempted to solve the TV-norm approximation by extending the ℓ_1 norm. One notable work is from Krishnan et al. (2011), where the author extended the ℓ_1-norm to a normalized version as

$$\Psi(\nabla_*) = \frac{\|\nabla_f\|_1}{\|\nabla_f\|_2}. \tag{3.16}$$

In this formulation, the authors proposed a regularization function that uses the ratio of the ℓ_1-norm to the ℓ_2-norm on the high frequencies of an image. The simplest interpretation of the ℓ_1/ℓ_2 function is that it is a normalized version of ℓ_1, making it scale-invariant. To understand this regularizer, let us focus on the denominator, ℓ_2 norm. In the blurring process, similar to ℓ_0 or ℓ_1, it also reduces the ℓ_2-norm of the gradients. Fortunately, ℓ_2 is reduced more than the numerator ℓ_1 norm, leading to an increased ratio of ℓ_1/ℓ_2. Figure 3.3(f) illustrates that the minimum of this ratio lies along the axes, which makes the blurry effect to drive the ratio away from the axes. Therefore, minimizing this regularizer will deduce the blurry effect in the image without destroying the magnitude of the true gradient because ℓ_1/ℓ_2 is evidently scale-invariant.

Owing to the TV properties such as convexity, homogeneity, rotation, and translation invariance, over the year, the TV-norm has remained a favorite regularization function simply because of its flexibility in implementation. Some recent examples that adopted TV-norm regularizers for image deblurring tasks are those from (Yanovsky & Dragomiretskiy, 2018; Ma, Lou & Huang, 2017; Cheng et al., 2018). In (Yanovsky & Dragomiretskiy, 2018), the authors used the ℓ_1-norm TV to solve image destripping problems. The variational problem is solved using an alternating direction method of multipliers (ADMM). To overcome the suboptimal results of (Ma, Lou & Huang, 2017) in sparsity approximation, Cheng et al. (2018) introduce a point-wise ℓ_2-norm TV with hybrid hyper-laplacian and Tikhonov prior for Retinex.

Note that the above regularizers are all based on first-order derivatives. While the second-order regularization techniques have proven to be useful in image denoising tasks, they also have been introduced to deblurring images. Lefkimmiatis et al. (2012) extended the first-order TV functional to two second-order cases by defining the mixed norms (e.g., ℓ_1 with ℓ_∞ and ℓ_1 with ℓ_2). These regularizers are found to be able to maintain the favorable properties of TV, and also can effectively suppress the staircase effect (Liang & Zhang, 2015; Li & Hao, 2018). Rather than only enforcing the second-order regularization in deblurring tasks, Papafitsoros and Schönlieb (2014) applied both first- and second-order regularizers thus become a combined regularization function. The benefit of the combined function regularization is that the first-order term recovers the step-edges as well as possible, while the second-order term eliminates the staircase artifacts produced by the first-order regularizer, without introducing any severe blur in the reconstructed image.

One limitation of most regularizers is that they are based on the local principle (i.e., regularizing the local structures). Fortunately, they can be overcome using the nonlocal principle. Inspired by the development of nonlocal TV (Gilboa & Osher 2007, 2008) in the image deblurring task (Lou et al., 2010), Jung et al. (2011) derived a nonlocal *Mumford-Shah* (MS) regularizer by applying the nonlocal operators to the multichannel approximations of the MS regularizer. Due to the nonlocal self-similarity image properties (as discussed in Subsection 3.1.1.1), this regularizer performs better than the local counterpart in various image applications.

In a variational framework, with the utilization of the matrix-vector expression in Equation (3.2), the general formulation in image deblurring problem is defined as,

$$\min_{f} \frac{1}{2} \|g - Hf\|^2 + \lambda \Psi(f), \tag{3.17}$$

where λ is the regularization parameter. A crucial issue in solving the variational problem is the determination of the regularization parameter. A good selection of the parameter will result in a promising deblurring result, whereas a bad choice may lead to slow convergence as well as the existence of severe artifacts in the results. Generally, when the degradation in the blurry image is significant, the value of λ needs to be set large, to reduce the blur as much as possible. However, in the continuing iterations, the blurry effect is decreased gradually. In this case, a small value of λ is required since a large value will damage the fine detail in the image. By considering these effects, a direct implementation is to set λ from large to small according to an empirical reduction rule (Tai et al., 2011; Almeida & Almeida 2010; Faramarzi et al., 2013):

$$\lambda^{t+1} = max(\lambda^{t}.\varphi, \boldsymbol{\lambda_{min}}), \tag{3.18}$$

which depends on the initial value $\boldsymbol{\lambda_0}$, the minimal value $\boldsymbol{\lambda_{min}}$ and the reduction factor $\varphi \in (0, 1)$. Usually, $\varphi = 0.5$. This setting ensures the improvement of the convergence speed of the algorithm if, at each step in the outer iteration, the optimal solution of its immediate predecessor is used as a starting point for the inner iterative steps. The adaptive adjustment of the parameter by considering the intermediate images in each iteration is more favorable.

3.3.2 Alternating Minimization

Solving an optimization problem over two variables in a product space is central to many applications in areas such as signal processing, information theory, statistics, control, and finance. The alternating minimization (Csiszár & Tusnády, 1984) has been extensively used in such applications due to its iterative nature and simplicity. Some of the notable works from the literature that use the alternating minimization algorithm for optimization are (Krishan & Fergus, 2009; Cho & Lee, 2009; Xu & Jia; 2010; Šroubek, & Milanfar, 2012; Liu, T., et al., 2016; Shen et al., 2014; Yang et al., 2016).

The alternating minimization algorithm attempts to solve a minimization problem of the following form: given A, B and a function $D: A \times B \rightarrow R$, minimize D over $A \times B$. That is, find

$$\min_{(A,B) \in AxB} D(A, B) \tag{3.23}$$

Often minimizing both variables simultaneously is not straightforward. However, minimizing with respect to one variable while keeping the other one fixed is often easy and sometimes possible analytically. In such a situation, the alternating minimization algorithm described next is well suited: start with an arbitrary initial point $B_0 \in B$; for n ≥ 1, iteratively compute

$$A_n \in \max_{A \in A} D(A, B_{n-1}), \tag{3.24}$$

$$B_n \in \max_{B \in B} D(A_N, B), \tag{3.25}$$

In other words, instead of solving the original minimization problem over two variables, the alternating minimization algorithm solves a sequence of minimization problems over only one variable. If the algorithm converges, the converged value is returned as the solution to the original problem. Conditions for the convergence and correctness of such an algorithm, that is, conditions under which have been of interest since the early 1950s.

$$\lim_{n \to \infty} D(A_n,\ B_n) \in \min_{(A,B) \in AxB} D(A, B) \tag{3.26}$$

3.4 Practical Issues in Image Deblurring Design

In practice, there are several issues usually encountered in designing the deblurring method. The following subsections discuss two of the most common issues, namely (1) boundary Condition and (2) noise and outliers.

3.4.1 Boundary Conditions

The image deblurring problem is often complicated by so-called boundary conditions (BC) caused by sharp intensity differences on the image boundaries. This is because, in the image deblurring task, pixels located around the boundary of the blurry image are dependent upon the unknown pixels outside the observed region. Inappropriate processing of these pixels can bring severe artifacts. Figure 3.5 illustrates the boundary conditions of an image.

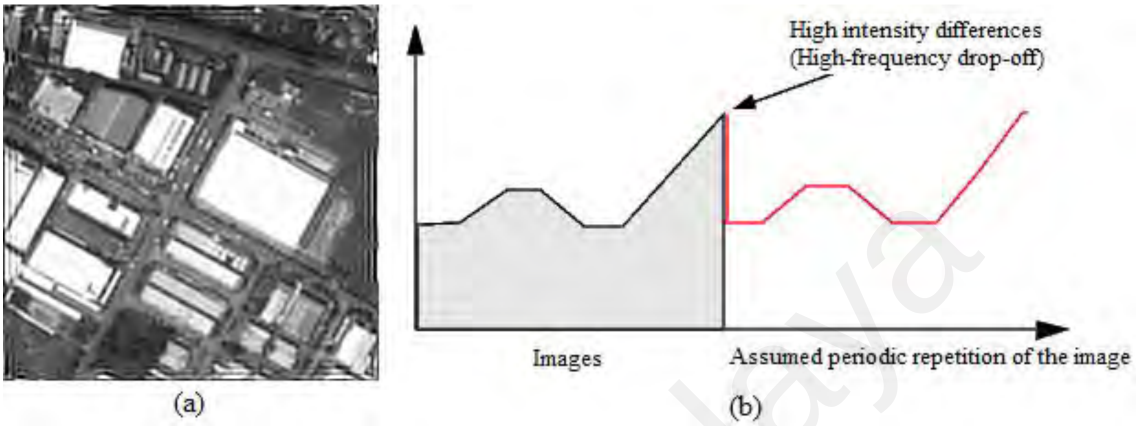

Figure 3.4: Illustration of boundary effects on (a) an image and (b) its brief explanation.

Over the years, the practical issue of boundary conditions has been taken substantial efforts and some excellent techniques have been developed by researchers (e.g. Matakos et al., 2013; Zhou, et al. 2014; Zhang, X. et al., 2017; Chen, & Zhu, 2018; Khristenko et al., 2019). Woods et al. (1995) was the first to discuss the boundary truncation artifact. Later, Tan et al. (1991) have discussed the boundary artifacts and proposed optimal window techniques. Despite that, the well-known zero-padding method (Andrew & Hunt, 1977) that smoothes the boundary to zeros using the zero-padding method has been accepted as a common solution to eliminate the boundary effect. This method improves the image deblurring results but still compromises with some distortions, especially along the edges. Subsequently, Aghdasi & Ward (1996) proposed a method to smooth the edge by reflecting the original image to extend the image. Although this method improved the result further, there are not effective for dealing with images with holes or highly irregular shapes such as remotely sensed images. Hence, it remains as active research in image deblurring problem.

In the literature, several kinds of BC are typically utilized to formalize the boundary issue, which includes Zero-padding (i.e., Zero Dirichlet)(Andrew & Hunt, 1977), periodic Liu & Jia, 2006), reflective (also known as Neumann) (Ng et al., 1999) and anti-reflective (Serra-Capizzano, 2003). Among all, the periodic BC, which assumes a periodic convolution, is frequently used. This condition utilizes the Fast Fourier Transform (FFT) and thus speeds up the optimization. The zero-padding BC works by padding the external region with zero values, whereas the reflective BC treats the pixels outside the image as a mirror reflection of those near the boundary, therefore preserves the continuities at the boundary. Even though these BCs make the deblurring tasks addressable and computationally convenient, they are intrinsically an approximate procedure and do not correspond to the real imaging systems. Moreover, they produce staircase artifacts in the deblurred image during the deconvolution process. Unlike reflective BC, anti-reflective BC preserves not only the continuity of image but also the continuity of the normal derivative. In the case of reflective or anti-reflective BC, if the PSF is strongly symmetric, the resulting convolution matrix H can be diagonalized by 2-D discrete cosine transform or 2-D discrete sine transform, respectively. Chen & Zhu, (2018) is one of the most recent works that applied anti-reflective BC. The good property of anti-reflective BC allows efficient implementation of direct filtering type methods, such as spectra filtering methods. However, these ''reflective'' boundary structures, which are designed for computation purposes, seldom exist in a real practical application.

Instead of using the aforementioned BC, Zhou et al. (2014) treat the BC issues by building a relationship between the missing boundary pixel values and the available image data. They called their method as boundary treatment undetermined BC. This method was able to yield similar quality images if the observed image is not severely blurred, however, if the observed image is severely blurred, it failed to recover the details in the image boundary. Recently, Tu et al. (2015) proposed an improved edge-preserving regularization (IEPR) term with structure adaptive map at blurry motion boundaries to reduce boundary errors that are caused by blur. However, it is compromised with the computational burden, as it costs about 50% of the run-time of the whole optimization process to reduce the boundary artifacts. Most recently, Zhang, S. et al. (2017) have attempted to solve the image restoration problem with the four aforementioned BC and a mean BC. In the experiments, the quantitative restoration results obtained using the anti-reflective BC and mean are equal and higher than the other BCs. This shows that the anti-reflective BC performs better than Dirichlet, periodic, and refective BC.

3.4.2 Noise and Outliers

Noises in images are typically caused by insufficient exposure time during the image acquisition process. While blur can be reduced by using a shorter exposure, this comes at an unavoidable trade-off with increased noise. Generally, if the noises in blurry images have not reached an extreme level, they can be effectively removed by appropriately choosing the parameters of the noise model using the Bayesian inference framework or the regularization parameters in variational methods (e.g., Fergus et al., 2006; Shan et al., 2008; Whyte et al., 2014; Pan et al. 2016; Hu et al., 2018). Conversely, if the noises have reached an extreme level, deblurring an image with noticeable noise will produce ringing artifacts in the restoration results. To handle this issue, researchers from the literature will usually apply image denoising as a preprocessing step in the image deblurring task. For example, Tai and Lin (2012) applied an existing denoising algorithm as a preprocessing step, and successively conducted blind deconvolution on the denoised image to estimate the blur kernel and the sharp image. However, directly applying image denoising methods to the observed image often partially damages the blur information that needed to be extracted from the observed image, which leads to biased kernel estimation. To overcome this problem, Zhong et al. (2013) designed a set of denoising filters based on the directional filters to preserve the blur information in the orthogonal direction to the filter so that the denoising operation does not affect the estimated blur kernel result. Later, Wong and Chan (2015) proposed to restore a burred-noisy image using bilevel programming to decouple the denoising and deblurring operation in different sub-problem. Instead of handling the noise in the spatial domain, the authors applied a curvelet-based denoising algorithm to penalize the noise while preserving the blur information for the deblurring operation.

Another source of deblurring that should be adequately addressed is outliers. One common outlier is saturated pixels, which usually happened when a low lighting scene is taken with a long exposure time, resulting in saturation in the scene with bright spots as illustrated in Figure 3.5.

Figure 3.5: Illustration of outliers in an observed scene.

According to Cho et al. (2011), outliers include all factors which cannot be explained by the linear convolution model defined in Equation (3.2), including dead pixels of sensor, saturated or clipped pixels, non-Gaussian noise, and nonlinear impulse response function. If these outliers are processed using the linear convolution model, it will result in ringing artifacts in the restored image. Cho et al. (2011) proposed to solve the image deblurring problem by classifying the blurry image into two parts, namely inliers and outliers. In their method, they imposed different statistical assumptions on these two parts in a binary map and later employed the Expectation–maximization (EM) algorithm to alternately find the estimation of the sharp image and the classification of the inlier/outlier until a reasonable restoration result is obtained. Hu et al. (2014) and Whyte et al. (2014), the authors address blurred images with outliers using domain-specific properties (i.e., light streaks), where they explicitly take the light streaks and corresponding light sources into account, then pose them as constraints in a non-linear blur model for estimating the blur kernel in an optimization framework. However, as this method heavily relies on light streaks, it becomes less effective when the light streaks cannot be extracted, besides, it does not perform well for other types of outliers, such as non-Gaussian noise. To improve the outlier handling method, Pan et al. (2016) proposed a method that detects the regions of outliers to refine the edge information for blur kernel estimation. Although this method performs well on several kinds of outliers, e.g., saturated pixels and non-Gaussian noise, it comes with computational complexity. Moreover, it does not produce quality results when the edges are not correctly selected or the regions of outliers cannot be detected. Recently, Dong, J. et al., (2017) proposed computational simple algorithms to overcome complexity issues in the existing algorithms. According to the authors, since the outliers significantly affect the goodness-of-fit in function approximation, therefore, instead of explicitly handle the outlier, the authors proposed an algorithm to model the data fidelity term so that the outliers have little effect on kernel estimation. The proposed algorithm does not require any heuristic outlier detection step, thus it is computational much simpler.

3.5 Determining Image Quality Assessment Metrics

The evaluation for image deblurring can be subjective quality assessment or objective quality assessment. The subjective quality assessment predicts the observers' perception without a well-defined numerical quantification. Although the subjective image quality assessment is the most direct and most accurate metric to reflect a person's perception, it is too subjective to cater for different persons. In contrast, objective quality assessment metrics can operate automatically and numerically.

According to whether the reference clean image is available or not, existing image quality assessment (IQA) metrics can be generally divided into two categories: 1) full reference IQA; and 2) no reference IQA.

Full reference IQA metrics assume that the clean image is available in order to compute a measure, while no reference IQA metrics can perform quality assessments without the reference image. The full reference IQA metrics, which are widely utilized to evaluate the performance of image deblurring algorithms include the root mean square error, peak signal-to-noise ratio, and the structural similarity index, improvement of signal-to-noise ratio, structural similarity index, and Feature-Similarity index.

Given a restored image $y \in R^{m \times n}$ and the original clean image $x \in R^{m \times n}$ with m × n size dimension.

Root Mean Square Error (RMSE): RMSE of the restored image y with reference to (w.r.t.) the original clean image x is defined as the square root of the mean square error (MSE). The RMSE is usually employed to measure the ℓ_2-norm distance between the denoised image and the original clean image. It is a full reference IQA metric that is closely related to the peak signal-to-noise ratio. Usually, a smaller RMSE value indicates better image quality. The definition of RMSE is:

$$RMSE(x,y) = \sqrt{\frac{1}{MN}\sum_{I=1}^{M}\sum_{J=1}^{N}\left(x_{ij} - y_{ij}\right)^2} \tag{3.27}$$

Peak Signal-to-Noise Ratio (PSNR): **PSNR** is the most commonly used full reference IQA metric for many image restoration tasks. The definition of PSNR can be formulated as follows (for an 8-bit image):

$$PSNR = 20log_{10}\left(\frac{2^8}{RMSE\ (x,y)}\right). \tag{3.28}$$

As one can see, PSNR is closely related to the ℓ_2-norm distance between two images. The unit of PSNR is the decibel (dB) and a higher dB value indicates better image quality and lower RMSE. Though PSNR is very simple and intuitive, higher PSNR does not mean higher visual structural similarity. Hence, researchers resort to find alternative and better IQA metrics.

Improvement of Signal to Noise Ratio (ISNR): Similar to PSNR, ISNR is closely related to the ℓ_2-norm distance between two images. The unit of ISNR is the decibel (dB) and a higher dB value indicates better image quality. The definition of ISNR can be formulated as

$$ISNR = 10\ log_{10}\left(\frac{\sum_{ij}[g(x,y) - f(x,y)]^2}{\sum_{ij}\left[\hat{f}(x,y) - f(x,y)\right]^2}\right) \tag{3.29}$$

Structural Similarity Index Metric (SSIM) by Wang et al. (2004): One seminal work in IQA is the, which is also a full reference IQA metric. In SSIM, each image patch is decomposed into three different components indicating three core informative parts of the original patch. The three components are luminance (mean value of the pixels in the patch), contrast (the standard deviations of the patch), and structure (the mean subtracted patch). SSIM considers the fact that the human visual system is very sensitive to the relative changes in luminance, rather than the absolute changes in luminance.

SSIM method can be expressed through these three terms as

$$SSIM\ (x,y) = \ [l(x,y)]^{\alpha}.[c(x,y)]^{\beta}.[s(x,y)]^{\gamma}. \tag{3.30}$$

Here, *l* is the luminance (used to compare the brightness between two images), c is the contrast (used to differ the ranges between the brightest and darkest region of two images) and s is the structure (used to compare the local luminance pattern between two images to find the similarity and dissimilarity of the images) and *α*, *β,* and *γ* are the positive constants. Again luminance, contrast, and structure of an image can be expressed separately as:

$$l(x,y) = \frac{2\mu_x\mu_{y+}C_1}{\mu_x^2+\mu_y^2+C_1}, \tag{3.31}$$

$$c(x,y) = \frac{2\sigma_x\sigma_{y+}C_2}{\sigma_x^2+\sigma_y^2+C_2}, \tag{3.32}$$

$$s(x,y) = \frac{\sigma_{xy+}C_3}{\sigma_x\sigma_y+C_3}, \tag{3.33}$$

where μ and μ are the local means, σ and σ are the standard deviations and σ is the cross-covariance for images x and y sequentially. If *α = β = γ = 1*, then the index is simplified as the following form using Equations (3.31) -(3.33):

$$SSIM(x,y) = \frac{(2\mu_x\mu_{y+}C_1)(2\sigma_x\sigma_{y+}C_2)}{(\mu_x^2+\mu_y^2+C_1)(\sigma_x^2+\sigma_y^2+C_2)}. \tag{3.34}$$

The value range of SSIM is between 0 and 1, where a higher value indicates higher similarity (SSIM=1 indicates that the two images are the same), as well as better image quality. From Equation (3.34), one can see that SSIM is on a normalized scale (values between 0 and 1) that can be expressed in the dB scale as 10log10 [SSIM (x, y)].

Feature-SIMilarity (FSIM) index (Zhang, L., et al. 2011): The underlying principle of FSIM is that the human visual system perceives an image mainly based on its salient low-level features. Specifically, two kinds of features, the phase congruency (PC) and the gradient magnitude (GM), are used in FSIM, and they represent complementary aspects of the image visual quality.

Phase Congruency (PC): A new method for detecting image features is phase congruency. One of the important characteristics of phase congruency is that it is invariant to light variation in images. Besides, it is also able to detect more some interesting features. It stresses on the features of the image in the domain frequency. Phase congruency is invariant to contrast.

Gradient magnitude (GM): The computation of the image gradient is a very traditional topic in digital image processing. Convolution masks are used to express the operators of the gradient. There are many convolutional masks to measure the gradients. If f(x) is an image and Gx, Gy of its horizontal and vertical gradients, respectively. Then the gradient magnitude of f(x) can be defined as

$$\sqrt{G_x^2 + G_y^2}. \tag{3.35}$$

Let two images are f_1 (test image) and f_2 (reference image) and their phase congruency can be denoted by PC_1 and PC_2, respectively. The Phase Congruency (PC) maps extracted from two images f_1 and f_2 and the Magnitude Gradient (GM) maps G_1 and G_2 extracted from the two images too. FSIM can be defined and calculated based on PC_1, PC_2, G_1, and G_2. At first, the similarity of these two images can be calculated as

$$S_{PC} = \frac{2PC_1PC_2T}{PC_1^2 + PC_2^2 + T_1} \tag{3.36}$$

where T_1 is a positive constant that increases the stability of S_{pc}. Practically T_1 can be calculated based on the dynamic range of PC values. The above equation describes the measurement to determine the similarity of two positive real numbers and its range is within 0 to 1.

Similarly, the similarity between G_1 and G_2 can be calculated as

$$S_G = \frac{2G_1G_2+T_2}{G_1^2 + G_2^2+T_2} \tag{3.37}$$

where T_2 is a positive constant that depends on the dynamic range of gradient magnitude values. In this paper, both T_1 and T_2 are constant so that the FSIM can be conveniently used.

Now S_{PC} and S_G are combined to calculate the similarity S_L of f_1 and f_2. S_l can be defined as

$$S_{L\,(x)} = [S_{PC}(x)]^{\mu_1}.[S_G(x)]^{\mu_2}. \tag{3.38}$$

where the parameters μ_1 and μ_2 are used to adjust the relative importance of PC and GM features. In this paper, $\mu_1 = \mu_2 = 1$ is set for convenience. From Equations (3.36) to (3.38), it is evident that FSIM is normalized (values between 0 and 1).

3.6 Summary

This chapter has reviewed the ill-posed problem of blind image restoration, particularly the image deblurring problem. Table 3.1 summarizes the literature review of the existing approaches or methods that solve the ill-posed blind image restorations problem. Based on the review of literature, there is a diverse variety of applied techniques for image restoration problems; each of them shows its importance and usefulness in several domains, and their goal is always to lead to better results than existing ones.

Nevertheless, all those techniques suffer from heavy mathematical baggage implicated to carry out the task, consequently, more complex formulas are developed.

Table 3.1: Summary of approaches and methods for blind image restorations.

Approach Method/	Principle	Advantages	Disadvantages
Optimization approaches for a regularized-based image restoration problem.			
Pixel-based	utilizes local structural patterns of the image and is built on the assumption that images are locally smooth except at edges.	simpler algorithms and effective in preserving edges and recovering smooth regions.	• smear out image details and cannot deal well with fine structures. • cannot characterize the multi-scale properties and multi-level structures of an image.
Sparsity-based	assumes that each patch of an image can be accurately represented by a few elements from a basis set called a dictionary, which is learned from natural images.	• adaptable to the images through the learned dictionary, thereby enhancing the sparsity for image details preservation. • Can be modeled in transform domain coefficient that characterizes the multi-scale properties and multi-level structures of an image.	not capable of characterizing the nonlocal self-similarity of an image.
Patch-based	based on a pointwise selection of small image patches of fixed size in the variable neighborhood of each pixel that can be modeled by a sparse linear combination of learnable basis elements.	• have sparsity properties to improve image details preservation. • effective in characterizing the nonlocal self-similarity of an image for edge preservation and recovering smooth regions.	requires high computational complexity as it is non-convex problem due to large-scale dictionary learning.
Group-based	Utilize a group of similar patches as a basic unit of sparse coding.	• can be precisely represented by a sparse linear combination of basic elements of the dictionary. • acquires lower computational complexity than patch-based algorithms.	• suffer an over-smooth effect in the restored image. • requires higher computational complexity compared to pixel- and sparsity-based algorithms.

Table 3.1, Continued.

Approach Method/	Principle	Advantages	Disadvantages
Exploiting image priors for blur estimation in Blind Image Deblurring			
Gradient-based	utilize statistical priors of gradient distributions.	• simpler algorithms. • highly effective for blur kernel estimation.	highly non-convex models, which are computationally expensive.
Intensities-based	utilize the knowledge on image intensities.	• can be modeled in sparse representation. • able to restore rich textured regions.	often generates hallucinated high-frequency contents that complicate the subsequent kernel estimation steps.
Low-rank priors	utilize the sparsity (i.e., low-rankness) of image vector-matrix.	• can exploit the nonlocal self-similarity on the patch level.	• produces over-smooth and holo effects in the restored image. • computationally expensive
Graph-based	utilize the graph signal processing.	• highly effective in edge preservation promote image sharpness. • Data-adaptive.	prompt to produce an over-smooth effect in the restored image.
Structure-texture decomposition for blur estimation in Blind Image Deblurring			
Filtering-based	utilize weight averaging of neighbor pixels based on their distances in space and range.	simpler algorithms and can produce quality edge-preserving and smoothing results.	limited in their ability to extract detail at arbitrary scales, which results in halo artifacts.
Optimization-based	utilize multi-scale detail decomposition in an iterative process.	Produce better edge-preserving and smoothing results than Filtering-based by suppressing the oscillating patterns induced from texture while estimating the structure image as similar as possible to the input image.	• computation costs are higher than Filtering-based. • cannot easily be parallelized.

In reviewing the literature on how to make a well-posed blind image deblurring, several interesting findings were found. There exists a poor compromise among computational complexity, convergence properties, and portability of the algorithm for the existing blind deconvolution methods. For example, in the structure extraction method for blur kernel estimation. In the case of optimization-based approaches (e.g., Xu et al., 2011; Xu et al., 2012; Hua et al., 2014), this approach can globally suppress the oscillating patterns induced from texture while guessing the structure image as similar as possible to the input image. Although they obtain high-quality results, these methods are comparably complex and cannot easily be parallelized, thus not allowing the algorithm to handle large images and used in interactive applications. Whereby, filtering-based algorithms (Cho et al, 2014; Paris et al. 2011; Karacan et al. 2013; Zhang, Q. et al. 2014) are highly efficient as compared to the optimization approach. Besides, it can be an effective filter kernel to suppress texture. However, often fail to accurately detect structure for edges and corners of the image. Image deblurring methods that exploit the nonlocal self-similarity methods have demonstrated successful results. However, they require a heavy mathematical model to carry out the task effectively and consequently suffer from the complexity of computation.

The relative importance of each of the above factors depends on the imaging application. For remoted sensed images, which require a near real-time image restoration, reducing computational complexity and convergence speed is of the utmost importance. Nevertheless, the reliability of the solution is also one of the primary considerations. Therefore, the challenge is to design a method that exhibits the most appropriate compromise among computation complexity, reliability, and portability for a given application

With the above considerations, this thesis proposes to exploit the TV variational methods to utilize nonlocal self-similarity to develop an accurate blur kernel estimation for on-orbit spatial characterisation. Whereas to create a well-posed problem for optical satellite image restoration, this thesis exploits the merit of image prior characteristic in both local smoothness and nonlocal self-similarity properties of an image in a hybrid domain (viz., space spatial and frequency), to design effective regularization terms that reflect these image properties.

CHAPTER 4: ON ORBIT SPATIAL CHARACTERISATION BASED ON STOCHASTIC CHARACTERISTIC TARGET

This chapter presents a major contribution to the thesis. In this chapter, this thesis proposes a flexible approach for on-orbit spatial characterisation. Different from the existing approach, it does not require the use of a fixed-characteristic target, instead, it utilizes the stochastic characteristic of an imaged scene. This approach encompasses an image-based MTF measurement method that aims to obtain an accurate estimate of the Point Spread Function (PSF) kernel by solving a constrained optimization problem. To this end, this work presents several strategies to realize the aim of this work. First, this work proposes a segmentation method to select the ideal candidates for MTF measurement. Second, this work develops an adaptive structure selection method that removes detrimental structures and selects useful information for PSF estimation. Finally, this work puts forward a robust estimation method by introducing a spatial prior that is able to simultaneously suppress noises while preserving the sparsity and continuity of the PSF kernels for on-orbit spatial characterisation.

4.1 Introduction

The spatial characterisation is a nontrivial task in the calibration and validation of EOS data (WGCV, 2019). The MTF as intensively discussed in Chapter 2 is one important measure in spatial characterisation effort. It is a widely used quantifying metric for characterizing the spatial detail resolved by the EOS electro-optical imaging system. Specifically, it describes the ability of the optical system to transfer the detail (i.e., contrast) information of an object (e.g., a scene on the earth's surface) to an image at different spatial frequencies (Holst, 2017). There exist many known methods that can be used for measuring the MTF of an imaging system (e.g., Masaoka et al., 2014; Anam et al., 2019). However, for an EOS that is already in orbit, many of these known methods are not applicable. The appropriate and practical method, thus, is to determine the MTF from its remotely sensed images with the use of specific artificial or natural targets on the ground (e.g., Helder et al., 2004; Pagnutii et al., 2010; Viallefont-robinet et al., 2018).

Based on the literature review in Section 2.2, two main challenges have been discovered: (1) The existing approach is non-versatile as it highly relies on the existence of well-separated fixed characteristic targets, and (2) while random targets methods are available but they are under-explored, and most of are not suitable for on-orbit characterisation (Xie et al., 2015).

Natural scene inherently possesses nonlocal, self-similarity, and multiple scales characteristics which can be described as stochastic characteristic targets (Al-Hamdan et al. 2012; Bahadir & Xin, 2012). Corresponding to natural scenes, optical satellite images also possess those stochastic characteristics that can be decomposed from the image. Based on this knowledge, we, thus inspired to introduce an insight that a degradation spectrum (i.e the MTF) can be estimated, by analyzing the nonlocal self-similarity characteristics, namely the structural component, in the observed image.

This chapter proposes a flexible approach to conduct on-orbit characterisation. Differs from the existing methods that rely on the presence and manual identification of well-separated characteristics target such as edges and lines in the image, the proposed method is an automatic MTF measurement method that exploits the stochastic characteristic (i.e., nonlocal self-similarity characteristic of image properties) using a blind image deconvolution (BID) method in the spatial domain.

Based on the studies of previous work in Chapter 3, to reduce the ill-posedness of blur (i.e., Point Spread Function (PSF)) kernel estimation in the BID problem, this work develops three strategies to warrant an efficient and effective MTF measurement framework based as follows: First, to reduce the computation complexity in this work, a segmentation method is formulated to select the ideal candidates that wholly represent the data precisely and effectively. Second, to remove detrimental structures and obtain useful information for the MTF measurement, this work develops an adaptive structure selection method, which can select reliable structures effectively. Finally, to preserve the sparsity and continuity of the PSF kernels for MTF measurement, this work proposes a robust PSF kernel estimation method by introducing a sparsity-based image prior. It also helps to suppress the noise effectively.

The remainder of the chapter is organized as follows. Section 4.2 provides the philosophy that formulates the solution to the research problem. Next, Section 4.3 introduces the proposed MTF measurement method for a flexible on-orbit spatial characterisation approach. Then the experimental results and discussions are provided in Section 4.4. Finally, Section 4.5 concludes this chapter.

4.2 Problem formulation

This section describes the important characteristic that introduces insights to formulate the problem. The solutions that were applied to design and develop the MTF Measurement framework are also described in this section.

Image properties: Image properties inherently containing local smoothness and nonlocal self-similarity characteristics (Bahadir & Xin, 2012). Of particular interest is the nonlocal self-similarity characteristics that depict the repetitiveness of higher level patterns, namely the textures and structures embodied by the images within the nonlocal area (see Figure 4.1). Recall that the model of image degradation as described in subsection 2.3.1 is the convolution of an ideal image with the PSF that formed the observed degraded image. Therefore, these characteristics can be exploited to decouple the PSF, and the ideal image recorded by an EOS electro-optical imaging system. In this framework, this thesis defines reliable structures as the salient edges that form the structural component of an image.

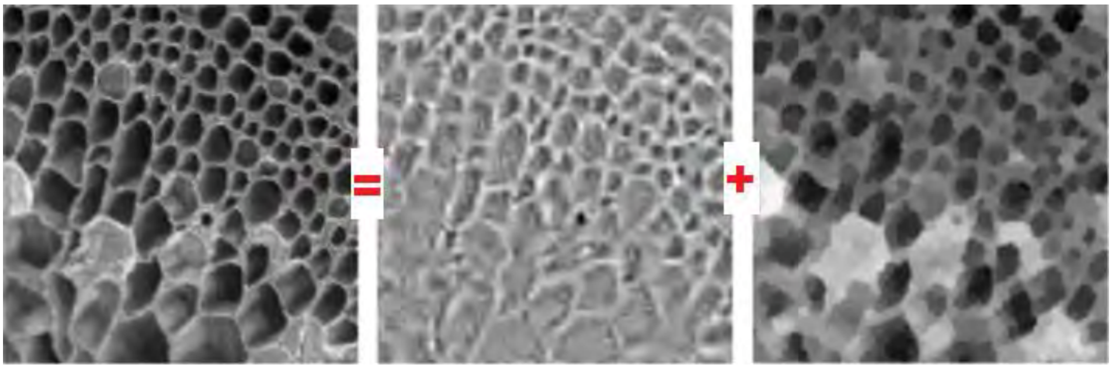

(a) (b) (c)

Figure 4.1: Illustration of image properties. (a) a region with nonlocal self-similarity properties, (b)-(c) depict decomposition of (a) into texture and structure region, respectively

Based on the studies in Chapter 3, several aspects that are critical for ensuring accurate MTF measurement have been identified. One of them is structure extraction; it is critical to ensure accurate MTF measurement because different extraction of structures may lead to a different radial profile of PSF. An image with a reliable image structure possesses a more salient edge that can be extracted to estimate the PSF radial profile will yield better PSF estimation results compare with an image that contains weak edges and a more smooth region. These can be described by the examples shown in Figure 4.2. This figure demonstrates that sub-images obtained from the same scene but each results in different PSF kernel results as highlighted in the red box, which obviously demonstrates the influence of image structure in the PSF estimation.

In addition to the extraction of reliable structure, other aspects including noise suppression, edge restoration, and good region selection are also important for ensuring accurate MTF measurement. The next section will explain the important aspects of noise suppression, edge restoration, and good region selection, subsequently, propose the techniques to mitigate the problem.

Figure 4.2: Influence of image structure in PSF kernel estimation. The red box denotes the estimated PSF radial profile with respect to the structural component of the sub-image. In comparison, the sub-image in the bottom right corner contains weaker structures and a flatter region, therefore, it yields an ambiguity in the PSF estimation. On the contrary, sub-image in the upper left and right-corner sub-images yield a better PSF estimation profile, as they contain more salient structures (i.e., the structure of the stadium).

In this framework, besides reliability, efficiency in processing the satellite images is also another crucial issue. Therefore, this work studied the influences of region selection (refer to Subsection 3.2.2), to determine how to extract and what kind of image structures within the observed image can benefit the PSF kernel processing. In consideration of all factors discussed in the literature review, this work decided to select a salient structure with the use of an edge map. Here, the area and the size of a good region to select will be discussed.

Good region selection: To estimate the PSF of a single image, intuitively, one will consider using the whole image, since it is a sole representation of that image. However, studies demonstrated that regions with short length edges could adversely affect the deblurring results (Joshi et al. 2008, Hu & Yang, 2015). Besides, it may cause computational efficiency issues. For example, given a high-resolution optical satellite image with a 4096×4096-pixel size, it is rather time-consuming to apply deblurring algorithms with the whole image. Hence, the obvious solution is to select a region within the input image to estimate a blur kernel. The selection process can often be partly alleviated by manual selection; however, this requires tedious human intervention. Therefore, an automatic method to select a good region is proposed in this work, in other words, a segmentation method to select ideal candidates for PSF estimation. This work will demonstrate that using a region of the blurred image for kernel estimation may render better deblurring results rather than using the whole image in Subsection 4.4.2.

Next, let us return briefly to the fundamental of the image degradation model and describe the philosophy that guides the problem formulation of this framework.

Image degradation model: No instrument, remote-sensing imaging systems included, can measure a physical signal with infinite precision (Schowengerdt, 2007). Without loss of generality, this work recalls the image formation model.

If $f(x, y)$ represents an input signal and $h(x, y)$ is a linear, spatially-invariant operator, then generally, the output signal $g(x, y)$ of the instruments (i.e., EOS electro-optic imaging system) can be expressed as

$$g(x, y) = f(x, y) \otimes h(x, y) + \eta(x, y), \tag{4.1}$$

which reads "the output signal equals the input signal convolved $\otimes$ with the system response." Note that *x* and *y* are continuous variables in the *x*- and *y*-plane, respectively.

According to the convolution theorem, the spatial domain convolution between $h(x, y)$ and $f(x, y)$ can be expressed in the frequency domain as the multiplication of the Fourier transforms (FT) of those quantities. In other words, the system's output is computed in the frequency domain according to the following equation:

$$G(u, v) = H(u, v) \circ F(u, v) + N(u, v). \tag{4.2}$$

where u and v are the spatial frequency coordinates; $G(u,v)$, $F(u,v)$ and $N(u,v)$denote the degraded image spectrum, the ideal image spectrum, and random noise spectrum, respectively; and $H(u,v)$denotes the optical transfer function (OTF). The symbol $\circ$ denotes an element-wise multiplication operator.

Suppose for a moment that $h(x,y)$is unknown and a unit impulse (i.e., a point of a light source) is applied to the system. Assuming that the Fourier transform of a unit impulse, $F(u,v)$, is equal to one; therefore, based on Equation (4.2), the inverse Fourier transform of the output, $G(u,v)$, will result in $h(x,y)$. Alternatively, applying the impulse as an input signal directly yields $h(x,y)$ for the output signal. Thus, the inverse transform of the system transfer function, $h(x,y)$, can be known as the impulse response in linear spatially-invariant systems theory. In optics, $h(x,y)$, the inverse of the OTF, is called the PSF (Gonzalez & Woods, 2017). Hence, the OTF and the PSF of an imaging system, is thus, constitute an FT pair, which can be defined as follows:

Definition 4.1: Given a remotely sensed image, the on-orbit characterisation problem is to determine its MTF by the modulus of the system PSF, which, in turn, is the FT of the system's PSF described as:

$$MTF(u,v) = \frac{|H(u,v\,)|}{|H(0,0)|},\ H(u,v) = \digamma\{PSF(x,y)\}. \tag{4.3}$$

where Ƒ represents the FT.

Explanation of the proposal to make use of digital image processing techniques to develop a method for on-orbit MTF measurement will be described in the following subsection.

BID problem: To estimate the PSF in Equation (4.3), this work seeks a solution in digital natural image processing techniques. Of particular the BID technique is used to recover image sharpness and signal-to-noise ratio. With reference to Equation (4.1), it is obvious that one major task in BID processing is the estimation of the two-dimensional (2-D) kernel function, $h(x, y)$ of the degraded image, $g(x, y)$, which is the PSF. The net 2-D sensor of PSF for electro-optical imaging consists of several components. Nevertheless, based on the literature review in Section 2.1, an important assumption in EOS electro-optical imaging is that the net 2-D sensor PSF is given by a product of two 1-D PSFs in the cross-track and along-track directions (Schowengerdt, 2007). Therefore, the PSF can be determined based on this assumption as follows:

Definition 4.2: Given a remotely sensed image, the estimated 2-D kernel function can be defined as the PSF of the in-flight EOS electro-optical imaging system as

$$PSF_{net}(x, y) = PSF_c(x)PSF_a(y). \tag{4.4}$$

where $PSF_c(x)$ and $PSF_a(y)$ is the output measurement of this framework. Accordingly, they represent the 1-D PSF in the cross-track and along-track directions, respectively.

By the definition of 2-D convolution and lexicographically ordering of the image data, Equation (4.1) can be expressed in vector-matrix form as

$$g = fh + \eta. \tag{4.5}$$

Solving for h and f simultaneously in Equation (4.5) is an ill-posed non-linear minimization problem. As discussed in Chapter 3, the problem is generally intractable, unless prior knowledge on h or f is assumed to be available to stabilize the solution space.

Given an observed g, therefore, this work proposes to estimate the PSF kernel h by solving the following constrained optimization problem with ℓ_2-norm regularization.

$$C(f, h) = \|g - h \otimes f\|_2^2 + \lambda\Psi(h) + \gamma\Psi(f), \tag{4.6}$$

where $C(f,h)$ is the cost function with respect to the unknown f and h. The first term, $\|g - h \otimes f\|_2^2$ is the data fitting function that ensures the fidelity between the observed images (i.e., degraded image) and the latent sharp image (i.e., ideal image). The last two terms, $\Psi(h)$ and $\Psi(f)$ are the priors function, which models the priors distributions of the PSF and the latent sharp image, respectively. Variables λ and γ are the corresponding regularization parameters to balance the trade-off between the data fidelity function and the priors function. The intended outputs from this cost function are the 2-D PSFs, which later will be processed to become one single 1-D PSF. The MTF can be directly found by taking the 1-D Fast FT of the 1-D PSF.

So far, this work has explained how the research problem in this framework is formulated. The next section will establish the framework for on-orbit spatial characterisation through the estimation of MTF from image structures.

4.3 MTF measurement from Image Structures

This section provides an extensive explanation of the development of a new approach to on-orbit spatial characterisation. Figure 4.3 illustrates the overall framework of the proposed MTF measurement method. The process of this framework is divided into three phases: (1) Selection of ideal candidates, (2) Robust PSF estimation, and (3) MTF calculation.

Accordingly, this work begins with the development of a method for the selection of ideal candidates; the ideal candidates are the sub-images with reliable structure, which will be used as input to the second phase of the framework. The second framework which is the robust PSF estimation method is the core of this framework that aims to derivate accurate PSFs estimate. In order to achieve that aim, this work adopts a strategy named alternating minimization (AM) that was originally proposed by You and Kaweh (1996) to solve the cost function in Equation (4.6). After completed the PSFs kernel estimation process for all ideal candidates, finally, the third phase will input the PSFs estimate. With the underlying assumption that the PSF is linear Spatially-invariant, in Phase 3: MTF calculation, this work interlaces all PSF kernel to become one single PSF kernel to wholly represent the PSF of the original imaged scene. The FWHM value of PSF and MTF at the Nyquist frequency is derived to ultimately quantify the spatial quality of the EOS optical imaging system and its data product.

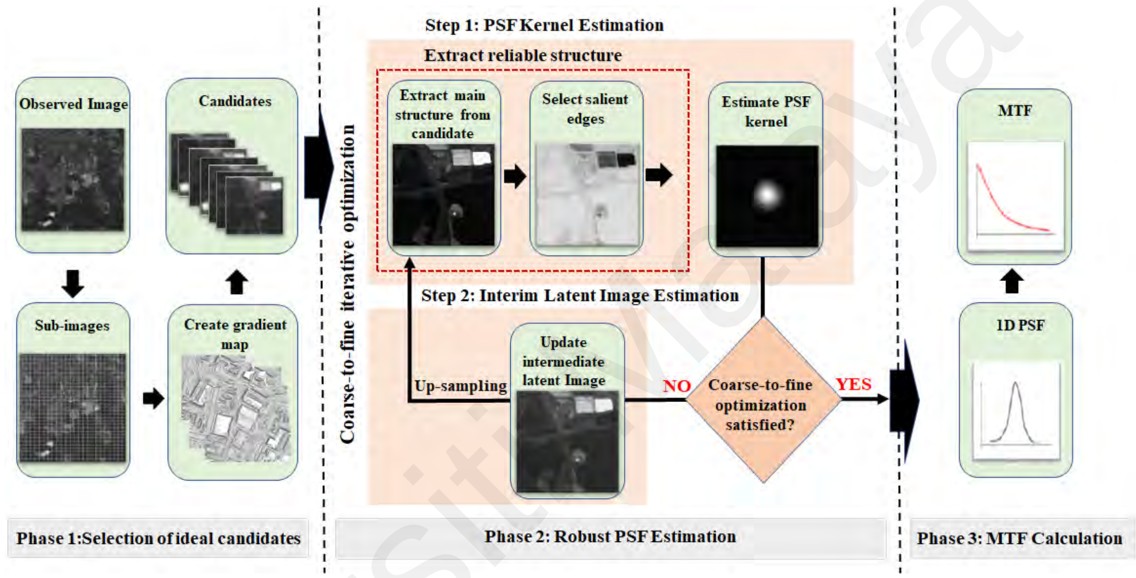

Figure 4.3: The framework of the proposed on-orbit MTF measurement

Accordingly, this work begins with the development of a method for the selection of ideal candidates; the ideal candidates are the sub-images with reliable structure, which will be used as input to the second phase of the framework. The second framework which is the robust PSF estimation method is the core of this framework that aims to derivate accurate PSFs estimate. In order to achieve that aim, this work adopts a strategy named alternating minimization (AM) that was originally proposed by You and Kaweh (1996) to solve the cost function in Equation (4.6). After completed the PSFs kernel estimation process for all ideal candidates, finally, the third phase will input the PSFs estimate. With the underlying assumption that the PSF is linear Spatially-invariant, in Phase 3: MTF calculation, this work interlaces all PSF kernel to become one single PSF kernel to wholly

represent the PSF of the original imaged scene. The FWHM value of PSF and MTF at the Nyquist frequency is derived to ultimately quantify the spatial quality of the EOS optical imaging system and its data product.

The subsections that follow will discuss each of the phases in detail.

4.3.1 Phase 1: Selection of Ideal Candidates

Generally, satellite images are large in size, intuitively, using the whole image for PSF kernel estimation is computationally expensive. Therefore, to reduce the computational burden, this work adopts two strategies as follows:

First, to utilize intensity derivatives (i.e., gradient value) rather than intensity (i.e., pixel value) in the optimization function for PSF kernel estimation. Since an image gradient depicts a directional change in the intensity of an image, therefore, it highlights the edge of image features which is effective in determining the image structure. Using only the image gradient, the numerical optimization process of Equation (4.6) can be accelerated by excluding pixel values in the formulation.

Second, instead of using the whole image, the original scene is split into segments of sub-images and creates a gradient profile for each of the sub-image. Among the sub-images, only those with salient edges will be selected as ideal candidates for PSF estimation. The radiometric resolution of images is then measured, where each bit typically records an exponent of power 2. So, the processing time for an image is expected to run in $O(N^2)$. This work conducted an analysis to decide on the size of sub-images, as it is using good region selection based on edge map, a $2^8 \times 2^8$ sub-image size was found sufficient, therefore the size of the sub-image is fixed to $2^8 \times 2^8$.

The strategies used to reduce the computational burden in this framework have been explained in this subsection. The next subsection will explain how to select the ideal candidates, which will be used as the inputs to the proposed PSF estimation method.

4.3.1.1 r-map for potential candidate selection

In this phase, first, the observed image g of size $2^n \times 2^n$ is split into a total of sub-images, j with the size of $2^8 \times 2^8$.

$$g \mapsto \{\tilde{g}_1, \tilde{g}_{2,\dots} \tilde{g}_{j,}: \text{j} = (2^n/2^8)^2\}, \tag{4.7}$$

As discussed in subsection 3.2.2, insignificant edges will make PSF estimation vulnerable to noise. Besides, this work cannot estimate a PSF kernel on a region with a constant intensity. Hence, to select ideal candidates for PSF estimation, this work proposes to use a technique that capable of measuring useful gradient in the sub-image. Inspired by the structure extraction method proposed by Xu and Jia (2012), this work adopted their ideal and used a relative windowed TV to select reliable candidates from the Equation (4.7).

For each pixel $x \in g$, $r(x)$ measures the usefulness of gradients by

$$r(x) = \frac{\left\|\sum_{y \in N_m(x)} \nabla \tilde{g}(y)\right\|}{\sum_{y \in N_m(x)} \|\nabla \tilde{g}(y)\| + \beta}, \tag{4.8}$$

where $\tilde{g}$ denotes the sub-image and $N_m(x)$ is an $m \times m$ window centered at pixel x. The $\sum_{y \in N_m(x)} \|\nabla \tilde{g}(y)\|$ measures the absolute spatial difference within $N_m(x)$, while $\left\|\sum_{y \in N_m(x)} \nabla \tilde{g}(y)\right\|$ captures of the overall spatial variation of $\nabla \tilde{g}(y)$. The β in Equation (4.8) is a control parameter. It is used to avoid division by zero that causes invalid data outputs. This parameter is set as a small positive number with $0 < \beta < 1$). Empirical analysis shows that higher β filter out more image gradient results in the possibility of exclusion of salient edges, in contrast, smaller β may retain more small-scale structures that could adversely affect the selection results, since it inevitable random noise. Hence, for this work, the β is set to 0.5, which the average value, since statistically, it measures the central tendency of the r-map profile to retain useful edges. For the relative window, this work uses a size of 5×5 window. A small r implies that the local region is flat, whereas a large r implies exist of strong image structures in the local window. Figure 4.4

shows examples of sub-image with two different image properties, where Figure 4.4(a) contains mainly local smooth properties, whereas Figure 4.4(c) contains mainly nonlocal self-similarity properties. Figures 4.4(b) and 4.4(d) are the *r*-map profile derived using Equation (4.8) for Figures.4.4 (a) and 4.4(c), respectively. It can be noticed that the structure magnitude of Figure 4.4(b) is very weak compared to Figure 4.4(d), which exhibits small *r*-map profile values. Note that the *r* value is a decimal value comprised between 0 and 1, the closer the *r* value to 1 the stronger the structure magnitude, vice versa.

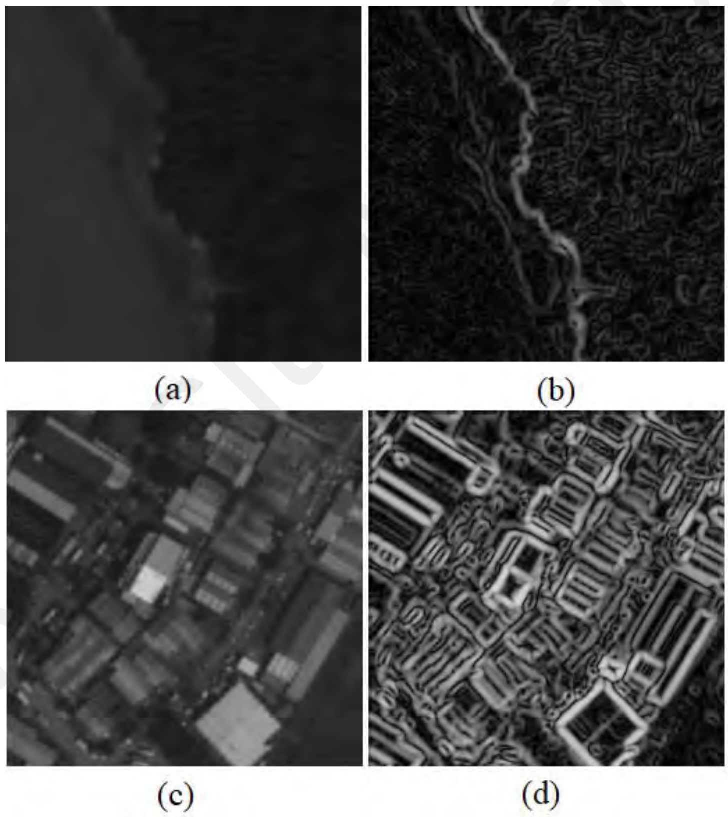

Figure 4.4: Examples of r-map profile: a sub-image with (a) and (b) local smoothness properties and its *r*-map profile. (c) and (d) nonlocal self-similarity properties and its *r*-map profile

Although large *r* implies the existence of strong image structures in the sub-image, it might not necessarily have the salient edge that is suitable for PSF kernel estimation. Therefore, this work proposes additional criteria to filter unreliable candidates in the following subsection.

4.3.1.2 Determining ideal candidates

To warrant reliable structures, the ideal candidates are selected according to the following criteria: Let $\tilde{g}_{rmax}$ be the sub-image with the largest *r*, measure the variance values, σ^2 of *r*. The potential candidates, $\acute{g}$ are selected from

$$\acute{g}(i+1) \;\leftarrow\!\!\mid\; \{\, \tilde{g}_{i..j} : r > \; t, i = 1, \dots j\}, \tag{4.9}$$

where *t* is the threshold value of $pT \times (\sigma^2)\;_{\tilde{g}_{rmax}}$. pT is a value ranging from 0% to 100%.

Recall that the proposed PSF estimation method is based on the BID method in the spatial domain. BID is an ill-posed problem, therefore, the predefined assumption that sub-image with the highest variance value of r, $\tilde{g}_{rmax}$ is the most perfect candidate for PSF kernel estimation may not be always true. However, there is a certainty about the existence of strong image structures in the sub-image. Therefore, more potential candidates can be included to increase the sample size, to reduce the uncertainty of the estimation result. To determine the preliminary threshold value to include potential candidates, an analysis was conducted using 10 data samples with synthetic Gaussian blur with 2.6 standard deviations (SD). As mentioned in subsection 4.3.1.1, the predetermined pixel size for the sub-image is $2^8 \times 2^8$. Therefore, each data sample with a pixel size of 4096 x 4096 will obtain 256 sub-images. By applying 75% × $(\sigma^2)\;_{\tilde{g}_{rmax}}$ as initial threshold rule (which is about one-sigma confidence interval), the selected sub-images are expected to have at least 75% r variance values. In this analysis, from the 10 groups of 256 subimages, the obtained minimum, maximum and mean value of sub-images is 42, 104, and 79, respectively. Furthermore, from these sub-images, three sets of 30 sub-images with approximately 75% of r variance values are selected for further analysis. The purpose of further analysis is to measure the relative SD of the FWHM value at PSF from the selected sub-images. The FWHM value at PSF of the selected sub-images is derived using the existing edge method of Khom (2004). Table 4.1 tabulates the results of this analysis. The data analysis yields a relative SD of < 1.9% of FWHM value at PSF among the selected sub-images, which demonstrates high precision measurement. With the resulting relative SD and the mean value. Therefore, based on the empirical analysis, 75% × $(\sigma^2)\ _{\tilde{g}rmax}$ is a good choice for the inclusion of potential candidates. Moreover, by taking 30 sub-images instead of 79 (mean value) sub-images, the results of this analysis also demonstrate that the input image for PSF estimation can be reduced.

Table 4.1: The FWHM of PSF for 3 x 30 sub-images of approximately 75% of *r* variance values

Gaussian blur, σ = 2.6; FWHM of Ground truth = **6.13** pixel					
Sample 1: Average = 6.12 pixel; SD = 0.12; Relative SD = 1.90%					
6.21	6.14	6.29	6.09	5.99	6.29
6.21	6.21	5.82	5.90	6.10	6.16
6.25	6.06	6.21	6.16	5.82	6.08
6.04	6.17	6.02	6.18	6.20	6.06
6.19	6.13	6.19	6.21	6.17	6.14
Sample 2: Average = 6.15 pixel; SD = 0.04; Relative SD = 0.66%					
6.13	6.17	6.12	6.09	6.21	6.09
6.14	6.12	6.17	6.14	6.17	6.11
6.19	6.13	6.08	6.12	6.17	6.14
6.17	6.11	6.12	6.11	6.21	6.12
6.16	6.16	6.14	6.12	6.19	6.11
Sample 3: Average = 6.14 pixel; SD = 0.10; Relative SD = 1.60%					
6.20	6.04	6.15	6.07	6.17	6.21
6.16	6.25	6.15	6.14	6.11	6.04
6.06	6.14	6.12	6.19	6.02	6.23
6.15	6.25	6.29	6.09	5.77	6.19
6.21	6.06	6.25	6.21	6.13	6.06

Since the computational time is the other concern in this framework, so this work chooses to limit the input images by only including those sub-images with a 10% deviation of variance values from $(\sigma^2)\ _{\tilde{g}rmax}$. The threshold is selected by multiply the $(\sigma^2)\ _{\tilde{g}rmax}$ with a value ranging from 75% to 90%, depending on the intuitive judgment on the characteristic of the input images. For instance, if the input image consists of more urban areas, the value can be higher than 85%, else it should be lower but not lesser than 75%. In the experiment of this work, the pT is set to 90%, this is because from the preliminary analysis that uses 10 data samples, on average there are more than 30 candidates can be selected from each data sample, and previous analyses also show that this amount is sufficient.

Figure 4.5 shows an example of sub-images from Equation (4.10) with its respective r map profile by Equation (4.9). Based on the analysis, with r_5 as the $\tilde{g}_{rmax}$, the percentage of r variance values relative to $\tilde{g}_{rmax}$ for r_1, r_2, r_3 and r_4 is 9.8%, 28.2%, 93.5% and 98.8%, respectively. Since r_3 and r_4 exceeded the predefined threshold value, therefore, they are selected as the potential candidates. From Figure 4.6, it is clearly shown that r_3, r_4, and r_5 contain strong image structures in the sub-image.

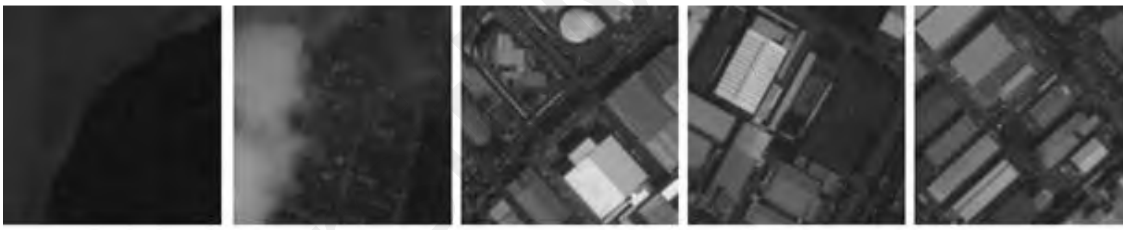

$\tilde{g}_1$ $\tilde{g}_2$ $\tilde{g}_3$ $\tilde{g}_4$ $\tilde{g}_5$

(a)

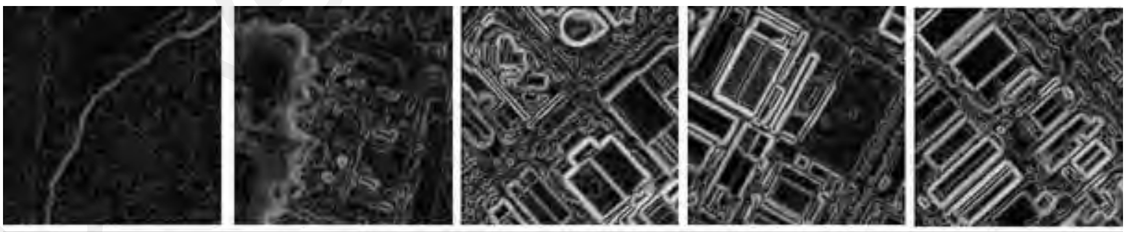

r_1	r_2	r_3	r_4	r_5
$\sigma_{r_1}^2 = 0.004$	$\sigma_{r_2}^2 = 0.012$	$\sigma_{r_3}^2 = 0.036$	$\sigma_{r_4}^2 = 0.038$	$\sigma_{r_5}^2 = 0.039$

(b)

Figure 4.5: Sub-images with its *r* map profile: (a) images $\tilde{g}_{1..5}$ are some of the sub-images from the segmentation process and (b) images are the respective *r* map profile (with variance values) of each sub-image **from (a).**

To further reduce the computation effort, the number of ideal candidates, $\hat{c}$ to be selected for phase 2 is determined by

$$\widehat{c} = \begin{cases} c = \frac{\sqrt{j}}{2}, \ \ddot{p} \geq c \\ \ddot{p}, \ otherwise \end{cases}. \tag{4.10}$$

where $\ddot{p}$ is the total number of potential candidates from sub-images, $\acute{g}(i+1)$. The ideal candidates, therefore, are described as $\acute{g}_i^p \mapsto \{\acute{g}_i, \acute{g}_{i+1,\ldots,}\acute{g}_p\text{: i} = 1, 2 \ldots \ddot{p}\ \}$.

The next subsection will discuss all methods used to solve the proposed robust PSF estimation in the second phase of the proposed framework.

4.3.2 Phase 2: Robust PSF Estimation

In this phase, the PSF estimation method is formulated as a constrained optimization problem. It is the core of the proposed on-orbit spatial characterisation Framework.

As was mentioned in Section 4.2, to enable accurate PSF kernel estimation, two important aspects other than the good region selection and reliable structure extraction, are the ability of algorithms to restore a sharp edge and suppress noise in the smooth regions. In fact, to achieve sharp edge restoration and noise suppression, it is critical to select only useful or reliable structures within the ideal candidates as the input for PSF kernel estimation. For that reason, the priors function in Equation (4.6) is decoupled into two steps: (1) PSF kernel estimation and (2) latent image estimation, and alternately optimize the h and f to progressively refine the PSF kernel at the k-th iteration, such that the Equation (4.6) becomes

$$\begin{cases} h_{k+1} & = \min\limits_{h} \ \|g - h_k \oplus f\|_2^2 + \lambda_h \Psi_h(h), & (4.11) \\ f_{k+1} & = \min\limits_{f} \ \|g - h \oplus f_k\|_2^2 + \lambda_f \Psi_f(f). & (4.12) \end{cases}$$

The fact that noise suppression in smooth regions is important, is because such regions usually occupy much larger areas than strong edges in an image. If the noise has not been suppressed in smooth regions, the data fitting function in Equation (4.12) would be significantly affected by the noise, compromising the accuracy of kernel estimation from strong edges in Equation (4.11).

Since this work is using the alternating minimization approach and its convergence rate depends heavily on the initial guess, one method to improve the search is by building a multi-scale image pyramid. Hence, a multi-scale image pyramid is developed to perform the optimization process of PSF kernel estimation (i.e., Equation (4.11)) and latent image estimation (i.e., Equation (4.12)) step in a coarse-to-fine approach. This kind of setup is useful to avoid convergence to unfavourable local minima. Given an ideal candidate, $\acute{g}_i^p$, an image pyramid is constructed with a scaling factor of $\frac{\sqrt{2}}{2}$ to get the coarsest level. By starting from the coarsest level, the sharp and large-scale edges can be predicted in low resolution, where the extent of degradation has been narrowed and most of the edges can be predicted without severe localization errors. The number of pyramid levels is adaptively determined by the size of the PSF kernel. In this experiments, the kernel size was specified by the user, however, empirically, it did not have much influence on the accuracy of PSF kernel estimation if the size is large enough to contain the estimated kernel.

In this work, the size of the PSF kernel at the coarsest pyramid level is a 7 × 7 kernel. Start with the coarsest level, the PSF kernel, h in Equation (4.11) and the latent image, f in Equation (4.12) is updated alternately at each level of the pyramid and propagates the solution to the next finer level. At each pyramid level, this work performed five iterations to estimate the latent image and up-sampled it to the next finer level by bilinear interpolation.

The overall process of the PSF estimation phase has been described in this subsection. Thus, the following subsections will move on to describe the steps for PSF kernel estimation and latent image estimation in further detail.

4.3.2.1 Step 1: PSF kernel estimation

Estimation of PSF relies on solving the problem in Equation (4.11), which is a least-square fitting problem. The minimizer of Equation (4.11) is to best fit the solution to g and h. If f is the true estimate, then the minimizer h is the best solution to the original problem in the ℓ_2-norm residue sense. If f is an incorrect estimate, then h cannot be the solution of the original problem, even if it is the minimizer of Equation (4.11).

In the early success of the single BID problem, Fergus et al. (2006) pointed out that h can be better estimated if f is replaced by ∇f, where ∇f is the image gradient of f. The idea can be intuitively understood by observing Figure 4.6, which shows an image blurred by different variance σ^2 of Gaussian PSFs. When the variance of the Gaussian PSF increases, the texture of the image is smeared out, but the edges can remain to be seen clearly. This result implies that a significant portion of the information is preserved in ∇f. Hence, similar to the method for the selection of ideal candidates in Subsection 4.3.1, the image gradient is utilized rather than image intensity. The minimization in Equation (4.11), thus can be rewritten as

$$\min_{h} \; \|\nabla g - h \otimes \nabla f\|_2^2 + \lambda_h \|h\|_\alpha^\alpha, \tag{4.13}$$

where $\nabla f = [\partial_x f, \partial_y f]^T$ is the gradient of f, and $0 < \alpha \leq 2$.

The drawback of Equation (4.13) is that it relies on the initial estimation of ∇f, which suggests that ∇f must be sharp, for otherwise $h \otimes \nabla f$ is not a good estimate of ∇g. So, the question now is: how to obtain a sharp ∇f without solving the h? There exists an edge sharpening technique, such as the renowned shock filter by Osher & Rudin (1990). However, even if a sharp ∇f that denotes all edges of the image is available, it generally includes both strong and weak edges. Furthermore, studies have shown that more edges do not necessarily benefit kernel estimation.

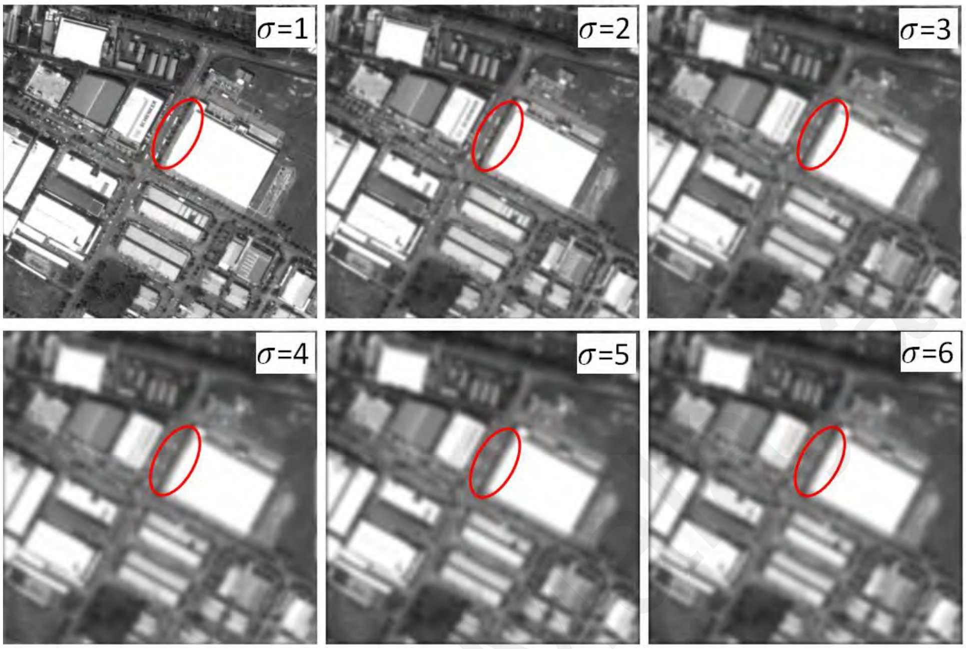

Figure 4.6: An image is blurred using Gaussian PSFs with different variance σ^2.The texture regions are smoothed when σ increases, but strong edges are still clearly seen although blurred.

Taking all these factors into consideration, this work further studies the nonlocal self-similarity characteristic of an image. It is ubiquitous that the structural component of an image contains major objects in the image, whereas the texture component comprises the fine-scale details and noise. Therefore, as was mentioned in Section 4.2, the capability to extract reliable structures is critical to ensure accurate MTF measurement because different extraction of structures can lead to different PSF estimation results. In addition, although the r-map from Equation (4.8) contains structure information of the ideal candidate, some of them often contain many small-scale structures that usually lead to large kernel estimation errors. Thus, this work target extracting more reliable structures using several key steps, which will be explained in the next subsection.

*(a) **Extraction of reliable structure***

As aforementioned, the texture component contains fine-scale details and noise that will jeopardize the kernel estimation results. Hence, to increase the robustness of extracting reliable structure, this work employs a structure–texture decomposition method to exclude the texture component. TV regularizer method, as originally proposed in Rudin, Osher & Fatemi (1992) is known to be one of the best for preserving large-scale edges in the structure–texture decomposition methods.

A study by Aujol et al. (2006) that compared four different models of TV (Rudin, Osher & Fatemi, 1992; Aujol et al, 2006; Yin et al., 2005; Meyer, 2001), concluded that the TV-ℓ_2 model of Rudin et al. (1992) is the most favorable to use for unknown texture pattern. Therefore, this work adopts the TV-ℓ_2 model that uses a quadratic penalty to enforce structural similarity between the input and output. This model is expressed as

$$\min_{\acute{g}_s} \sum \left\{ \frac{1}{2\mu} \| \acute{g}_s - \acute{g} \|_2^2 + \| \nabla \acute{g}_s \|_2 \right\}, \tag{4.14}$$

where $\acute{g}_s$ is the decomposed structure from the ideal candidate, $\acute{g}_i^p$, and μ is an adjustable parameter that requires extensive manual-tuning. The data fidelity function $\| \acute{g}_s - \acute{g} \|_2^2$ is to make the extracted structures similar to those in the input image. $\sum \| \nabla \acute{g}_s \|_2$ is a TV regularizer. Although highly effective for denoising, the ℓ_2-norm also penalizes large gradient magnitudes that possibly affect contrast during denoising. It causes an undesirable effect such as staircasing in the smooth region.

Studies in Subsection 3.1.1.2 found that image gradients typically exhibit heavy-tailed distributions, which can be fitted by the hyper-laplacian model. As such, to mitigate this staircasing effect by the model in the Equation (4.14), the μ is replaced with a hyper-laplacian prior, $\omega(x)$, and incorporate $r(x)$ as defined in Equation (4.8) as an adaptive smoothness weight to Equation (4.14) such that it becomes a sparse adaptive model defined as

$$\min_{\acute{g}_s} \sum \left\{ \frac{1}{2\omega(x)} \|\acute{g}_s - \acute{g}\|_2^2 + \|\nabla \acute{g}_s\|_2 \right\}, \text{ where } \omega(x) = e^{-\|r(x)\|^{0.8}}, \quad (4.15)$$

To demonstrate the validity of Equation (4.15), an experiment as shown in Figure 4.7 was conducted in this work.

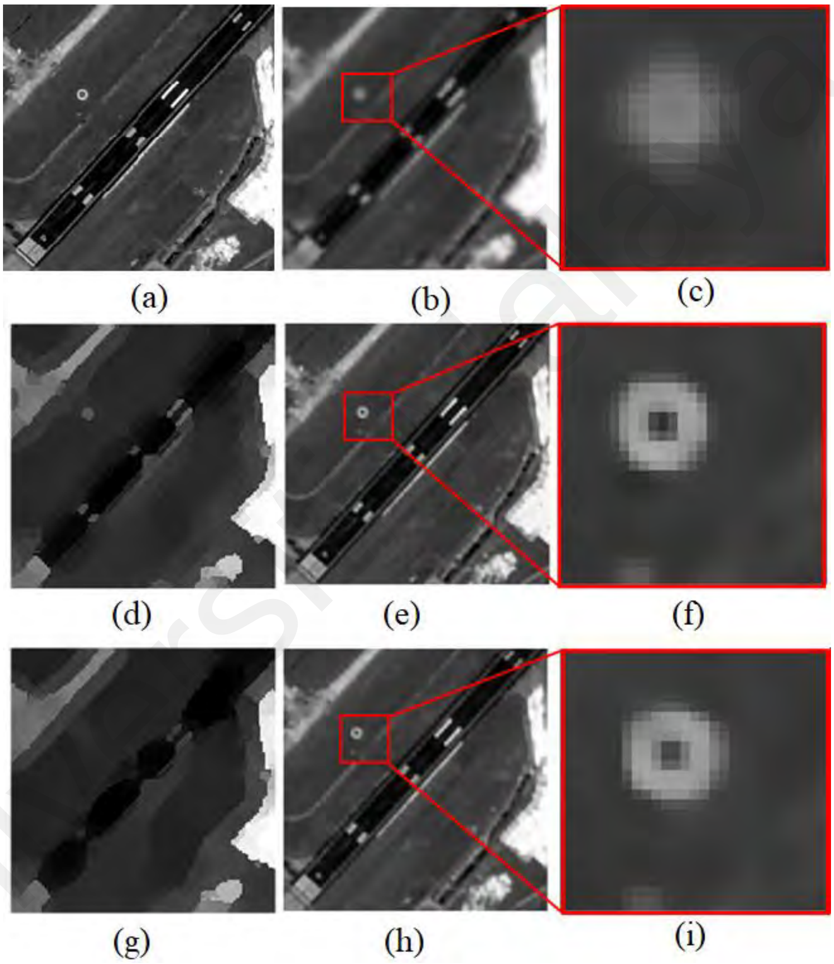

Figure 4.7: Comparison of the latent image results with Equations (4.14) and (4.15), respectively. (a) Original image, (b) and (c) blurred image with closed-up view, (d) structures extraction with Equation (4.15), (e) and (f) results with Equation (4.15), (g) structures extraction with Equation (4.14), and (h) and (i) results with Equation (4.14).

From Figure 4.7(b), it can be visualized that the blurred image contains some vague structures, which may have detrimental effects on PSF kernel estimation. But with the sparse adaptive smoothness weight of *r(x)* from Equation (4.8), it can be noticed that more reliable structures are extracted in Figure 4.7(d) for PSF estimation. In addition, the close-up view from Figure 4.7(f) shows a much sharper image without a staircasing effect. Figures 4.7(h) and 4.7(i) show latent image results obtained by Equation (4.14) after an exhausting tuning of parameter μ. To quantify the validity of Equation 4.15, this work uses the structural similarity index (SSIM) quality assessment of Wang et al. (2004). The SSM index is a decimal value comprised between -1 and 1, where the closer the SSIM value to 1 the higher is the quality of the measured image. In comparison, Equation (4.15) obtains a higher SSIM value (0.98) as compared to Equation (4.14)(0.81). These experimental results demonstrate that the latent image by the Equation (4.15) is significantly better than the Equation (4.14).

After obtained the $\acute{g}_s$, the structure will be enhanced using the shock filter of Osher & Rudin (1990) and further enhance by diminishing the small gradient value using the Heaviside step function to ensure that only salient structures with large gradient values remain for kernel estimation.

The shock filter is an iterative algorithm developed for anisotropic diffusion problems. Given an image $\acute{g}_s$, in the k-th iteration of the shock filter, the algorithm will iteratively update the image as

$$\breve{g}_s{}^{k+1} = \breve{g}_s{}^{k} - \beta \text{sign}\left(\Delta \acute{g}_s{}^{k}\right)\left\|\nabla \acute{g}_s{}^{k}\right\|_2. \tag{4.16}$$

where $\Delta \acute{g}_s = \acute{g}_{s_x}^{\,2} \acute{g}_{s_{xx}} + 2\acute{g}_{s_x}\acute{g}_{s_y}\acute{g}_{s_{xy}} + \acute{g}_{s_y}^{\,2}\acute{g}_{s_{yy}}$ is the Laplacian of $\acute{g}_s$, β(=1) is the step size.

The final selected salient structures for kernel estimation, thus, are determined as

$$\nabla s = \nabla \breve{g}_s \,.\, \Pi(\|\nabla \breve{g}_s\|_2, \tau_s) \tag{4.17}$$

where $\breve{g}_s$ denotes the shock filtered images using Equation (4.16), $\Pi(.)$ is the Heaviside step function, and τ_s is a threshold of the gradient magnitude, $\|\nabla \breve{g}_s\|_2$. $\Pi(.)$ outputs ones for ($\|\nabla \breve{g}_s\|_2 \geq \tau_s$) and zeros otherwise. By applying$\Pi(.)$, some noise in the $\nabla \breve{g}_s$ can be eliminated and maintaining only useful salient edges for kernel estimation.

(a) $\acute{g}_s$ (b) $\breve{g}_s$ (c) ∇s

Figure 4.8: Illustration for the extraction of reliable structure. (a) Structure $\acute{\boldsymbol{g}}_s$extracted using Equation (4.15), (b) shock filtered image $\breve{\boldsymbol{g}}_s$ by Equation (4.16), and (c) Salient structure $\boldsymbol{\nabla s}$ by Equation (4.17).

(b) ***Kernel refinement***

At the beginning of the kernel refinement process, the threshold τ_s for truncating gradients is determined according to Cho and Lee (2009). As the kernel refinement iteration progresses, similar to Xu and Jia (2010), the threshold τ_s is gradually adjusted by dividing 1.1 at each iteration to include more edges for inferring subtle structures during kernel refinement. Figures 4.9(b) to 4.9(d) show the coarse-to-fine pyramid of interim ∇s maps in the iterative optimization process. It can be noticed that as the iteration increases, more and sharper edges are included in the subsequent level for kernel estimation.

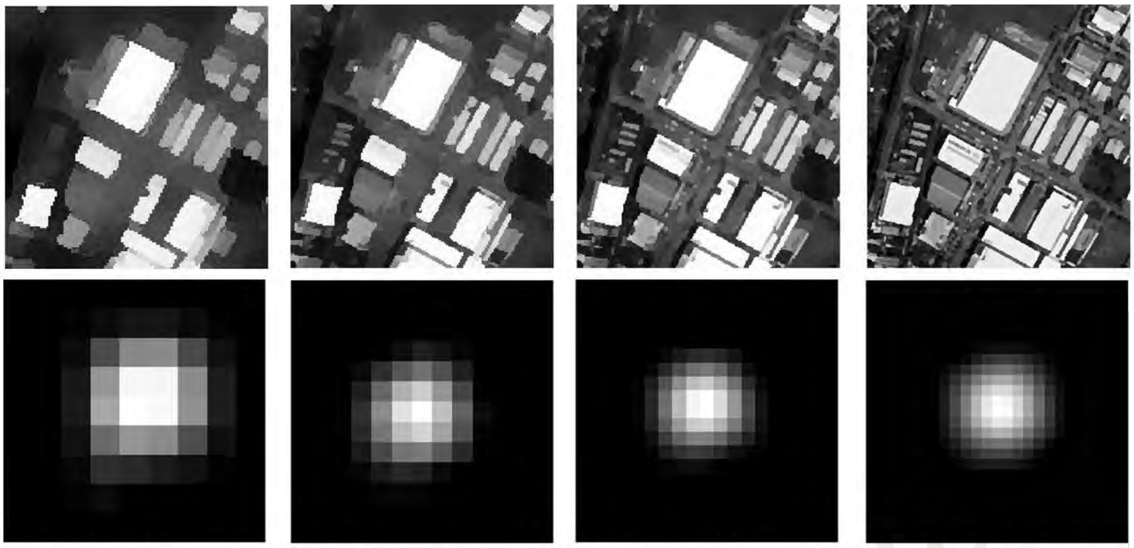

Figure 4.9: The coarse-to-fine pyramid optimization process for kernel refinement. (a)-(d) interim ∇s maps at each level pyramid using Equation (4.17); The first row shows the interim ∇s maps, whereas the second row shows its corresponding estimated PSF kernel.

*(c) **Kernel estimation***

With the shock filter and structure extraction method, the minimization of finding h in Equation (4.11) becomes

$$\min_{h} \|\nabla g\text{-}h\otimes \nabla s\|_2^2 + \lambda_h \|h\|_\alpha^\alpha \tag{4.18}$$

$$\text{s.t. } h(x,y) \geq 0,\ \textstyle\sum_{\{x,y\}} h(x,y) = 1,$$

where ∇s is the salient structure.

Most of the state-of-the-art works adopted a single Gaussian (Shan, Jia & Agarwala, 2008; Pan et al., 2017) or hyper Laplacian (Krishnan & Fergus, 2009, Liu et al., 2016) regularizer to guarantee the sparseness of PSF kernel. However, it neglects the continuity of the PSF kernel, and sometimes it induces noisy kernel estimates. Noisy interim kernels will damage the interim latent image estimation, and this further leads to unreliable kernels during the kernel refinement. To address these problems, this work includes a new spatial function that simultaneously suppresses noise in the kernel and ensures sparsity and continuity of the kernel.

Given an interim PSF kernel ∇h, the new spatial function only counts the number of the non-zeros image gradient in both directional, thus the new spatial function is defined as

$$P(h) = \{(x, y): |\partial_x h(x, y)| + |\partial_y h(x, y)| > 0\}, \tag{4.19}$$

With the introduction of Equation (4.19), the total energy of the kernel estimation model, later, is defined as

$$\min_h \|\nabla g\text{-}h \oplus \nabla s\|_2^2 + \lambda_h \|h\|_\alpha^\alpha + \gamma P(h) \tag{4.20}$$

$$\text{s.t. } h(x, y) \geq 0,\ \textstyle\sum_{\{x,y\}} h(x, y) = 1,$$

where the first term is the data fidelity function that provides reliable edge information, the second function provides a sparsity priors to the kernel; and the new spatial function $P(h)$ promotes continuity by maintaining the non-zero gradients, with parameter γ to constrain the spatial smoothness of the kernel h.

It is difficult to minimize Equation (4.20) as f is non-linear and its concrete form is assumed to be unknown in this work. To overcome this problem, this work proposes to minimize the energy function of Equation (4.20) by decoupling the functions of the prior into separate steps with the bilevel programming (BLP) approach (Fehrenbach et al. 2015) such that the model becomes

$$\min_h h(h, \hat{h})\, subject\ to\ (s.t.) \begin{cases} \|\hat{h}\text{-}h\|_\alpha^\alpha + \gamma P(\hat{h}). \\ h\ solves \begin{cases} \hat{h} = \arg min\ \|\nabla g\text{-}h{*}\nabla s\|_2^2 + \lambda_h \|h\|_\alpha^\alpha \\ s.t. \quad h(x, y) \geq\ 0,\ \sum_{\{x,y\}} h(x, y) = 1, \\ \text{where } 0 < \alpha \leq 1, \end{cases} \end{cases} \tag{4.21}$$

where the lower-level problem is solved using the constrained iterative reweighed least square (IRLS) method of Levin et al. (2007), whereas the Upper-level problem is solved using the ℓ_0 gradient minimization of Xu et al. (2011). The choice of BLP because it has an advantage as compared to the conventional iterative method that frequently uses in image restoration technique, is that it has the ability to optimize many parameters simultaneously.

4.3.2.2 Step 2: Interim latent image estimation

Recall that in the PSF kernel estimation problem, finding h is an iterative process in which f must be also updated before a new h is found. In this step, this work applies deconvolution to estimate the latent image f from the estimated kernel h of Equation (4.21). To guide the recovery of the latent image, this work employs the anisotropic TV-ℓ_1 model, as this model is well known for suppressing noise while preserving strong edges (Chen et al., 2015). The total energy function in Equation (4.12) associated with f is rewritten as

$$\min_{f} \|g-h*f\|_2^2 + \lambda_f \|\nabla f\|_{TV1} \ , \qquad (4.22)$$

where $\|\nabla f\|_{TV1}$ is the spatial priors that enforces a smooth gradient in f. Since sparse priors choose to concentrate derivatives at a small number of pixels, leaving the majority of image pixels constant, hence, the optimization problem is no longer convex, so it cannot be minimized in closed form. To solve this problem, the IRLS method is utilized in the spatial domain using the conjugate gradient algorithm (Barrett et al. 1995).

So far, the overall procedures of the PSF estimation method have been discussed. The PSF estimation contains two major steps. The first step is the estimation of h, whereas the second step is the estimation of f. The output from this method is a set of PSF estimate, K. Given a set of PSF estimate, K is described as

$$K \mapsto \{h_i, h_{i+1,\ldots,} h_p \colon \mathrm{i} = 1, 2 \ldots p\} \qquad (4.23)$$

The next subsection will present the final phase of this framework, which is the MTF measurement method.

4.3.3 Phase 3: MTF calculation

In this phase, first, a parametric model is developed to analyze and measure the PSF for MTF measurement. In practical remote sensing imaging, most imaging sensors cannot produce symmetric PSF due to inherently imperfect imaging behavior and image motion. Therefore, parametric PSF modeling essential to eliminate noise and also to promote high fidelity representation of PSF.

In most science and engineering fields, including remote sensing, it is often mathematically convenient to assume a Gaussian distribution for independent, identically distributed samples from a random process (Schowengerdt, 2007; Holst, 2017). In general, the 2-D Gaussian function is the common generic model for a measured PSF, where its end-to-end system transfer function can be represented by a Gaussian curve (Storey, 2001; Helder et al., 2006; Kang, 2015). Thus, the 2-D Gaussian model is considered to be the most appropriate model for the MTF measurement of this framework.

4.3.3.1 Parametric PSF modeling

Before the 2-D Gaussian model is being applied, for each blur kernel $h_{i,}$in K, first, determine its peak location by finding the brightest pixel value in the kernel, and then shift the peak to the center position of the kernel. Recall that the PSF is assumed to be a linear Spatially-invariant system, we, therefore interlace the PSF kernels in K by averaging all $h_{i,}$ K using Equation (4.24), the intermediate $\overline{PSF}$, thus become

$$\overline{PSF} = \frac{1}{p}\sum_{i=1}^{p} h_i \, , where \ h_i \in K, \tag{4.24}$$

The purpose of the interlacing process is to reduce the uncertainty in the kernel estimation process in phase 2. Figure 4.10 shows an example of $\overline{PSF}$ and its corresponding distribution of brightness in a 3-D view.

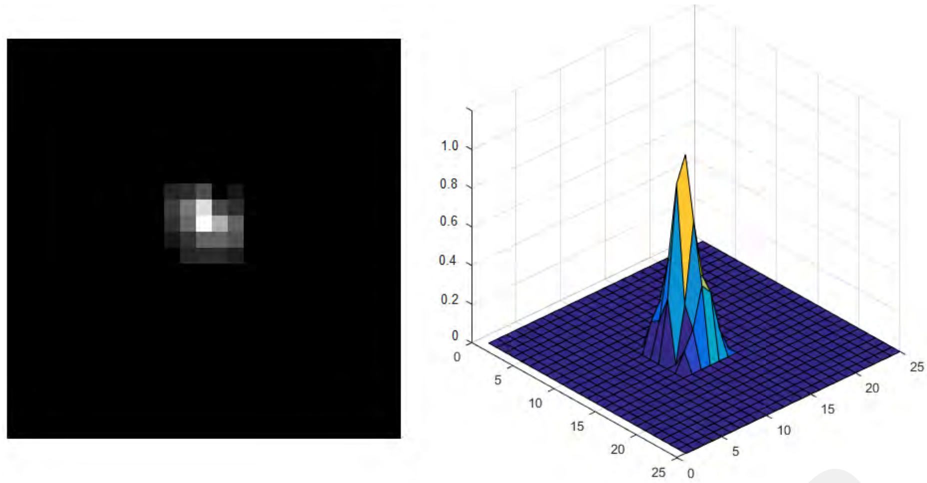

(a) (b)

Figure 4.10: Estimated PSF kernel, (a) an example of $\overline{PSF}$ estimated from a real satellite image, and (b) is its corresponding distribution of brightness.

After obtained the $\overline{PSF}$, a 2-D Gaussian distribution function is applied for sub-pixel interpolation and curve fitting using the following equation

$$PSF(x, y) = Ae^{-\frac{1}{2}\left(\frac{x^2}{\sigma_x^2}+\frac{y^2}{\sigma_y^2}\right)}, \tag{4.25}$$

where A is an amplitude of the Gaussian distribution, σ_x and σ_y are the standard derivation of the Gaussian distribution along x- and y-direction, respectively. By applying the natural logarithm of the Gaussian distribution in Equation (4.25), then yield

$$\begin{aligned} ln\,PSF(x, y) &= -\frac{1}{2\sigma_x^2}x^2 - \frac{1}{2\sigma_y^2}y^2 + lnA, \\ &= a_1x^2 + a_2y^2 + a_3, \end{aligned} \tag{4.26}$$

In order to estimate the parameters in Equation (4.25), the weighted least-square Gaussian curve fitting (Gua, 2011) is employed since it can effectively eliminate the influences of random fluctuations on the PSF estimation. The weighted least-square Gaussian curve fitting algorithm of Gua (2011) is defined as follows

$$
\begin{pmatrix}
\sum \hat{h}_{k-1}^2 x^4 & \sum \hat{h}_{k-1}^2 x^2 y^2 & \sum \hat{h}_{k-1}^2 x^2 \\
\sum \hat{h}_{k-1}^2 x^2 y^2 & \sum \hat{h}_{k-1}^2 y^4 & \sum \hat{h}_{k-1}^2 y^2 \\
\sum \hat{h}_{k-1}^2 x^2 & \sum \hat{h}_{k-1}^2 y^2 & \sum \hat{h}_{k-1}^2
\end{pmatrix}
\begin{pmatrix} a_{1,k} \\ a_{2,k} \\ a_{3,k} \end{pmatrix}
=
\begin{pmatrix}
\sum \hat{h}_{k-1}^2 lnPSFx^2 \\
\sum \hat{h}_{k-1}^2 lnPSFy^2 \\
\sum \hat{h}_{k-1}^2 \ln PSF
\end{pmatrix}. \tag{4.27}
$$

where $\hat{h}(k) = \begin{cases} PSF & for\ k = 0 \\ e^{a_1x^2+a_2y^2+a_3} & for\ k > 0 \end{cases}$ and $a_{1,k}$, $a_{2,k}$, $a_{3,k}$ are refined values of a_1, a_2, a_3 after k-th iteration.

From Equation (4.26), accordingly, yield $a_1 = -\frac{1}{2\sigma_x^2}, a_2 = -\frac{1}{2\sigma_y^2}$, and $a_3 = lnA$. By applying the estimates of Gaussian parameters (i.e., $\sigma_x, \sigma_y, and\ A$) to Equation (4.25), finally obtain the parametric PSF model as demonstrated in Figure 4.11.

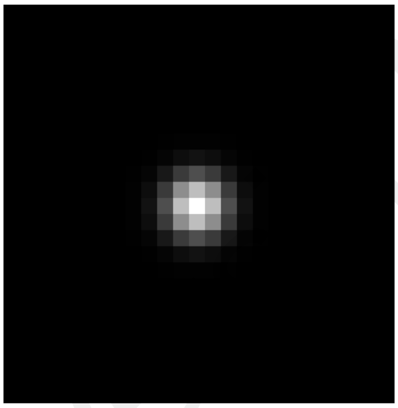

(a)

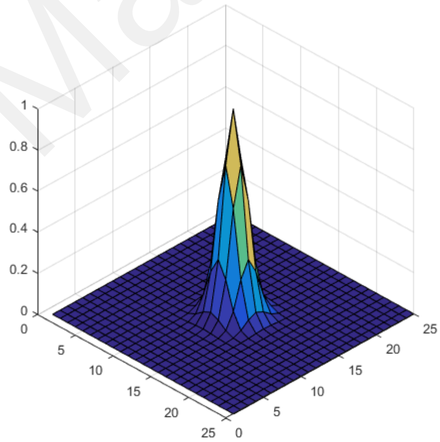

(b)

Figure 4.11: Parametric PSF. (a) 2-D PSF after applying Equations (4.25)-(4.27), and (b) its corresponding distribution of brightness.

4.3.3.2 Spatial resolution measurement

Finally, in this framework, the spatial resolution is characterized using spatial quality metrics as follows:

(a) ***Full-width at the half-maximum measurement***

To obtain an estimate for the overall FWHM, firstly, slice the 2-D PSF representation from Equation (4.25) into 1-D PSFs through the peak in the cross-track and along-track directions. Each 1-D PSF slice is then normalized such that the peak value is 1.0. An example of the 2-D PSF plot and its corresponding 1-D PSF is shown in Figure 4.8.

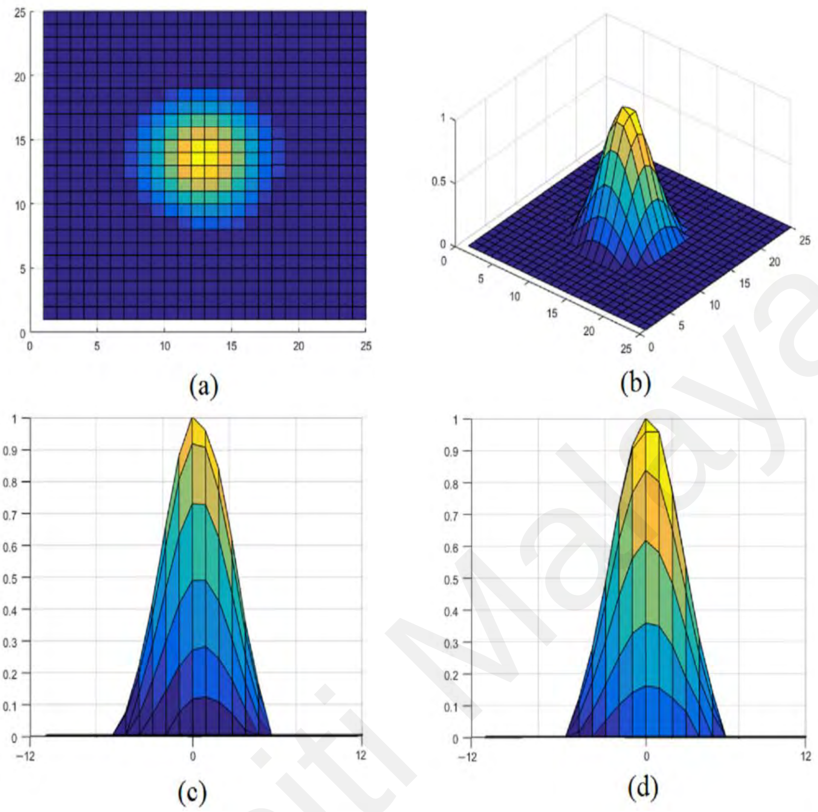

Figure 4.12: Illustration of the intermediate PSF kernel: the y-axis is the normalized PSF value, whereas the x-axis is the pixel position. (a) PSF kernel in the 2-D view. (b) PSF in the 3-D view. (c) Slice of 1-D PSF in the cross-scan direction, and (d) Slice of 1-D PSF in the along-track direction.

The PSF values were interpolated using the cubic spline interpolation with a sampling resolution of 0.05 pixels. Next, the sliced 1-D PSF profile in both directions was trimmed to minimize the frequency leakage. The FWHM of PSF value is typically described as either the width of a spectrum curve or the function measured between points on the curve at which the function reaches half its maximum value, as shown in Figure 4.13. In Figure 4.13, those points are labeled as the starting points (SP) and ending points (EP), respectively. The half-maximum value on the *y*-axis is always 0.5 because the 1-D PSF plot is normalized.

The FWHM value of the estimated PSF can be determined by finding the points on the x-axis that reside in the half-maximum value. Figure 4.13 shows the technique used to calculate the FWHM values of the estimated PSF. From the depicted figure, the starting x point, x_s of SP, and the ending x point, x_e of EP can be calculated using the linear interpolation between points (P1, P2) and points (P3, P4), respectively. Once x_s and x_e are found, the FWHM could be calculated by measuring the distance between these two points using the following equation:

$$FWHM = x_e - x_s. \tag{4.28}$$

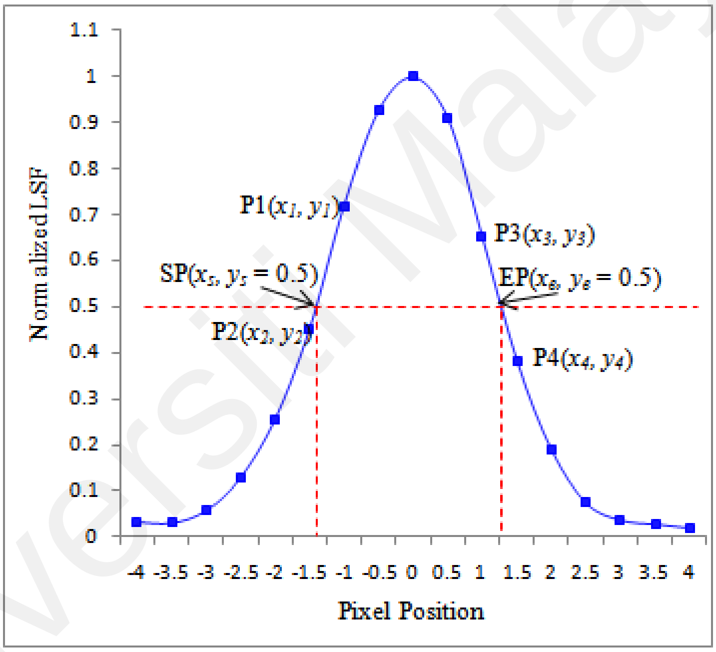

Figure 4.13: FWHM measurement of PSF.

(b) ***MTF values at Nyquist frequency***

Finally, 1-D FT is applied to the 1-D PSF. The resulting transfer function was then normalized by the DC term to obtain the MTF. The MTF values at Nyquist frequency are determined based on the Nyquist frequency location. The Nyquist frequency location was calculated using the dataset size and the predetermined spline resolution of 0.05 pixels is described as

$$Nyquist\ frequency\ location = (whole\ dataset \times 0.05)\ /\ 2 + 1 \quad (4.29)$$

Figure 4.14 shows an example of the normalized MTF plot with its MTF value at the Nyquist frequency.

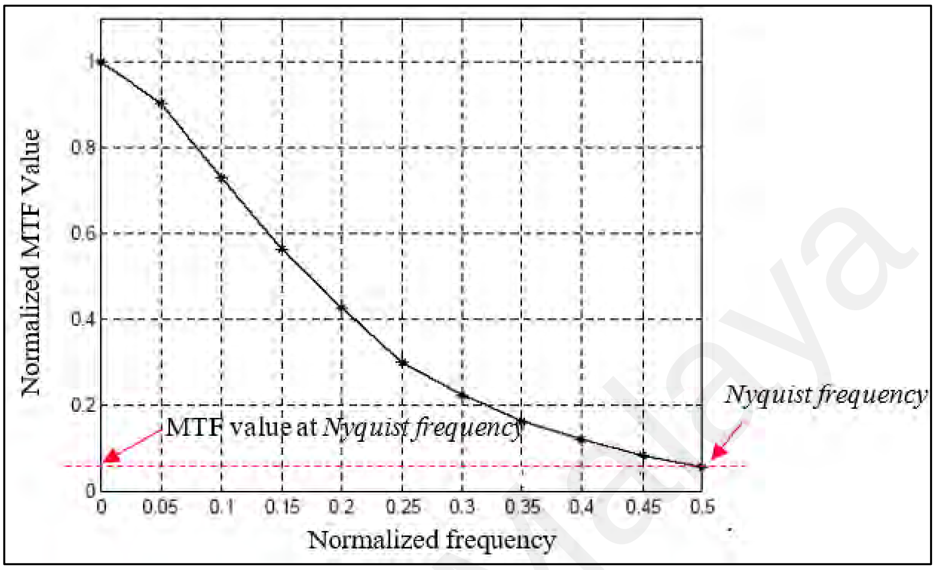

Figure 4.14: An example of a normalized MTF.

4.4 Analysis and Experimental Results

The test analysis and experiment results for MTF measurement evaluation are elaborated in four separate sub-sections. For the test analysis, this work provides an insightful analysis of the complexity and computational time of the algorithm, and analyses of the ideal candidate selection method. Whereas, for the experiment results, the performance of the algorithm is assessed by conducting experiments on synthetically blurred satellite images and real satellite images with unknown blur.

4.4.1 Sources of Data and Evaluation Measures

The dataset used for this research consists of remotely-sensed images from IKONOS (Dial et al., 2003) and RazakSAT (ATSB, 2010). The general characteristics and imaging system specification for both IKONOS and RazakSAT are presented in Table 2.2. The rationale of the dataset selection from IKONOS, among many other satellites, is that the performance of this satellite is made available through NASA's Science Data Purchase Program. Besides, it is available in the Level-2A product format, which implies that it has gone through radiometric correction and geo-rectification. Therefore, it can be used ground-truth data for this research. Whereas for RazakSAT, it is available in raw Level-0 product format, which is suitable to use as real satellite images with unknown degradation effects.

For a comprehensive analysis and evaluation, this work considers a wide range of test images, consisting of synthetic Gaussian blur and real unknown blur. The first dataset is the synthetically blurred satellite images simulated from IKONOS data. Using synthetic (i.e., stimulating) imagery, image acquisition, and processing variability can be removed from this discussion.

As mentioned in Subsection 4.3.3., a common generic model for a measured optical PSF is the 2-D Gaussian function. Therefore, a total of 50 data samples is collected by synthetically blurred the ground-truth data with Gaussian kernels of 25×25 for three different SD σ, 1, 2 and 2.6; Gaussian kernel of 35×35 with an SD of 3 and Gaussian kernel of 45×45 with an SD of 4. Apart from blurring, Gaussian white noise with 0.1 variances is added to all synthetic data to test the robustness of the proposed MTF measurement method. The second dataset is the real unknown blur satellite images. The real unknown blur images for this research comprise 50 data samples from RazakSAT data in the Panchromatic (PAN) band. The general characteristics and imaging system specifications for both IKONOS and RazakSAT satellite are presented in Table 4.2. This work conducted a series of experiments with the proposed MTF measurement algorithm and the experimental results are evaluated quantitatively using two metrics, namely the FWHM of PSF and MTF values at Nyquist frequency.

Table 4.2: General specification and characteristics of IKONOS and RazakSAT.

Parameter	IKONOS	RazakSAT
Orbit	98.1°, sun-synchronous	9°, near-equatorial
Altitude (km)	681	685
Spectral band	PAN, Multispectral (MS): blue, green, red, near-infrared	PAN, Multispectral (MS): blue, green, red, near-infrared
GSD	1-m PAN; 4-m MS	2.5-m PAN; 5.0-m MS
Image swath (km)	13.8	20
MTF @ Nyquist frequency	PAN > 9%, MS > 17%	PAN > 8%, MS > 15%
Signal quantization	11-bits per pixel	8-bits per pixel

4.4.2 Algorithm Complexity and Computational Time

The main complexity of the proposed method comes from the pyramid image process, where it iteratively solve Equations (4.21) and (4.22), that involve non-convex models and a few convolution operations. The proposed method is implemented in Matlab on an Intel Core i5 CPU with 8GB of RAM.

In this experiment, to estimate the PSF kernel from the synthetically blurred satellite images, the kernel size is specified based on the size of the known Gaussian kernel which comprises 25×25 kernels, 35×35 kernel, and 45×45 kernels. Meanwhile, for real satellite images with unknown blur, which is the RazakSAT images, this work empirically set the kernel size to 15×15, as it is found to be large enough to contain the estimated PSF kernel. In addition, an analysis using a 35×35 kernel is included, in order to comprehend the influence of kernel size with regards to the PSF kernel estimation accuracy.

For the computational time with an image size of 256×256, this work spends about 22 second(s) to estimate a 15×15 PSF kernel, 48 seconds, 75 to 81 seconds, and 210 seconds to estimate a 25×25 PSF kernel, 35×35 PSF kernel and 45×45 PSF kernel, respectively. For the RazakSAT satellite image with a pixel size of 4096×4096, based on the segmentation method proposed in Subsection 4.3.1, in most cases, a total of 8 sub-images will be selected for PSF kernel estimation. Therefore, on average, the total computational time for the MTF measurement is about 176 seconds. The average processing time of the proposed method is tabulated in Table 4.3. In this framework, the number of pyramid levels for kernel estimation is adaptively determined by the size of the PSF kernel. Therefore, the processing time is expected to increase, since increasing the size of the kernel increases the pyramid level. One notable observation from this analysis is that the MTF_{Nyq} difference between 15 × 15 kernel and 35 × 35 kernel is not significant, which indicates that kernel size does not have much influence on the accuracy, nevertheless, it does influence computational efficiency.

Table 4.3: Average processing time of datasets with different kernel size

Data Type	**Kernel size**	**Pyramid level**	**Time (s)**
Synthetically blurred satellite images, 256 × 256 pixels	25 × 25	5	47.56 ± 1.01
	35 × 35	6	80.84 ± 3.97
	45 × 45	7	209.82 ± 13.87
Real Satellite with unknown blur, 256 × 256 pixels	15 ×15	5	21.57 ± 0.54 **(MTF_{Nyq} = 0. 0784)**
	35 × 35	6	74.56 ± 3.02 **(MTF_{Nyq} = 0. 0779)**
4096 × 4096 pixels	**15 × 15**	**5**	**175.74 ± 1.52**

Based on the analysis of 30 datasets as presented in Table 4.4, the processing time for a method that uses the whole image with size ($2^n \times 2^n$: n = 1, 2...) is expected to run in $O(N^2)$, which means whenever N doubles, the running time increases about fourfold.

Table 4.4: Processing time using the whole image ($2^n \times 2^n$: n = 8, 9, 10, 11.) without the proposed segmentation method.

Dataset	Size of Image (pixel)			
	256 × 256	**512 × 512**	**1024 × 1024**	**2048 × 2048**
1	73.05	324.93	1348.33	6624.96
2	74.12	327.11	1347.27	6645.94
3	72.89	308.37	1336.48	6578.52
4	73.44	319.31	1340.02	6610.85
5	72.88	321.09	1351.66	6643.54
6	73.71	322.02	1342.25	6647.28
7	72.73	315.88	1342.51	6608.12
8	73.18	319.09	1341.80	6610.92
9	71.85	315.25	1338.48	6642.59
10	72.16	319.82	1343.13	6582.94
11	72.92	315.08	1343.64	6614.45
12	71.90	313.50	1341.66	6510.85
13	75.74	320.20	1341.98	6643.54
14	72.54	318.97	1342.25	6652.45
15	74.95	317.25	1338.92	6654.56
16	75.51	322.36	1342.59	6599.23
17	72.74	322.92	1345.73	6594.06
18	75.01	317.96	1342.26	6647.22
19	74.92	327.09	1341.98	6681.02
20	73.74	314.98	1339.78	6588.84
21	71.16	313.60	1341.27	6613.89
22	72.62	315.54	1340.90	6629.73
23	73.93	317.44	1342.98	6622.99
24	73.36	321.96	1334.29	6605.47
25	72.73	315.98	1342.08	6669.59
26	75.18	317.54	1335.03	6651.56
27	72.85	316.19	1341.81	6681.89
28	72.16	311.19	1342.25	6609.47
29	74.19	318.98	1344.71	6629.23
30	75.20	323.39	1342.38	6651.02
Average	**73.43**	**318.54**	**1341.98**	**6624.96**

Figure 4.15 shows the processing time of the segmentation method as a function of the size of the image. In comparison with the average processing time in Table 4.4, from the figure, it is clearly shown that the proposed method achieves significantly faster computational speed compared to a method without the used segmentation.

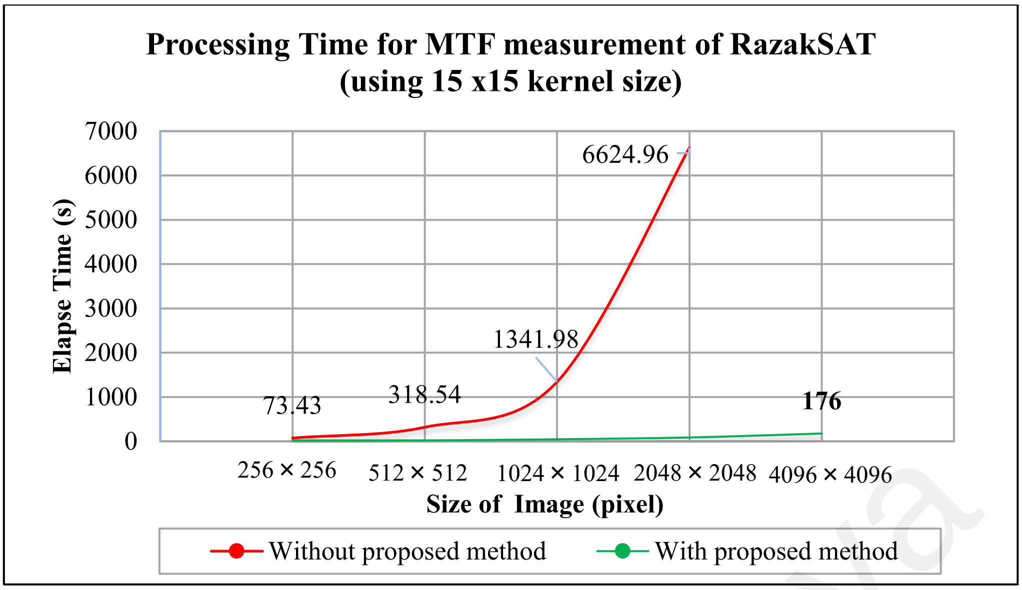

Figure 4.15: Processing time for MTF measurement of RazakSAT

4.4.3 Analysis of Selection of Ideal Candidate

The selection of ideal candidates is a crucial measure for this work as it ultimately determines the effectiveness of the proposed MTF measurement method. As explained in Subsection 4.3, the algorithm is set to select ideal candidates according to Equation (4.8) in phase 1, then it measures their average PSF value to characterize the spatial quality of the observed image and the performance of the imaging system in phase 3. To determine the accuracy and precision of the proposed algorithm, in this analysis, the measurement bias and error results are identified from the proposed algorithm. In the former, identification of systematic errors can improve the overall accuracy of the measurement; while in the latter quantification of precision allows error estimates to be associated with individual measurements. The measurement bias shall be determined by the relative SD.

The proposed segmentation method experiments on all the synthetic and real satellite images in this work. In this analysis, the results of three samples of synthetic images are presented with a size of 4096 × 4096 pixels, but each with different blurring effects by SD and σ in Gaussian function. Each sample consists of eight sub-images selected by Equation (4.8) and the results are shown in Table 4.5.

Table 4.5: The FWHM of PSF for 3 different samples.

Dataset	Sample-1		Sample-2		Sample-3	
	Gaussian blur, σ = 1, FWHM of Ground truth = **2.45** pixel		Gaussian blur, σ = 2.6 FWHM of Ground truth = **6.13** pixel		Gaussian blur, σ = 4, FWHM of Ground truth = **9.43** pixel	
	FWHM (pixel)	Relative Error (%)	FWHM (pixel)	Relative Error (%)	FWHM (pixel)	Relative Error (%)
1	2.48	1.2	6.15	0.1	9.46	0.3
2	2.56	4.2	6.12	-0.3	9.44	0.1
3	2.52	2.7	5.99	-2.4	9.31	-1.3
4	2.46	0.4	6.17	0.5	9.37	-0.7
5	2.47	0.8	6.11	-0.3	9.38	-0.5
6	2.58	5.1	6.12	-0.2	9.48	0.5
7	2.51	2.5	6.33	3.1	9.23	-2.1
8	2.55	4.2	6.21	1.3	9.51	0.7
Average	2.52	2.6	6.15	1.0	9.40	0.8
Relative SD (%)	**1.7**		**1.6**		**1.0**	

From Table 4.5, it can be observed that the relative SD for all three samples is relatively small. This indicates the proposed algorithm is able to produce high precision results of FWHM. Then, it is observed that the average relative error of FWHM results by the proposed algorithm is < 2.6%. This demonstrates that the proposed algorithm is capable of producing results with a 2-sigma confidence interval. Among all samples, Sample-3 has the highest degree of blur but has the lowest relative SD. Besides that, it also obtains small relative errors in the range of −2.2% to 0.5%. On the contrary, Sample-1 contains the lowest degree of a blur but has the highest value of relative SD, with a relative error as high as 5.1%. These observations suggest that the proposed method handles large-scale blur more effectively.

Figure 4.16 depicts the visual output of the PSFs estimate for sample 3. From Figure 4.16(c), it can be noticed that the estimated 1-D PSFs fit the reference (i.e., Blue) closely.

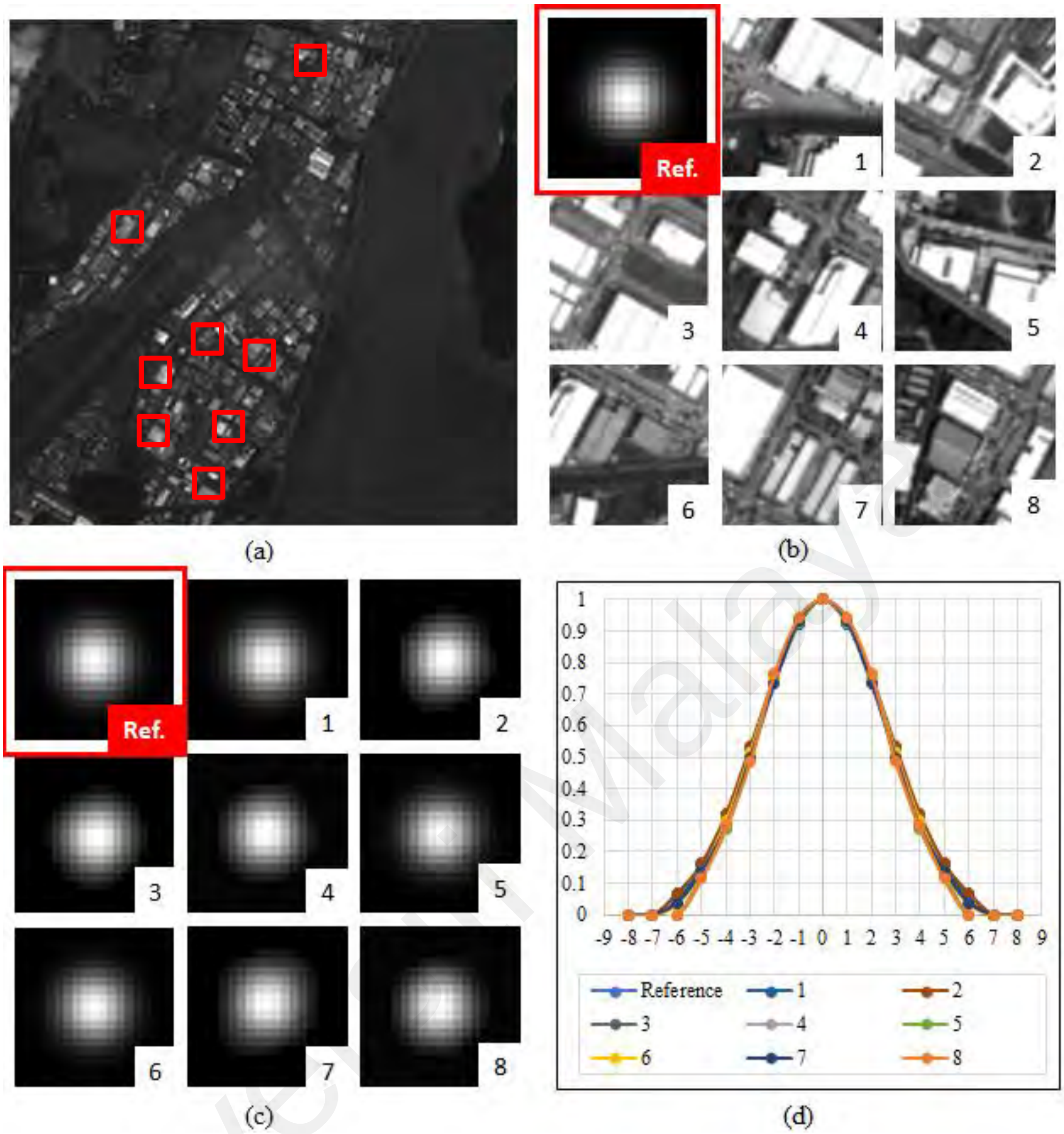

Figure 4.16: PSF estimation for sample 3 with Gaussian blur, σ = 4. (a) The main scene (i.e., Sample 3), (b) Selected candidates$_{1,2..8}$ (i.e., datasets), (c) g 2-D PSF$_{1,2..8}$ estimate correspond to (b), and (d) The corresponding 1-D PSF$_{1,2..8}$ distribution of (c) with relative to the reference (i.e., ground truth).

In the second analysis, experiments on the real satellite images with unknown blur are conducted in this work. The results are presented for three data samples from three different scenes. The observed images used in this analysis are as shown in Figure 4.17. Each sample is the segmented sub-images from the main scene with 4096× 4096 pixel size. Table 4.6 shows the experimental results of the three samples.

(a) (b) (c)

Figure 4.17: Sample of the RazakSAT satellite images used in the second analysis

The results from Table 4.6 show the average FWHM of PSF for the scene from Figures. 4.17(a)-4.17(c) is relatively close, with a relative SD of 0.95%. The MTFs value at the Nyquist frequency for Sample-4, Sample-5, and Sample-6 is within the range of 0.061 to 0.084, 0.061 to 0.086, and 0.065 to 0.087, respectively. These results demonstrated that the proposed method can provide high precision data. From Figure 4.17, it can be observed that Figure 4.17(a) has the most urban area, while Figure 4.17(b) has more cloud coverage and a less urban area. This is because salient edges are easier to find in the urban area and so this type of scene usually provides more selection of reliable structures. In particular, as the number of reliable structures increases, the SD of MTF and FWHM decreases, conversely, when the relative SD decreases, the confidence level of results increases.

Based on the analyses, it is evident that the proposed segmentation method for ideal structure selection is able to deliver reliable candidates to estimate the MTF for the observed image.

Table 4.6: The estimated MTF_{Nyq} results of 3 different Samples

Dataset	Sample-4		Sample-5		Sample-6	
	FWHM	MTF_{Nyq}	FWHM	MTF_{Nyq}	FWHM	MTF_{Nyq}
1	2.76	0.061	2.99	0.073	3.05	0.072
2	2.96	0.065	2.67	0.062	2.77	0.086
3	2.77	0.068	2.75	0.079	2.70	0.076
4	2.78	0.066	2.78	0.086	2.66	0.079
5	2.96	0.070	2.92	0.080	2.72	0.065
6	2.75	0.071	2.64	0.073	2.94	0.071
7	2.64	0.084	2.99	0.086	2.70	0.068
8	2.89	0.067	2.61	0.061	2.66	0.076
9	2.84	0.070	3.28	0.085	3.10	0.087
10	3.05	0.066	3.05	0.077	2.83	0.084
Average	2.84		2.87		2.81	
SD (SD)	0.12	0.006	0.22	0.009	0.16	0.008
Relative SD (%)	**4.1**		**7.5**		**5.9**	

4.4.4 Experiments on Synthetically Blurred Satellite Images

In this experiment, the accuracy of the proposed method is assessed by measuring the FWHM relative error of the estimated PSF for both scan directions. To this end, this work experiments with four groups of the sample which are generated synthetically using the incremental blur SD σ from 1 to 4. Table 4.7 presents the experimental results obtained by the proposed method. These results indicate that the algorithm is capable of producing acceptable results with average relative error as low as ±0.2 and with the highest relative error of ±5.3. It can be noted that the errors are relatively larger for smaller blurs (i.e. σ = 1).

Table 4.7: The measured FWHM value from four different scales of blur

Scan Direction	**Across-scan**		**Along-scan**		**Across-scan**		**Along-scan**	
Sample	FWHM (pixel)	Relative Error (%)	FWHM (pixel)	Relative Error (%)	FWHM (pixel)	Relative Error (%)	FWHM (pixel)	Relative Error (%)
	Gaussian blur, σ = 1, FWHM of Ground truth = 2.45 pixel				Gaussian blur, σ = 2, FWHM of Ground truth = **4.76** pixel			
Penang1	2.60	6.0	2.60	5.9	5.03	5.8	4.86	2.1
Penang2	2.59	5.5	2.57	4.9	4.81	1.2	4.83	1.5
Penang 3	2.52	2.8	2.56	3.8	4.76	0.1	4.82	1.3
Penang 4	2.65	8.1	2.68	9.5	4.83	1.5	4.85	2.0
Penang 5	2.57	4.9	2.56	4.2	4.83	1.6	4.89	2.8
Penang 6	2.49	1.5	2.52	2.8	4.95	4.0	4.87	2.4
Penang 7	2.54	3.6	2.50	1.8	4.93	3.8	4.76	0.1
Penang 8	2.66	8.6	2.56	4.3	4.93	3.6	4.78	0.5
Penang 9	2.70	10	2.65	8.2	4.95	3.9	4.89	2.9
Penang 10	2.52	2.7	2.52	2.8	4.84	1.7	4.80	1.0
Average	**2.59**	**5.3**	**2.58**	**4.8**	**4.89**	**2.7**	**4.84**	**1.6**
	Gaussian blur, σ = 3, FWHM of Ground truth = **7.09** pixel				Gaussian blur, σ = 4, FWHM of Ground truth = **9.43** pixel			
Penang1	7.26	2.4	7.11	0.2	9.43	-0.02%	9.23	-2.1
Penang2	7.05	-0.5	7.13	0.5	9.56	1.33%	9.38	-0.7
Penang 3	7.21	1.6	7.41	4.5	9.18	-2.72%	9.45	0.2
Penang 4	7.42	4.6	7.27	2.4	9.41	-0.28%	9.61	1.8
Penang 5	7.06	-0.4	7.14	0.7	9.37	-0.81%	9.82	4.0
Penang 6	7.08	-0.2	7.27	2.6	9.72	3.09%	9.42	-0.1
Penang 7	7.08	-0.2	7.27	2.6	9.73	3.11%	9.44	0.1
Penang 8	7.26	2.4	7.11	0.2	9.58	1.59%	9.40	-0.4
Penang 9	7.55	6.5	7.55	6.5	9.42	-0.19%	9.40	-0.4
Penang 10	7.35	3.6	7.23	1.9	9.31	-1.32%	9.05	-4.0
Average	**7.22**	**2.0**	**7.25**	**2.2**	**9.47**	**0.4%**	**9.42**	**-0.2**

4.4.5 Experiments on Real Satellite Images with Unknown Blur

For this experiment, the MTF value at the Nyquist frequency is calculated, where the along-scan and across-scan components are averaged. To validate the proposed MTF measurement method on real satellite images from RazakSAT, the MTFs value obtained from the proposed method is compared with the well-established edge method by Kohm (2004). For this experiment, this work presents one sample of real unknown blur satellite images with 4096 × 4096 pixel size and split it into 256 sub-images with a size of 256 × 256 pixels. The search for the ideal candidates with knife-edge features from the 256 sub-images is conducted manually. After some tedious search, six potential sub-images were eventually found. This work applied both methods to these sub-images and found out only 3 sub-images can be processed by the Edge method (Kohm, 2004), while the proposed method is able to derive the MTF value at the Nyquist frequency for all the sub-images. The MTF value at the Nyquist frequency from these experiments is tabulated in Table 4.8, where MTF_{Nyq} represents the MTF at the Nyquist frequency and RE_{Nyq} represents the relative error of both methods at the Nyquist frequency. The MTF plot results are shown in Figure 4.18.

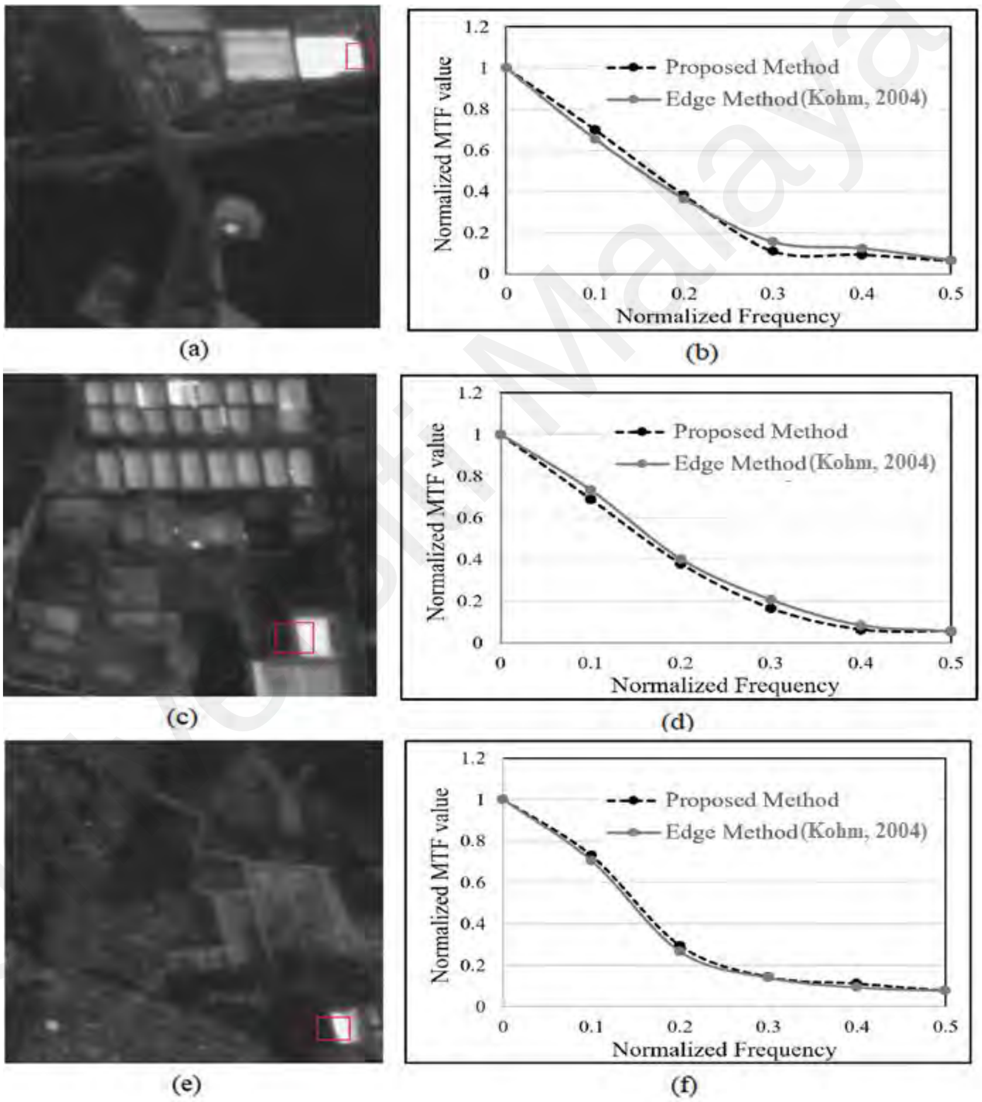

Figure 4.18: A comparison of the model verification using the edge method and the proposed method (Kohm, 2004). (left) Sample image. (right) Respective MTF plot. Red box = ideal candidate for the Edge Method (Kohm, 2004).

Table 4.8: Comparison between the proposed method and the Edge method (Kohm, 2004)

	Data-1	Data-2	Data-3
MTF_{Nyq} from Edge Method (Kohm, 2004)	0.0541	0.0758	0.0637
MTF_{Nyq} from proposed Method	0.0553	0.0767	0.0650
RE_{Nyq} between two methods	2.3%	1.2%	2.1%

From Figure 4.18 and Table 4.8, it can be observed that the MTFs of both methods are very close. The MTFs value from this proposed method is larger than the edge method at the Nyquist frequency. The relative errors at the Nyquist frequency between the two methods are also very small and within the range of 1.2 to 2.3%.

As explained in Subsection 2.2.1, there are a few criteria to determine the ideal candidate from an observed image using the Edge method. Figures 4.19(a) to 4.19(c) show examples of potential candidates for the MTF measurement using manual search.

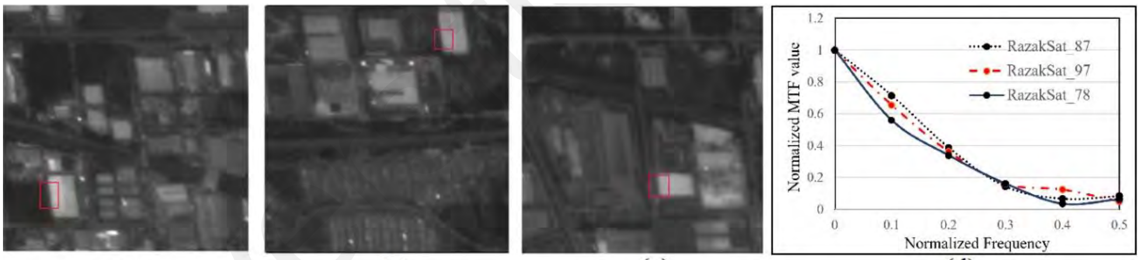

(a) (b) (c) (d)

Figure 4.19: The experiment results in low-contrast real satellite images with unknown blur. Red box = potential candidate but not ideal for the method by Kohm (2004).

Based on the visual observation, even though these candidates possess natural characteristic targets such as edge target, but they do not meet certain criteria such as noise and contrast level. Therefore, it failed to estimate the MTF value of the images. According to Helder et al. (2006), the contrast level of the target divided by the target's noise SD should be greater than 50. On the contrary, the proposed method is based on the structural component of an image, thus it does not require to meet such stringent criteria as imposed by the Edge method. Figure 4.19(d) shows the MTFs plot results from the proposed method for sub-image Figures. 4.19(a)-4.19(c). It can be visualized that the MTFs plot for these images are relatively close.

Figure 4.20 shows a few more experiment results of real unknown blur satellite images produce by the proposed method. The rest of the experiment results are available in Appendix A.

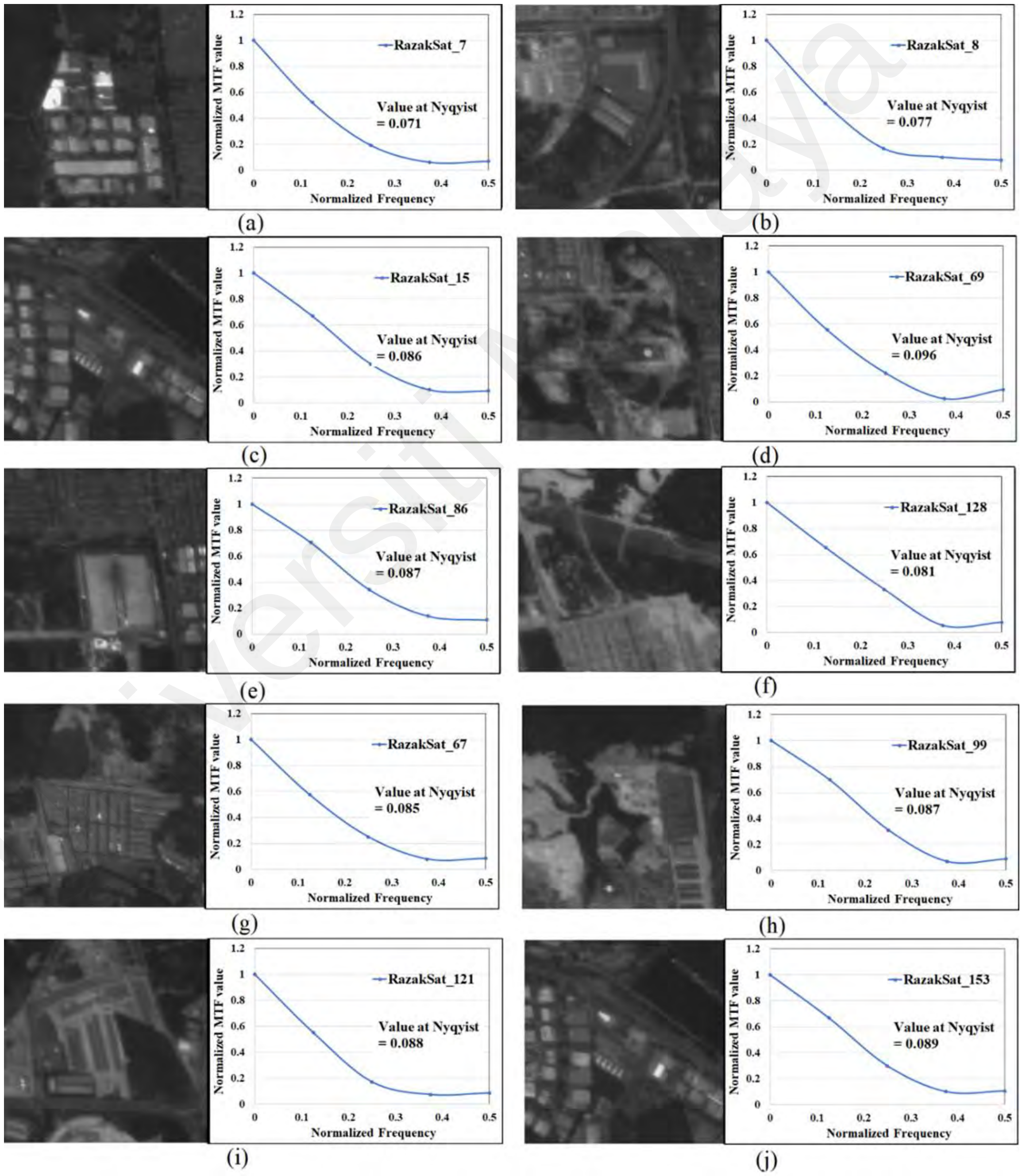

Figure 4.20: MTF profile of real unknown blur satellite images (RazakSAT) by the proposed method.

The MTF value at the Nyquist frequency for each sample is tabulated in Table 4.9. These experimental results show that the degradation function of the RazakSAT imaging system is non-linear and spatially variant. It means the PSF changes with the spatial position of the pixels. This makes sense because the spatial properties of a scene can be modified or distorted due to defocus and motion blur effects from the imaging chain process. From Table. 4.9, the estimated MTF_{Nyq} values of the sub-images are between 0.071 to 0.096, and the average MTF_{Nyq} value is 0.084. The average MTF value obtained from the proposed method suggests that the RazakSAT Satellite's imaging system has the ability to resolve 8.4% of the object contrast to the image at Nyquist frequency. This result shows that the MTF measurement from the proposed method is consistent with the MTF specification published by (ATSB, 2010). Also, this experiment demonstrates the robustness of the proposed method for spatial characterisation and its suitability for MTF measurement of optical satellite images with low spatial resolution.

Table 4.9: MTF estimate of real unknown blur satellite images by the proposed method.

Sample	MTF_{Nyq} from proposed Method
RazakSAT_7	0.071
RazakSAT_8	0.077
RazakSAT_15	0.086
RazakSAT_67	0.085
RazakSAT_69	0.096
RazakSAT_86	0.087
RazakSAT_99	0.088
RazakSAT_121	0.088
RazakSAT_128	0.081
RazakSAT_153	0.089
Average	0.0845
SD	0.007

4.5 Conclusion

This chapter proposed a robust MTF measurement method based on the nonlocal self-similarity characteristics, namely the structural component of optical satellite images. The novelty of this method is twofold, first is the introduction of a segmentation method that automatically identifies the ideal candidates for MTF measurement; second, an adaptive structure selection method that finds reliable structures effectively for MTF measurement. In addition, the proposed method is able to overcome the hassle of manual identification and dependency on the presence of a well-separated characteristic target, which shows that it is a convenient approach. Experimental results were conducted using the synthetically blurred and real satellite images. It showed that the relative SD of the Nyquist frequency between the well-established edge method and the proposed method is < 2.3%. These indicate that the proposed MTF measurement method can accurately predict the imaging system's performance and the degradation function for image restoration. Also, the computation time for the MTF measurement of a real satellite image only takes about 3 min. Based on the experimental results, in summary, it can be reckoned that the proposed MTF measurement method is effective and practical for on-orbit spatial characterisation.

CHAPTER 5: RESTORATION OF SPATIALLY BLURRED OPTICAL SATELLITE IMAGES

This chapter continues to analyze and evaluate the proposed MTF measurement algorithms from Chapter 4 experimentally as a blur kernel estimation method for spatially blurred optical satellite image restoration. Over the years, numerous prior-based kernel estimation algorithms have been proposed to restore latent sharp images under spatial invariant or varying blur. However, these algorithms are mainly evaluated for natural images. It is thus unclear how these algorithms perform on optical satellite images, especially for other types of blur besides Gaussian blur. To this end, this chapter presents a perceptual study and analysis of blind single image restoration, particularly in blur kernel estimation that utilizes the principle of sparse representation, to gain further understanding of image priors that appropriate for blur removal in optical satellite images. The datasets for this work comprise synthetically blurred satellite images and real satellite images with unknown blur. Using these datasets, a comparative study is conducted on various sparse representation methods from some viewpoints, including their motivations, mathematical representations, and the main algorithms. The evaluation and analysis indicate the need for an efficient and robust sparse representation method in single optical satellite image blind deblurring.

5.1 Introduction

Blur is the deterministic component of the image degradation model, which is generally assumed to be a linear Spatially-invariant with Gaussian-like shape in passive remote sensing imaging. However, in a real-world situation, it is mostly non-linear and spatially varying (Holst, 2017; Gonzalez & Woods, 2017). As was mentioned in Chapter 2, based on the sources, there are three groups of blurs. For sources of blur such as lens blur, their point spread function (PSF) can be approximated through a parametric model (e.g., disk, Gaussian) that characterized by a single parameter indicating its scale (e.g., radius, standard deviation (SD), etc.); whereas, for other situations such as motion blur and environmental blur, the PSF can have a somewhat arbitrary form with a high degree of freedom, which makes its measurement quite challenging.

Over the years, there are a large number of published studies on deblurring spatial varying blur (e.g., Levin et al., 2007; Zhu, Cohen, Schiller, & Milanfar, 2013; Cheong, Chae, Lee, Jo, & Paik, 2015; Zhang, Wang, Jiang, Wang, & Gao, 2018) or Spatially-invariant blur (e.g., Cho & Lee, 2009; Xu et al., 2013; Zhang, J., et al. 2014; Tang et al., 2018; Cao, He, Zhao, Lu, & Zhou, 2018) problems using image statistic priors. Based on the literature, this thesis identifies few issues: (1) Even though there is abundant work on prior-based image deblurring, there is a notable paucity of studies that seek to identify the most suitable prior in optical satellite image deblurring application; (2) Most of the works concentrate on one group of blur only (i.e., Gaussian blur), whereby in a real situation of passive remote sensing imaging, challenging imaging conditions as described in Subsection 2.3 which are adversely affected the quality of the acquired imagery; and (3) While many of the proposed algorithms (e.g., Ma et al, 2017; Zha et al.2018; Gong et al. 2018) are effective, they usually suffer from computational complexity due to the implication of heavy mathematical baggage implicated to carry out the task.

Currently, sparse representation methods have become one of the main streams of research on image restoration, since it provides data-authentic priors in the kernel estimation, where it can guide the intermediate latent image restoration and thus facilitate blur kernel estimation. The concept of sparse representation has its roots in compressed sensing (CS). The original theory of CS coined by Donoho (2006) suggests that if a signal is sparse or compressive the original signal can be reconstructed by exploiting a few measured values. The rationale of CS theory has been demonstrated by Candès et al.

(2006) from the mathematical perspective. Motivated by the concept of sparse representation, a new approach for MTF measurement was developed in Chapter 4; for which it utilizes the merit of sparsity properties in an image with an improved ℓ_2-norm TV model to ensure extraction of salient edge, thus become a sparsity prior for PSF kernel estimation. In Chapter 4, the proposed MTF measurement method was shown to be effective and practical for on-orbit spatial characterisation. However, it has not been evaluated for its effectiveness and robustness in blind image restoration, particularly for optical satellite images. As mentioned in Section 1, knowledge of the MTF for a given image acquisition system is not only important for imaging performance assessment but also can be utilized as an image degradation function in blind image restoration techniques for spatial image quality improvement. Subsequently, this chapter evaluates its performance and conducts a comparative study of blind single image restoration, particularly in blur kernel estimation that utilizes the principle of sparse representation; to gain further understanding of image priors that appropriate for blur removal in optical satellite images regardless of the blur type. To carry the task, this thesis develops and examines two advanced image priors that use sparse representation algorithms, namely the low-rank priors and graph-based priors. This thesis studies their significance in blur kernel estimation and validates the viewpoint that complex formulations are generally assumed to produce restoration results more effectively. Furthermore, two non-blind image deconvolution (ID) methods were employed for image restoration and show that with a proper estimation rule, blind image restoration can be performed even with a simple prior.

In this work, the aim is not to propose a new low-rank and graph-based prior blur kernel estimation method. Instead, the low-rank and graph-based priors blur kernel estimation methods were developed according to Ren et al. (2016) and Bai et al. (2019), respectively; the aim is to gain in-depth knowledge about these image priors for future works in optical satellite images restoration. In recent works, studies found that the combination of the sparsity and the self-similarity properties of natural images are usually achieved better performance (Zhang, J., et al. 2014; Yu, Chang, & Xiao, 2019; Wu, Wang, Kong, & Yin, 2016). Therefore, the rationale for choosing the low-rank and graph-based priors method is because they are among the recent successful existing image deblurring method that advanced the sparse representation and the self-similarity properties of natural images, and they have been applied successfully to both Spatially-invariant and varying blur images. Besides, although the low-rank approximation has been widely applied to image restoration, it is still unclear whether it is able to help blind deblurring and how it affects the blur kernel estimation.

The remainder of the chapter is organized as follows. In Section 5.2, this work first describes the enhanced low-rank priors blur estimation method of Ren et al. (2016), later the Graph-based priors blur estimation method of Bai et al. (2019), and finally, it presents the overall algorithm of the proposed sparsity priors blur estimation method. Next, Section 5.3 briefly introduces the non-blind ID methods that were employed for the comparative study of the aforementioned blur estimation methods. Section 5.4 presents analysis and experimental evaluations. Furthermore, this work provides more discussion including the limitation of the proposed blur estimation method in Section 5.5. Finally, section 5.6 provides the conclusion of this work.

5.2 Blur Kernel Estimation

As aforementioned in the introduction, for an effective comparative study in the blind single image restoration, the priori blur estimation methods will be used, in which the PSF (i.e., blur kernel) will be identified separately from the observed image as a preprocessing step using three different blur estimation methods: (1) sparsity prior with improved ℓ_2-norm TV model that was proposed in Chapter 4, (2) Graph-based priors using reweighted Graph Total Variation (RGTV) Model (Bai et al., 2019), and (3) enhanced Low-rank priors using low-rank matrix approximation (LRMA) method (Ren et al., 2016). Since the related works for LRMA and RGTV have been discussed in Subsection 3.2.1, hence, in this section, this work focuses on the philosophy of these methods.

5.2.1 Low-rank Prior

Let us again recall the vector-matrix form of the image degradation model in Equation (4.5). Here, the observed blurry image, latent sharp image, and the corresponding blur kernel are expressed as $b, l,$ and k, respectively. The degradation process is modeled as

$$b = l \otimes k + \eta. \tag{5.1}$$

Suppose there is a matrix of degraded image patches, Y. The latent low-rank matrix $\hat{X}$ can be estimated from Y using the following nuclear norm minimization (NNM) problem.

$$\hat{X} = \min_{X} \|Y - X\|_F^2 + \ddot{\lambda}\|X\|_*. \tag{5.2}$$

where $\ddot{\lambda}$ is a threshold and $\|X\|_*$ is the nuclear norm of matrix M, which is the sum of its singular values. The $\| \quad \|_F^2$ denotes the Frobenius norm.

The rank of a data matrix X counts the number of non-zero singular values of it, which is nondeterministic polynomial time (NP)-hard to minimize. Alternatively, the nuclear norm of X, defined as the ℓ_1-norm of its singular values -the formula is a convex relaxation of matrix rank function. The low-rankness of X can be viewed as a two-dimensional (2-D) sparsity prior. It encodes the input 2-D data matrix over a set of rank-1 basis matrices and assumes its singular values to be sparsely distributed, which means it has only a few non-zero or significant singular values.

The NNM has one distinct advantage, where it lies in the tightest convex relaxation of the original rank minimization problem with certain data fidelity terms. However, Candés and Recht (2009) proved that most low-rank matrices can be perfectly recovered by solving an NNM problem. Besides, Cai, Candés, and Sheng (2010) also proved that the NNM based low-rank matrix approximation problem with F-norm data fidelity can be easily solved by a singular value thresholding (SVT) model. However, although the NNM has a closed-form solution with a good theoretical guarantee by the SVT model (Cai et al., 2010), it tends to over-shrink the singular values (i.e., rank components) equally by the threshold λ, ignoring the different significances of matrix singular values. Therefore, it achieves unsatisfactory accuracy for approximating the matrix rank. For that reason, Gu et al. (2013) propose a weighted nuclear norm minimization (WNNM) model that can be expressed as

$$\hat{X} = \min_{X} \|Y - X\|_F^2 + \lambda \|X\|_{w,*}. \tag{5.3}$$

where $\|X\|_{w,*} = \sum_i \|w_i \sigma_i(X)\|_1$is the weighted nuclear norm. In this model, larger singular values are shrunk less, and smaller singular values are shrunk more to preserve the major data components, thereby making this model flexible for dealing with numerous problems. Later, Dong, W. et al. (2013) propose a powerful image model in the patch space that connects low-rank methods with simultaneous sparse coding (Mairal, 2009). In this model, they demonstrate a relationship between singular values of a data matrix (likelihood term) and pseudo-metric norm $\|A\|_{1,2}$ (prior term) in simultaneous sparse coding resulted in a novel interpretation of singular value decomposition (SVD) from a bilateral variance estimation perspective. Besides Dong, W. et al. (2013), another notable work that provides connection among the sparse representation, nonlocal self-similarity, and low-rank matrix approximation is that of Wang, S. et al. (2013). Inspired by the works of Dong, W. et al. (2013) and Wang, S. et al, (2013), Pan et al. (2014) also employed low-rank prior in their image restoration model. Different from the two previous works that used the image priors to restore images, they use it for edge preservation in the kernel estimation process. Recently, Ren et al. (2016) pointed out that the WNNM model in Equation (5.3) can be used to deblur an image to a certain degree using any kernel information. In contrast to the WNNM model by Gu et al. (2013), where a weighting scheme is designed specifically for denoising, they proposed an algorithm to estimate weights for deblurring. In their works, they showed that low-rank properties of both intensity and gradient images can be exploited for effective deblurring.

5.2.1.1 General formulation

Generally, the deblurring problem based on LRMA can be formulated under the framework of Bayesian inference. One common model is the maximum a posteriori (MAP) framework (e.g., Dong, J. et al. 2017; Wang et al., 2012; Ren et al., 2016) which is defined as

$$\{\hat{l}, \hat{k}\} = \min_{l,k} p(l, k|b) = \min_{l,k} p(b|l, k)p(k)p(l), \tag{5.4}$$

where $p(k)$ and $p(l)$ are the priors of the blur kernel and latent sharp image, respectively. By taking the negative log-likelihood of Equation (5.4), then Equation (5.4) can be rewritten as,

$$\{\hat{l}, \hat{k}\} = \min_{l,k} p(l \otimes k, b) + \mu_1 \Psi(k) + \mu_2 \Psi(l) \tag{5.5}$$

where the first, second, and third term denotes the data fidelity function, kernel prior, and image prior function, respectively.

The objective functions are typically formulated based on the intended application. For this comparative study, the interest is to examine a low-level vision application such as image deblurring that utilizes the benefits among the sparse representation, nonlocal self-similarity, and low-rank matrix approximation. For instance, the works by Ren et. al. (2016), where they used the nonlocal self-similarity of both intensity and gradient patches based on low-rank prior for blind image deblurring. Gu et al. (2013) have shown that a better approximation of prior function can be obtained by assigning different weights on different singular values in the LRMA process. Hence, the image prior function in Equation (5.5) can be formulated as

$$\varphi(l) = \sum_i \|l_i\|_{w,*} + \frac{\sigma}{\lambda}\sum_i \|\nabla l_i\|_{w,*}. \tag{5.6}$$

where $\nabla = (\nabla_h, \nabla_v)^T$ denotes the image gradient operator. The l_i and ∇l_idenotes the matrices stacked by the nonlocal similar image and gradient patches with low-rank property, respectively. According to Ren et al. (2016), the w should be inversely proportional to the singular values of l_i and ∇l_i. Thus the objective function for a single image blind deblurring model based on enhanced prior (i.e., sparse nonlocal low-rank prior) can be expressed as

$$\{\hat{l}, \hat{k}\} = \min_{l,k} \| l \otimes k - b\|_1 + \gamma\|k\|_2^2 + \lambda \sum_i \|l_i\|_{w,*} + \frac{\sigma}{\lambda} \sum_i \|\nabla l_i\|_{w,*}. \tag{5.7}$$

subject to $k_i \geq 0$ and $\sum_i k_i = 1$.

5.2.1.2 Optimization

In order to solve Equation (5.7) efficiently, similar to most single image deblurring problems, the alternating minimization based on half-quadratic splitting is adopted. That is, to separate the intermediate latent images and blur kernels estimation into subproblems, then estimate the subproblems alternatively by assuming one of them is known in the ℓ_2-norm minimization, Equation (5.7), thus becomes

$$\hat{l} = \min_l \| l \otimes k - b\|_2^2 + \lambda \sum_i \|l_i\|_{w,*} + \frac{\sigma}{\lambda}\sum_i \|\nabla l_i\|_{w,*}. \tag{5.8}$$

$$\hat{k} = \min_k \| l \otimes k - b\|_1 + \gamma\|k\|_2^2. \tag{5.9}$$

where the tasks in Equations (5.7) and (5.8) are to update the latent images and estimate the blur kernel, respectively, in a multi-scale blind deconvolution approach (Fergus et al., 2008).

Updating the latent images: Similar to the proposed methods in Chapter 4, new auxiliary variables d, p, and g are introduced to solve the Equation (5.8), thus become

$$\hat{l} = \min_l \| l \otimes k - b - d\|_2^2 + \beta\|l - p\|_2^2 + \tau\|\nabla l - g\|_2^2 + n\|d\|_1 + \tag{5.10}$$

$$\lambda \sum_i \|l_i\|_{w,*} + \frac{\sigma}{\lambda} \sum_i \|\nabla l_i\|_{w,*}.$$

where n, β, and τ are positive parameters. Using the half-quadratic splitting technique (Xu et al., 2011), the optimization problem in Equation (5.10) can be divided into four subproblems, each designed to solve *l*, *d*, *p*, and g, separately.

Subproblem *l*: to solve *l*, the energy function in Equation (5.10) becomes,

$$l = \min_l \| l \otimes k - b - d\|_2^2 + \beta\|l - p\|_2^2 + \tau\|\nabla l - g\|_2^2. \tag{5.11}$$

which is a least squared problem that can be solved efficiently using the FFT, according to Parseval's theorem.

$$l = \mathcal{F}^{-1}\left(\frac{\mathcal{F}(b+d)^{\circ}\overline{\mathcal{F}(k)} + \beta\mathcal{F}(\mathrm{p}) + \tau\mathcal{F}_g}{\mathcal{F}(k)^{\circ}\overline{\mathcal{F}(k)} + \tau\mathcal{F}(\nabla)^{\circ}\overline{\mathcal{F}(\nabla)}}\right), \tag{5.12}$$

where $\mathcal{F}(.)$ and $\mathcal{F}^{-1}(.)$ denote the FFT and inverse FFT, respectively; and $\overline{\mathcal{F}(.)}$ is the complex conjugate operator.

Subproblem *d*: since closed-form solution is available to solve subproblem *d*, given *l*, the *d* can be computed by one-dimensional shrinkage operator as

$$d = sign(l \otimes k - b)\max\left(\|l \otimes k - b\| - n, 0\right). \tag{5.13}$$

Subproblems *p* and *g*: The subproblems with respect to p and g can each be estimated by solving

$$\hat{p} = \min_p \beta\|l - p\|_2^2 + \lambda \sum_i \|p_i\|_{w,*}, \tag{5.14}$$

and

$$\hat{g} = \min_g \beta\|\nabla l - g\|_2^2 + \sigma \sum_i \|g_i\|_{w,*}. \tag{5.15}$$

According to Gu et al. (2013), Equations (5.14) and (5.15) can be solved efficiently by the WNNM, and the weight vector w in these equations can be defined as

$$w_j = 2\sqrt{2m}/(\sigma_j(.) + \epsilon). \tag{5.16}$$

where m is the number of column of the matrix l_i or ∇l_i (i.e., the selected number of similar patches), $\sigma_j(.)$ denotes $\sigma_j(l_i)$ and $\sigma_j(\nabla l_i)$ for Equation (5.14) and (5.15), respectively. In Equation (5.16), $\sigma_j(l_i)$ is the j^{th} singular value of l_i, whereas $\sigma_j(\nabla l_i)$ is the j^{th} singular value of ∇l_i, and ϵ is an infinitely small number. With the well-defined weight vector w, the singular values of $\widehat{l_i}$ shrunk by the generalized soft-thresholding operator $S_w(\Sigma)_{ii}$,

$$S_w(\Sigma)_{ii} = \max\left(\Sigma_{ii} - w_j, 0\right). \tag{5.17}$$

The proposed weight vector w and the soft-thresholding operator $S_w(\Sigma)_{ii}$ in Equation (5.17) play an important role in eliminating the texture details and tiny edges while maintaining the main fine structures in blurry images.

Estimating Blur Kernels: In Ren et al. (2016), the Equation (5.9) was solved using the fast deblurring of Cho and Lee (2009) based on on the gradient images and ℓ_2-norm of data fidelity function,

$$\hat{k} = \min_k \| \nabla l \otimes k - \nabla b\|_2^2 + \tau\|k\|_2^2. \tag{5.18}$$

As it is a least-squares minimization problem with Tikhonov regularization, therefore it leads to a closed-form solution for k.

$$\hat{k} = \mathcal{F}^{-1}\left(\frac{\mathcal{F}(\nabla \mathrm{b})^{\circ}\overline{\mathcal{F}(\nabla l)}}{\mathcal{F}(\nabla l)^{\circ}\overline{\mathcal{F}(\nabla l) + \gamma}}\right), \tag{5.19}$$

5.2.1.3 Algorithms

The overall algorithm of the enhanced low-rank prior based on LRMA for estimating the blur kernel k is shown in Algorithm 5.1.

Algorithm 5.1: Deblurring by Enhanced Low-Rank Prior (Ren et al., 2016)

Input: Blurry image b and kernel size $m \times m$

Downsample the observed blurry image b to generate the image pyramid $\{b_0, b_1, \ldots, b_n\}$

Estimate the blur kernels $\hat{k}_i$ and latent images $\hat{l}_i$ $(i = 1, 2, \ldots, n)$ in the intermediate layers using Xu et al. (2012) and output $\hat{k}_i$

Upsample $\hat{k}_i$ to generate initial blur kernel k_0 for full resolution image b_0

for $j = 1, 2, \ldots 5$ do

  solve d by minimizing Equation (5.13)

  $\beta \leftarrow 2\sigma$

  repeat

    solve p by minimizing Equation (5.14)

    $\tau \leftarrow 2\lambda$

    repeat

      solve g by minimizing Equation (5.15)

      solve *l* by minimizing Equation (5.12)

      $\tau \leftarrow 3\tau$

    until $\tau > \tau_{max}$

    $\beta \leftarrow 2\beta$

  until $\beta > \beta_{max}$

  Solve blur kernel k by Equation (5.19)

  $\lambda \leftarrow 0.9\lambda, \sigma \rightarrow 0.9\sigma$

end for

Output: Blur kernel k.

5.2.2 Graph-based Prior

Owing to Graph signal processing (GSP), a new type of image priors based on an adapted nonlocal graph has emerged (Peyŕe, 2008). In image processing, recently, there has been a surge of interest in graph-based filtering methods that build on nonlocal and semi-local graphs (i.e., weighted edge) to connect the pixels of the image based on their physical proximity as graph signals to solve the inverse problem (Hu et al., 2016; Pang & Cheung, 2017; Kheradmand & Milanfar, 2014; Liu et al., 2017; Bai et al. 2019). Of particular interest here is the reweighted graph total variation (RGTV) type of graph-based prior. Most recently, Bai et al. (2019) argued that a skeleton image, which is a PWS proxy is sufficient to estimate the blur kernel. Since the edge weights of a graph for the skeleton image patch have a unique bi-modal distribution, they inspired to propose an RGTV prior in promoting the desirable bi-modal distribution given a blurry patch. Furthermore, they introduced a graph weight function so that the RGTV can be expressed as a graph ℓ_1-Laplacian regularizer, for which the prior can then be interpreted as a low-pass graph filter with desirable spectral properties.

According to the GSP concepts of Peyŕe (2008), signals on a weighted directed graph $\ddot{G} = (V, E, w)$ consist of a finite nonempty set V of vertices (i.e., image pixels), a finite set $E \subset V \times V$ of M edges, and $w: E \rightarrow \mathbb{R}$ is a weight function, where each edge $M(i, j) \in E$ is undirected with a corresponding weight w_{ij} that describes the strength of connection from nodes i and j. Here, the weight is computed using a Gaussian kernel (Shuman et al., 2013) as follows

$$[W]_{i,j} = w_{i,j} = exp\left(-\frac{\|l_i - l_j\|^2}{\sigma^2}\right), \tag{5.20}$$

where $\boldsymbol{W}$ is an adjacency matrix of size $M \times M$, l_i and l_j are the intensity values at pixels i and j of the image l, and σ is a parameter. $0 \leq w_{i,j} \leq 1$ and the larger $w_{i,j}$ is, the higher the connection strength (i.e., similarity) of the nodes i and j are to each other.

Given the adjacency matrix $\boldsymbol{W}$, a combinatorial graph Laplacian matrix $\boldsymbol{L}$ is a symmetric matrix defined as:

$$\boldsymbol{L} \triangleq diag(\boldsymbol{W}\mathbf{1}) - \boldsymbol{W} \tag{5.21}$$

where 1 is a vector of all 1's. diag(·) is an operator constructing a square diagonal matrix with the elements of the input vector on the main diagonal.

Based on Spectral Theorem, the symmetric matrix $\boldsymbol{L}$ in Equation (5.21) can have an orthogonal matrix $\boldsymbol{U}$ that diagonalizes $\boldsymbol{L}$, such that it becomes

$$\boldsymbol{L} = \boldsymbol{U\Lambda U^T} \tag{5.22}$$

where $\boldsymbol{\Lambda}$ is a diagonal matrix containing eigenvalues $\lambda_k, k \in \{1, \dots, N\}$. Each column u_k in $\boldsymbol{U}$ is an eigenvector corresponding to λ_k. Given $w_{i,j}$ is non-negative from Equation (5.20) and $\boldsymbol{L}$ is a positive semi-definite (PSD) matrix, therefore, $\lambda_k \geq 0$ for each *k* and $l^T L l \geq 0$ for the arbitrary graph signal *l*. In Bai et al., (2009), the authors adopted the idea of Shuman et al., (2013), where they interpreted the non-negative eigenvalues λ_k of GSP as *graph frequencies* and corresponding eigenvectors in $\boldsymbol{U}$ as graph *frequency components*. Here, together, they (i.e., *graph frequencies* and *frequency components*) define the graph spectrum for graph G.

Skeleton Image and its Bi-modal Weight Distribution: Instead of using a structure extracted image (Xu et al., 2012) or an edge-aware smoothed image (Xu et al., 2011), Bai et al. (2019) proposed a skeleton image (i.e., PWS version of the observed image) as a proxy for the blind image deblurring problem. Figure 5.1(c) illustrates an example of a skeleton image proposed by Bai et al., (2019). In Figure 5.1, it can be noticed the skeleton image retains the strong gradients in a natural image but smooths out the minor details.

To show the significance of the proposed skeleton image and its bi-modal distribution, Bai et al. (2019) construct a fully connected graph for each of three representative local patches highlighted in Figures 5.1(d), 5.1(e), and 5.1(f) and compute its respective edge weight $w_{i,j}$ using Equation (5.18) to examine its edge weight distribution. The edge weight distributions of these patches are as illustrated in Figures 5.1(g), 5.1(h), and 5.1(i). The *x*-axis of the histogram is the discrete inter-pixel difference $d = |l_i - l_j|$ for edge weight $w_{i,j}$, whereas the y-axis shows fractions of weights of a given d for different image patches. Note that the edge weight $w_{i,j}$ in Equation (5.20) is a monotonically decreasing function of d.

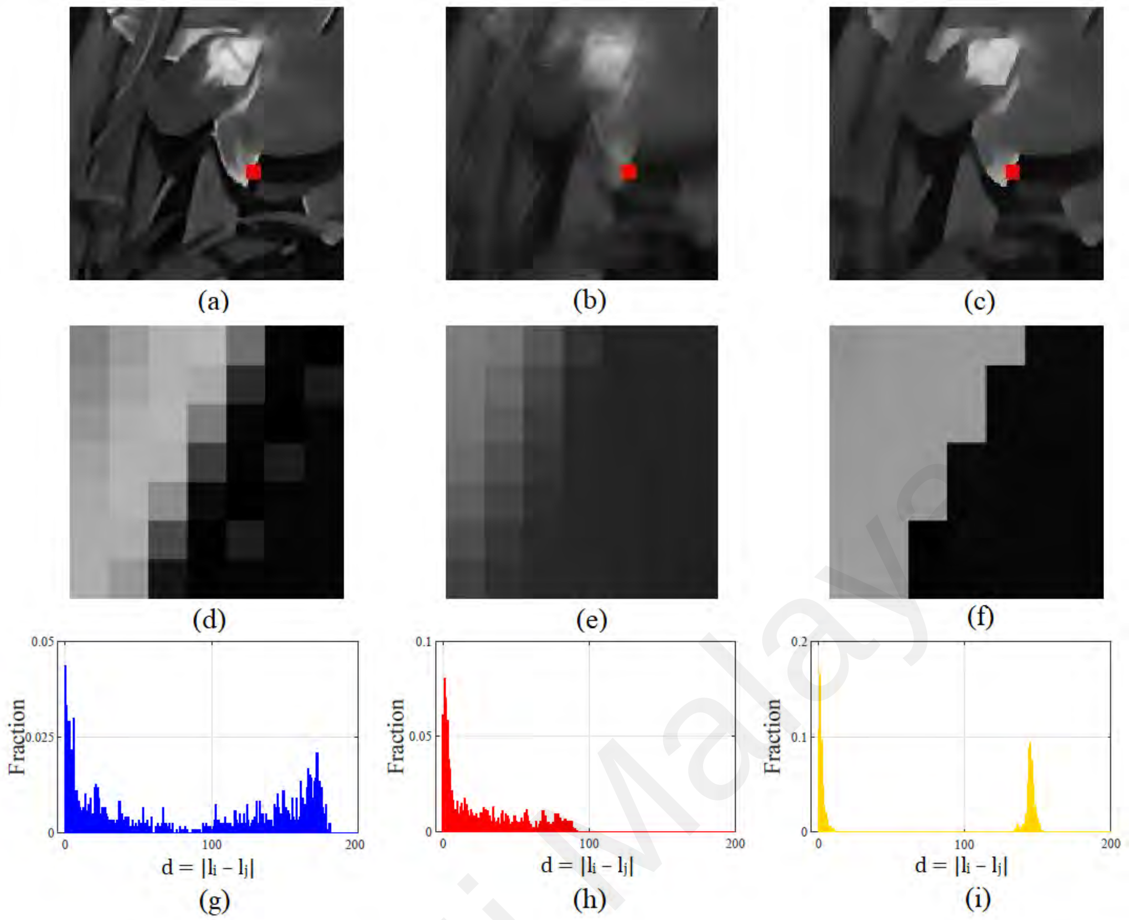

Figure 5.1: Illustrations of different kinds of images (Bai et al, 2019). (a) a real natural image. (b) a blurry image. (c) a skeleton image. (d), (e) and (f) are cropped region in red box of (a), (b) and (c), respectively; whereas (g), (h) and (i) are the Edge weight distribution around image edges of (a), (b) and (c), respectively.

One notable observation from the histograms in Figure 5.1 is that both the real natural patch and its skeleton version have bi-modal distributions of edge weights, but not the blurred patch. The bi-modal distribution means that the inter-pixel differences in an image patch are either very small or very large, which shows that the patch is PWS. The PWS property of the skeleton patch exhibits similar characteristics as the real natural image for an appropriate blur kernel estimation. Moreover, according to the authors, with its sparse representation, the skeleton patch can be more easily reconstructed from a blurry patch than the natural patch with less processing time.

Reweighted Graph Total Variation Prior: In order to incorporate the aforementioned bi-modal edge weight distribution in a target pixel patch using the RGTV. First, the gradient operator of a graph signal l must be defined. The gradient of node $i \in \boldsymbol{V}$ is defined as $\nabla_i l \in \mathbb{R}^N$ and its j-th element is

$$(\nabla_i l)_j \triangleq l_j - l_i \tag{5.23}$$

Typically, the graph total variation (GTV) (Elmoataz et al., 2008; Hidane, et al., 2013; Berger et al., 2017) is defined as

$$\|l\|_{GTV} = \sum_{i \in v} \| diag(W_{i,}.)\nabla_i l\|_1 = \sum_{i=1}^{M}\sum_{j=1}^{M} w_{i,j}\left|l_j - l_i\right| \tag{5.24}$$

where $W_{i,}.$ is the i-th row of the adjacency matrix W. The GTV initializes W using Equation (5.20). Since it is kept fixed, therefore, it does not use the bi-modal distribution of edge weights. The behavior of GTV in Equation (5.24) is separable, which means it can be analyzed using a single node pair (i, j) by treating it separately like a two-node graph. With $d = \left|l_j - l_i\right|$ and fixed $w_{i,j}$, the regularizer $w_{i,j}$ for pair (i, j) becomes $w_{i,j}d$, which is a linear function of d with slope $w_{i,j}$. Minimizing Equation (5.24) will push d towards 0, thus making the image l smoother.

In Bai et al. (2019), the GTV is extended to RGTV, where the graph weights $W(l)$ are also functions of l defined as

$$\|l\|_{RGTV} = \sum_{i \in v} \|\text{diag}(W_{i},.(l))\nabla_i l\|_1$$

$$= \sum_{i=1}^{M}\sum_{j=1}^{M} w_{i,j}(l_i, l_j)|l - l_i| \tag{5.25}$$

where $W_{i,}.(l)$is the i-th row of $W(l)$ and $w_{i,j}(l_i\, l_j)$ is the (i, j) element of $W(l)$. With the extension, the RGTV has changed the regularizer pair (i, j) into $w_{i,j}\left(l_i\, l_j\right)\left|l_j - l_i\right| = \exp\left(-\frac{d^2}{\sigma^2}\right).d$, and making the curve of this regularizer to have one maximum at $\sigma/\sqrt{2}$ and two minima at 0 and $+\infty$. Minimizing Equation (5.25) will reduce d if d is smaller than $\sigma/\sqrt{2}$ and vice versa. Using Equation (5.25), the RGTV regularizer can effectively promote the desirable bi-modal edge weight distribution of sharp images.

Spectral Analysis of GTV and RGTV: Inspired by Elmoataz et al. (2008), Bai et al. (2019) formulated an ℓ_1-Laplacian operator on a graph based on the spectral interpretation of GTV. According to the authors, the new graph spectral interpretation with RGTV regularizer can lead to an efficient algorithm for the non-convex and non-differentiable blind image deblurring problem, and an accelerated graph spectral filtering implementation specifically for Gaussian blur. The graph spectrum of RGTV is defined with respect to a graph Laplacian variation operator, towards a spectral interpretation for GTV by sub-differentiating and applying an upper-bound function to the sub-derivative of Equation (5.24), yields

$$\begin{aligned}(\partial\|l\|_{GTV})_i &= \acute{c}.\sum_{j=1}^{N}\gamma_{i,j}.\left(l_i - l_j\right),\\ &= \acute{c}.\left(\sum_{j=1}^{N}\gamma_{i,j}\, l_i - \sum_{j=1}^{N}\gamma_{i,j}\, l_j\right)\end{aligned} \tag{5.26}$$

where $\acute{c}$ is a coefficient derived from the derivative apart from the Laplacian operator and

$$\gamma_{i,j} = \frac{w_{i,j}}{\max\{|l_i - l_j|, \epsilon\}}\,. \tag{5.27}$$

where ϵ is introduced as a small constant for numerical stability around 0. When $|l_i - l_j| < \epsilon$, then $\gamma_{i,j} = \left(\frac{1}{\epsilon}\right) w_{i,j}$, which is upper-bounded by $\frac{1}{\epsilon}$, and ϵ is fixed at 0.01. Considering $\gamma_{i,j}$ as a new graph weight defined by Equation (5.27), a new adjacency matrix Γ with the new weight function of Equation (5.27) can be defined, such that the Equation (5.26) can be reformulated in matrix form for GTV as

$$L_\Gamma \triangleq diag(\Gamma 1) - \Gamma. \tag{5.28}$$

where L_Γ is the ℓ_1-Laplacian matrix. $L_\Gamma$is a real symmetric PSD matrix.

5.2.2.1 General formulation

Given an image degradation model in Equation (5.1), the optimization of the blind single image restoration problem using the proposed RGTV prior of Bai et al. (2019) can be expressed as:

$$\hat{l}, \hat{k} = \min_{l,k} \frac{1}{2} \|l \otimes k - b\|_2^2 + \tau_1 \|l\|_{RGTV} + \tau_2 \|k\|_2^2 \tag{5.29}$$

where the first term is the data fidelity function, and the remaining two functions are regularization terms for variables *l* and k, respectively. τ_1 and τ_2 are two corresponding weights for the two regularization terms.

Equation (5.29) is a non-convex and non-differentiable optimization, therefore solving it can be challenging. Similar to the low-rank prior-based blur estimation method in subsection 5.2.1, Bai et al. (2019) applied a coarse-to-fine strategy (Fergus et al., 2006) to solve Equation (5.29). Note that the minimizer $\hat{l}$ is the PWS proxy (i.e., the skeleton image) for estimating a good blur kernel $\hat{k}$.

Skeleton Image Restoration: Given $\hat{k}$, optimization of Equation (5.29) to solve l becomes:

$$\hat{l} = \min_{l} \frac{1}{2} \left\|l \otimes \hat{k} - b\right\|_2^2 + \beta \|l\|_{RGTV} \tag{5.30}$$

Recall that RGTV is a non-differentiable and non-convex prior, where the edge weights are functions of l. To solve Equation (5.30), Equations (5.27) and (5.28) in the spectral analysis, and an alternating scheme with the proposed ℓ_1-Laplacian of GTV are employed for RGTV approximation. In the alternating scheme, the l is first optimized with an initialized L_Γ, and then the L_Γ is updated using L_Γ $(\hat{l})$ to optimize l again. The alternating algorithm runs iteratively until reaching convergence according to Equation

(5.30). By fixing L_Γ and $\hat{k}$ to solve l, the problem thus becomes a non-blind image deblurring problem with a graph Laplacian regularizer

$$\hat{l} = \min_{l} \frac{1}{2} \left\| l \otimes \hat{k} - b \right\|_2^2 + \beta . l^T L_\Gamma \, l \tag{5.31}$$

Since Equation (5.31) is a quadratic convex optimization function, hence, it is equivalent to solving the following system of linear equations,

$$\left(\widehat{K}^T \widehat{K} + 2\beta . L_\Gamma\right) \hat{x} = \widehat{K}^T b \tag{5.32}$$

where $\widehat{K}$ is a block circulant with circulant blocks (BCCB) matrix, which means it is the matrix representation of convolving with $\hat{k}$. The matrix $\widehat{K}^T \widehat{K} + 2\beta . L_\Gamma$ is a real symmetric positive definite matrix. In order to verify if Equation (5.32) is well-conditioned numerically, the Power Method (Wilkinson, 1987) is used to compute the maximum and minimum eigenvalues of $\widehat{K}^T \widehat{K} + 2\beta . L_\Gamma$ and to check the condition number $\lambda_{max}/\lambda_{min}$. In the rare case when the condition number is large, in order to stabilize the solution in Equation (5.32), an iterative refinement term ϵI is added iteratively according to Parikh & Boyd (2014). Since the left-hand-side matrix is sparse, positive definite, and symmetric, therefore Equation (5.32) can be solved efficiently using the Conjugate Gradient (CG) method (Boyd & Vandenberghe, 2004). In practice, the $\widehat{K} l$ can be implemented as 2-D convolution and accelerates with the FFT. Besides, the $L_\Gamma l$ can be implanted as a locally graph filter, instead of matrix computation.

5.2.2.2 Optimization

Blur Kernel Estimation: Given a latent image $\hat{l}$, the blur kernel k in Equation (5.29) can be solved by the following optimization

$$\hat{k} = \min_{k} \frac{1}{2} \left\| l \otimes \hat{k} - \nabla b \right\|_2^2 + \mu \|k\|_2^2 \tag{5.33}$$

where ∇ is the gradient operator. Equation (5.33) is a quadratic convex function and has a closed-form solution, there it can be accelerated via FFT (Cho & Lee, 2009). After obtaining $\hat{k}$, the negative elements of $\hat{k}$ is thresholded to zeros and $\hat{k}$ is normalized to ensure $\sum_i \hat{k} = 1$. According to the authors, the rationale for a successful kernel estimation with a skeleton image l is that Equation (5.30) is an over-determined function. Since the kernel k is much smaller than the image l, the skeleton image $\hat{l}$ with restored sharp edges is sufficient for kernel estimation.

Acceleration for Specific Gaussian Blur Deblurring: In image restoration applications, such as out-of-focus deblurring or image super-resolution (Cheol, Kyu & Gi, 2003; Farsiu et al., 2004). Typically, Gaussian blur is seemingly the most widely-assumed type of blur when solving Equation (5.33). In the deblurring task, a general blur kernel $\hat{k}$ typically takes most of the running time. Fortunately, under the assumption of Gaussian blur, the $\hat{k}$ (or $\hat{K}$) can be replaced with graph filter $I + a.L_\Gamma$, where L_Γ is first initialized as an unweighted graph Laplacian. The filter $I + a.L_\Gamma$ with $a < 0$ is a smoothing process, which is considered as an approximation of Gaussian blur. To set a suitable initial value for parameter a, the images are blurred with Gaussian blurs. From the experiments, the optimal $a = -0.07$ from the sharp and blurred image pairs using the least square method,

$$a = \min_a \|(I + a.L_\Gamma)X - Y\|_2^2. \tag{5.34}$$

where matrix $X = [l_{1,} l_2, \dots, l_n]$ represents n sharp images, matrix $Y = [y_{1,} y_2, \dots, y_n]$ represents corresponding blurred images.

With $I + a.L_\Gamma$, the skeleton image restoration function in Equation (5.30) is reformulated to Equation (5.35) as

$$\hat{l} = \min_{x} \frac{1}{2} \|(I + a.L_{\Gamma})l - b\|_2^2 + \beta \|l\|_{RGTV}. \tag{5.35}$$

The advantage of Equation (5.35) is that $I + a.L_{\Gamma}$ and graph Laplacian closed-form in Equation (5.31) now share the same graph frequency bases. The closed-form solution in Equation (5.32) now becomes:

$$\begin{aligned} \hat{x} &= \left(\frac{g(L_{\Gamma})}{g^2(L_{\Gamma}) + 2\beta.L_{\Gamma}}\right) b \\ &= U_{\Gamma} \left(\frac{g(\mathbf{\Lambda}_{\Gamma})}{g^2(\mathbf{\Lambda}_{\Gamma}) + 2\beta.\mathbf{\Lambda}_{\Gamma}}\right) U_{\Gamma}^T b \end{aligned} \tag{5.36}$$

where $g(X) = I + a.X$. Equation (5.36) is a polynomial graph filter to signal b that can be implemented with an accelerated Lanczos method (Susnjara et al., 2015). The Lanczos method computes an orthonormal basis $V_z = [v_{1,} v_2, \dots, v_n]$ of the Krylov subspace $K_z(L_{\Gamma}, b) = span\{b, L_{\Gamma}b, \dots, L_{\Gamma}^{z-1}b\}$ and the corresponding symmetric scalar tridiagonal matrix H_Z as

$$V_Z^* L_{\Gamma} V_Z = H_Z = \begin{bmatrix} \alpha_1 & \beta_2 & & & \\ \beta_2 & \alpha_2 & \beta_3 & & \\ & \beta_3 & \alpha_3 & \ddots & \\ & & \ddots & \ddots & \beta_M \\ & & & \beta_M & \alpha_M \end{bmatrix} \tag{5.37}$$

The approximation of $\hat{x}$ with order Z Lanczos method is

$$\hat{l} = f(L_{\Gamma})b \approx \|b\|_2 V_Z f(H_z) e_1 \coloneqq fz, \tag{5.38}$$

where $e_1 \in \mathbb{R}_Z$ is the first unit vector. $f(H_z)$ is inexpensive given $Z << M$. The $\hat{l}$, $L_{\Gamma} = L_{\Gamma}(\hat{l}\,)$ and the parameter a is updated using Equation (5.39) iteratively until convergence,

$$a = \min_{a} \left\|(I + a.L_{\Gamma})\hat{l} - b\right\|_2^2. \tag{5.39}$$

When a satisfactory skeleton image l is restored, the blur kernel $\hat{k}$ can be computed using Equation (5.33).

5.2.2.3 Algorithms

The optimization algorithm in each scale is sketched in Algorithm 1.

Algorithm 5.2: Blur Kernel Estimation by RGTV prior

Input: Blurry image b and kernel size $m \times m$

1: Initialize $\hat{k}$ with delta function or the result from a coarser scale

2: While not converge do

Compute $\hat{l}$ according to Algorithm 5.2.1

Compute k by solving Equation (5.33)

$\beta \leftarrow \beta/1.1$

end while

Output: estimated blur kernel k

Algorithm 5.2.1: Accelerated Blind Gaussian Blur Deblurring

Input: Blurry image b and kernel size $m \times m$

1 Initialize L_Γ as an unweighted graph Laplacian;

Initialize blur with $I + a. L_\Gamma$ smoothing.

2 Computing $\hat{l}$ by solving Equation (5.35):

while not converge do

Update $\hat{l}$ using the Lanczos method Equation (5.37) and Equation (5.38).

Update $L_\Gamma = L_\Gamma(\hat{x})$ using Equation (5.27) and Equation (5.28).

Update a using Equation (5.39).

end while

3 Compute $\hat{k}$ by solving Equation (5.33).

Output: estimated blur kernel $\hat{k}$ and skeleton image $\hat{l}$.

5.2.3 The proposed Sparsity Prior

The overall algorithm of the proposed robust PSF estimation based on sparsity prior is shown in Algorithm 5.3.

Algorithm 5.3. Robust PSF Estimation

Input: Ideal candidates $\{ \acute{g}_s : s =$ image b and kernel size $h \times h \}$ selected using the method described in subsection 4.3.1.

Determine the number of image pyramid n according to the size of the kernel;
for $i = 1 \rightarrow n$ do
Downsample b according to the current image pyramid to get b_i;
for $j = 1 \rightarrow m$ (m iterations) do
Select salient edges ∇S according to Equation (4.17);
% Estimate kernel k
for $j = 1 \rightarrow itr$ do
Solve k by minimizing the Upper-level problem of bilevel programming in Equation (4.21);
Solve $\hat{k}$ by minimizing the lower-level problem of bilevel programming in Equation (4.21);
$k \leftarrow \hat{k}$;
end for
Estimate latent image I_j according to Equation (4.22);
$t \leftarrow t/1.1, \theta \leftarrow \theta/1.1$.
end for
Upsample image I_i and set $I_{i+1} \leftarrow I_i$
end for

Output: Blur kernel k.

5.3 Final Image Restoration

The main objective of this chapter is to evaluate the effectiveness of various images prior in blur estimation methods for an accurate blur kernel estimation. For this work, although Equations (4.12), (5.12), and (5.35) can be used to estimate the final latent sharp image for sparsity prior, low-rank prior, and graph-based prior, respectively, however, these methods are less effective for the images with rich details. In order to make a fair comparison on the effectiveness of the blur estimation method and to recover a latent sharp image with fine details, this work employed the non-blind image restoration (IR). In contrast to blind IR (i.e., image restoration through estimation of degradation function from an unknown blur) that has been comprehensively explained in Section 3, the main goal of non-blind IR is to estimate the ideal image assuming the blur is known. In another word, it restores images with the degradation model and parameters given by users. This research work employed the non-blind IR method of Levin et al. (2007) that uses a sparse prior. Furthermore, another non-blind IR method that uses hyper-laplacian prior is employed to gain further insight into the role of the image prior in image restoration. The non-blind IR method is that of Krishan & Fergus (2009). This method was adopted in Bai et al. (2019) to evaluate the proposed graph-based blind image deblurring in final image restoration.

5.4 Analysis and Experimental Results

In this section, comprehensive experiments are conducted to evaluate the effectiveness of three different blur estimation methods as described in Section 5.3, namely, the enhanced low-rank prior method (Ren et al, 2016), graph-based prior method (Bail et al., 2019), and the proposed sparsity prior method. Of particular in this experiment, this work intends to validate the proposed MTF measurement algorithms in Chapter 4 as a blur estimation method in solving various blind deblurring problems. For a comprehensive evaluation, similar to Chapters 4, synthetically blurred data and real unknown blurred data are used; the level 2A product of IKONOS was used as ground truth and level-0 product of RazakSAT as real unknown blur data. For experimental with synthetic data, the three blur estimation methods were evaluated on three groups of blurred cases, including defocus, Gaussian blur, and motion blur. Intuitively, the larger the blur, the larger the spread over a pixel, meaning more pixel will be needed to fit the blur. Therefore, different kernel size is applied on different blur type with different amount of blur. This work sets up two different disk radius sizes for defocus, two different σ (i.e., SD) for Gaussian blur, one linear motion with 20-pixel length and 30-degree angle of motion, and three complex blurs with nonlinear motion. Hence, these made up to eight types of blurred cases for these experiments.

For a set of data $P = \{P1, P2, .., P10\}$, which comprises of 512×512-pixel test data samples with diverse scenes as shown in Figure 5.3, each data sample in P was synthetically blurred with the eight different blur kernels and added white additive Gaussian noise with zero mean and 0.5 SD. Thus, eight different datasets were collected, each consists of 10 samples of synthetic data. Table 5.1. summarizes the dataset characteristic and setting for the experiments.

Table 5.1: Dataset and experimental setting

Dataset		**Blur type and parameter**	**Kernel size**	**Total sample**
IKONOS (level 2A product)	P1, P2, P3, P4, P5, P6, P7, P8, P9 and P10 (pixel size: 512 x512)	(1) Defocus blur, disk radius size, d = 5; ($D_{d=5}$)	25 × 25	80
		(2) Defocus blur, disk radius size, d = 10; ($D_{d=10}$)	45 × 45	
		(3) Gaussian blur, $\sigma = 1$; ($G_{\sigma=1}$)	25 × 25	
		(4) Gaussian blur, $\sigma = 4$; ($G_{\sigma=4}$)	45 × 45	
		(5) Linear motion, M_l , length = 20; angle = 30 degree	25 × 25	
		(6) Nonlinear motion blur -1, M_{nl-1}	45 × 45	
		(7) Nonlinear motion blur -2, M_{nl-2}	25 × 25	
		(8) Nonlinear motion blur -3, M_{nl-3}	55 × 55	
RazakSAT (level-0 product)	R1, R2,…..R50 (pixel size: 512 x512)	Unknown bur	15 × 15	50

For real satellite data, 50 data samples with 512×512-pixel were collected. Figure 5.2 shows the ground truth data used for simulating synthetic data, whereas Figure 5.3 shows part of the test data for experiments on real unknown blur. The rest of the test datasets from the level-0 product of RazakSAT are presented in Appendix B.

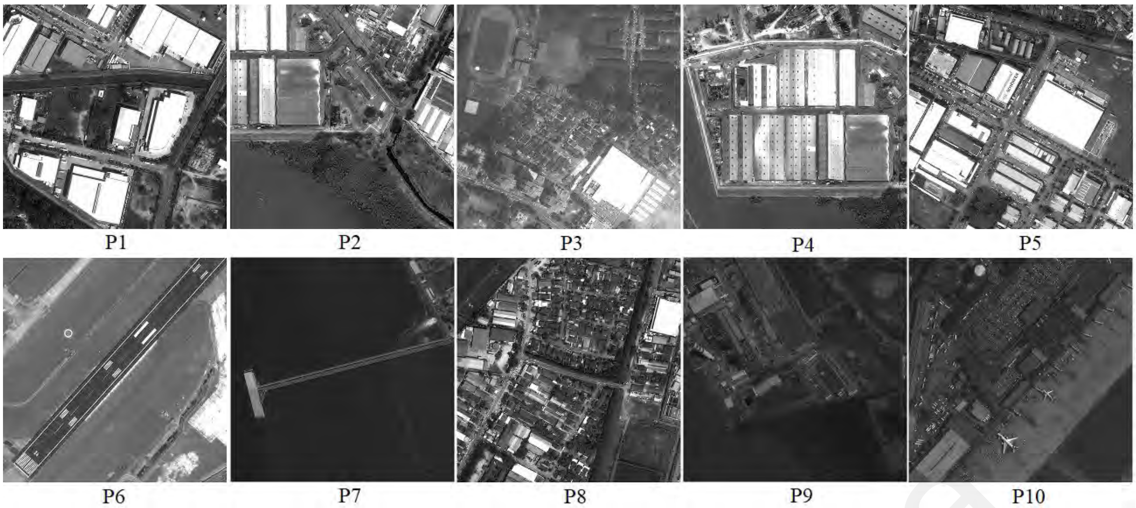

Figure 5.2: Test data from level 2A product of IKONOS. Note that P1 and P5 are images with rich high contrast edges and details, whereas P9 and P10 are images with low contrast edges and details. P2 and P4 represent images with large-scale edges and some smooth regions; P3 and P8 are images with complex structures and rich narrow edges, and P6 and P7 are images with large smooth regions and limited edge structures.

Figure 5.3: Test data from the level-0 product of RazakSAT with unknown blur.

For these experiments, the competing algorithms are evaluated from the aspects of effectiveness and efficiency. As such, the experimental results are discussed in three subsections, first, the experimental on synthetic data, followed by experimental on real data, and lastly, the evaluation on algorithm complexity and computational time.

5.4.1 Experiments on Synthetically Blurred Data

For synthetically blurred data, two sets of experiments were conducted: (1) to evaluate the accuracy of the estimated blur kernels and (2) to evaluate the quality of the restored image.

To evaluate the effectiveness of the blur estimation methods on the accuracy of estimated blur kernels. For numerical experimental results, this work adopts the sum of squared differences error (SSDE) (unitless: interval [0 1]), which is defined as follows:

$$SSDE = \sum_{(x,y)} [k_{ref}(x,y) - k(x,y)]^2 \tag{5.40}$$

where k and k_{ref} denote the estimated blur kernel and ground truth blur kernel, respectively. The closer the SSDE value to 0 the higher is the accuracy of the estimated results.

Whereas for evaluation of the restored images (i.e., final output) using the competing blur estimation algorithms, the ISNR (unit: dB), and FSIM (unitless: interval [0 1]) are employed according to Equation (3.31) and Equation (3.40), respectively. In order to compare the overall performances (i.e., level of significance) of the proposed method to the competing methods, this work uses the two-tailed binomial test that is known as the Sign test (Sheskin, 2011). For this evaluation, the null hypothesis is that there is no significant difference of performance between the competing methods; with an underlying level of significance, $\ddot{s}$ = 0.05, the proposed method is deemed significantly better with calculated probability, p-value < 0.05, thus rejecting the null hypothesis.

In addition to quantitative measurement, this work also includes visual observation for qualitative evaluation. In order to make fair comparisons, the same kernel size is used for all the algorithms to estimate the blur kernel in each case. Then, the same non-blind image deblurring algorithms are used to recover sharp images with estimated blur kernels.

5.4.1.1 Effectiveness of blur estimation method

In this experiment, this work estimates the blur kernel for all blur cases using the kernel size according to the ground truth kernel size as listed in Table 5.1. The SSDE results among competing methods on the datasets are presented in Table 5.2.

Table 5.2: SSDE comparison of blur estimation methods with different prior types for blur kernel estimation. The bold numbers are the lowest SSDE, which indicates the best performance.

Type of Blur	**Algorithm**	**Dataset**				
		P1	**P2**	**P3**	**P4**	**P5**
Defocus, d = 5	Graph-based Prior	0.0134	0.0227	0.0262	0.0202	0.0165
	Low-rank Prior	0.0142	0.0184	0.0152	0.0196	0.0146
	Sparsity Prior	**0.0042**	**0.0052**	**0.0073**	**0.0052**	**0.0059**
Defocus, d = 10	Graph-based Prior	0.0812	0.1400	0.1802	0.1634	0.1059
	Low-rank Prior	0.1067	0.0711	0.0942	0.0796	0.1042
	Sparsity Prior	**0.0173**	**0.0561**	**0.0897**	**0.0378**	**0.0231**
Gaussian, σ = 1	Graph-based Prior	**0.0001**	0.0004	0.0007	0.0019	**0.0009**
	Low-rank Prior	0.0021	0.0018	0.0019	0.0009	0.0022
	Sparsity Prior	0.0002	**0.0002**	**0.0003**	**0.0006**	0.0009
Gaussian, σ = 4	Graph-based Prior	0.0007	0.0009	0.0262	**0.0007**	0.0005
	Low-rank Prior	0.0009	0.0021	0.0023	0.0022	0.0016
	Sparsity Prior	**0.0005**	**0.0003**	**0.0004**	0.0008	**0.0004**
Linear motion	Graph-based Prior	0.0080	0.0106	0.0039	0.0286	**0.0087**
	Low-rank Prior	0.0315	0.0204	0.0282	0.0081	0.0307
	Sparsity Prior	**0.0031**	**0.0097**	**0.0007**	**0.0061**	0.0129
Nonlinear motion 1	Graph-based Prior	0.0143	0.0121	0.0155	0.0115	**0.0091**
	Low-rank Prior	0.0408	0.0349	0.0256	0.0172	0.0396
	Sparsity Prior	**0.0079**	**0.0074**	**0.0083**	**0.0107**	0.0154
Nonlinear motion 2	Graph-based Prior	**0.0037**	0.0128	0.0084	**0.0035**	0.0055
	Low-rank Prior	0.0097	0.0138	0.0295	0.0067	0.0100
	Sparsity Prior	0.0065	**0.0072**	**0.0083**	0.0142	**0.0054**
Nonlinear motion 3	Graph-based Prior	**0.0054**	**0.0049**	0.0054	**0.0054**	**0.0055**
	Low-rank Prior	0.0088	0.0061	0.0110	0.0123	0.0095
	Sparsity Prior	0.0068	0.0062	**0.0053**	0.0065	0.0067

Table 5.2, continued.

Type of Blur	Algorithm	Dataset				
		P6	**P7**	**P8**	**P9**	**P10**
Defocus, d = 5	Graph-based Prior	0.0244	0.0291	0.0176	0.0496	0.0394
	Low-rank Prior	0.0170	0.0278	0.0147	0.0166	0.0156
	Sparsity Prior	**0.0101**	**0.0127**	**0.0024**	**0.0052**	**0.0097**
Defocus, d = 10	Graph-based Prior	0.2734	0.2363	0.1713	0.2029	0.2674
	Low-rank Prior	0.1194	**0.1290**	0.0971	0.1045	0.1122
	Sparsity Prior	**0.0477**	0.1448	**0.0206**	**0.0828**	**0.0743**
Gaussian, σ = 1	Graph-based Prior	**0.0007**	**0.0001**	0.0015	**0.0010**	0.0021
	Low-rank Prior	0.0031	0.0048	0.0014	0.0024	0.0008
	Sparsity Prior	0.0066	0.0058	**0.0002**	0.0015	**0.0008**
Gaussian, σ = 4	Graph-based Prior	0.0025	0.0019	0.0011	0.0384	0.0316
	Low-rank Prior	0.0011	0.0023	0.0017	0.0054	0.0025
	Sparsity Prior	**0.0005**	**0.0008**	**0.0005**	**0.0012**	**0.0009**
Linear motion	Graph-based Prior	0.0393	0.0211	0.0087	0.0188	0.0031
	Low-rank Prior	0.0257	0.0353	0.0281	0.0163	0.0278
	Sparsity Prior	**0.0196**	**0.0040**	**0.0070**	**0.0039**	**0.0015**
Nonlinear motion 1	Graph-based Prior	**0.0145**	0.0195	**0.0125**	**0.0146**	**0.0215**
	Low-rank Prior	0.0289	0.0306	0.0138	0.0359	0.0313
	Sparsity Prior	0.0439	**0.0054**	0.0154	0.0198	0.0218
Nonlinear motion 2	Graph-based Prior	**0.0032**	0.0230	0.0091	0.0074	0.0038
	Low-rank Prior	0.0185	0.0348	0.0095	0.0124	0.0323
	Sparsity Prior	0.0168	**0.0141**	**0.0050**	**0.0035**	**0.0033**
Nonlinear motion 3	Graph-based Prior	**0.0080**	0.0173	**0.0050**	0.0056	**0.0048**
	Low-rank Prior	0.0334	0.0188	0.0083	0.0088	0.0095
	Sparsity Prior	0.0134	**0.0053**	0.0061	**0.0055**	0.0062

Figure 5.4 presents a visual estimation of the blur kernels from one of the datasets for all blur types by the competing methods. Based on visual observation, for this dataset (i.e., Sample P1), it can be noticed that the estimated results in Figure 5.4 (b) and 5.4 (c) are comparable to the ground truth in Figure 5.4 (a), whereas Figure 5.4 (d) show a discrepancy in comparison.

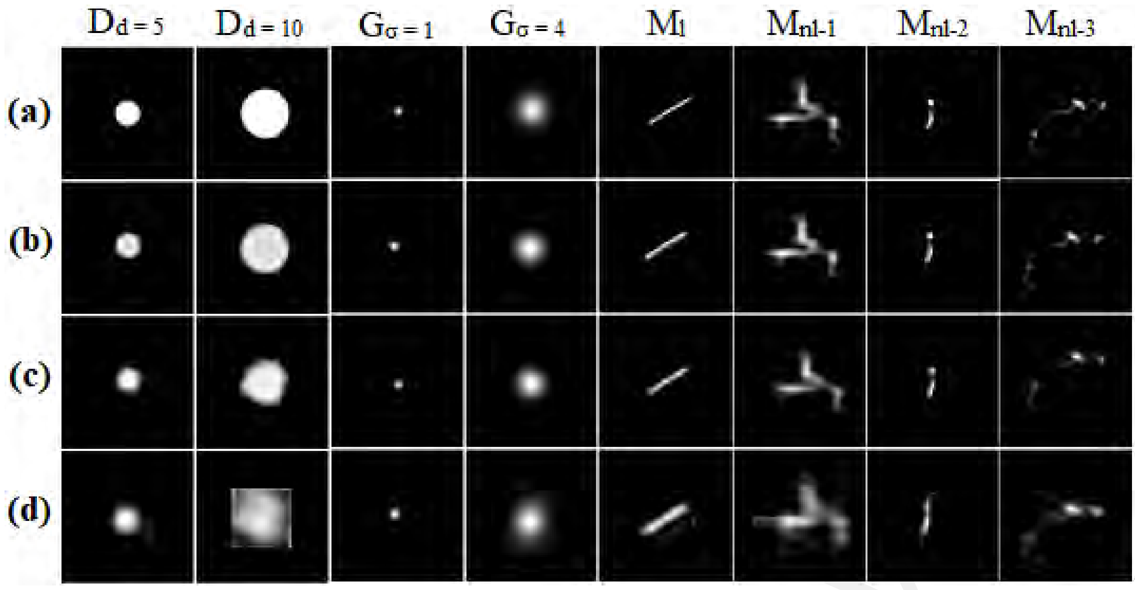

Figure 5.4: Comparison of the estimated kernels for sample P1. (a) the ground truth blur kernels; estimated kernel results by (b) proposed method, (c) Ren et al. (2016), and (d) Bai et al. (2019).

For better observation, a comparison (in terms of SSDE) of the estimated kernels by the three different prior-based methods is provided in bar graph representation as illustrated in Figures 5.5. The bar height in the figures indicates the SSDE of the estimated kernels; lower bars indicate better performance.

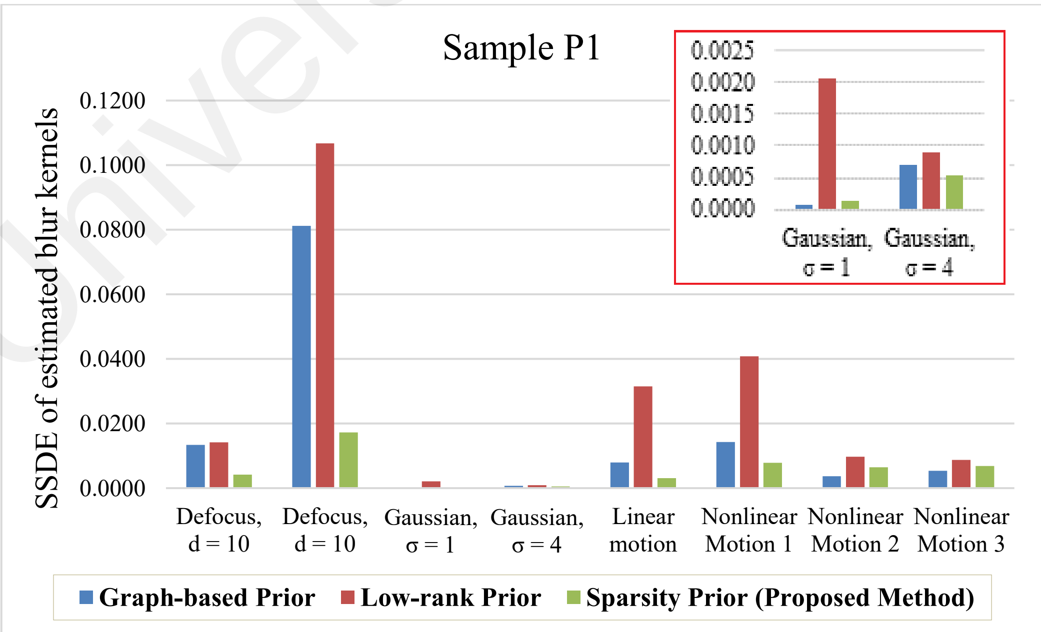

Figure 5.5: Comparison of the estimated kernels in terms of SSDE. Bar height indicates the SSDE of the estimated kernels; lower bars indicate better performance. The red box in the right top corner is the closed up view of Gaussian blur results

The SSDE value graph bars in Figure 5.5 show that in this test sample, the proposed method estimated a more accurate blur kernel than the other methods as it obtains the five lowest SSDE out of eight blur cases.

For a more effective evaluation, instead of based on the test samples, the experimental results will be discussed according to the group of blur cases.

Defocus blur: From Figure 5.6(a), it is can be noticed that all green bars are shorter than the red and blue bars for all datasets. Whereas in Figure 5.6(b), only one of the 10 green bars is not the shortest among the three bars. From this experiment, it is obvious that the proposed method is able to estimate defocus blur better than the other methods with 95% (i.e., 19 of 20) lowest SSDE, with one case outperformed by the low-rank prior method. The graph-based prior method, on the contrary, has the highest SSDE for all defocus blur cases, which indicates that it provides the least accurate estimated defocus blur.

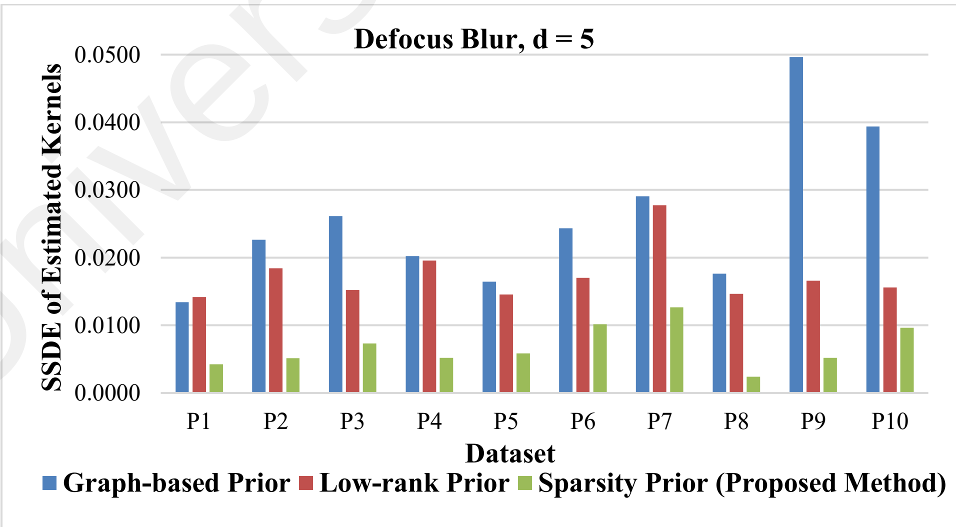

(a)

Figure 5.6: Comparison of estimated kernels in SSDE value for (a) Defocus blur, d = 5; (b) Defocus blur, d = 10.

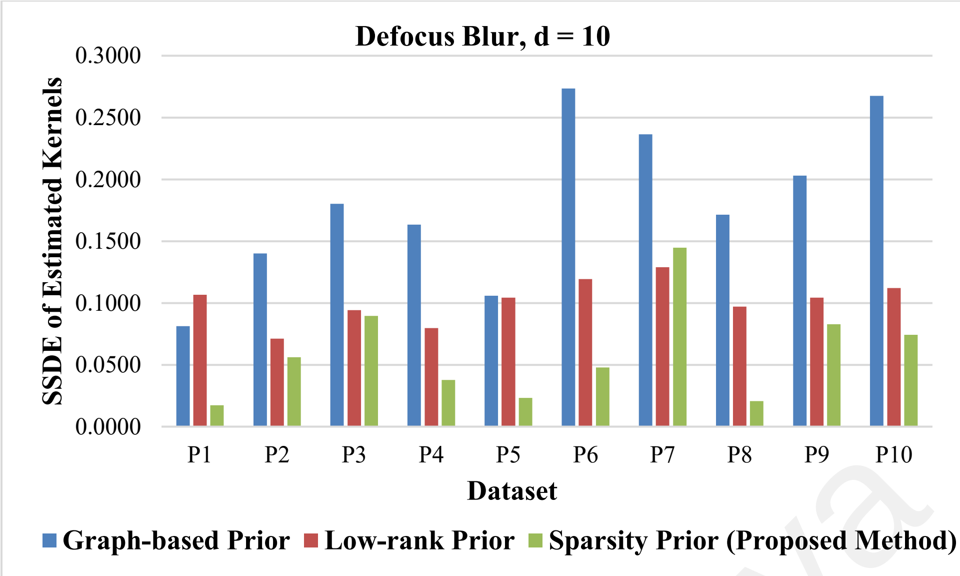

(b)

Figure 5.6, continued.

Gaussian blur: Based on the experimental results on 10 datasets for each blur case, there are only five and nine datasets with the shortest green bars found in Figures 5.7 (a) and 5.7 (b), respectively. These results show that the proposed method performs better than other methods, particularly for large Gaussian blur (e.g., σ = 4). Whereas, for the small gaussian blur (e.g., σ = 1), the proposed method is comparable to the graph-based prior method with 50% lowest SSDE. Furthermore, from Figure 5.7 (a), it is noticed that the proposed method has an obvious spike for datasets P6 and P7, whereas, in Figure 5.7 (b), the graph-based prior methods show an obvious spike for dataset P3, P9, and P10.

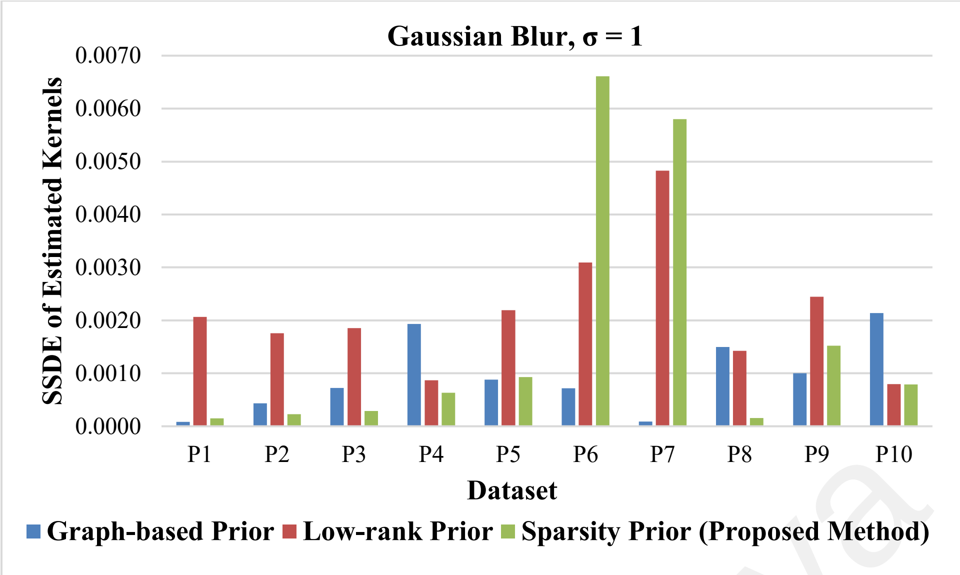

(a)

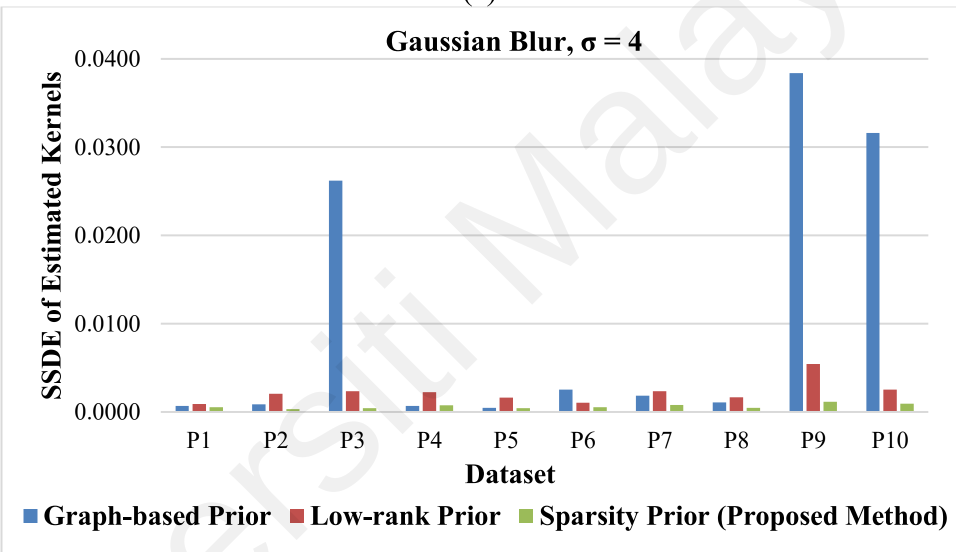

(b)

Figure 5.7: Comparison of estimated kernels in SSDE value for (a) Gaussian Blur, σ = 1; (b) Gaussian Blur, σ = 4.

Motion blur: There are nine, six, eight, and three datasets with the shortest green bars found in Figures 5.8(a), 5.8(b), 5.8(c), and 5.8(d), respectively. In percentage, the proposed method with sparsity prior outperforms the other methods by 90% (i.e., 9 of 10) in estimating linear motion. Whereby in nonlinear motion blur, the performances between the proposed method and graph-based prior method are almost comparable, with the proposed method somewhat slightly better by obtaining 57% (i.e., 17 of 30) lowest SSDE over the 43% (i.e., 13 of 30) lowest SSDE of the graph-based prior method.

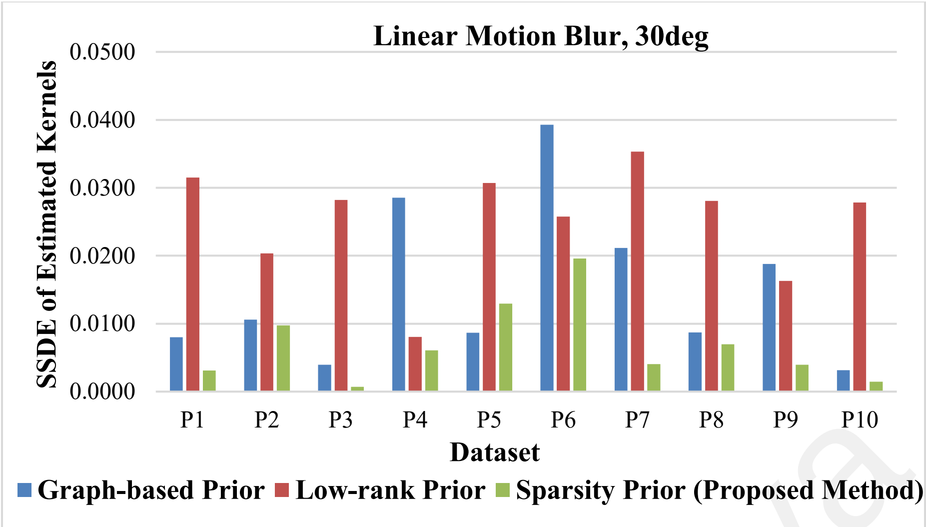

(a)

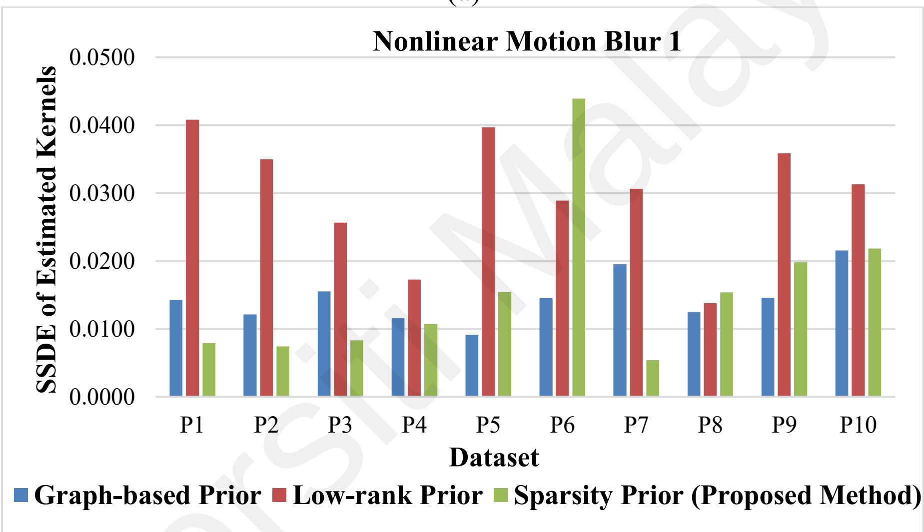

(b)

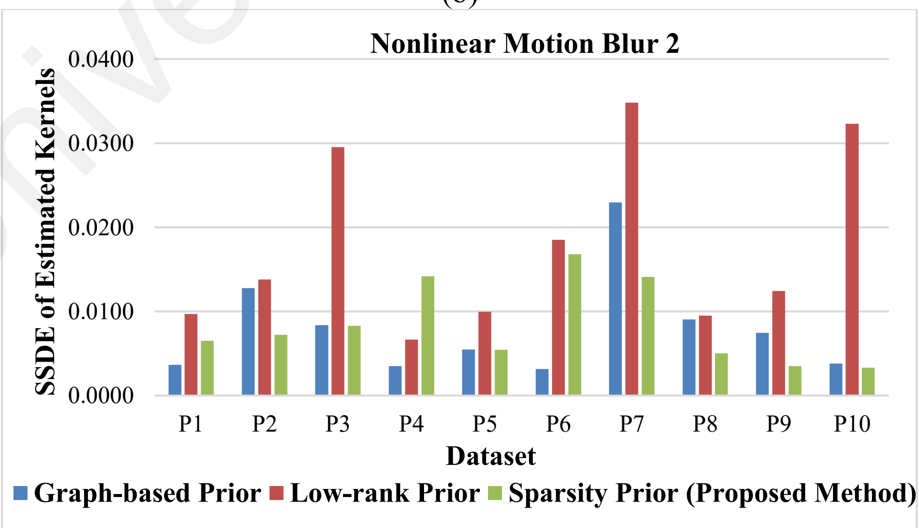

(c)

Figure 5.8:Comparison of estimated kernels in SSDE value for (a) Linear motion blur, angle = 30 degree; (b) nonlinear motion blur, M_{nl-1}; (c) nonlinear motion blur, M_{nl-2}; and (d) nonlinear motion blur, M_{nl-3}.

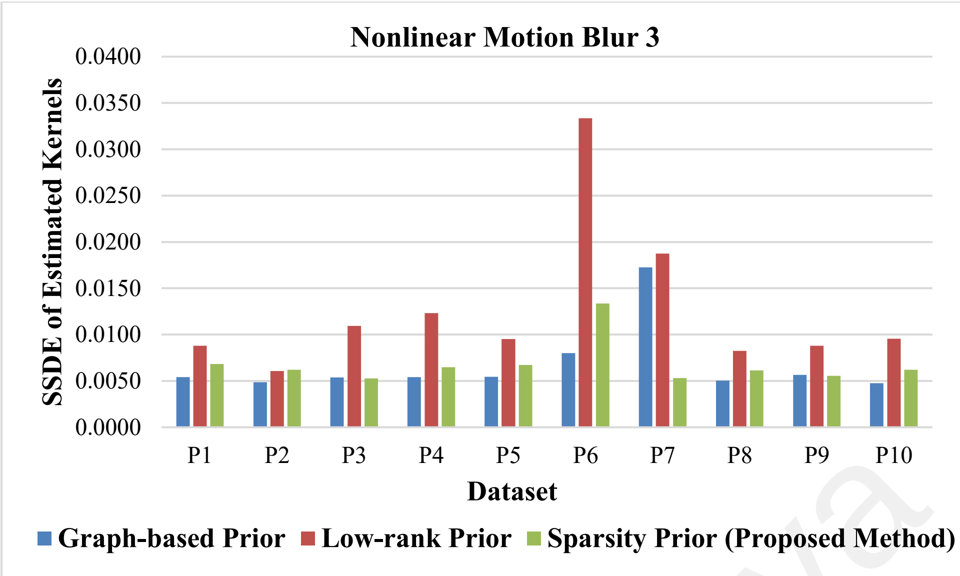

(d)

Figure 5.8, continued.

Based on Table 5.2 and Figures 5.6 to 5.8, it is obvious that the proposed Sparsity Prior is significantly better than the low-rank based prior in estimating blur kernel regardless of the blur type. Therefore, for this evaluation, only the Sign test between proposed Sparsity Prior and Graph-based Prior is conducted. From the pairwise comparisons results between these methods as presented in Table 5.3. The proposed Sparsity Prior shows significantly better performance over Graph-based Prior with a level of significance, $\ddot{s}$ of 0.005 for defocus and 0.05 for linear motion blur, respectively. However, the proposed method is not significantly better than the Graph-based Prior for nonlinear motion blur. For Gaussian blur, the level of significance $\ddot{s}$ is only 0.1.

Table 5.3: Sign test for pairwise comparisons between proposed Sparsity Prior and Graph-based Prior; The '-' sign indicates *p*-value > 0.1

Sparsity Prior	**Graph-based Prior**							
	Defocus		**Gaussian**		**Linear motion**	**Nonlinear**		
	d = 5	**d = 10**	**σ = 1**	**σ = 4**		**1**	**2**	**3**
Wins (+)	10	10	5	9	9	5	7	3
Loses (-)	0	0	5	1	1	5	3	7
Detected differences	$\ddot{s}$ = 0.005		$\ddot{s}$ = 0.1		$\ddot{s}$ = 0.05	-		

From Table 5.2, Table 5.3, and Figures 5.6 to 5.8, several observations were found. First, the proposed method considerably outperforms the other methods with about 74% (i.e., 59 of 80 cases) with the lowest SSDE in all the cases, whereas the graph-based prior and low-rank prior have 25% (i.e., 20 of 80) and 1% (i.e., 1 of 80), respectively. Second, the defocus blur is the most challenging type of blur to solve, as the obtained SSDE values for estimated defocus blur kernels from each dataset are relatively higher than other groups of blurred cases(i.e., Gaussian and motion blur). Among the three blur estimation methods, the proposed method estimates the best result with the lowest SSDE, whereas the graph-based prior method estimates with the highest SSDE value. The proposed method is very effective in estimating large Gaussian blur. Third, the graph-based prior method is not as effective compared with the other methods when restoring low contrast images with large Gaussian blur. For example, in Figure 5.7(b), it is obvious that the SSDE values of P3, P9, and P10 are relatively high compared with SSDE values in other data samples. As shown in Figure 5.2, the contrast of these data samples is lower compared to other images. Fourth, since the proposed method is designed to estimate the blur kernel based on the region with salient structures, the accuracy is reduced when estimating blur from the data sample with a large smooth region and such as sample P6 and P7. This can be noticed in Figure 5.7(a), where it has relatively high SSDE values for samples P6 and P7 among others. Lastly, the proposed method performs better than other methods in estimating linear motion. For nonlinear and complex motion blur, the proposed method outperforms the low-rank based prior method but comparable to the graph-based prior method.

5.4.1.2 Effectiveness of image restoration

In this experiment, this work evaluates the effectiveness of the three blur estimation methods that were discussed in the previous subsection in estimating an accurate blur kernel for image restoration. To quantitatively evaluate the restored images (i.e., final output), ISNR (unit: dB), and FSIM (unitless: interval [0 1]) were used. Furthermore, this work also includes visual observation for qualitative evaluation.

In order to make fair comparisons with different blur estimation algorithms, in each experiment, all three blur estimation algorithms are applied to estimate the blur kernel, and then the same ID methods are used for final image restoration. As mentioned in Section 5.3, here, this work uses two ID methods are used: (1) the sparse prior ID method of Levin et al. (2007) and (2) the fast hyper-laplacian prior ID method of Krishnan and Fergus (2009), for which, throughout this experiment, will be referred as SPID and HPID, respectively.

Similar to Subsection 5.4.1.1, the experimental results will be discussed based on the group of blurred cases, which include defocus, Gaussian blur, and motion blur.

(a) ***Defocus***

Table 5.4 tabulates the FSIM and ISNR of restored images by the competing methods. From Table 5.4, this work finds the combination methods with the highest FSIM and ISNR value and gives a count for each winner then records the total counts in Table 5.5.

Table 5.4: Quantitative evaluation in terms of ISNR and FSIM for the competing algorithms in restoring defocus blurred images. The bold numbers are either the highest FSIM or ISNR, which indicate the best performance.

Dataset	Type of Blur	Defocus, d = 5				Defocus, d = 10			
	Algorithm	**SPID**		**HPID**		**SPID**		**HPID**	
	Quantitative metrics	FSIM	ISNR	FSIM	ISNR	FSIM	ISNR	FSIM	ISNR
Sample P1	Graph-based Prior	0.9967	2.18	0.9957	1.85	0.9783	1.69	0.9696	1.59
	Low-rank Prior	0.9964	1.72	0.9959	1.53	0.9684	-0.63	0.9681	0.24
	Sparsity Prior	**0.9979**	**2.90**	**0.9967**	**2.50**	**0.9888**	**3.32**	**0.9796**	**2.51**
Sample P2	Graph-based Prior	0.9951	1.42	0.9943	1.31	0.9769	1.22	0.9712	1.29
	Low-rank Prior	0.9941	0.99	0.9935	0.83	0.9627	0.65	0.9597	0.83
	Sparsity Prior	**0.9973**	**2.74**	**0.9957**	**2.14**	**0.9838**	**2.68**	**0.9768**	**2.08**
Sample P3	Graph-based Prior	0.9941	0.90	0.9934	0.84	0.8739	-0.06	0.9547	0.69
	Low-rank Prior	**0.9966**	1.47	**0.9951**	1.08	0.9673	0.54	0.9592	0.65
	Sparsity Prior	0.9964	**1.84**	0.9947	**1.30**	**0.9735**	**1.63**	**0.9674**	**1.27**
Sample P4	Graph-based Prior	0.9942	1.43	0.9951	1.67	0.9580	0.45	0.9507	0.77
	Low-rank Prior	0.9929	0.95	0.9927	0.87	0.9702	0.53	0.9635	0.99
	Sparsity Prior	**0.9974**	**2.85**	**0.9956**	**2.15**	**0.9852**	**3.14**	**0.9729**	**2.31**
Sample P5	Graph-based Prior	0.9965	1.95	0.9951	1.59	0.9739	1.32	0.9612	1.22
	Low-rank Prior	0.9971	2.03	0.9959	1.65	0.9758	0.60	0.9664	1.00
	Sparsity Prior	**0.9978**	**2.61**	**0.9962**	**2.11**	**0.9867**	**2.92**	**0.9756**	**2.13**
Sample P6	Graph-based Prior	0.9920	0.22	0.9909	0.32	0.9566	0.05	0.9537	0.01
	Low-rank Prior	0.9953	1.15	0.9932	0.87	0.9616	-0.29	0.9595	0.04
	Sparsity Prior	**0.9971**	**2.10**	**0.9954**	**1.38**	**0.9837**	**1.77**	**0.9787**	**1.37**
Sample P7	Graph-based Prior	0.9879	0.48	0.9858	0.47	0.9657	0.50	0.9653	0.56
	Low-rank Prior	0.9778	-2.47	0.9776	-2.02	0.9533	-0.48	0.9528	-0.10
	Sparsity Prior	**0.9895**	**1.77**	**0.9879**	**1.23**	**0.9740**	**1.69**	**0.9727**	**1.39**
Sample P8	Graph-based Prior	0.9951	1.70	0.9937	1.38	0.9599	0.35	0.9435	0.55
	Low-rank Prior	0.9966	2.00	0.9948	1.51	0.9624	-0.18	0.9520	0.49
	Sparsity Prior	**0.9970**	**2.80**	**0.9949**	**2.16**	**0.9805**	**2.67**	**0.9660**	**1.84**
Sample P9	Graph-based Prior	0.9854	-0.45	0.9853	-0.37	0.9569	0.62	0.9551	0.55
	Low-rank Prior	**0.9949**	1.34	0.9939	0.99	0.9664	0.88	0.9610	0.76
	Sparsity Prior	0.9942	**1.84**	**0.9933**	**1.29**	**0.9712**	**1.92**	**0.9685**	**1.52**
Sample P10	Graph-based Prior	0.9922	0.40	0.9919	0.57	0.9541	0.24	0.9516	0.34
	Low-rank Prior	**0.9950**	1.42	0.9935	0.94	0.9612	0.51	0.9546	0.44
	Sparsity Prior	0.9947	**1.80**	**0.9931**	**1.17**	**0.9712**	**1.57**	**0.9662**	**1.16**

In Table 5.5, it can be seen that SPID with the input from blur kernel estimated by the proposed blur estimation method (i.e., sparsity prior) outperforms HPID with about 85% (i.e., 17 of 20 cases) higher FSIM value and 100% (i.e., 20 of 20 cases) higher ISNR value for all datasets, respectively. The SPID with the input blur kernel estimated by the method of the low-rank prior produces the highest FSIM in sample P3, P9, and P10, which indicates the low-rank prior can recover the structure of a low contrast image better than sparsity prior.

Table 5.5: Blind image restoration Performance for a combination of methods in restoring defocus blurred images. The number denotes the total count of the highest achievement (i.e., winner) in the FSIM or ISNR value.

Blind image restoration	$D_{d=5}$		$D_{d=10}$	
	FSIM	ISNR	FSIM	ISNR
Graph-based Prior + SPID	0	0	0	0
Low-rank Prior + SPID	**3**	0	0	0
Sparsity Prior + SPID	**7**	**10**	**10**	**10**
Graph-based Prior + HPID	0	0	0	0
Low-rank Prior + HPID	0	0	0	0
Sparsity Prior + HPID	0	0	0	0

One interesting observation from this experiment is that with the use of SPID, the graph-based prior method, even though they were reported to have the highest SSDE for all datasets in subsection 5.4.1.1 is able to produce better restoration results than the low-rank prior method in some cases. Besides, it can be learned from Table 5.4 that with the graph-based prior input kernel, SPID considerably outperforms HPID by achieving 90% higher FSIM and 60% higher ISNR value in all cases. For low-rank prior, SPID achieves 95% higher FSIM and 55% higher ISNR in all cases, whereas for sparsity prior blur, it achieves 100% for both FSIM and ISNR in all cases. These results indicate that the three blur estimation priors favor SPID. Since the overall performance result is significant, therefore, the Sign test is not conducted for this evaluation.

Figures 5.9 and 5.10 show the quantitative evaluation of restored images by SPID for defocus with disk radius sizes of 5 and 10, respectively. In Figures 5.9 and 5.10, the FSIM and ISNR are presented in graph bars, the higher bar indicates better performance, whereby the bars in the negative y-axis indicate a fail result. From both figures, in comparison, it can be observed that SPID can achieve better restoration results in terms of FSIM and ISNR using the estimated blur kernel of the proposed blur estimation method (i.e., with sparsity prior). For example, Figure 5.11 shows the visual quality of restoration results of sample P1, $d = 10$. From the figure, with the higher ISNR value compared to graph-based prior and low-rank prior, it can be noticed that the sparsity prior restores a sharper and artifact-free image. In this case, the low-rank prior method obtains a negative ISNR, visually, even though it has a sharper appearance, however, suffers from aliasing effects.

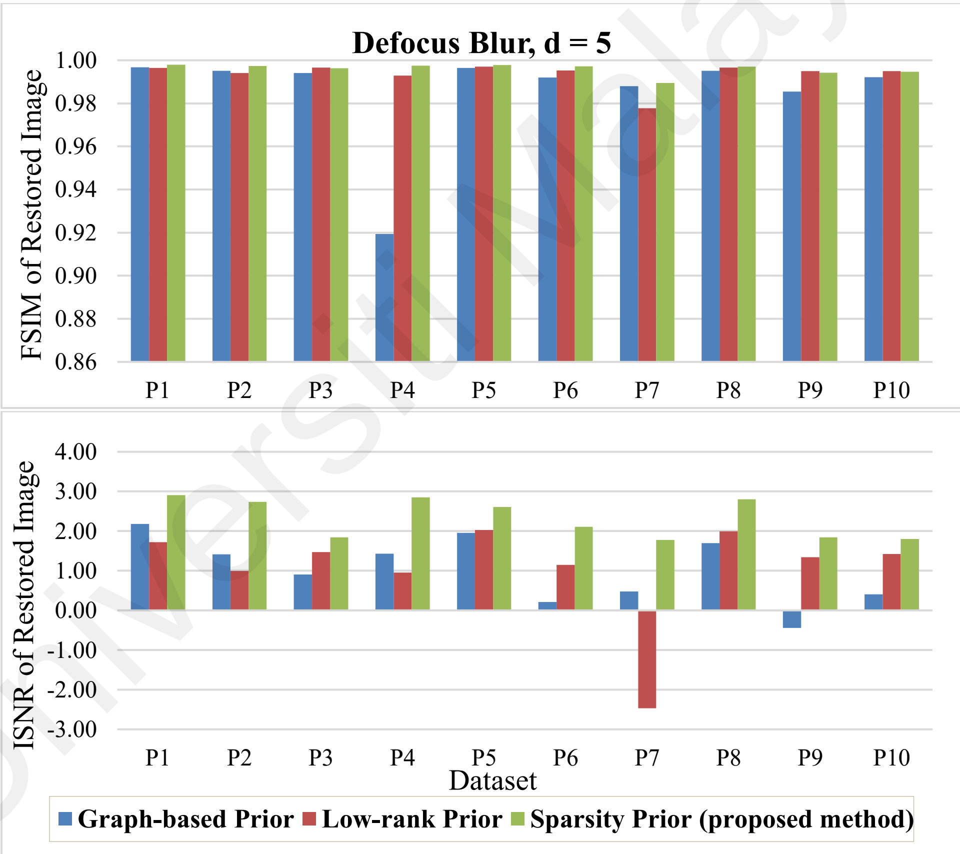

Figure 5.9: Quantitative evaluation for defocus blur, $d = 5$ in terms of ISNR, and FSIM on all datasets.

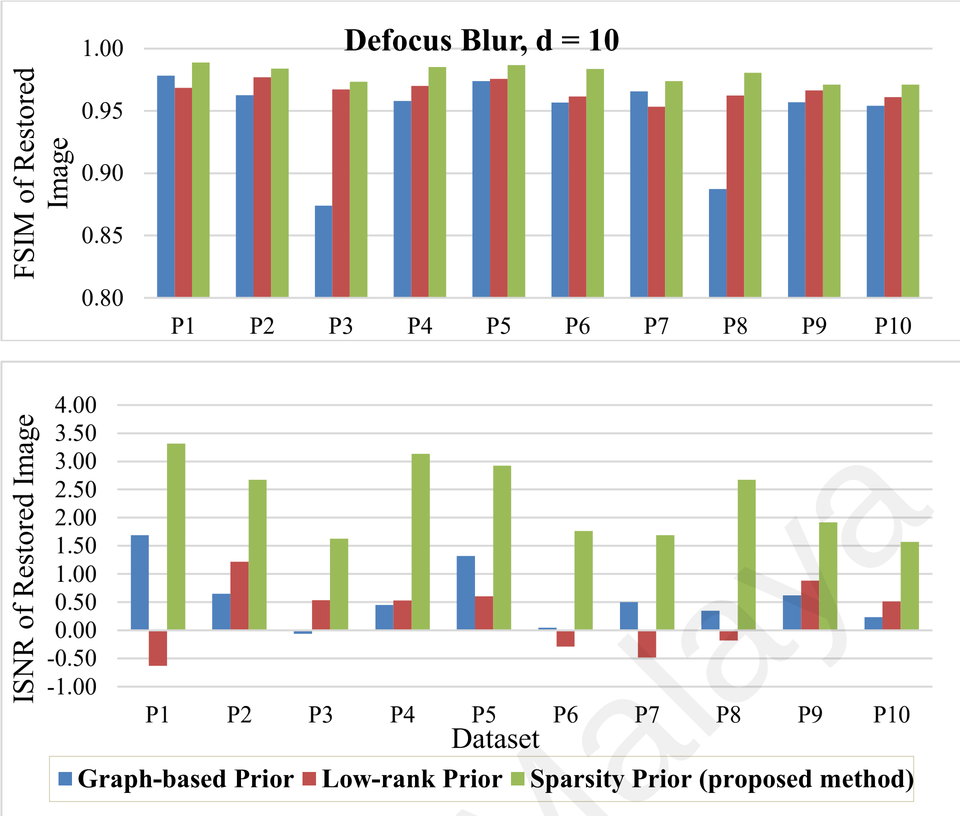

Figure 5.10: Quantitative evaluation for defocus blur, $d = 10$ in terms of ISNR and FSIM on all datasets.

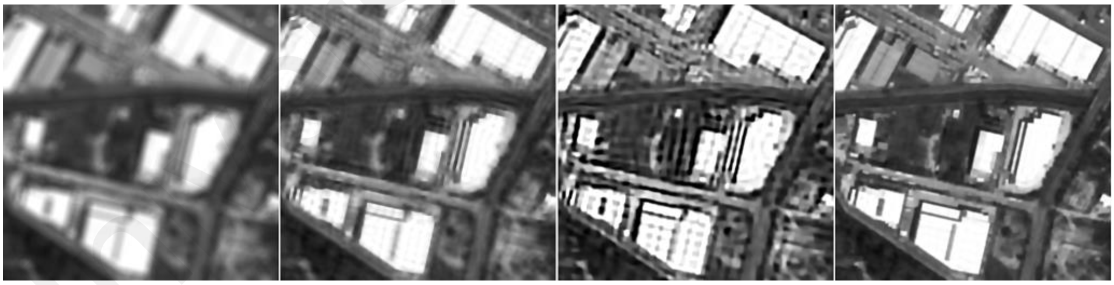

Figure 5.11: Restoration results for Sample P1 of Figure 5.10 (a) Defocus (d_{10}) image. Restored image using the estimated kernel from (b) Graph-based prior, (c) Low-rank prior, and (d) Proposed sparsity prior blur estimation method. Note that (c) depicts a fail case due to inaccurate blur kernel estimation using low-rank prior.

(b) ***Gaussian blur***

Table 5.6 tabulates the FSIM and ISNR of restored images by competing methods, whereas Table 5.7 keeps the winner counts of the combination methods in Table 5.6. Based on the observation from Table 5.6, similar to the previous experiments on defocus datasets, the three blur estimation priors favor SPID to produce better restoration results.

Table 5.6: Quantitative evaluation in terms of ISNR and FSIM for the competing algorithms in restoring Gaussian blurred images. The bold numbers are either the highest FSIM or ISNR, which indicate the best performance.

Dataset	**Type of Blur**	**Gaussian, σ = 1**				**Gaussian, σ = 4**			
	Algorithm	**SPID**		**HPID**		**SPID**		**HPID**	
	Quantitative metrics	FSIM	ISNR	FSIM	ISNR	FSIM	ISNR	FSIM	ISNR
Sample P1	Graph-based Prior	**0.9999**	2.89	**0.9998**	**2.95**	0.9871	**1.53**	0.9848	1.33
	Low-rank Prior	0.9989	-0.30	0.9990	-0.41	0.9894	1.12	**0.9874**	1.07
	Sparsity Prior	0.9994	2.49	0.9994	2.50	**0.9873**	1.52	0.9852	**1.34**
Sample P2	Graph-based Prior	**0.9995**	1.69	0.9848	1.14	0.9869	1.36	0.9994	1.28
	Low-rank Prior	0.9885	0.69	**0.9869**	0.77	0.9992	0.19	0.9991	-0.23
	Sparsity Prior	0.9893	**1.52**	0.9868	1.30	**0.9998**	**2.60**	**0.9998**	**2.23**
Sample P3	Graph-based Prior	0.9993	0.66	0.9993	0.66	0.9492	-2.95	0.9797	0.82
	Low-rank Prior	0.9993	0.26	0.9994	0.27	0.9848	0.61	**0.9817**	0.51
	Sparsity Prior	**0.9996**	**1.52**	**0.9995**	1.22	**0.9848**	**1.14**	0.9825	**0.92**
Sample P4	Graph-based Prior	**0.9991**	0.70	0.9839	1.28	0.9869	1.52	0.9992	0.26
	Low-rank Prior	0.9871	0.75	**0.9859**	0.73	0.9989	0.03	0.9990	-0.32
	Sparsity Prior	0.9881	**1.50**	0.9854	1.27	**0.9994**	**1.63**	**0.9993**	1.09
Sample P5	Graph-based Prior	**0.9993**	0.60	0.9992	**0.62**	0.9880	**1.49**	0.9849	**1.24**
	Low-rank Prior	0.9991	-0.15	0.9991	-0.42	**0.9894**	0.95	**0.9865**	0.90
	Sparsity Prior	0.9992	0.58	**0.9992**	0.55	0.9881	1.44	0.9848	1.19
Sample P6	Graph-based Prior	**0.9995**	**1.95**	**0.9994**	1.93	0.9842	0.60	0.9823	0.47
	Low-rank Prior	0.9972	-1.57	0.9974	-1.70	0.9829	-0.02	0.9806	0.10
	Sparsity Prior	0.9915	-2.64	0.9918	-2.51	**0.9887**	**0.98**	**0.9865**	**0.76**
Sample P7	Graph-based Prior	0.9797	0.97	**0.9987**	**1.59**	**0.9987**	**2.03**	0.9790	0.83
	Low-rank Prior	0.9903	-5.36	0.9907	-5.21	0.9663	-3.08	0.9668	-2.57
	Sparsity Prior	**0.9919**	-5.07	0.9921	-5.00	0.9807	1.14	**0.9797**	**0.92**
Sample P8	Graph-based Prior	0.9869	1.36	0.9994	1.28	**0.9995**	**1.69**	0.9848	1.14
	Low-rank Prior	0.9992	0.19	0.9991	-0.23	0.9885	0.69	**0.9869**	0.77
	Sparsity Prior	**0.9998**	**2.60**	**0.9998**	2.23	0.9893	1.52	0.9868	**1.30**
Sample P9	Graph-based Prior	0.9991	**0.08**	0.9990	-0.20	0.9344	-4.34	0.9752	0.64
	Low-rank Prior	0.9991	-0.31	**0.9994**	-0.34	0.9767	-0.37	0.9750	-0.30
	Sparsity Prior	0.9986	-0.47	0.9985	-0.71	**0.9800**	**1.04**	**0.9791**	**0.90**
Sample P10	Graph-based Prior	0.9976	-1.74	0.9976	-1.84	0.9268	-3.50	0.9718	-0.03
	Low-rank Prior	**0.9999**	**2.02**	**0.9998**	1.35	0.9827	0.40	0.9798	0.32
	Sparsity Prior	0.9992	0.90	0.9991	0.45	**0.9813**	**0.77**	**0.9802**	**0.63**

From Table 5.7, it is evident that SPID performs better than HPID. Consistent with the SSDE results of the Gaussian blur kernel estimation in Subsection 5.4.1.1, the sparsity prior when combined with SPID is more effective in recovering large Gaussian blur (e.g., σ = 4), whereas, for small Gaussian blur (e.g., σ = 1), it is comparable to graph-based prior. These results can be observed in Figures 5.12 and 5.13.

Table 5.7: Blind image restoration Performance for a combination of methods in restoring Gaussian blurred images. The number denotes the total count of the highest achievement (i.e., winner) in the FSIM or ISNR value.

Blind image restoration	$D_{\sigma=1}$		$D_{\sigma=4}$	
	FSIM	ISNR	FSIM	ISNR
Graph-based Prior + SPID	**5**	**2**	**2**	**3**
Low-rank Prior + SPID	**1**	**1**	**1**	0
Sparsity Prior + SPID	**2**	**4**	**7**	**7**
Graph-based Prior + HPID	**1**	**3**	0	0
Low-rank Prior + HPID	1	0	0	0
Sparsity Prior + HPID	0	0	0	0

Figure 5.12 shows the quantitative evaluation of restored images by SPID for Gaussian blur, σ = 1. In Figure 5.12, overall, the proposed algorithm performs favorably against HPID with sparsity, except for Samples P6 and P7. From Figure 5.12, with the negative ISNR value, this result indicates that the sparsity prior fails to recover Sample P6 and P7 with adverse effects. These results are expected as the sparsity prior is not effective in the recovering degraded image with a large smooth region and small Gaussian blur. This observation is also found in low-rank prior. Figure 5.13 shows the visual comparison of restoration results of Sample P7 in Figure 5.12.

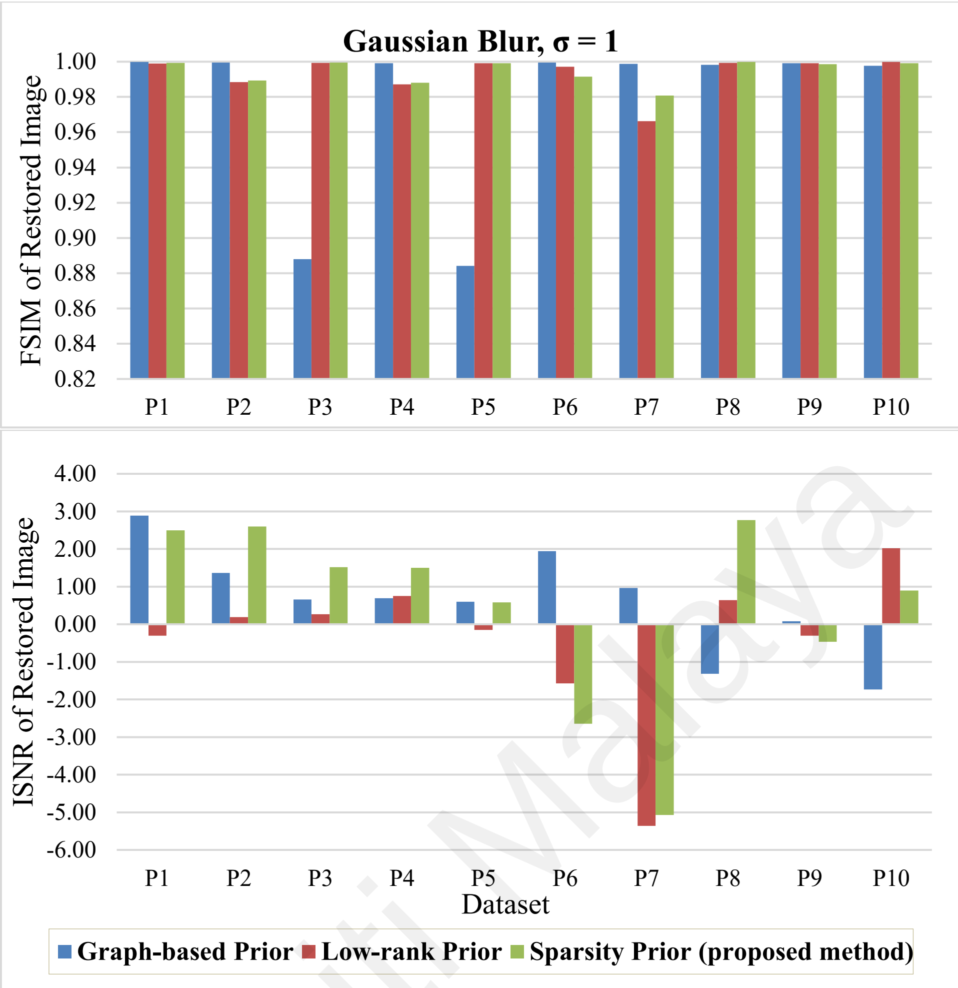

Figure 5.12: Quantitative evaluation for Gaussian blur, σ =1 in terms of ISNR, and FSIM on all datasets.

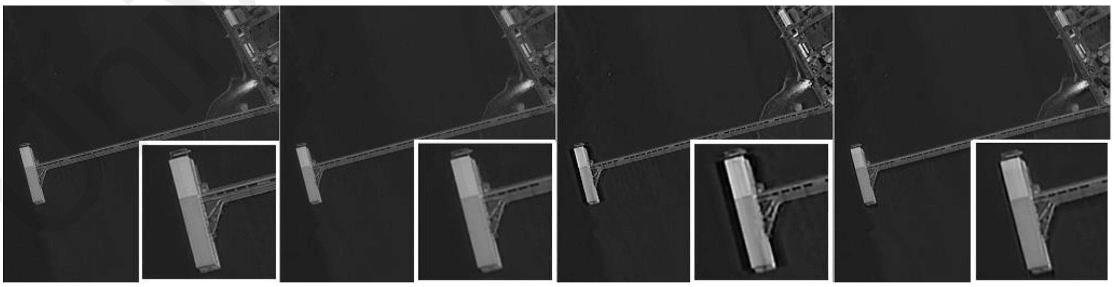

(a) (b) (c) (d)

Figure 5.13: Restoration results for Sample P7 of Figure 5.12 (a) Ground truth of Sample P7. Restored image using the estimated kernel from (b) Graph-based prior, (c) Low-rank prior, and (d) Sparsity prior blur estimation technique. It can be observed from the closed-up view, (c) appears as over sharp with halo effect; the halo effects are also noticeable in (d).

Figure 5.14 shows the quantitative evaluation of restored images by SPID for Gaussian blur, σ = 4. In Figure 5.14, overall, the proposed method performs better than the other methods. From the figure, with the negative ISNR value, this indicates the graph-based prior method is not as effective compared with the other methods when restoring low contrast images with large Gaussian blur.

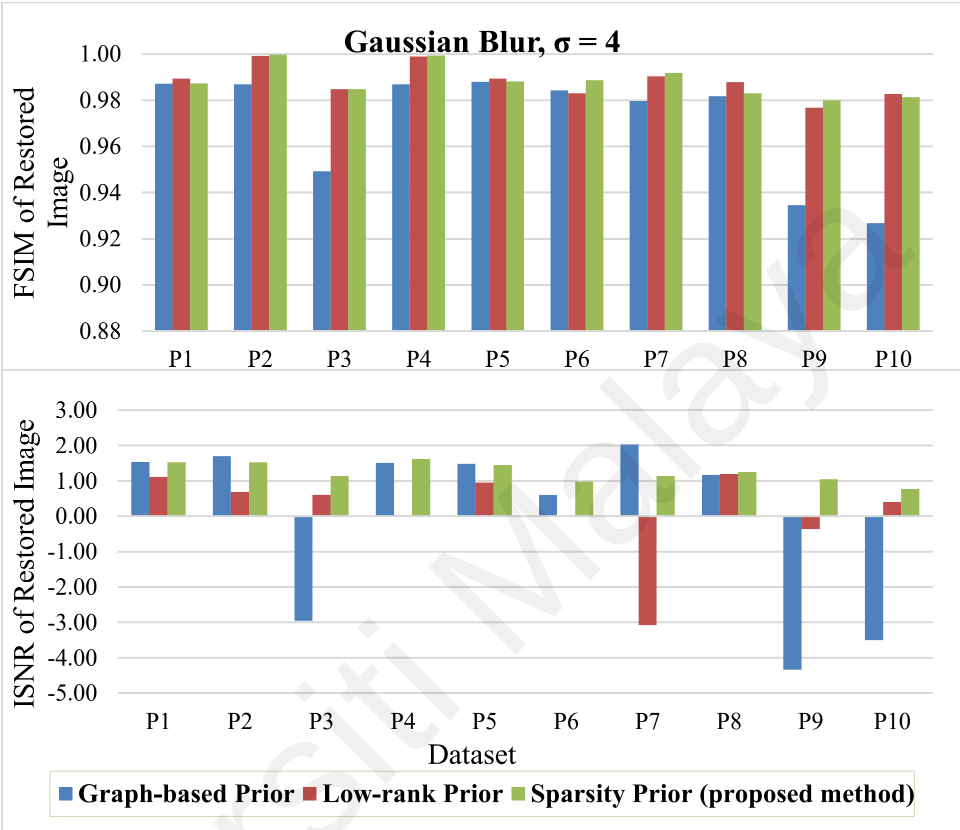

Figure 5.14: Quantitative evaluation for Gaussian blur, σ =4 in terms of ISNR, and FSIM on all datasets.

For this evaluation, the Sign test is used to better evaluate the level of significance for the proposed Sparsity Prior when combined with SPID. Table 5.8 presents the pairwise comparison results for the Sign test. For removal of large Gaussian blur, $\mathbf{D}_{\sigma = 4}$, the combination of proposed Sparsity Prior with SPID shows a significant performance over other combination methods except for the combination of Graph-based Prior with SPID. Whereas for small Gaussian blur, $\mathbf{D}_{\sigma = 1}$, the performance is generally not significant.

Table 5.8: Pairwise comparisons of proposed Sparsity Prior + SPID to other combination Gaussian blur removal; The '-' sign indicates *p*-value > 0.1.

Sparsity Prior + SPID		Graph-based Prior + SPID	Low-rank Prior + SPID	Graph-based Prior + HPID	Low-rank Prior + HPID	Sparsity Prior + HPID
Gaussian blur, $D_{\sigma=1}$						
FSIM	Wins (+)	5	7	6	6	5
	Loses (-)	5	3	4	4	5
Detected differences		-	-	-	-	-
ISNR	Wins (+)	5	9	6	7	8
	Loses (-)	5	1	4	3	2
Detected differences		**-**	s̈ = **0.05**	**-**	**-**	s̈ = **0.1**
Gaussian blur, $D_{\sigma=4}$						
FSIM	Wins (+)	7	9	10	10	9
	Loses (-)	3	1	0	0	0
Detected differences		**-**	s̈ = **0.05**	s̈ = **0.005**	s̈ = **0.005**	s̈ = **0.05**
ISNR	Wins (+)	6	10	10	10	10
	Loses (-)	4	0	0	0	0
Detected differences		**-**	s̈ = **0.005**	s̈ = **0.005**	s̈ = **0.005**	s̈ = **0.005**

(c) Motion blur

In these experiments, this work tested four motion blur cases which comprise one linear motion blur and three examples of nonlinear motion blur. The FSIM and ISNR of restored motion blur images by competing methods are tabulated in Table 5.9 and Table 5.10.

Table 5.9: Quantitative evaluation in terms of ISNR and FSIM for the competing algorithms in restoring linear motion and nonlinear motion-blurred images. The bold numbers are either the highest FSIM or ISNR, which indicate the best performance.

Dataset	Type of Blur	Linear motion, angle = 30 degree				Nonlinear Motion 1, M_{nl-1}			
	Algorithm	**SPID**		**HPID**		**SPID**		**HPID**	
	Quantitative metrics	**FSIM**	**ISNR**	**FSIM**	**ISNR**	**FSIM**	**ISNR**	**FSIM**	**ISNR**
Sample P1	Graph-based Prior	0.9959	3.91	0.9927	3.48	0.9515	-1.44	**0.9754**	**1.60**
	Low-rank Prior	0.9948	3.18	0.9930	2.84	0.9261	-3.92	0.9553	-2.59
	Sparsity Prior	**0.9970**	**4.60**	**0.9934**	**4.01**	**0.9920**	**2.95**	0.9433	-1.20
Sample P2	Graph-based Prior	0.9880	2.34	0.9870	2.22	0.9314	-1.31	**0.9766**	**1.11**
	Low-rank Prior	0.9917	2.05	0.9895	1.92	0.9269	-2.53	0.9644	-0.66
	Sparsity Prior	**0.9961**	**4.19**	**0.9912**	**3.14**	**0.9849**	**2.62**	0.9313	-1.38
Sample P3	Graph-based Prior	0.9930	2.93	0.9887	2.30	0.9449	-0.54	**0.9667**	**0.50**
	Low-rank Prior	0.9876	0.74	0.9846	1.03	0.9511	-1.95	0.9445	-1.77
	Sparsity Prior	**0.9944**	**3.60**	**0.9895**	**2.67**	**0.9787**	**1.90**	0.9464	-1.00

Table 5.9, continued.

Dataset	Type of Blur	Linear motion, angle = 30 degree				Nonlinear Motion 1, M_{nl-1}			
	Algorithm	SPID		HPID		SPID		HPID	
	Quantitative metrics	FSIM	ISNR	FSIM	ISNR	FSIM	ISNR	FSIM	ISNR
Sample P4	Graph-based Prior	0.9828	2.13	0.9846	2.41	0.9378	-1.40	**0.9806**	**1.91**
	Low-rank Prior	0.9830	0.57	0.9845	0.86	0.9368	-2.63	0.9734	0.43
	Sparsity Prior	**0.9962**	**4.65**	**0.9917**	**3.72**	**0.9871**	**2.35**	0.9407	-0.91
Sample P5	Graph-based Prior	0.9943	3.44	0.9907	2.93	0.9434	-1.11	**0.9621**	**-0.36**
	Low-rank Prior	0.9950	3.28	0.9915	2.66	0.9368	-4.08	0.9610	-1.63
	Sparsity Prior	**0.9965**	**4.12**	**0.9921**	**3.38**	**0.9842**	**1.35**	0.9409	-1.11
Sample P6	Graph-based Prior	**0.9968**	**3.19**	0.9906	-0.25	**0.9290**	-1.02	**0.9720**	**0.30**
	Low-rank Prior	0.9928	1.92	**0.9922**	**1.53**	0.9206	-2.83	0.9555	-1.07
	Sparsity Prior	0.9913	0.06	0.9903	0.15	0.9117	-2.11	0.9155	-1.27
Sample P7	Graph-based Prior	**0.9902**	**2.82**	0.9846	1.09	0.9345	-0.98	**0.9647**	**-0.19**
	Low-rank Prior	0.9835	0.46	0.9827	0.56	0.9327	-2.19	0.9318	-1.93
	Sparsity Prior	0.9886	1.74	**0.9851**	**1.64**	**0.9729**	-0.37	0.9419	-0.65
Sample P8	Graph-based Prior	0.9937	3.31	0.9865	2.38	0.9408	-1.43	**0.9814**	**1.65**
	Low-rank Prior	0.9943	2.89	**0.9897**	2.39	0.9404	-2.20	0.9829	2.08
	Sparsity Prior	**0.9944**	**3.87**	0.9891	**3.08**	**0.9846**	1.49	0.9386	-1.21
Sample P9	Graph-based Prior	**0.9895**	**2.48**	0.9671	-0.20	0.9302	-0.93	**0.9595**	**-0.28**
	Low-rank Prior	0.9852	1.11	0.9804	0.96	0.9179	-1.76	0.9528	-1.05
	Sparsity Prior	0.9856	2.23	**0.9833**	**1.80**	**0.9697**	**-0.75**	0.9350	-0.86
Sample P10	Graph-based Prior	0.9900	2.56	0.9896	1.90	0.9303	-1.15	**0.9733**	**-0.36**
	Low-rank Prior	0.9930	2.13	**0.9897**	1.53	0.9345	-2.43	0.9507	-1.53
	Sparsity Prior	**0.9938**	**3.11**	0.9895	**2.14**	**0.9758**	**-0.29**	0.9251	**-0.82**
Dataset	**Type of Blur**	**Nonlinear Motion 2, M_{nl-2}**				**Nonlinear Motion 3, M_{nl-3}**			
Sample P1	Graph-based Prior	0.9864	-0.40	**0.9971**	5.34	0.9263	-2.27	0.9348	-0.67
	Low-rank Prior	0.9790	-1.84	0.9929	0.24	0.9268	-2.39	**0.9784**	**0.75**
	Sparsity Prior	**0.9993**	**7.12**	0.9865	-0.70	**0.9741**	**1.32**	0.9291	-1.54
Sample P2	Graph-based Prior	0.9821	-1.73	**0.9948**	**1.89**	0.9030	-2.42	**0.9485**	**-0.36**
	Low-rank Prior	0.9784	-2.67	0.9945	0.44	0.9340	-0.98	0.9220	-1.83
	Sparsity Prior	**0.9959**	1.01	0.9868	-1.50	**0.9554**	**0.40**	0.9117	-1.60
Sample P3	Graph-based Prior	0.9847	-0.47	**0.9903**	0.84	0.9158	-2.32	0.9512	**-0.43**
	Low-rank Prior	0.9633	-3.45	0.9780	-2.43	0.9229	-3.08	**0.9575**	-0.69
	Sparsity Prior	**0.9959**	**1.54**	0.9858	-0.19	**0.9452**	**-0.04**	0.9312	-0.67
Sample P4	Graph-based Prior	0.9834	-0.89	**0.9973**	4.64	0.9002	-3.23	0.9493	-0.66
	Low-rank Prior	0.9881	-0.60	0.9779	-2.83	0.9081	-3.42	**0.9769**	**1.53**
	Sparsity Prior	**0.9990**	**5.71**	0.9806	-1.27	**0.9660**	1.19	0.9106	-2.06
Sample P5	Graph-based Prior	0.9857	-0.63	**0.9957**	**4.55**	0.9213	-2.23	0.9240	-0.62
	Low-rank Prior	0.9811	-1.71	0.9918	-0.25	0.9234	-2.48	**0.9811**	**1.91**
	Sparsity Prior	**0.9987**	4.32	0.9877	-0.23	**0.9629**	0.18	0.9247	-1.31

Table 5.9, continued.

Dataset	Type of Blur	Nonlinear Motion 2, M_{nl-2}				Nonlinear Motion 3, M_{nl-3}			
	Algorithm	**SPID**		**HPID**		**SPID**		**HPID**	
	Quantitative metrics	**FSIM**	**ISNR**	**FSIM**	**ISNR**	**FSIM**	**ISNR**	**FSIM**	**ISNR**
Sample P6	Graph-based Prior	**0.9802**	0.36	**0.9874**	**1.45**	**0.9448**	**-1.01**	**0.9386**	**-1.37**
	Low-rank Prior	0.9568	-4.33	0.9577	-4.48	0.9246	-5.56	0.9289	-5.15
	Sparsity Prior	0.9650	-1.85	0.9614	-2.47	0.9065	-6.19	0.9291	-3.04
Sample P7	Graph-based Prior	0.9771	-1.51	**0.9727**	**-1.18**	0.8943	-3.25	0.9315	-0.52
	Low-rank Prior	0.9577	-5.28	0.9620	-4.97	0.9312	-2.97	0.8903	-3.49
	Sparsity Prior	**0.9874**	**-0.64**	0.9687	-1.57	**0.9451**	**-0.19**	**0.9398**	**-0.32**
Sample P8	Graph-based Prior	0.9830	-1.33	**0.9964**	**3.22**	0.9203	-2.31	0.9771	**1.33**
	Low-rank Prior	0.9823	-1.82	0.9968	3.10	0.9703	0.96	0.9244	-1.56
	Sparsity Prior	**0.9995**	**6.45**	0.9861	-0.53	**0.9291**	-0.71	**0.9784**	0.96
Sample P9	Graph-based Prior	0.9819	-0.67	**0.9923**	**-0.22**	0.9134	-0.76	0.9331	**-0.12**
	Low-rank Prior	0.9773	-1.31	0.9876	-0.88	0.9210	-0.95	**0.9577**	-0.47
	Sparsity Prior	**0.9977**	**-0.05**	0.9818	-0.54	**0.9456**	-0.14	0.9306	-0.23
Sample P10	Graph-based Prior	0.9845	-0.65	**0.9917**	**2.84**	0.9166	-0.91	0.9419	**-0.59**
	Low-rank Prior	0.9731	-4.47	0.9729	-4.65	0.9257	-1.32	**0.9650**	-0.67
	Sparsity Prior	**0.9981**	**4.02**	0.9827	-0.38	**0.9603**	**0.50**	0.9246	-0.73

From Tables 5.9, it can be observed that, in most of the cases, the sparsity prior method can attain the highest FSIM and ISNR values. For better observation, the restoration results of the linear motion blur, M_l, and the three nonlinear motion blur, M_{nl-1}, M_{nl-2}, and M_{nl-3} are summarized in Table 5.9. Then, the count of the combination methods that achieved the highest FSIM and ISNR value is recorded in Table 5.10. For M_l blur estimation, SPID outperforms HPID with 100% highest FSIM and ISNR value for all cases, whereas, there are only 90% highest FSIM and 60% highest ISNR, 90% highest FSIM and 70% highest ISNR, and 90% highest FSIM and 70% highest ISNR cases found for nonlinear motion blind M_{nl-1}, M_{nl-2}, and M_{nl-3}, respectively.

Table 5.10: Blind image restoration Performance for a combination of methods in restoring motion-blurred images. The number denotes the total count of the highest achievement (i.e., winner) in the FSIM or ISNR value.

Blind image restoration	M_l		M_{nl-1}		M_{nl-2}		M_{nl-3}	
	FSIM	ISNR	FSIM	ISNR	FSIM	ISNR	FSIM	ISNR
Graph-based Prior + SPID	**3**	**3**	0	0	0	0	0	1
Low-rank Prior + SPID	0	0	0	0	0	0	0	0
Sparsity Prior + SPID	**7**	**7**	**9**	**6**	**9**	**7**	**4**	**4**
Graph-based Prior + HPID	0	0	**1**	**4**	**1**	**3**	0	**2**
Low-rank Prior + HPID	0	0	0	0	0	0	**5**	**4**
Sparsity Prior + HPID	0	0	0	0	0	0	1	0

Based on the winner counts in Table 5.10, it can be noted that for the nonlinear blur, the proposed method is considerably effective to restore the structure of the image since 9 out of 10 cases are achieving the highest FSIM. However, in terms of SNR, the result of the graph-based prior is almost comparable to sparsity prior.

To further evaluate these results, the Sign test is conducted as presented in Table 5.11. In this table, it can be noted that the combination of proposed Sparsity Prior with SPID shows significant performance in linear motion blur removal compared to other combination methods except for the combination of Graph-based Prior with SPID. Whereas for nonlinear motion blur removal, this combination is significantly better than the combination of Graph-based Prior with SPID, Low-rank Prior with SPID, and Sparsity Prior with HPID. It is considered significant for the combination of Low-rank Prior with HPID, but not for the combination of Graph-based Prior with HPID.

Table 5.11: Pairwise comparisons of proposed Sparsity Prior + SPID to other combination methods in motion blur removal; The '-' sign indicates *p*-value > 0.1.

Sparsity Prior + SPID		Graph-based Prior + SPID	Low-rank Prior + SPID	Graph-based Prior + HPID	Low-rank Prior + HPID	Sparsity Prior + HPID
Linear motion, angle = 30 degree						
FSIM	Wins (+)	7	9	10	9	10
	Loses (-)	3	1	0	1	0
Detected differences		**-**	$\ddot{s}$ = **0.05**	$\ddot{s}$ = **0.005**	$\ddot{s}$ = **0.05**	$\ddot{s}$ = **0.005**
ISNR	Wins (+)	7	9	10	9	9
	Loses (-)	3	1	0	1	1
Detected differences		**-**	$\ddot{s}$ = **0.05**	$\ddot{s}$ = **0.005**	$\ddot{s}$ = **0.05**	$\ddot{s}$ = **0.05**
Nonlinear Motion 1, M_{nl-1}						
FSIM	Wins (+)	9	9	9	9	9
	Loses (-)	1	1	1	1	1
Detected differences		$\ddot{s}$ = **0.05**	$\ddot{s}$ = **0.05**	$\ddot{s}$ = **0.05**	$\ddot{s}$ = **0.05**	$\ddot{s}$ = **0.05**
ISNR	Wins (+)	9	10	7	9	9
	Loses (-)	1	0	3	1	1
Detected differences		$\ddot{s}$ = **0.05**	$\ddot{s}$ = **0.005**	**-**	$\ddot{s}$ = **0.05**	$\ddot{s}$ = **0.05**
Nonlinear Motion 2, M_{nl-2}						
FSIM	Wins (+)	9	10	9	10	10
	Loses (-)	1	0	1	0	0
Detected differences		$\ddot{s}$ = **0.05**	$\ddot{s}$ = **0.005**	$\ddot{s}$ = **0.05**	$\ddot{s}$ = **0.005**	$\ddot{s}$ = **0.005**
ISNR	Wins (+)	9	10	7	10	10
	Loses (-)	1	0	3	0	0
Detected differences		$\ddot{s}$ = **0.05**	$\ddot{s}$ = **0.05**	**-**	$\ddot{s}$ = **0.005**	$\ddot{s}$ = **0.1**
Nonlinear Motion 3, M_{nl-3}						
FSIM	Wins (+)	9	9	7	3	9
	Loses (-)	1	1	3	7	1
Detected differences		$\ddot{s}$ = **0.05**	$\ddot{s}$ = **0.05**	**-**	**-**	$\ddot{s}$ = **0.05**
ISNR	Wins (+)	9	9	7	7	8
	Loses (-)	1	1	3	3	2
Detected differences		$\ddot{s}$ = **0.05**	$\ddot{s}$ = **0.05**	**-**	**-**	$\ddot{s}$ = **0.1**

For better illustration of the restoration results in motion blur removal, Figures 5.15, 5.16, 5.17, and 5.18 plot the graph bars of restoration results using SPID for linear motion blur M_l, nonlinear motion blind M_{nl-1}, M_{nl-2}, and M_{nl-3}, respectively.

In Figure 5.15, it is clearly shown that the proposed sparsity prior method outperforms the other methods in most cases, except for data samples P6 and P7. These results again showed that the sparsity prior is not effective in restoring degraded images with characteristics of sample P6 and P7 (i.e. dataset with images with large smooth regions and limited edge structures), on the contrary, the graph-based prior is more effective in restoring this type of image.

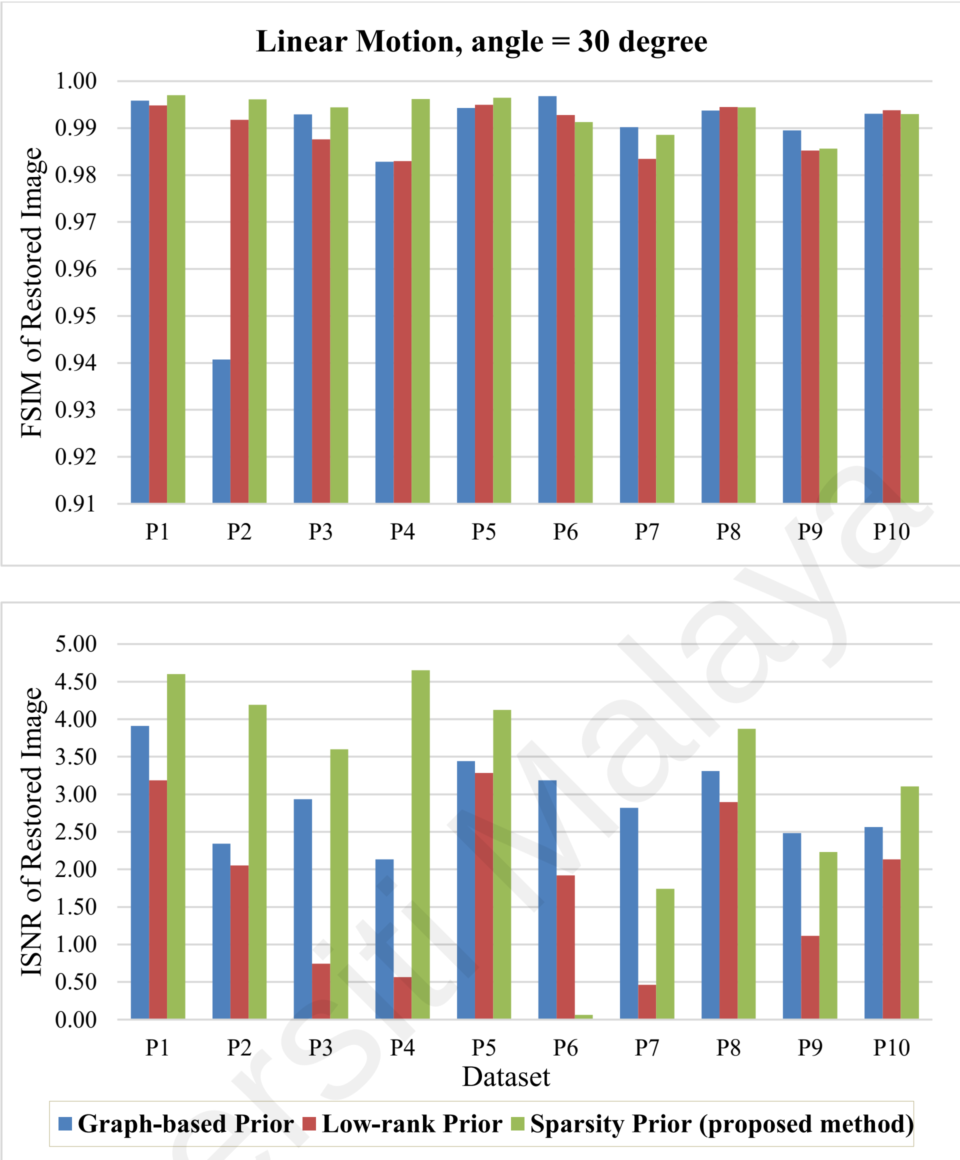

Figure 5.15: Quantitative evaluation for linear motion blur, angle = 30 degrees in terms of ISNR and FSIM on all datasets.

Figure 5.16 shows the comparison of FSIM and ISNR achieved by the three prior-based estimation methods on all datasets with complex motion blur. As shown in Figure 5.16, the restoration results with the proposed blur kernel estimation attain the highest FSIM in most cases except data sample P6, whereas in terms of ISNR, six out of 10 datasets have the highest ISNR.

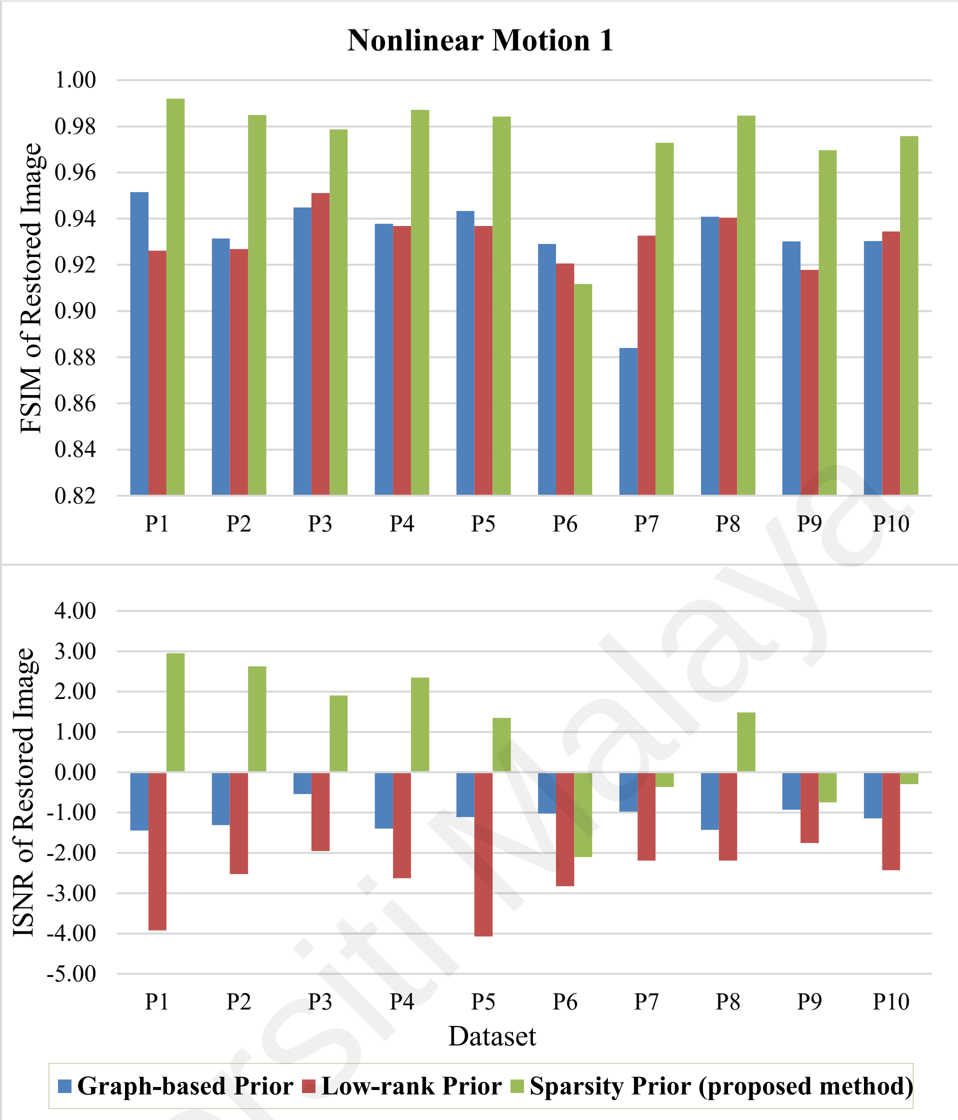

Figure 5.16: Quantitative evaluation for nonlinear motion blur 1 in terms of ISNR and FSIM on all datasets.

Figure 5.17 shows the comparison of FSIM and ISNR achieved by the three prior-based estimation methods on all datasets with another example of complex motion blur. In terms of FSIM, the proposed sparsity prior-based blur estimation method significantly outperforms the other method except for data sample P6. Whereas in terms of ISNR, the proposed method attains the highest ISNR value in seven cases except for data samples P6, P7, and P9.

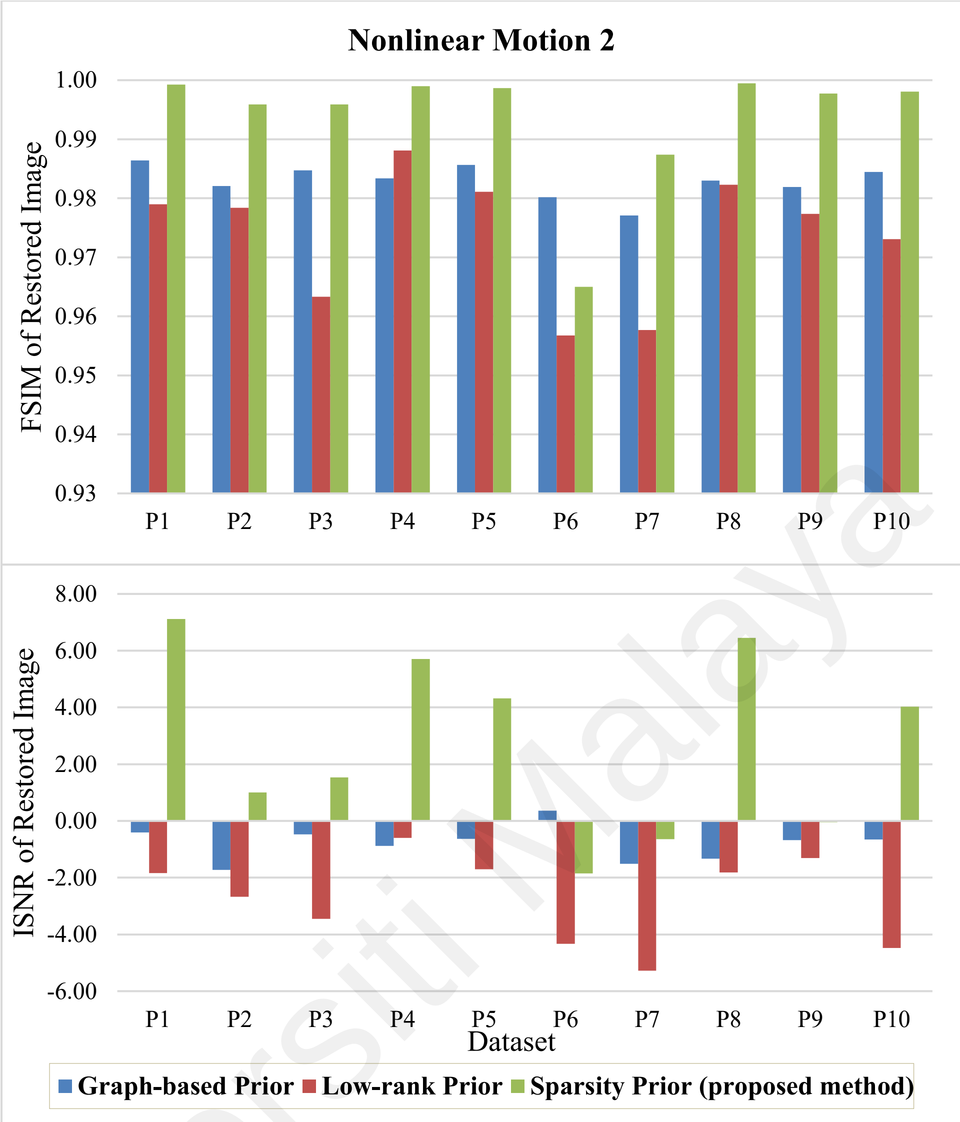

Figure 5.17: Quantitative evaluation for nonlinear motion blur 2 in terms of ISNR and FSIM on all datasets.

Figure 5.18 plots the FSIM and ISNR achieved by the three prior-based estimation methods on all datasets with another example of complex motion blur. In terms of FSIM, the proposed sparsity prior-based blur estimation method outperforms the competing methods except for data sample P6. Whereas in terms of ISNR, the proposed method only attains the highest ISNR value in five cases.

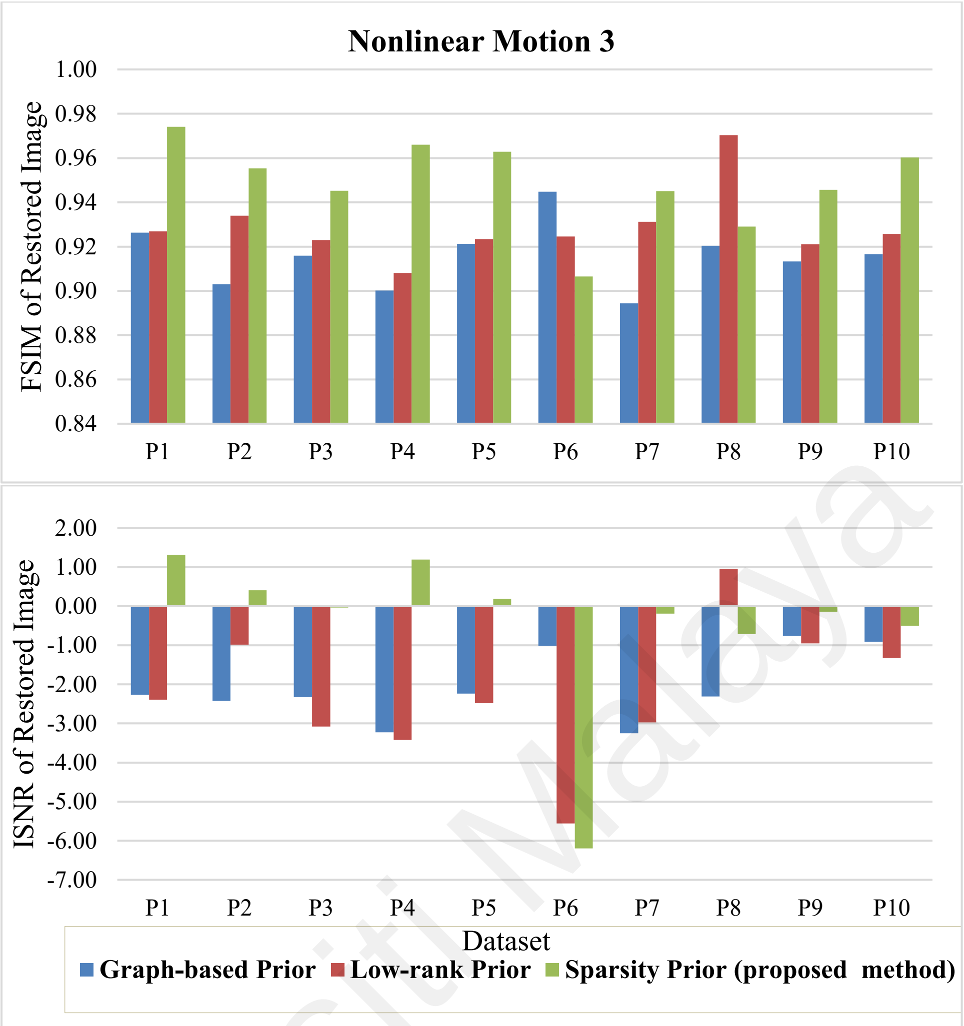

Figure 5.18: Quantitative evaluation for nonlinear motion blur 3 in terms of ISNR and FSIM on all datasets.

Based on the effectiveness evaluations presented in this subsection. In comparison with other algorithms in terms of SSDE, FSIM, and ISNR, and the Sign test, the sparsity prior algorithms achieve the best overall performance, followed by the graph-based prior algorithms, and then the low-rank prior algorithms. Further details about the findings will be discussed in Section 5.5.

5.4.1.3 Visual Observation

In this subsection, eight sets of visual restoration results are presented, which demonstrate deblurring of the eight blur cases (i.e., listed in Table 5.1), respectively.

Figure 5.19 shows a comparison of the three algorithms on defocus blurred images with low contrast edge structures and details. Due to inaccurate blur kernel estimation, the restored image of the graph-based prior method (Bai et al., 2019) in Figure 5.19(d) still contains a large blur that smears out image details. The low-rank prior method of Ren et al. (2016) shows better results (see Figure 5.19(e)) than the graph-based prior method, but cannot small details (e.g., building floor levels cannot be differentiated in the red box). The result of the proposed sparsity prior is shown in Figure 5.19(a) performs best in both kernel estimation and latent sharp image restoration; it can be noticed the size and shape of the estimated blur kernel are closer to the ground truth, thus it recover more image details.

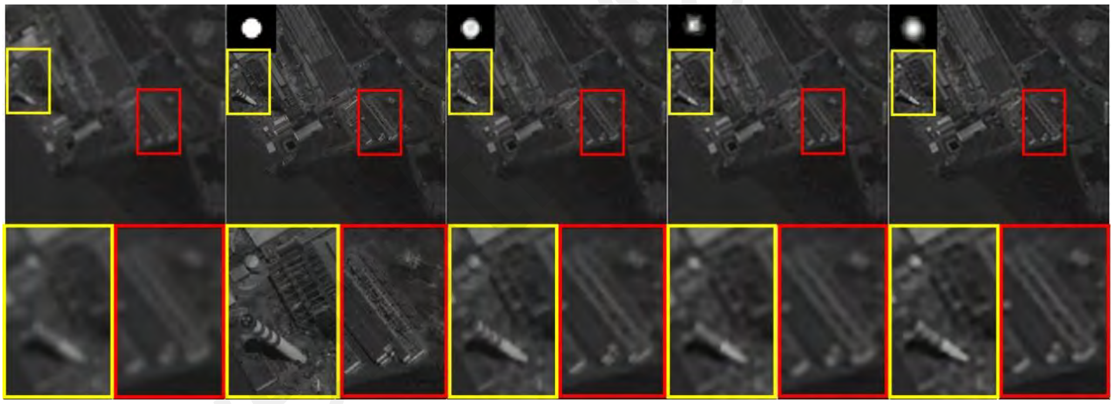

(a) (b) (c) (d) (e)

Figure 5.19: Visual comparison of restored image for defocus case (disk size = 5); The red and yellow boxes denote a cropped region in (a) Blurry-noisy image. (b) Ground truth Image and blur kernel (c) results using the proposed sparsity prior (d) results of Ren et al. (2016) using low-rank prior, and (e) results of Bai et al. (2019) using graph-based prior. The images are better viewed in full size on the computer screen.

Figure 5.20 shows the visual observation of restoration results for another defocus blur case (i.e, defocus with a disk radius size of 10). In comparison, visually, it is can be noticed that the estimated blur kernel in Figure 5.20 (c) is more accurate compared to the estimated blur kernels of the graph-based prior method and low-rank prior method in Figures 5.20 (d) and 5.20 (e), respectively. Among all, the graph-based prior perform the worse restoration results.

(a) (b) (c) (d) (e)

Figure 5.20: Visual comparison of restored image for defocus case (disk size = 10); The red and yellow boxes denote a cropped region in (a) Blurry-noisy image. (b) Ground truth Image and blur kernel (c) results using the proposed sparsity prior, (d) results of Bai et al. (2019) using graph-based prior, and (e) results of Ren et al. (2016) using low-rank prior. The images are better viewed in full size on the computer screen.

In Figure 5.21, a comparison of visual restoration results for a challenging example (i.e., data sample with low contrast and narrow edge structure) is presented.

(a) (b) (c) (d) (e)

Figure 5.21: Visual comparison of restored image for Gaussian blur, σ = 1; The red and yellow boxes denote a cropped region in (a) Blurry-noisy image. (b) Ground truth Image and blur kernel (c) results using the proposed sparsity prior, (d) results of Bai et al. (2019) using graph-based prior, and (e) results of Ren et al. (2016) using low-rank prior. The images are better viewed in full size on the computer screen.

From the close-up view, it can be observed that the graph-based prior method presents a clearer and pleasant appearance compared to the other methods. However, the sparsity prior presents a restored image with better contrast than the graph-based prior. The lowrerank prior estimated a much larger PSF compared with the ground truth, thus presenting visual restoration results with a slight halo effect.

In the next figure, this work demonstrates an example of visual comparison restoration results for data samples with large-scale edge structures and smooth regions. Visually, the restoration results of the sparsity prior in Figure 5.22 (c) and the graph-based prior in Figure 5.22 (d) are comparable. In the close-up view, visually, the sparsity prior is slightly better as it presents a better contrast and sharper edge that results in a more natural appearance, whereby the graph-based prior presents a flat appearance. The visual restoration of the low-rank prior in Figure 5.22 (e) suffers from an aliasing effect due to the obvious deviation between the estimate blur kernel and the ground truth kernel.

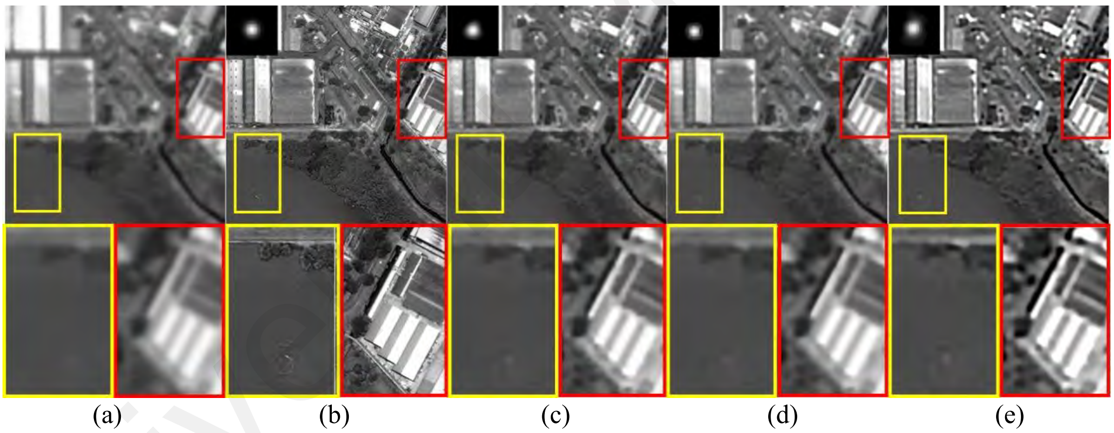

Figure 5.22: Visual comparison of restored image for Gaussian blur, σ = 4; The red and yellow boxes denote a cropped region in (a) Blurry-noisy image. (b) Ground truth Image and blur kernel (c) results using the proposed sparsity prior, (d) results of Bai et al. (2019) using graph-based prior, and (e) results of Ren et al. (2016) using low-rank prior. The images are better viewed in full size on the computer screen.

For the linear motion blur image in Figure 5.23(a), the proposed sparsity prior method estimate a more accurate blur kernel compared to the other methods, hence the restored image as shown in Figure 5.23(c) is visually better than those in Figures 5.23(d) and 5.23(e). Among others, again, in this case, the low-rank-based prior method performs the worse qualitative evaluation results.

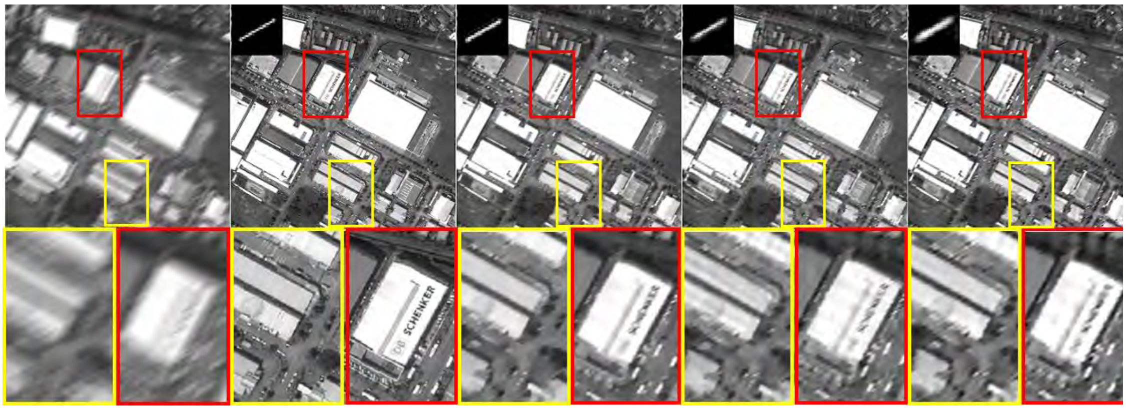

(a) (b) (c) (d) (e)

Figure 5.23: Visual comparison of restored image for linear motion blur (angle direction = 30 degrees); The red and yellow boxes denote a cropped region in (a) Blurry-noisy image. (b) Ground truth Image and blur kernel (c) results using the proposed sparsity prior, (d) results of Bai et al. (2019) using graph-based prior, and (e) results of Ren et al. (2016) using low-rank prior. The images are better viewed in full size on the computer screen.

In addition to the capability in dealing with the blurred image containing rich textures and small details, the proposed sparsity method also can deal with complex motion blur kernels, as shown in Figure 5.24.

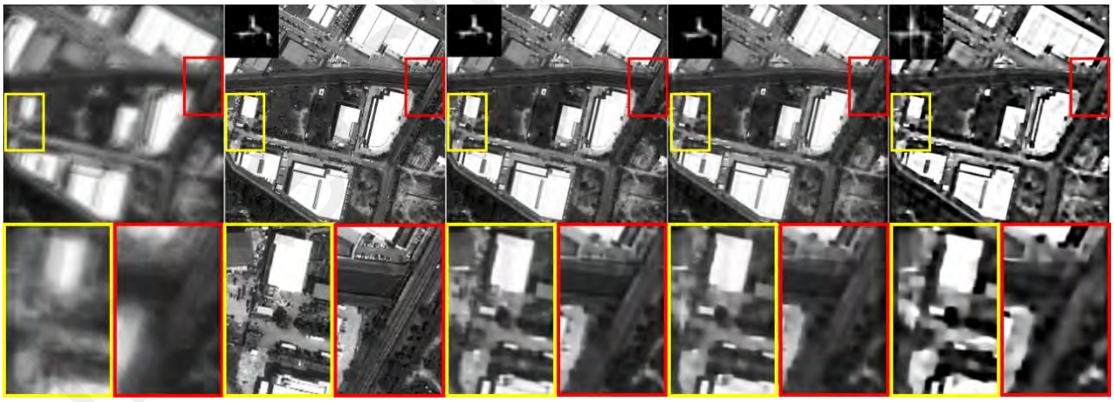

(a) (b) (c) (d) (e)

Figure 5.24: Visual comparison of restored image for nonlinear motion blur (i.e., M_{nl-1}); The red and yellow boxes denote a cropped region in (a) Blurry-noisy image. (b) Ground truth Image and blur kernel (c) results using the proposed sparsity prior, (d) results of Bai et al. (2019) using graph-based prior, and (e) results of Ren et al. (2016) using low-rank prior. The images are better viewed in full size on the computer screen.

Due to the complex blur, the low-rank prior method of Ren et al. (2016) cannot estimate the blur kernel accurately; as the kernel estimation results in Figure 5.24 (c) contain some obvious noise, hence the restored image suffers from obvious noise and ringing artifacts. The blur kernel estimated by the graph-based prior method of Bai et al. (2019) in Figure 5.24 (e) is over smooth, hence it cannot recover fine details in the blurred image. Visual comparison in Figure 5.24 demonstrates that the proposed algorithm estimates a more accurate blur kernel compared to other methods, thus recover sharper edges and more image details.

Figure 5.25 shows another example of a nonlinear motion blur. From Figures 5.25 (c), 5.25(d), and 5.25 (e), one can easily see the visual improvement in the images by the competing methods, and the results are almost comparable. However, from the close-up view, there are boundary artifacts observed in the restored image by the graph-based prior and low-rank prior methods. Besides, the restored image by the low-rank prior still contains some blur. In contrast, the kernels estimated by the proposed sparsity prior method are most similar to the ground truth, thus, it presents a restored image with sharper edges and fine details.

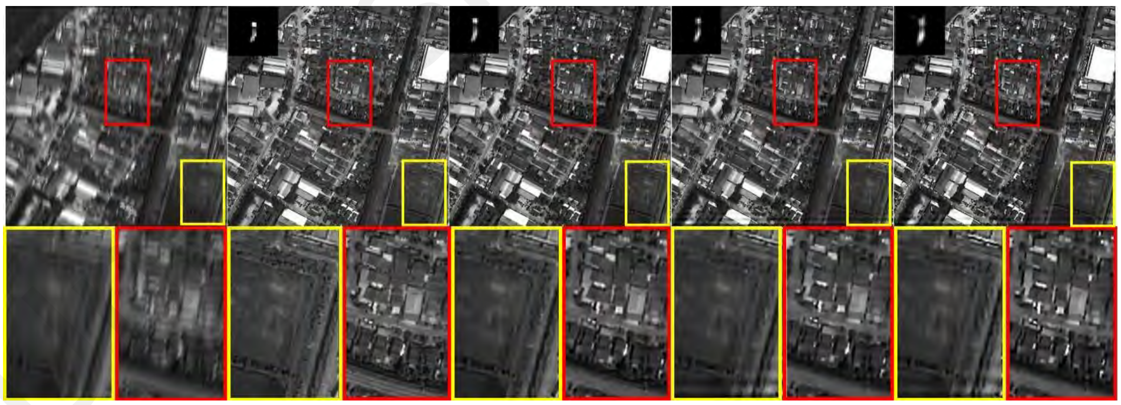

(a) (b) (c) (d) (e)

Figure 5.25: Visual comparison of restored image for nonlinear motion blur (i.e., $M_{nl\text{-}2}$); The red and yellow boxes denote a cropped region in (a) Blurry-noisy image. (b) Ground truth Image and blur kernel, (d) results of Bai et al. (2019) using graph-based prior, and (e) results of Ren et al. (2016) using low-rank prior. The images are better viewed in full size on the computer screen.

Figure 5.26 shows another comparison of restoration results for a large and complex motion blur data sample. From this figure, it can be noticed that the kernels estimated by the proposed method and graph-based prior method are more similar to the ground truth whereas the results by low-rank prior methods contain some amount of noise. Based on this observation, it can be noted that the deblurred images by Ren et al. (2016) contain ringing artifacts. The graph-based prior methods by Bai et al. (2019), although perform well on kernel estimation, but the final deblurred images appear to be flat and less detail is recovered. The proposed sparsity prior method performs the best in kernel estimation and the restored image by SPID recovers sharper edges and more fine details.

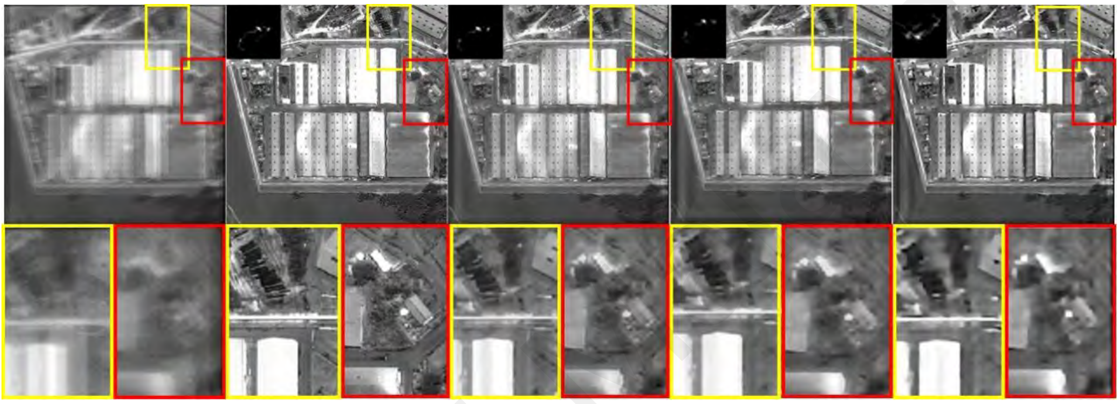

(a) (b) (c) (d) (e)

Figure 5.26: Visual comparison of restored image for nonlinear motion blur (i.e., $M_{nl\text{-}3}$); The red and yellow boxes denote a cropped region in (a) Blurry-noisy image. (b) Ground truth Image and blur kernel (c) results using the sparsity prior, (d) results of Bai et al. (2019) using graph-based prior, and (e) results of Ren et al. (2016) using low-rank prior. The images are better viewed in full size on the computer screen.

5.4.2 Experiments on Real Unknown Blurred Data

In addition to the synthetic blurred data, this work also uses real unknown blurred images to further demonstrate the effectiveness of the proposed method. Since the restoration results for synthetic blurred data in the previous subsection show that the graph-based prior is fairly comparable to the proposed sparsity prior in some cases, whereas low-rank prior is outperformed by the proposed sparsity prior. Therefore, in this experiment, this work excludes the low-rank prior method is excluded but concentrates on evaluating the performance of the SPID with the estimated sparsity prior kernel input against the state-of-art work of Bai et al. (2019) that uses estimated graph-based prior kernel input. Since the ground truth images and kernels are unknown in these cases, this work analyzes the restoration results qualitatively. Figure 5.27 shows some of the restoration results on the real blur satellite images of RazakSAT.

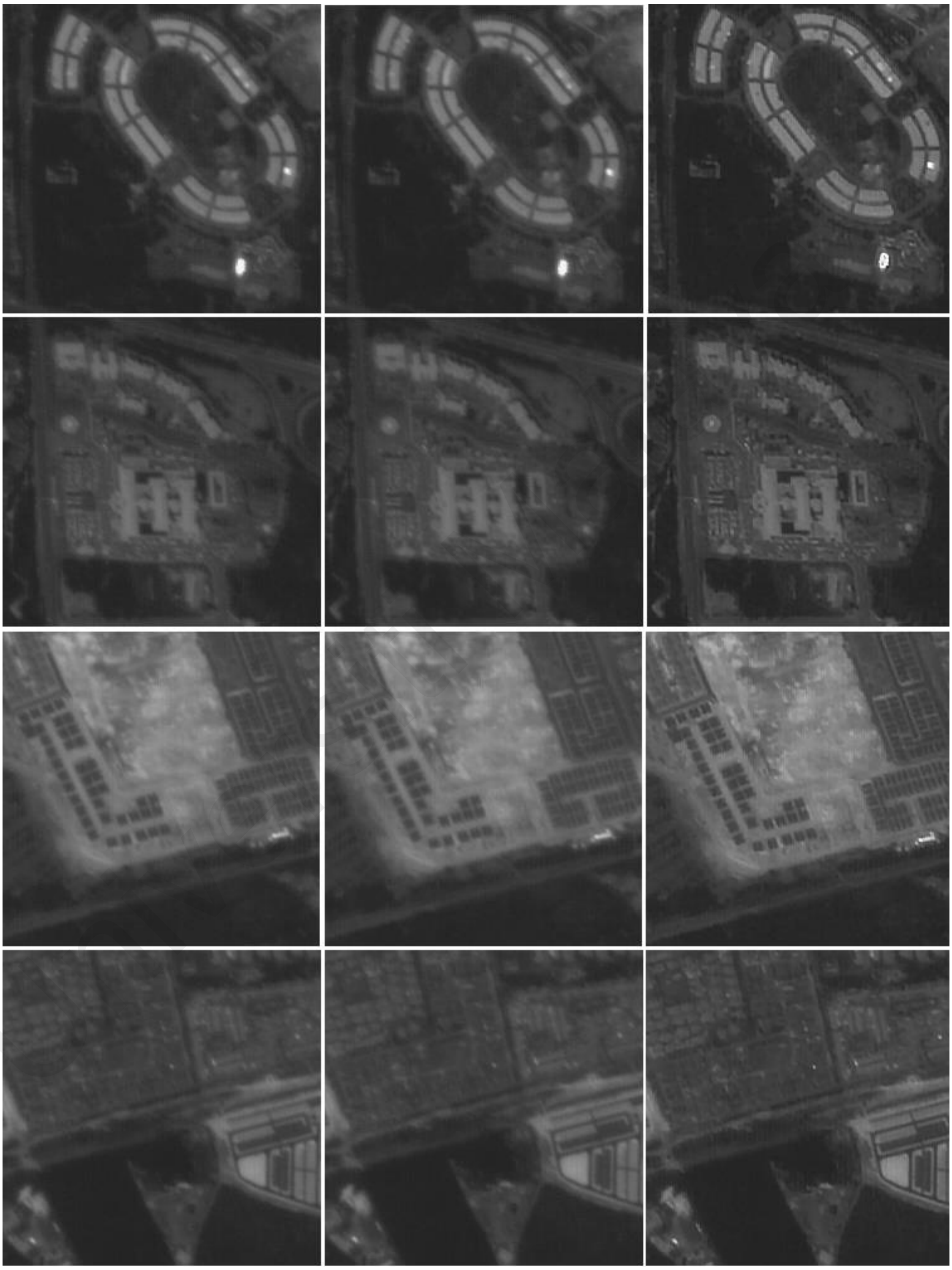

(a) (b) (c)

Figure 5.27: Visual comparison of competing methods. Deblurring results by SPID using (a) estimated blur kernel of the graph-based prior method, (b) original image without deblurring process, and (c) the estimated blur kernel of the proposed sparsity prior methods.

The rest of the experiment results are available in Appendix D. By contrast, it can be noticed that the restored images generated by the proposed algorithm are sharper and clearer whereas those recovered using estimated graph-based prior kernel input do not show much improvement from the real unknown blurred data. This indicates that the graph-based prior estimation method is not effective in restoring images with a small amount of blur and low contrast images.

5.4.3 Algorithm Complexity and Computational Time

The proposed IR algorithms, sparsity prior, and low-rank prior algorithms are implemented in MATLAB on an Intel Core i5 CPU with 8 GB of RAM. For a fair comparison, the executable program of graph-based prior is also run in the same setup. In the implementation, for an image of size 512×512, SPID costs (21.60 ± 0.89) seconds, whereas the competing IR method (Krishnan & Fergus, 2009) costs (1.24 ± 0.16). The average processing time of the three blur estimation algorithms on 512 × 512-pixel size datasets is presented in Table 5.9.

Table 5.12: Average processing time (minutes) of different methods on images of size 512×512.

Blur Type	Kernel size	Processing time (minutes)		
		Graph-based Prior	Low-rank Prior	Sparsity Prior
$D_{d=5}$	25 × 25	1.2 ± 0.07	24.35 ± 0.42	4.5 ± 0.12
$D_{d=10}$	45 × 45	1.7 ± 0.04	22.76 ± 0.80	8.1 ± 0.29
$G_{\sigma=1}$	25 × 25	1.1 ± 0.01	23.06 ± 0.78	4.3 ± 0.19
$G_{\sigma=4}$	45 × 45	1.8 ± 0.08	23.02 ± 0.66	8.6 ± 0.32
M_{l}	25 × 25	1.2 ± 0.03	21.69 ± 0.71	4.2 ± 0.28
M_{nl-1}	45 × 45	1.7 ± 0.05	21.36 ± 0.68	8.1 ± 0.31
M_{nl-2}	25 × 25	1.2 ± 0.02	23.58 ± 1.26	4.0 ± 0.13
M_{nl-3}	55 × 55	2.6 ± 0.13	21.37 ± 0.80	8.3 ± 0.21

Among the three blur estimation algorithms, the computational time of Graph-based prior algorithms is lower than the other algorithms. This is mainly because the optimization has a closed-form solution and the graph filter is implemented with an accelerated Lanczos method (Susnjara, Perraudin, Kressner & Vandergheynst, 2015). Even though the low-rank prior algorithms have a closed-form solution, it evitably suffers from high computational complexity as it requires solving costly SVD, which has complexity $O(N^3)$ in general. However, unlike methods by graph-based prior methods and the proposed sparsity prior, the low-rank prior blur estimation method is independent of the input size kernel. Both the graph-based and sparsity prior blur estimation method employed a coarse-to-fine strategy where its pyramid levels are determined by the size blur kernel. For example, in the proposed sparsity prior algorithm, a kernel size with 25 × 25 kernel will require four pyramids, whereas both 45 × 45 and 55 × 55 require five levels of the pyramid to yield the final estimated kernel results, thus require more processing time.

5.5 Discussion

Based on the experimental results presented in Section 5.4, the following observations were found. First, choosing a suitable type of prior for an accurate kernel estimation is a challenging task. As it depends not only on the type of blur but also on the amount of blur and the characteristic of images (e.g., contrast, dense or sparse image details). In comparison with other algorithms in terms of SSDE, FSIM, and ISNR, the sparsity prior algorithms achieve the best overall performance, followed by the graph-based prior algorithms, and then the low-rank prior algorithms. However, it can be noted all the prior-based blur estimation methods still cannot obtain satisfactory results on some challenging datasets. For example, all these representative algorithms achieve relatively higher SSDE in datasets with defocus type of blur in Subsection 5.4.1.1., these results indicate that they are not robust in deblurring defocus blur. Among the representative algorithms, the sparsity prior method achieves relatively better results than the other methods. With the highest SSDE, one can see that the graph-based prior algorithm has the lowest FSIM and ISNR in the final image restoration results. Moreover, the graph-based prior method is not as effective compared with the other methods when dealing with low contrast images. In this case, the low-rank prior can recover the structure of a low contrast image better than the sparsity prior. In this comparative study, although sparsity prior algorithms have achieved promising performance on both synthetically blurred and real unknown blur satellite data, efforts can be made in promoting the robustness of the sparse representation. Thus, devising a more robust blur estimation algorithm is an important issue.

Second, it can be noted from the experimental results that high computational complexity in the kernel estimation process is one of the drawbacks in blind image restoration. Generally, the restoration process for the final image restoration methods takes less than 30 seconds, but it is not the case for blur kernel estimation methods. In terms of speed (i.e., processing time), the low-rank prior and sparsity prior take a much longer time to converge than the graph-based prior. Moreover, compared with the low-rank and sparsity prior that used the ℓ_1-regularized sparse representation-based image restoration methods, the graph-based prior has very competitive restoration results with significantly low complexity.

Third, the extensive experimental results have demonstrated that there is no absolute winner between sparsity prior and graph-based prior in deciding which method achieves the best performance for nonlinear motion blur datasets. Nevertheless, the proposed algorithms were found more capable than the graph-based prior algorithms to deblur images with both small and large blur kernels especially when the blurred images contain rich details.

Fourth, the proposed sparsity prior-based kernel estimation algorithm is not without flaws. The method would fail when the blurred image is textureless. As mentioned in Chapter 4, Section 4.3.2.1, the proposed kernel prior assists to extract salient edges in the intermediate image to improve the accuracy of the estimated kernel. Thus, if the blurred image is textureless or less texture, salient edges cannot be obtained for kernel estimation. Figure 5.28 shows a failure case. As the input image only contains less texture and a more smooth area, the proposed algorithms fail to estimate the blur kernel, which leads to degraded deblurred results.

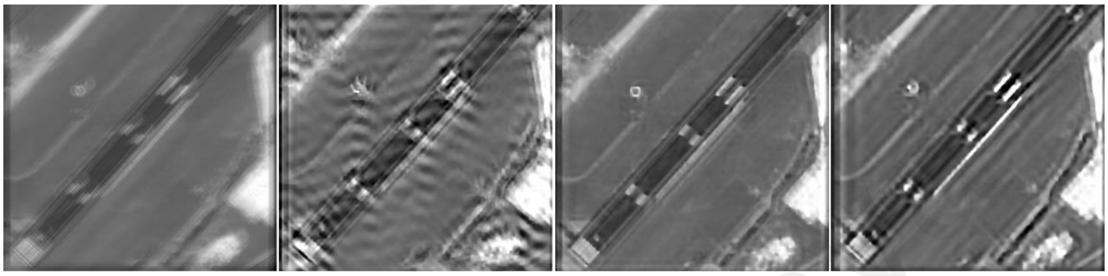

(a) (b) (c) (d)

Figure 5.28. One example of a limitation using the blur kernel that is estimated by the proposed sparsity prior-based method. (a) Blurred-noisy image, (b) restoration result using the proposed sparsity prior, (c) restoration result of Bai et al. (2019) using graph-based prior, and (d) restoration result of Ren et al. (2016) using low-rank prior. With limited salient structures in the input image that degraded with non-linear motion blur, the proposed method fails to estimate an accurate blur kernel. As a result, the deblurred images of (b) contain obvious artifacts compared to (c) and (d). Among others, the graph-based prior method by Bai et al., (2019) performs the best.

As explained in Section 5.2.1.2., the low-rank prior-based method work by shrinking small singular values which usually correspond to textures in an image. Thus, the low-rank prior method will fail if a blurred image contains rich textures because most of the textures will be removed and few sharp edges are retained for kernel estimation. Figure 5.29 shows an example and the deblurred result of the low-rank prior method as compared to other methods.

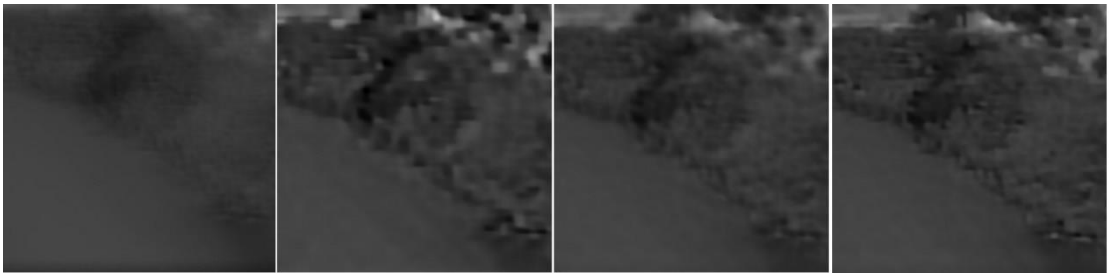

(a) (b) (c) (d)

Figure 5.29. One example of a limitation using the blur kernel that is estimated by the low-rank prior method. (a) Blurred-noisy image, (b) restoration result of Ren et al. (2016) using low-rank prior (c) restoration result of Bai et al. (2019) using graph-based prior, and (d) restoration result using the proposed sparsity prior. As the blurry image (a) contains rich textures (e.g., forest), the low-rank prior method fails to recover clear results and the deblurred result in (b) contains obvious ringing artifacts. For blurred images with rich textures, the proposed sparsity prior method performs the best since it recovers more textures as shown in (d) compared to other methods.

The limitation of the graph-based prior method by Bai et al. (2019) is that it tends to smear out minor details and creating a flattened image. As explained in 5.2.2., Bai et al. (2019) use a skeleton image to retain the strong gradients in an image that smooths out the minor details. Figure 5.30 shows an example and the deblurred result of the graph-based prior method as compared to other methods.

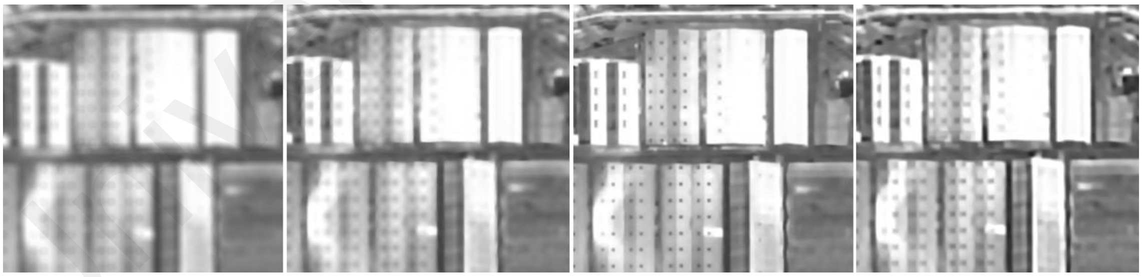

(a) (b) (c) (d)

Figure 5.30.One example of a limitation using the blur kernel that is estimated by the graph-based prior method. (a) Blurred-noisy image, (b) restoration result of Bai et al. (2019) using graph-based prior, (c) restoration result using the proposed sparsity prior, and (d) restoration result of Ren et al. (2016) using low-rank prior. As the blurry image (a) contains mostly large structures with fewer textures, it is obvious that the graph-based prior method cannot produce clear deblurred results (b) and recover small details in the blurred image. Among all, the proposed sparsity prior method performs the best.

Fifth, this work suggests that while the sparse prior is helpful, the key component making blind deconvolution possible is not solely based on the choice of prior, but also requires the thoughtful choice of estimator. For example, the graph-based prior method, even though they obtained the worse kernel estimation results (i.e., highest SSDE) for all datasets in subsection 5.4.1.1, but with SPID, it is shown to produce better restoration results than the Low-rank prior method using the same SPID in Figure 5.31. In Figure 5.31 and all figures that followed, the quantitative measurement value at the left of the slash denotes SSDE and the right of the slash denotes ISNR (dB).

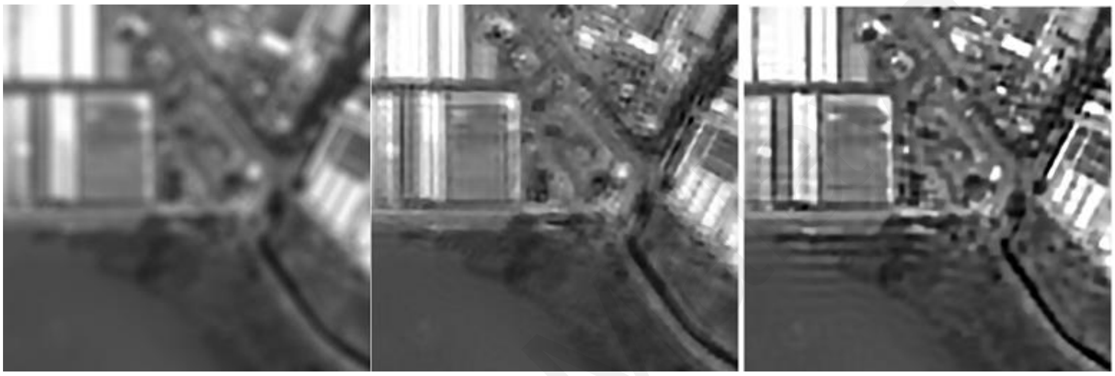

(a) (b) (c)

Figure 5.31. Comparison of restored image for defocus case (disk size = 10) using SPID between Graph- and low-rank prior kernel estimation methods; (a) Blurred-noisy image, (b) restoration results by Bai et al. (2019) using graph-based prior, (0.1400/1.22dB), and (c) restoration results by Ren et al. (2016) using low-rank prior, (0.0711/0.65dB).

For nonlinear motion blur kernel estimation of M_{nl-3} (as shown in Table 5.4(a)), among the three prior-based estimation methods, the graph-based prior method performs the best, whereas the low-rank prior method performed the worse. However, the low-rank prior method achieved the highest FSIM and ISNR in some cases using the HPID. Figure 5.32 shown a comparison of restoration results for a blurred image with M_{nl-3}.

(a) (b) (c)

Figure 5.32. Visual comparison of restored image for nonlinear motion blur (i.e., $M_{nl\text{-}3}$) using HPID among all the kernel estimation methods; (a) restoration results by the proposed sparsity prior method, (0.0067/-1.31dB), (b) restoration results by Ren et al. (2016) using low-rank prior, (0.0095/1.91dB), and (c) restoration results by Bai et al. (2019) using graph-based prior, (0.0055/-0.62dB).

Figure 5.33 shows another example of image restoration with nonlinear motion blur (i.e., $M_{nl\text{-}3}$). In this example, in terms of SSDE, the proposed sparsity-base prior method is outperformed by the graph-based prior method. In this case, the graph-based produce better restoration using the HPID instead of SPID. However, with the SPID as the image restoration estimator, the proposed method can produce better restoration results than the best restoration of the graph-based prior method.

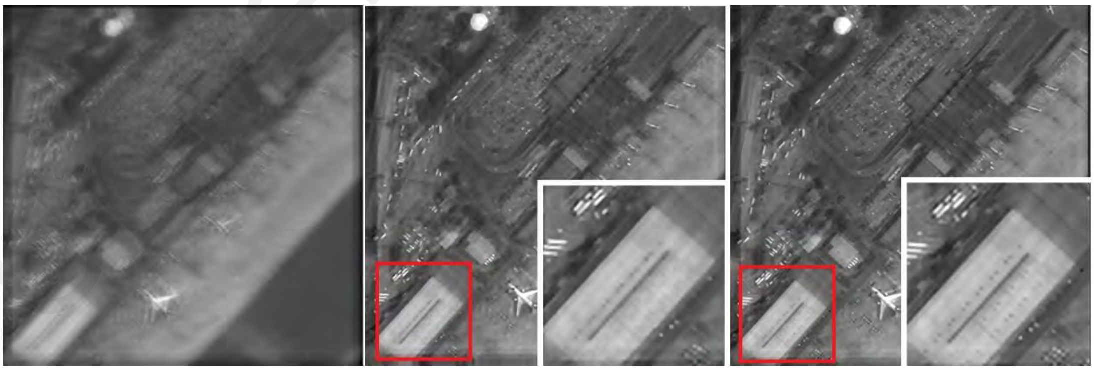

(a) (b) (c)

Figure 5.33. Visual comparison of restored image for nonlinear motion blur (i.e., $M_{nl\text{-}3}$) between the graph-based prior and the proposed sparsity prior kernel estimation methods using the HPID and SPID, respectively; red box denotes cropped region. (a) Blurry-noisy image, (b) restoration results by Bai et al. (2019) using graph-based prior, (0.0048/-0.59dB), and (c) restoration results by the proposed sparsity prior method, (0.0062/0.50dB). The zoom-in view of the cropped region results in (c) recovers more details than (b).

Figure 5.34 shows the last example of image restoration by the proposed kernel estimation method. Figures 5.34 (a) and 5.34 (b) show restoration results using the same kernel estimation results, but the different choice of estimator. Figure 5.34(a) is restored using the HPID, whereas Figure 5.34(b) is restored using the SPID. Based on the visual comparison, it is obvious that the SPID produces better restoration results than HPID.

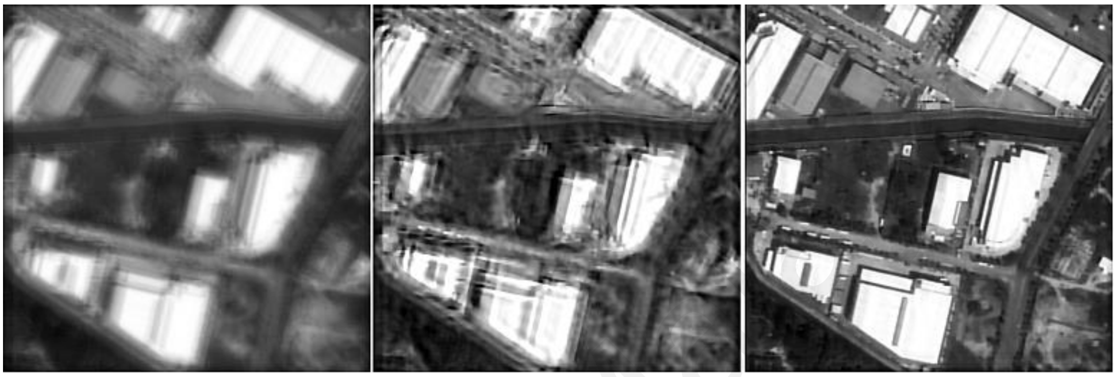

(a) (b) (c)

Figure 5.34. Visual comparison of restored images for nonlinear motion blur (i.e., M_{nl-1}) using the same kernel estimation results (i.e., by the proposed method), but the different choice of the estimator; (a) Blurry-noisy image, (b) image restoration result by HPID, and image restoration result by SPID.

Finally, based on the experimental results, and the presented examples, it can be concluded that the proposed sparsity prior kernel estimation method produces better image restoration results with the SPID as the choice of estimator.

5.6 Conclusion

This chapter presents three different prior-based blur kernel estimation algorithms, namely the graph-based prior, low-rank prior, and sparsity prior (i.e., the proposed kernel estimation algorithms in Chapter 4), which adopt the concept of sparse representation methods for image deblurring. This work discusses their motivations, mathematical representations, and applications. More specifically, this work conducts a comparative study to analyze and evaluate these algorithms experimentally to gain further understanding of image priors that appropriate for blur removal in optical satellite images regardless of the blur type. The type of blur includes defocusing, Gaussian, uniform blur, linear motion, and nonlinear motion blur. In this work, the graph-based prior and low-rank prior algorithms are developed based on the works from Bai et al., (2019), and Ren et al. (2016) respectively. In addition, this work employed two non-blind image deconvolution (ID) methods for the final image restoration. To evaluate the performance of the three prior-based blur kernel estimation algorithms, the SSDE was used as the quantitative measure, whereas for image quality assessment, ISNR, FSIM, and computation time are included as the quantitative measurement. Besides, numerical measurement, this work also includes visual observation for qualitative measurement. The evaluation for SSDE values shows that the proposed sparsity prior kernel estimation method achieves the best overall performance, followed by the graph-based prior algorithms, and lastly the low-rank prior algorithms. This indicates the robustness of the proposed method in recovering the various type of blur. Furthermore, the experimental results in the final image restoration also evident that the estimated blur kernel by the proposed method can effectively restore the blurry-noisy images with a more than 70% success rate. Based on the experimental studies and show that with a proper estimation rule, blind image restoration can be performed even with a simple prior. This study shows that with a proper estimation rule, blind deconvolution can be performed even with a simple prior such as the proposed sparsity prior. In particular, it shows that the proposed blur estimation with sparsity prior is effective for estimating the blur kernel of degraded optical satellite images, and with the use of the SPID and HPID method, it can remove the blur in the degraded image effectively. Nevertheless, experimental results have shown that the proposed method favors the SPID over HPID, this is because the remotely sensed optical satellite images are generally fuzzy, and HPID is not effective in restoring images with a small amount of blur and low contrast images. The proposed method is based on the structure extraction method, hence it is not efficient in estimating blur images with a largely smooth region, on contrary, the graph-based prior algorithm that uses skeleton images as a PWS proxy is more efficient and effective in estimating this type of image. Both the graph-based prior and low-rank prior method require complex formulations, however, with the use of an accelerated Lanczos method (Susnjara et al., 2015), the graph-based prior can estimate a blur kernel with a pixel size of 55×55 in not more than 2.6 seconds. Unfortunately, for the low-rank prior method that uses the SVD, it requires expensive computational time, but yet it performed the worse among the three prior-based kernel estimation methods. Therefore, in this study, it is concluded that complex formulations cannot be assumed to produce restoration results more effectively. Sparse representation has a wide potential for low-vision applications in the optical satellite image processing application. Thus, developing an efficient and robust sparse representation method for blur estimation is still the main challenge and to design a more effective and efficient sparse prior based kernel estimation is being expected and is beneficial to performance improvement.

CHAPTER 6: REGULARIZED-BASED MODULATION TRANSFER FUNCTION COMPENSATION FOR SPATIAL IMAGE QUALITY IMPROVEMENT

This chapter addresses the problems of noise and moiré patterns of the Modulation Transfer Function Compensation (MTFC) method in operational use. The existing MTFC is not effective in noise suppression and preserving image details, thus compromise the image quality (e.g., signal to noise ratio) in the delivered product data (Lee et al., 2016). While there are many image restoration methods available for typical natural images, they often compromised by the computational burden that not practical for remote sensing imagery. Hence, the purpose of this work is to propose a regularization-based MTFC method that executes an optimal trade-off between noise regularization and detail preservation for high fidelity low-level vision processing of EOS data products with minimum computational complexity. To design the regularization function, this work exploits the merit of image priors in both local smoothness and nonlocal self-similarity properties of an image in a hybrid domain (viz., space spatial, and frequency). Later, a simple joint statistical model in the Curvelet domain is established to combine these two properties. In order to make this regularization-based MTFC method tractable and robust, this work employs a bilevel optimization approach to compensate for degradation and subsequently improve the quality of the delivered product data.

6.1 Introduction

Spatial image quality is one of the key parameters for characterizing and validating image data (Chen, 1996). Hence, it is important to appreciate the spatial characteristics of image data, particularly if the data is to be used for image analysis since the quality of the analysis depends on the quality of the data. However, in the imaging chain, remotely sensed imagery from optical satellites frequently suffers from the inevitable effects of degradations. The degradations could happen due to extrinsic or intrinsic factors as discussed in Subsection 2.3. These sorts of degradations reduce the image quality, therefore, they need to be compensated; and they can be compensated using the MTF, which is the degradation function for that image restoration problem.

Based on the literature review in Section 2.3, two main challenges in spatial image restoration for optical satellite images have been discovered: (1) The adverse effects (i.e., noise amplification and aliasing) of existing MTFC compromise the signal to noise ratio (SNR) of the delivered product data (Albert, 2015; Lee et al., 2016). (2), while there are many image restoration methods available for image quality improvement, they are often accompanied by a higher computational cost (e.g, Ren et al., 2016; Zha et al., 2018).

Recall that the fundamental task of image restoration is to deconvolve the degraded image with the spread function that exactly describes the distortion. Convolution in the spatial domain incurs a high computational cost when compared with the cost of multiplication operation for the filters in the frequency domain. Moreover, a remotely sensed image is typically large with a massive amount of information encoded in each observation; and each scene contains abundant texture with small details compared to a typical natural image, this resulted in even higher computational cost. On the contrary, in the frequency domain, owing to the FFTs, multiplications correspond to convolution operations can be accelerated. Thus, it reduces the computation burden. However, it still has its drawbacks. For example, the Wiener Filter (Wiener, 1964); this filter is the most widely used MTFC method (e.g., Bretschneider, 2002, Li et al., 2015, Oh et al., 2014; Aouinti et al., 2016; Lee et al, 2018) because it is simple, fast, and give good results in the case of degradation with the relatively small blur. Nevertheless, it is still an ill-posed problem even though with known MTF. The ill-posed problem will give rise to artifacts such as ringing and noise amplification in the restored image. Figure 6.1 depicts some of the typical side effects of the restoration problem in spatial- and frequency-domain.

Figure 6.1: Comparison of visual quality for image restoration in different domains. The red box denotes the cropped region. (a) Original Image, (b) Restored image by Wiener filter (Lee et al., 2016), illustrating the rise of ringing effect and noise amplification, and (c) Restored image by Anisotropic TV model (Pan et al., 2017), illustrating over smooth effect that created an unnatural appearance.

Unlike typical natural images, in a realistic situation of remote sensing, the pixel intensity of acquired remote sensing images could be not uniform. In addition, most of their structures are submerged in the image and it is hard to distinguish the content of these images. Hence, seeking a robust method that will deblur, and penalize noise but preserves sharp discontinuities details in the restored image with minimum computation cost, is a significant challenge in the optical satellite image restoration problems.

Based on the studies of previous work, two shortcomings have been discovered. First, utilizing only one image property in the regularization-based framework is insufficient to obtain satisfying restoration results. For example, on one hand, image restoration using an anisotropic TV-prior by Pan et al., (2017) has shown to be effective in recovering the main structures of the image with less visible noise in the local smooth region, but not effective in preserving fine details as shown in Figure 6.2(a). On the other hand, the image restoration with a Laplacian prior (Oh and Choi, 2014) has been shown to be effective in preserving abundant tiny textures, but not effective in suppressing noise and ringing artifacts in the restored image as shown in Figure 6.2(b). Second, there is a need to design a framework for MTFC that exhibits the most appropriate compromise among computational complexity, reliability, and robustness to noise. Therefore, this work proposes a framework for high-fidelity MTF compensation for optical satellite image restoration by characterizing both local smoothness and nonlocal self-similarity of images in minimum computational complexity. Given the fact that non-blind deconvolution can be regarded as a separate step in the image restoration process which disregards the blur kernel estimation process. Moreover, in recent years, considerable literature has grown up around image restoration with blur kernel estimation. Little attention has been paid to the non-blind image restoration technique. Hence, this work considers a non-blind MTF Compensation that excludes the blur kernel estimation process and focuses on final image restoration with a known blur kernel. Technically, using a non-blind MTF Compensation excludes image acquisition and processing (e.g., blur kernel estimation) variability, but only concentrates on the restoration technique.

(a) (b)

Figure 6.2: Comparison of visual quality for image restoration in different domains. The yellow and red boxes denote the cropped regions. (a) Restored image using anisotropic TV-prior (Pan et al., 2017); As can be seen there are no visible noise and ringing artifacts in the cropped regions, but the forest tree and the roof are too smooth. (b) Restored image by Laplacian prior (Oh and Choi, 2014); as can be seen that the cropped regions are rich in detail, however, they also exhibit a few ringing artifacts.

The main contributions of this framework are listed as follows. First, from the perspective of image statistics, this work designs two regularization terms that exploit local smoothness and nonlocal self-similarity properties of the image in the hybrid spatial and frequency domain in Section 6.3. Following this, this work establishes a simple joint statistical model in the Curvelet domain to combine the two regularization terms to ensure a more reliable and robust estimation for MTFC. Second, a new form of minimization function for compensating MTF is formulated using the proposed regularization-based framework. Third, to have a tractable and robust regularization-based MTFC method, a bilevel optimization approach for MTFC is developed to efficiently solve the underdetermined inverse problem.

The remainder of the Chapter is organized as follows. Section 6.2 describes some common characteristics from the perspective of the image statistic and optimization approach that was employed to design the proposed MTFC framework. Next, Section 6.3 introduces the objection functions containing regularization terms in the bilevel optimization problems and elaborates on the details of solving optimization. The experimental results and discussions are provided in Section 6.4. Finally, Section 6.5 concludes this chapter.

6.2 Proposed Strategies and Solutions for MTFC

This section describes the strategies and solutions that are applied to design the MTFC framework to attain the objectives of this work. Remote sensing images, like any typical natural image, serve as the main stimuli of the human visual system; but in a more complex way to aid in observing the dynamic earth's surface on a greater scale and depth. As such, knowing more about the structure (and statistics) of these extremely complex and diverse stimuli is important for gaining a better understanding of the visual system. As aforementioned in Chapter 1, the scope of work is on spatial resolution, therefore, it excludes other characteristics such as radiometric and spectral out of this discussion. Hence, the remote sensing images and natural images can be treated in the same perspective, to find a good model that will tell us given an image g how likely it is that this image is natural by exploiting their properties and statistical structure, to design the image priors which is required to integrate information lost in the degradation processes.

6.2.1 Image Characteristic

Natural images have several important statistical properties that manifest themselves in different contexts, many of them relevant to the works presented. Of particular interest here are the multi-resolution representation of images and their non-Gaussian structure. Images can have multi-resolution representation, meaning that an image can be described at different levels of resolution in either spatial or frequency domain. One example is the image pyramid that was applied for kernel refinement in the proposed PSF kernel estimation in Section 4.3.2.1. (b). Another important property that plays a significant role in this work is the non-Gaussianity of natural images.

In the following subsections, the multi-resolution representation will be discussed, followed by a non-Gaussianity characteristic.

6.2.1.1 Multi-resolution representation

Curvelet, coined by Candès and Donoho (2000) provides a multi-resolution representation with several features that set them apart from other representations such as wavelets (Mallat, 1996), Gabor system (Feichtinger, 1989), steerable pyramids (Simoncelli & Freeman, 1995), etc. Besides having a strong directional character, Curvelets present a highly anisotropic behavior at a fine scale with effective support shaped according to the parabolic scaling principle.

The curvelet construction was originally developed for providing efficient representations of smooth objects with discontinuities along curves; It has been applied to many image processing problems such as data compression (e.g., Liu et al., 2016; Costa et al., 2015), image restoration (e.g., Swamy & Vani, 2016; Qiao et al, 2016; Panigrahi, Gupta & Sahu, 2018), image reconstruction (e.g., Durand, Frapart & Kerebel, 2017; Xiao, 2018), and image recognition (e.g., Elaiwat, 2015; Qiao et al., 2016).

One important property of curvelets that inspired us to employ them for this work is that it obeys the principle of harmonic analysis stating that it is possible to analyze and reconstruct an arbitrary function $f(x_1, x_2)$ as a superposition of such models (Candès et al. 2003). Hence, it can be used as a decomposition and reconstruction method.

There are two types of fast discrete Curvelet transforms (FDCT). The first one is based on unequally-spaced fast Fourier transforms (USFFT), whereas the other is based on the wrapping of specially selected Fourier samples (FDCT WARPING) (Candès et al., 2006). This work adopts the latter for this framework since this is the fastest Curvelet transform currently available (Candès et al., 2006; Luo et al, 2014).

6.2.1.2 Non-Gaussianity and heavy tails

One notable property of natural images is their non-Gaussianity. This can be explained by observing the marginal filter histograms in Figure 6.3. This figure depicted that the filter response histograms of zero mean filters, when applied to natural images always portray highly non-Gaussian shapes with strong peaks and heavy tails.

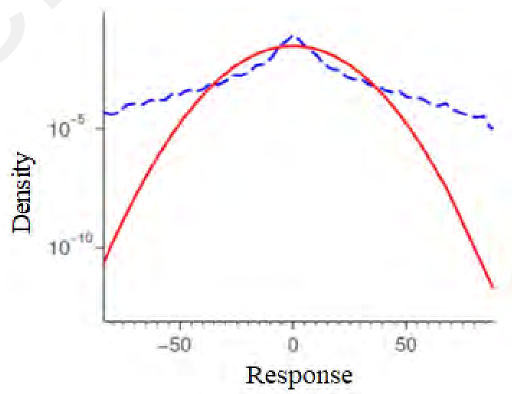

Figure 6.3: Non-Gaussianity of natural images. Illustrated is the histogram of horizontal derivative filter responses over a natural image, in a log scale. Note that the response histogram (blue dotted line) has much heavier tails than a Gaussian (solid red line). Correspondingly, the peak around zero is much narrower than a Gaussian.

The behavior of the marginal statistics of images modeled by general Gaussian distribution (GGD) has been explained in Subsection 3.1.1.2. The works from Pitkow

(2010), Wainwright & Simoncelli (1999), and Lam & Goodman (2000) explain why this non-Gaussian distribution arises in natural images. In the literature, studies have shown that the marginal distributions of image statistics have significantly heavier tails than a Laplacian, that well modeled by a hyper-Laplacian. Figure 6.4 presents four examples of an image with different characteristics and intensity; the first column displays the images in pixel-value, whereas the second and third column display gradient of the image in the horizontal direction and the histogram of the horizontal gradient image, respectively. Accordingly, as illustrated in Figure 6.4, optical satellite images also exhibit that heavy-tailed distribution.

(a)

(b)

(c)

(d)

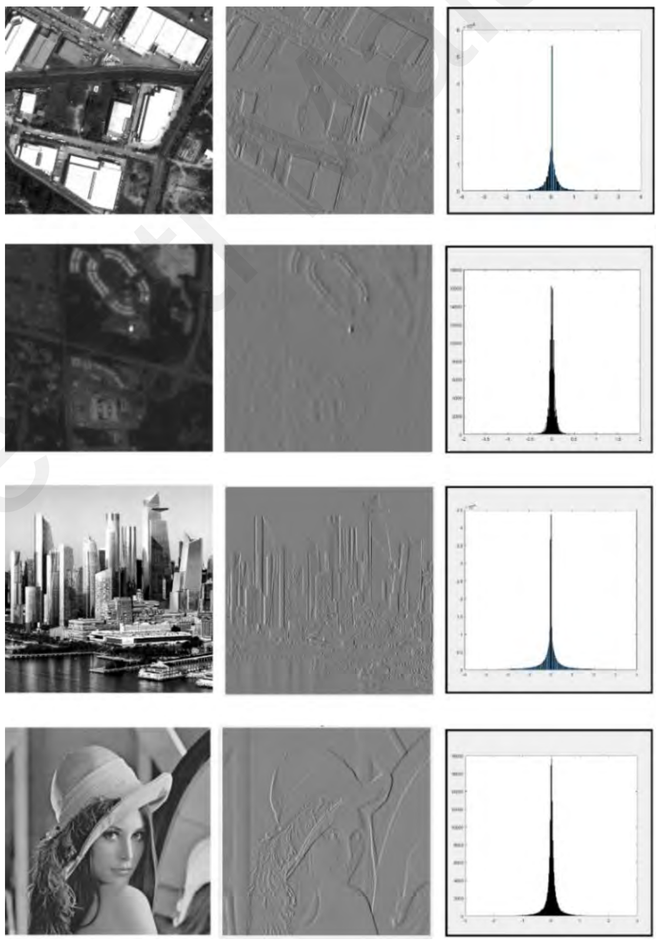

Figure 6.4: Various images with their respective gradient image and distribution in a horizontal direction. (a) IKONOS Image, (b) RazakSAT Image, (c) A real-world scene (d) The canonical images of Lena.

As mentioned in Subsection 3.1.1.2, one notable work about hyper-laplacian priors is that of Krishnan & Fergus (2009). Based on their works and many others (Xu, Hu & Peng, 2013; Chang & Wu 2015; Cheng et al., 2019), it can be noticed that regularization term using a hyper-Laplacian prior can obtain a clear image with main structures and fewer artifacts.

In order to further understand the attribute of image properties, an analysis is conducted to examine the frequency component of the restored image in different bands using the Curvelet transform as discussed in Subsection 6.2.1.1.

Let us recall the vector-matrix form of the image degradation model in Equation (4.5). Given a restored image, *f*, the subband decomposition model of Curvelet transform can be applied to yield a subband f_j described as

$$f_j = D_j(f), j \in \mathbb{Z}, \tag{6.1}$$

where D_j is a bandpass filter extracting frequency component of restored image *f* at each scale j in a corona of frequencies $|\xi| \in [2^j, 2^{j+1}]$, and $\mathbb{Z}$ is an integer number. The number of scales is determined by

$$N_j = [log_2(\min(m, n) - 3], \tag{6.2}$$

where *m* and *n* are the size of an image. For this analysis, this work uses synthetic images of 512×512-pixel size, therefore, subbands up to scale 6 are obtained for each image. The higher the scale the higher the frequency component in that subband, and vice versa. In this analysis, besides the hyper-Laplacian prior, this work also explores the characteristic of Gaussian prior and Laplacian prior.

This work employs a non-blind deconvolution method by Krishan & Fergus (2009), Cho & Lee (2009), and CLS filtering (Gonzalenz & Woods, 2017) that uses hyper-Laplacian prior, Gaussian prior, and Laplacian prior, respectively. This work analyzes two sets of 10 synthetic images, both sets are added Gaussian noise with standard deviation (SD) σ of 0.5, but different amounts of blur σ_b, (i.e., σ_b= 1 and σ_b= 4). In order to quantify the effectiveness of image priors, this work uses a Feature similarity index (FSIM) quality assessment (Zhang, L. et al., 2011). The FSIM index is a decimal value comprised between −1 and 1, where the closer the FSIM value to 1 the higher is the quality of the observed data.

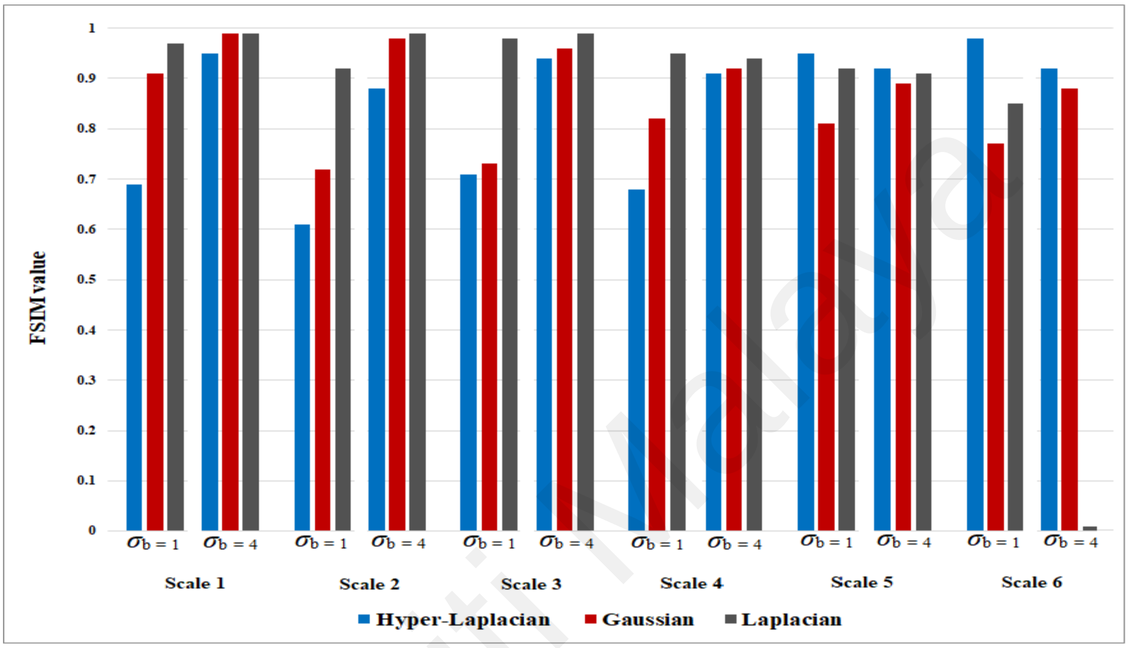

Figure 6.5: Comparison for image priors based on average FSIM of 10 synthetically blurred-noisy images.

Based on the graph presented in Figure 6.5, it can be noticed that hyper Laplacian prior (i.e., blue bars) at Scale 5 and 6 are taller than Gaussian prior (i.e., red bars) and Laplacian prior (i.e., dark grey bars). Hence, it is evident that the hyper Laplacian prior opts to concentrate derivatives at Scale 5 and 6. This indicates that it is more effective in maintaining the structure of an image regardless of the amount of blur compares to the other two priors.

For Gaussian prior, as expected, it is more effective in regularize smooth region (see Scale 1), since it prefers to distribute derivates equally over an image. One key observation from this analysis is that, regardless of the amount of blur, the CLS filter that employs Laplacian prior is very robust in the middle range frequencies (see Scale 2 to 4).

This indicates that it can preserve details of an image better than gaussian and hyper-Laplacian prior. However, as expected this filter is not efficient in restoring the high-frequency component of an image that contains a large amount of blur (see Scale 6, σ_b =4). The evidence reviewed here showed that different image priors characterize different and complementary aspects of natural image statistics. Thus, it will be beneficial to combine multiple priors to improve restoration performance.

Local smoothness and nonlocal self-similarity characteristics in image properties have been mentioned frequently in the previous chapters. From the description of the local smoothness and nonlocal self-similarity characteristic in image statistics, it implies that image properties can be perceived in three components, which comprises of smooth, texture, and structure as illustrated in Figure 6.6. Therefore, inspired by this, this work utilizes all three image priors, namely, the hyper-Laplacian priors, Gaussian, and Laplacian prior term to regularize the optimization solution in the proposed MTFC Framework. In the proposed framework, the hyper-Laplacian priors are designed to constrain the solution in preserving the structural component of nonlocal self-similarity, whereas the Laplacian priors are for preserving the texture component of nonlocal self-similarity. Furthermore, the Gaussian priors are designed to preserve the local smoothness component.

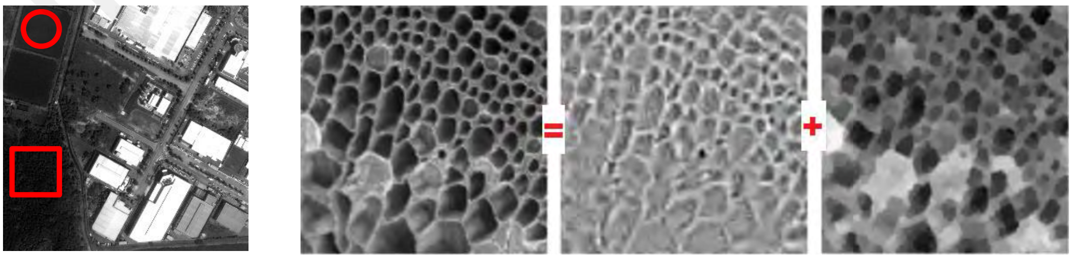

(a) (b) (c) (d)

Figure 6.6: Illustration of image properties. (a) Satellite image contains an example of local smoothness as shown by circular region, and nonlocal self-similarity as shown by square region, (b) a cropped region with nonlocal self-similarity properties, (c)-(d) depict decomposition of (b) into texture and structure region, respectively.

6.2.2 Hybrid Image Restoration Model through Bilevel Programming

Finding a solution to regularize noise while preserving image fidelity for natural images is unarguably a non-trivial problem. One successful approach is the hybrid approach. Some representative works in the literature are Joint Statistic Modelling (Zhang, J., 2014), Fourier-Wavelet Regularized Deconvolution (Neelamani, Choi & Baraniuk, 2004), Hybrid TV-Hyper-Laplacian (Zhang, X., 2015), and Joint Nonlocal Means Filter (Yang, 2015). These hybrid methods have demonstrated successful results. However, they require a heavy mathematical model to carry out the task effectively and consequently suffer from the complexity of computation.

Considering the respective advantages and limitations of different regularized-based approaches discussed in Subsection 3.1.2., and the merit of different image prior characteristics in different image properties. In contrast to the methods in the literature, this work develops two regularization models with different objective functions to characterize the image properties. The two-regularization model is optimized with multi-objective bilevel programming (MBP) for high fidelity of MTF compensation. Based on the literature review, until recently, image restoration techniques based on MBP have not yet received broad attention in the literature. Only a few articles related to this class of problems in the literature (Nikolova, Steidl & Weiss, 2015; Kunisch & Pock, 2013; Tappen, Liu, Adelson, & Freeman, 2007) were found, and the studies have tended to focus on parameter learning for variational image denoising models. These studies suggest that MBP has a few advantages as compared to the conventional iterative method that frequently uses in the image restoration technique, is that it can ease the difficulty of dealing with the disjunctive nature of the complementarity constraints and optimize many parameters simultaneously.

In this study, it is believed that MTF compensated image with significant improvement of signal to noise ratio can be achieved by incorporating the three image priors suggested in Subsection 6.2.1.2. into the ill-posed restoration problem and then solving it efficiently using the MBP.

6.3 Proposed Modulation Transfer Function Compensation Framework

Let us recall the image restoration model in Equation (4.1). Given a blur and noisy image, the goal of image restoration is to reliably remove blur and noise to restore coherent image details. In general, the regularization solution that copes with the ill-posed nature of image restoration can be described in the following minimization problem as

$$\min_{f} \frac{1}{2} \|f \oplus h - g\|_2^2 + \lambda \Psi(f), \tag{6.3}$$

where $\frac{1}{2}\|f \oplus h - g\|_2^2$ is the L_2 data-fidelity term, $\Psi(f)$ is called the regularization term denoting image prior and λ is the regularization parameter.

In the proposed framework of MTFC as presented in Figure 6.7, there are two regularization models; one is used for characterizing the properties of image smoothness and image structure, whereas the other one is used for characterizing the properties of image texture. With these regularization terms, the two complementary models are fused in the Curvelet domain to maximize their merits and minimize their weaknesses. In doing that, this work can obtain a high-fidelity image that portrays both local and nonlocal properties of the image more richly, which confines the solution space of the inverse problem and significantly improve the spatial quality of the observed image. The model for this framework is defined as

$$MTFC_3(F) = MTFC_1(F_A) + MTFC_2(F_{A'}), \text{ with } A' = \{s \in S: s \notin A\}. \tag{6.4}$$

where $MTFC_3(F)$ represent the Hybrid MTFC Model. $MTFC_1(F_A)$corresponds to the regularization model that contains image smooth and structure, whereas,

$MTFC_2(F_{A`})$corresponds to the regularization model that contains image texture. The $S = (s_0, \dots, s_{N_j})$ where N_j is determined by Equation (6.2).

To solve Equation (6.4), the two regularization terms are decoupled into separate steps and later optimize the solutions with MBP such that they become a new model expressed as

$$\min_{\hat{f}} MTFC_U(f_U, f_L) \left\{ \begin{array}{l} Q(f_U) > Q(f_L), Q(f_U) > Q(\bar{f}_U): \bar{f}_U \in X_U \\ f_L \; solves \left\{ \begin{array}{l} \arg\min_{\bar{f}_L} \{ MTFC_L(f_U, \bar{f}_L): \bar{f}_L \in X_L(f_U) \}, f_U \in X_U \\ subject\ to\ P_L(f_L, g) \sim 0, \end{array} \right. \end{array} \right. \quad (6.5)$$
$$subject\ to$$

Where X is the feasible set; U and L indicate Upper-and Lower-level, respectively; f represents the final decision of MBP (i.e. the restored image); and the $f_U, f_L, \bar{f}_L$ denote the Upper-level decision, lower-level decision, and the potential lower-level decision, respectively. The lower-level objective function $MTFC_L(f_U, \bar{f}_L)$ apply image priors $P_L(f_L, g)$ on degraded image g to obtain a latent sharp image f_L, whereas $MTFC_U(f_U, f_L)$ is the Upper-level objective function, and $Q(f_U) > Q(f_L), Q(f_U) > Q(\bar{f}_U)$ are the Upper-level inequality constraints of fitness value for the Upper-level problem. The fitness function for inequality constraint Q is formulated based on the most widely used quality metric, which is the recently proposed FSIM and ISNR as described in Section 3.5.

It should be noted that the lower-level optimization problem is optimized only with respect to the L variables, and the variable vector of f_U is kept fixed. The next section first describes the lower-level problem and follow by the Upper-level Problem. From Equation (6.5), it should be noted that the lower-level optimization problem is optimized only with respect to the L variables, and the variable vector of f_U is kept fixed. The next section will first describe the lower-level problem and followed by the Upper-level Problem.

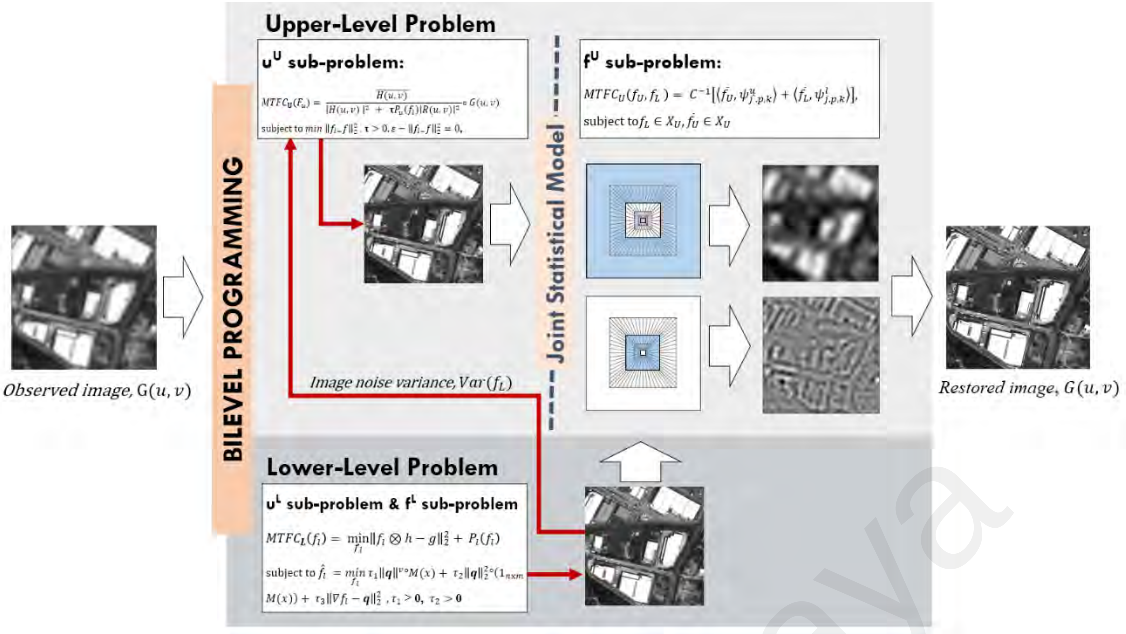

Figure 6.7: The framework of the proposed Modulation Transfer Function Compensation

6.3.1 Lower-Level Problem

The objective function for the Lower-level problem (LLP) is to obtain a clear image that emphasizes image smoothness without amplified noise, and image structure without image artifacts such as ringing near edges. To achieve this objective function, this work develops two strategies, where first a hyper-Laplacian image prior (Krishnan & Fergus, 2009) is adopted to make gradients in near-edge regions obey a heavy-tailed distribution to produce sharper edges; and to suppress noise and remove ringing artifacts. Secondly, this work introduces a mask to encode edge regions and use a Gaussian prior to eliminate noise and ringing artifacts in locally smooth regions. The combined image priors are thus defined as

$$P(f) = \tau_1 \|\nabla f\|^p \circ M(x) + \tau_2 \|\nabla f\|_2^2 \circ (1_{\mathrm{n}\times\mathrm{m}} - M(x)), \tag{6.6}$$

where $\nabla f = (\partial_x f, \partial_y f)^T$ is the gradient of the image *f*, τ_1, and τ_2 are the weights; the symbol $\circ$ represents the element-wise multiplication operator, $\|.\|^p$ is the hyper-Laplacian prior; p is the parameter with $\frac{1}{2} \le p \le \frac{4}{5}$. Smaller p leads to a smoother result. The p can be adjusted to get a satisfactory result. $1_{n\times m}$ denotes an all-ones matrix according to a a $n \times m$ image, and $M(x)$ is a 2-D binary mask function which is defined as

$$M(x) = \begin{cases} 1, & x \cap d_x \\ 0, & otherwise \end{cases} \tag{6.7}$$

and d_x is a dilated edge region. The d_x is obtained using two operations, where first is to detect edges in image g with the Canny edge detector, then to utilize mathematical morphological operations to dilate the edges with a disk model, with a radius that is equal to the kernel size.

The proposed prior $P(f)$ in Equation (6.6) is used as a regularization term to solve the objective function of LLP. Hence, the total energy of LLP is defined as

$$\begin{aligned} &MTFC_L(f_L) = \min_f \|f_L \otimes h - g\|_2^2 + P_L(\hat{f}_L) \\ &\text{subject to } \hat{f}_L = argmin\, \tau_1 \|\nabla f_L\|^p \circ M(x) + \tau_2 \|\nabla f_L\|_2^2 \circ (1_{nxm} - M(x)), \\ &\tau_1 > 0,\ \tau_2 > 0 \end{aligned} \tag{6.8}$$

Due to the L_p-norm regularization term in Equation (6.8), Equation (6.8) becomes a non-convex function that is commonly regarded as computationally intractable. Inspired by Pan et al. (Pan et al., 2017)'s method in solving non-convex function, this work introduces an auxiliary variable q to substitute ∇f_L and add another regularization term in Equation (6.8) to penalize the non-sparsity of the gradient. Therefore, Equation (6.8) is reformulated as

$$\begin{aligned} &MTFC_L(f_L) = \min_{f_L} \|f_L \otimes h - g\|_2^2 + P_L(f_L) \\ &\text{subject to } \hat{f}_L = \min_{f_L} \tau_1 \|q\|^p \circ M(x) + \tau_2 \|q\|_2^2 \circ (1_{nxm} - M(x)) + \\ &\tau_3 \|\nabla f_L - q\|_2^2,\ \tau_1 > 0,\ \tau_2 > 0. \end{aligned} \tag{6.9}$$

When τ_3 is close to ∞, the solution of Equation (6.9) converges to that of Equation (6.8). With the formulation of Equation (6.9), the optimization problem can be decoupled into two sub-problems and solved efficiently through alternatively minimizing (Geman

& Yang, 1995) f and q independently. Accordingly, the two sub-problems that are referred to as u^L sub-problem and f^L sub-problem will be discussed as follows.

u^L sub-problem: By fixing all variables except q, Equation (6.9) is reduced to

$$\tau_1 \|q\|^p \circ M(x) + \tau_2 \|q\|_2^2 \circ (1_{nxm} - M(x)) + \tau_3 \|\nabla f_L - q\|_2^2 . \tag{6.10}$$

Thus, optimal q can be found using the Newton-paphson method.

f^L sub-problem: Given a fixed value of q from the previous iteration, Equation (6.9) is quadratic in f. The optimal f_L thus becomes

$$\min_{f_L} \|f_L h - g\|_2^2 + \tau_3 \|f_L - q\|_2^2 . \tag{6.11}$$

As it is a closed-form least-squares minimization problem, this allows us to find optimal f directly using FFTs based on Parseval's theorem as follows:

$$f_L = \mathcal{F}^{-1}\left(\frac{\mathcal{F}(g)\circ\overline{\mathcal{F}(h)} + \tau_3\mathcal{F}(\mathrm{u})\circ\overline{\mathcal{F}(\nabla)}}{\mathcal{F}(h)\circ\overline{\mathcal{F}(h)} + \tau_3\mathcal{F}(\nabla)\circ\overline{\mathcal{F}(\nabla)}}\right), \tag{6.12}$$

where $\mathcal{F}(.)$ and $\mathcal{F}^{-1}(.)$ denote the FFT and inverse FFT, respectively; and $\overline{\mathcal{F}(.)}$ is the complex conjugate operator.

Figure 6.8 demonstrates the effectiveness of the combined image priors (i.e., hyper-Laplacian prior and Gaussian prior) used to achieve the objection function of the LLP in Equation (6.6). From Figure 6.8(a), it can be observed visually that the proposed image priors provide a smooth region without visible noise and structure preservation better than Krishan and Fergus (2009) in Figure 6.8(b). Another observation is that the boundary artifacts due to the periodicity property of FT are not visible in the intermediate latent image f_L in Figure 6.8(a). In quantitative comparison, the intermediate latent image in Figure 6.8(b) has a higher FSIM value (0.98) than the intermediate latent image in Figure 7(c) (0.95).

Figure 6.8: Effectiveness of the proposed prior, the block regions show the cropped region and their closed-up view. (a) Blurred-noisy input (gaussian blur, σ =2), (b) intermediate latent image f_L restored by Equation (6.7). (c) Restored results using the method by Krishnan & Fergus (2009). The closed-up view from the yellow box obviously shown boundary artifacts.

6.3.2 Upper-Level Problem

The Upper-level problem (ULP) comprises two objective functions, one is to recover the fines texture of the degraded image spectrum G based on $\bar{f}_L \in X_L(f_U)$, while the other one is to produce the ultimate restoration result. Similar to LLP, the ULP is solved in two steps; the two steps problem is described as u^U sub-problems and f^U sub-problems.

u^U sub-problem: The objective function that corresponds to solving the ULP is defined as

$$MTFC_U(F_U) = MTF(u,v) \circ G(u,v) \tag{6.13}$$

$$\text{where } MTF(u,v) = \frac{\overline{H(u,v)}}{|H(u,v)|^2 + \tau|R(u,v)|^2} \tag{6.14}$$

$$\text{subject to } \|g - Hf_L\|^2 = \|\eta\|^2, \tau > 0,$$

where u and v are the spatial frequency coordinate; τ is a weight, $R(u,v)$ is a Laplacian prior, which penalizes the PSFs that are not smooth; and $\overline{H(.)}$ is the complex conjugate of H. Note that Equation (6.14) has the same expression as the CLS filter defined in (Li et al., 2013). The regularization term Equation (6.14) has the advantages of convex optimization and a very low computational complexity (Mu et al, 2013; Gonzalez and Woods, 2017). As demonstrated in Subsection 6.2.1.2, the least-squares estimator is efficient in preserving the image in the middle range frequency. Moreover, compared with the Wiener filter, the CLS is known to yield better results for high- and medium-noise cases (Gonzlenz & Woods, 2017). There is no need to design a very complex regularization term since the task of restoring smooth regions and retaining the sharp edges will be accomplished by LLP. Nevertheless, to make it more tractable and robust, another prior term about the solution is introduced as

$$P_U(f_U) = \varepsilon / Var(f_L), \tag{6.15}$$

where ε is the noise level estimation using the method by Liu et al. (2013) and $Var(f_L)$ is the image variance of the estimated undegraded image (i.e. the output from LLP). The main problem of the classic CLS filter in image restoration is that the weights could not be estimated accurately based on the blurred noisy image. If a reference image that contains a much better estimate of the frequency information than the noisy image is available, then the regularization term could be estimated more accurately. In addition, the optimization of UPP is more efficient because α can be found must faster than the classic one as presented in Figure (6.10).

With the introduction of Equation (6.15), the objection function and constraints of ULP in Equation (6.14) are modified to become

$$MTF(u,v) = \frac{\overline{H(u,v)}}{|H(u,v)\,|^2 \; + \; \tau P_U(f_L)|R(u,v)|^2} \tag{6.16}$$
$$\text{subject to } min\,\|f_L - f\|_2^2\,, \tau > 0, \varepsilon - \|f_L - f\|_2^2 = 0,$$

where $min\,\|f_L - f\|_2^2$ denotes image fidelity of LLP. Based on the autocorrelation theorem, the $|H(u,v)\,|^2$ term in Equation (6.16) can be approximated to $\overline{H(u,v)} * H(u,v)$, hence, the modified constraint least square filter in Equation (6.14) can be described as

$$MTF\,(u,v) = \frac{1}{H(u,v)} \circ \frac{|H(u,v)|^2}{|H(u,v)|^2 \; + \; \tau P_u(f_l)|R(u,v)|^2}, \tag{6.17}$$

Note that Equation (6.17) can be perceived to have two separate part: an inverse filtering part $\frac{1}{H(u,v)}$, which contributes to the sharpness for deblurring, and a noise smoothing part $\frac{|H(u,v)|^2}{|H(u,v)|^2 + \tau P_u(f_l)|R(u,v)|^2}$ for denoising. Subsequently, it allows more degrees of freedom for image restoration that incorporate both deblurring and denoising techniques in one single filter. Therefore, this work proposes a modified constraint least square filter, which can be expressed as

$$MTF\,(u,v) = \left(\frac{1}{H(u,v)}\right)^{\mu_i} \circ \left(\frac{|H(u,v)|^2}{|H(u,v)|^2 + \tau P_u(f_l)|R(u,v)|^2}\right)^{\mu_s}, \tag{6.18}$$

where μ_i and μ_s represent the inverse control parameter and the smooth control parameter respectively. Empirically, the range of tuning for μ_i is between 0 and 2, while the range of tuning for μ_s is between 0 and 10. A lower value of μ_i produces low contrast restored image and higher value produces noise amplification and artifacts. Whereas, a conversely higher value of μ_s produces low contrast restored image and lower value produces noise amplification and artifacts.

The intermediate latent image of ULP is obtained by applying the inverse FFT to Equation (6.13) as follows,

$$\bar{f}_U = \mathcal{F}^{-1}(MTFC_U(F_U)), \tag{6.19}$$

Figure 6.9 present one example of the intermediate latent image f_U using Equation (6.19). They show the comparison of visual image quality and convergence analysis between the improved CLS and classic CLS, respectively. From the close-up views in Figures 6.9(b) and 6.9(c), it can be noticed that the proposed improved CLS produce sharper results than the classic CLS. Quantitatively, the intermediate latent image in Figure 8(b) has a higher FSIM value (0.97) as compared to the intermediate latent image in Figure 8(c) (0.95).

(a) (b) (c)

Figure 6.9: Visual quality comparison of image restoration (a) Blurred-noisy input (gaussian blur, σ =2), (b) Restored results by the proposed improved CLS using Equation (6.18), (c) Restored results by classic CLS. Note that the close-up views correspond to the red box in (b) and (c).

To prove the efficiency of the improved CLS, a convergence analysis is presented for both the improved and the classical CLS in MATLAB on an Intel Core i5 CPU with 8 GB of RAM in Figure 6.10. From this figure, it can be noted that the improved CLS converges much faster than the classical one. In an average of 10 datasets, it requires only 30 iterations as a stop criterion. It is five times faster than the classic CLS that requires at least 150 iterations as a stop criterion.

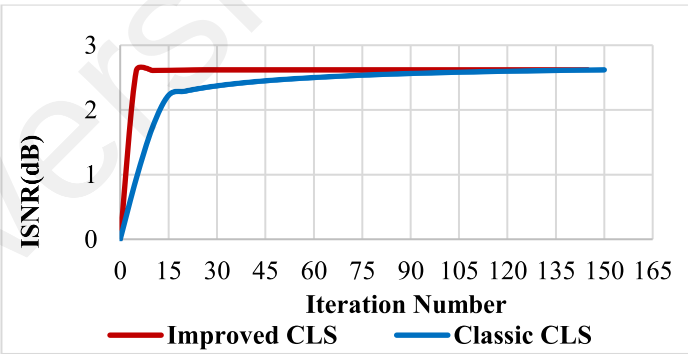

Figure 6.10: Convergence analysis for improved CLS and classic CLS.

f^U sub-problem: The objective function corresponds to combine local and nonlocal properties of the image from the bilevel problem, and implicitly determine the most optimal decision of this problem is defined as

$$MTFC_U(f_U, f_L) = C^{-1}\left[\langle \bar{f}_U, \psi^{u}_{j,p,k}\rangle + \langle \bar{f}_L, \psi^{l}_{j,p,k}\rangle\right], \quad \text{subject to } f_L \in X_U, \bar{f}_U \in X_U \tag{6.20}$$

where C^{-1}denotes the inverse curvelet transform function; $\psi^{u}_{j,p,k}$is the curvelet coefficient of the latent image from ULP at scale *j*, wedge location *p*, and coordinates *k,* whereas $\psi^{l}_{j',p,k}$ is the curvelet coefficient of the latent image from LLP at scale j' (i.e., the complement of *j*)

Given an intermediate latent image of ULP, $\bar{f}_U(x, y)$, the curvelet coefficients $\psi^{l}_{j',p,k}$ are obtained using the FDCT WARPING (Candès et al., 2006). For all images in $f = (\bar{f}_U, f_L)$ with the size of $m \times n$ pixel, Equation (6.2) is used to calculate the number of scales and apply Equation (6.1) to extract frequency coefficients of f at each scale and filter into a pool of subbands as follow

$$\left\{\bar{f}_U \mapsto (\Delta_0 \bar{f}_U, \Delta_1 \bar{f}_U, \Delta_2 \bar{f}_U, \ldots \Delta_{N_j} \bar{f}_U), f_L \mapsto (S_0 f_L, \Delta_1 f_L, \Delta_2 f_L, \ldots \Delta_{N_j} f_L)\right\}, \tag{6.21}$$

where $\Delta_{0 \ldots N_j}$ represent the band levels, with Δ_0 being the band with the lowest frequency, and Δ_{N_j} being the band with the highest frequency. Since low frequencies are responsible for the general appearance of images over smooth areas, whereas high frequencies are responsible for detail. The $f_L \mapsto (\Delta_0 f_L, \Delta_1 f_L, \Delta_{N_j} f_L)$ will represent the smooth region and structure, whereas, $\bar{f}_U \mapsto (\Delta_2 \bar{f}_U, \Delta_3 \bar{f}_U, \ldots, \Delta_{N_{j-1}} \bar{f}_U)$ will represent the texture. Thus, finally, the final decision of MBP is obtained as $f_U \mapsto (\Delta_0 f_L, \Delta_1 f_L, \Delta_2 \bar{f}_U, \Delta_3 \bar{f}_U, \ldots, \Delta_{N_{j-1}} \bar{f}_U, \Delta_{N_j} f_L)$, which is the ultimate restoration result.

6.4 Analysis and Experimental results

This section presents extensive experimental results to evaluate the performance of the proposed algorithm. For this experiment, eight sub-images with 512×512-pixel are selected from the level 2A product of IKONOS as presented in Figure 6.11. These sub-images are also the ground-truth data for this experiment.

As mentioned in the introduction, this work proposes a non-blind deconvolution method, which is a stand-alone problem that concentrates on recover the degraded image with a known degradation function. Therefore, the datasets that are used for analysis and experiments are synthetically blurred satellite images simulated from the ground-truth data. As the practical atmospheric PSF in optical satellite images is assumed to be a Gaussian-like shape, so the eight ground truth data are synthetically blurred with Gaussian blur for four different standard deviations (SD) σ of 1, 2, 3, and 4. Thus, four groups of eight datasets are collected, which are labeled as Dataset-1, Dataset-2, Dataset-3, and Dataset-4 that contain blur SD, σ of 1, 2,3, and 4, respectively. Apart from blurring, this work also added white additive Gaussian noise with zero mean and 0.5 SD to all datasets to test the robustness of the proposed algorithm.

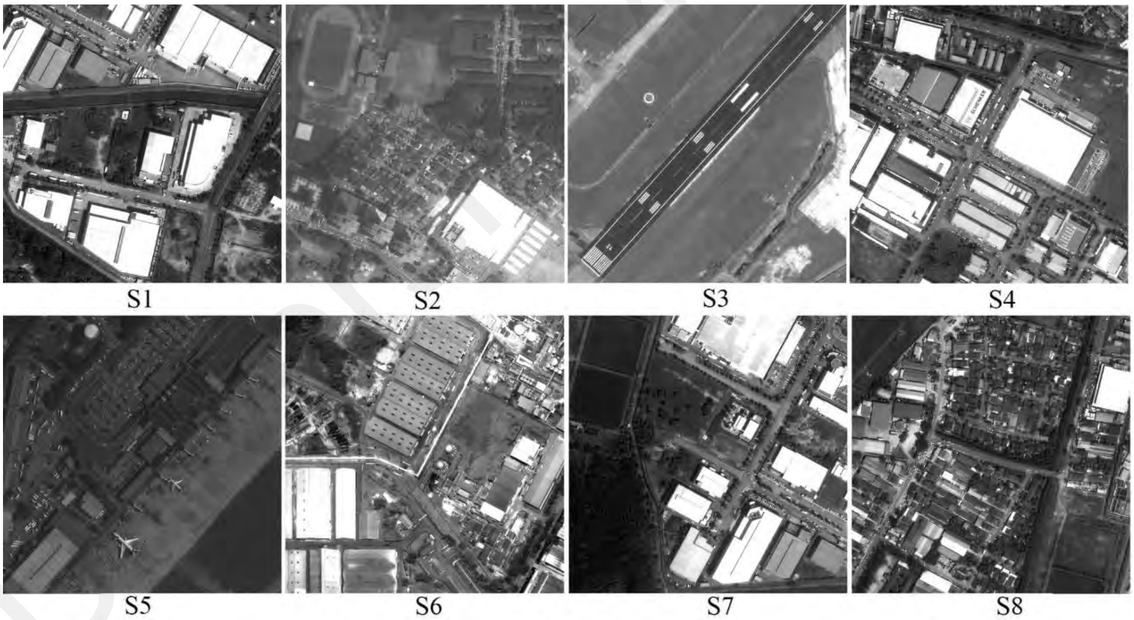

Figure 6.11: Ground truth data from level 2A product of IKONOS.

The proposed algorithm is compared with five competing methods. They comprise of an MTF-filtering based method which is the widely used Wiener filter (Mu et al., 2016), two recent representative non-blind deconvolution methods (i.e. Krishnan & Fergus (2009) and Pan et al., (2017)) that exploit image prior as regularization term, and two representative non-blind deconvolution methods (i.e., Zhang, J. et al. (2014), Zhang, X.

et al. (2015)), which use a hybrid model. The competing methods are evaluated from two aspects: efficiency and effectiveness. To evaluate the efficiency of the proposed algorithms, this work uses convergence speed (i.e., the number of iterations for convergence) and computational time. As to evaluate effectiveness, this work uses ISNR (unit: dB), and the recently proposed FSIM [unitless: interval [0 1]); FSIM is known to achieve much higher consistency with the subjective evaluations than state-of-the-art IQA metrics Zhang, L. et al., 2011). In addition to quantitative measurement, this work also uses visual observation for qualitative evaluation.

Nevertheless, to evaluate the effectiveness of the proposed method in a real-world practical situation, apart from experimental on synthetic data, this work also experiments with real unknown blur satellite data by employing the MTF measurement method from Chapter 4 to estimate the degradation function (i.e., PSF kernel), and later to be input to the proposed method to compensate for degradation. In these experiments, the MTF area (MTFA) ratio is used to quantitatively assess the restoration quality. The ISNR and FSIM are not applicable since the restoration process has become a blind deconvolution problem with unknown blur. For this experiment, 50 data samples are collected from RazakSAT data in the Panchromatic (PAN) band.

In this subsection, the numerical evaluation results for all data are presented. However for visual evaluation, only some of the results are presented, the rest of the experimental results are available in Appendix D.

6.4.1 Analysis of the effectiveness of Combined Prior in MTFC

This analysis evaluates the effectiveness of the proposed combined priors to MTFC using the four groups of datasets. Each restored image f by the proposed regularisation-based MTFC method is decomposed into subbands using Equation (6.1) in the curvelet domain and the FSIM is measured with reference to the ground truth. Figure 6.12 shows an example of decomposed images.

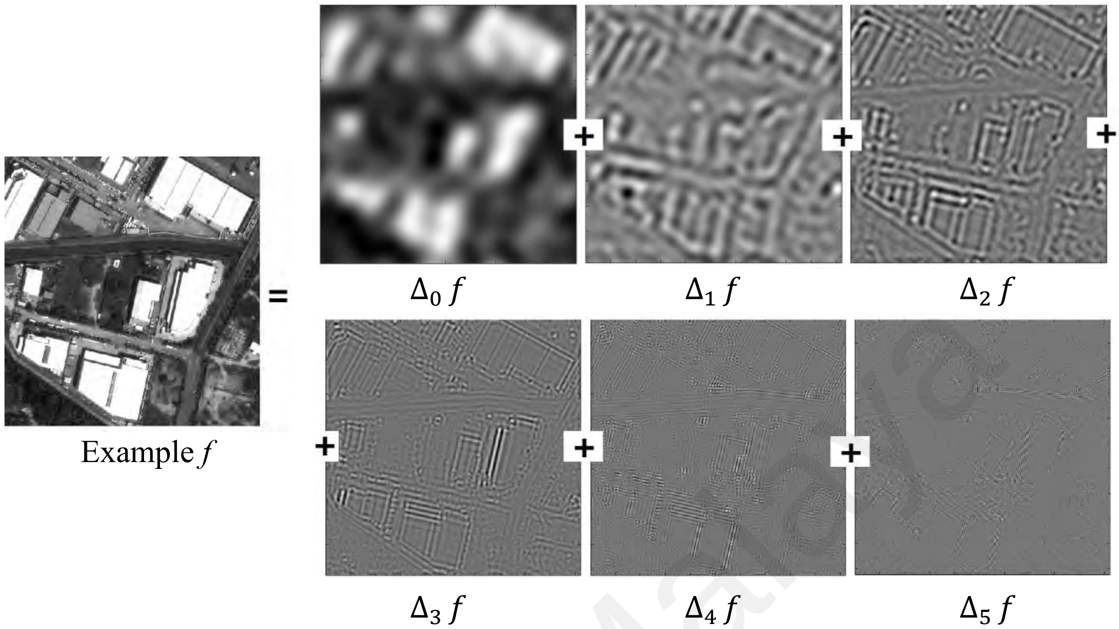

Figure 6.12: Decomposition of restored image *f* into six subbands

Table 6.1 tabulates the average FSIM and relative SD of each subband for all datasets. Furthermore, for better visualization, this work presents the analysis results in terms of average FSIM in Figure 6.13. From the analyses, as expected the dataset with the smallest blurring effect (i.e., Dataset-1, σ =1) has the best image reconstruction results with lower uncertainty, and vice versa. Note that, the tabulated relative SD for Dataset-1, Dataset-2, Dataset-3 and Dataset-4 is within the range of 0.0001 to 0.0054, 0.0018 to 0.0059, 0.0022 to 0.0061, and 0.0010 to 0.0088, respectively. The low relative SD of the datasets indicates the robustness of the proposed method, whereby the high FSIM value obtained by the reconstructed subbands shows the effectiveness of the proposed method. This is evident from Figure 6.13, where it can be noticed that all reconstructed subbands are obtaining an FSIM value higher than 0.9. In particular, the bar chart of FSIM value for subband $\Delta_1 f$ and $\Delta_2 f$ in Figure 11 is relatively high for all datasets, which indicates the proposed combined priors in the LLP can effectively characterize the local smooth region of the image. In addition, the FISM value of subband $\Delta_4 f$ and $\Delta_5 f$ in this analysis also shows that the proposed combined priors can preserve the structure effectively even in large blur conditions (see Dataset-3 and Dataset-4 in Table 6.1).

One key observation from the analyses is that the proposed priors in the ULP can mostly attain a near-perfect FSIM score (i.e., > 0.99) in the mid-range frequency (see subband $\Delta_2 f$ and $\Delta_3 f$ in Table 1), which indicates that it can preserve image detail effectively. Moreover, it can be noted that even with a large gaussian blur σ = 4, the proposed method is capable to recover the high-frequency components of an image up to 0.90352 FSIM value with relative SD as low as 0.0085%. The low uncertainty values and the high FSIM value of the reconstructed subbands tabulated in Table 1 demonstrate the high reliability of the priors employed by the proposed method. This merit can warrant the robustness of the proposed method.

Table 6.1: The average FSIM and relative SD of datasets in their respective subband.

Subband		**Dataset-1**	**Dataset-2**	**Dataset-3**	**Dataset-4**
		Gaussian blur, SD			
		$\boldsymbol{\sigma}$ **=1**	$\boldsymbol{\sigma}$ **=2**	$\boldsymbol{\sigma}$ **=3**	$\boldsymbol{\sigma}$ **=4**
$\Delta_0 f$	Average FSIM	0.99999	0.99967	0.99999	0.99864
	Relative SD (%)	0.0001	0.0018	0.0022	0.0010
$\Delta_1 f$	Average FSIM	0.99998	0.99957	0.99982	0.99889
	Relative SD (%)	0.0039	0.0048	0.0030	0.0044
$\Delta_2 f$	Average FSIM	0.99996	0.99691	0.99943	0.99189
	Relative SD (%)	0.0054	0.0051	0.0042	0.0073
$\Delta_3 f$	Average FSIM	0.99998	0.99744	0.99828	0.97167
	Relative SD (%)	0.0039	0.0059	0.0052	0.0075
$\Delta_4 f$	Average FSIM	0.99921	0.96084	0.93902	0.92584
	Relative SD (%)	0.0052	0.0039	0.0053	0.0088
$\Delta_5 f$	Average FSIM	0.99229	0.93121	0.92091	0.90352
	Relative SD (%)	0.0031	0.0055	0.0061	0.0085

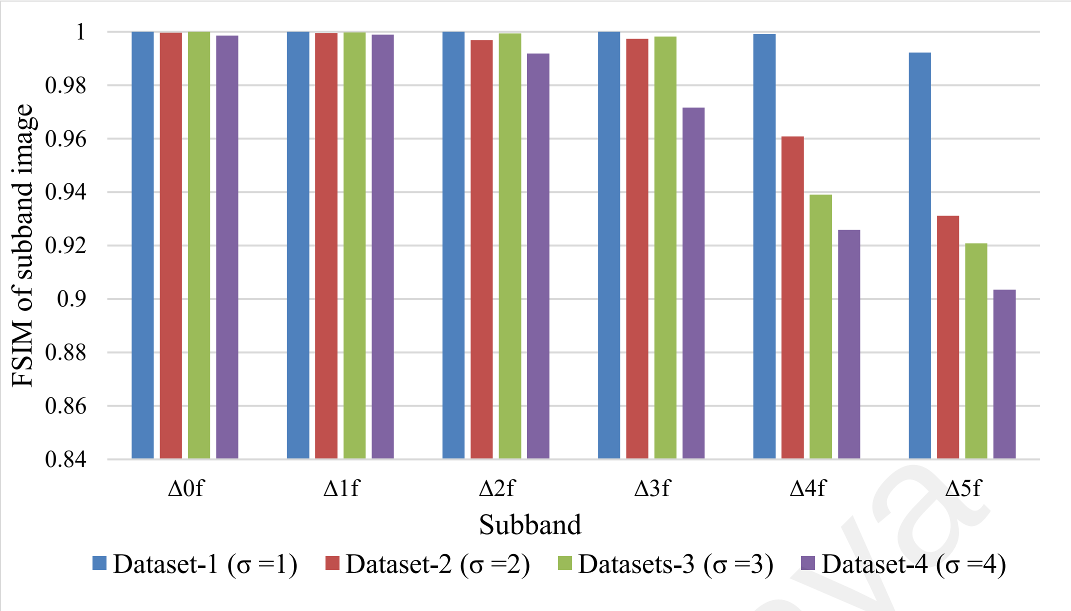

Figure 6.13: The average FSIM datasets in their respective subband

Figure 6.14 – 6.17 presents examples of synthetic blurred-noisy images used in this analysis and their respective restoration results by the proposed regularisation-based MTFC method. The restoration results as shown in these figures demonstrate the effectiveness of the combined priors in MTFC.

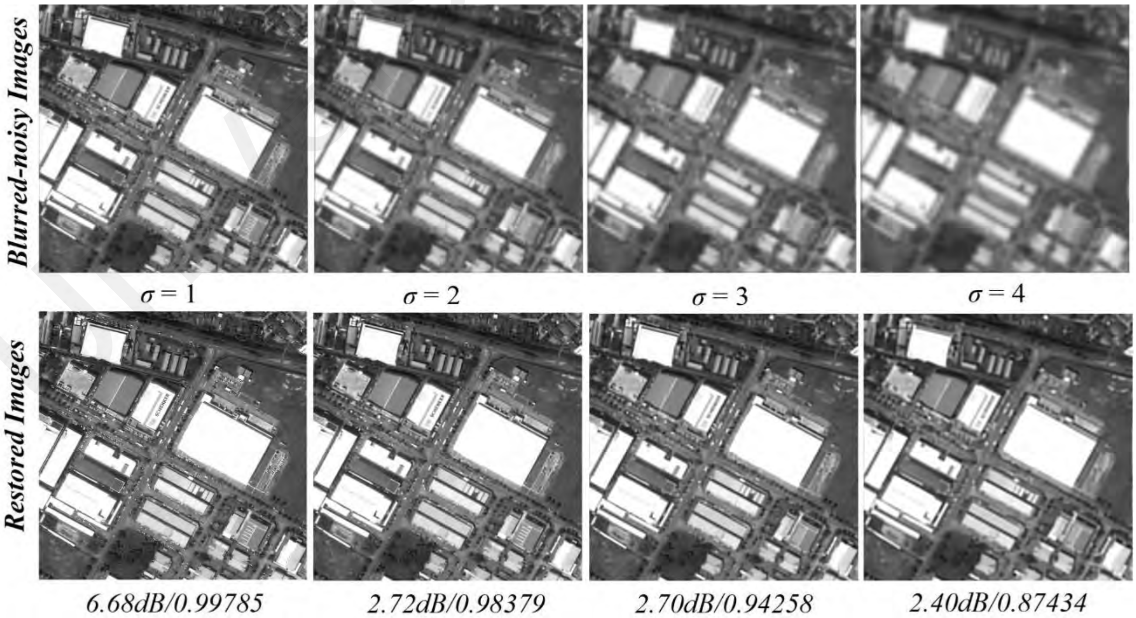

Figure 6.14: Experiment results of S4. The top row shows the blurred-noisy image with different amounts of blur, whereas the bottom row presents the respective image after the image restoration process. The quantitative measurement value at the left of the slash denotes ISNR (dB) and the right of the slash denotes FSIM.

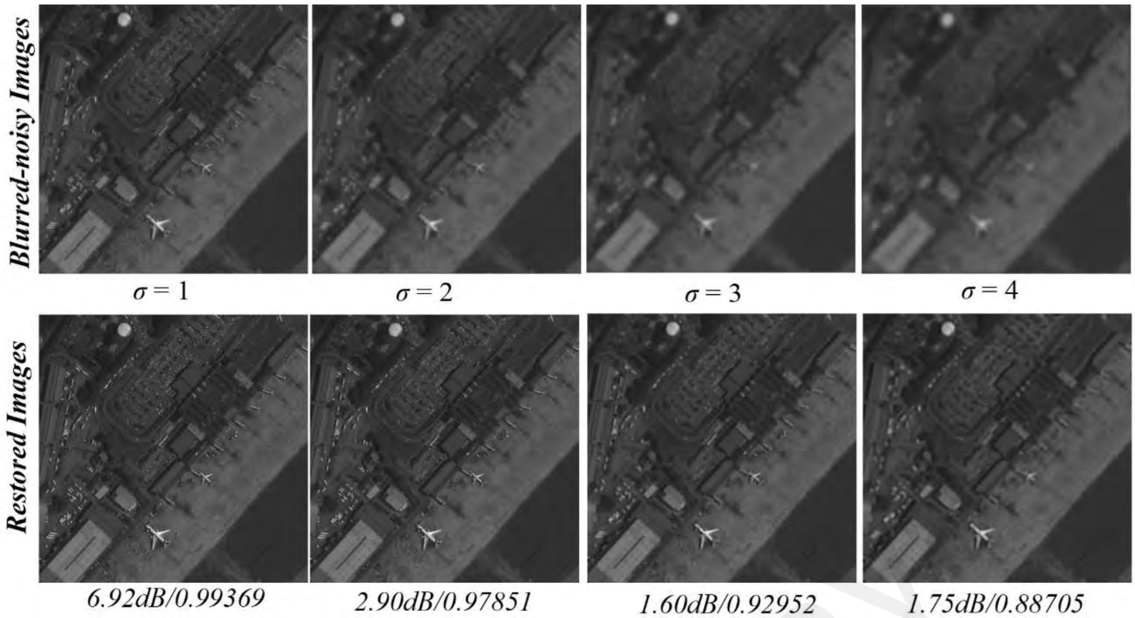

Figure 6.15: Experiment results of S5. The top row shows the blurred-noisy image with different amounts of blur, whereas the bottom row presents the respective image after the image restoration process. The quantitative measurement value at the left of the slash denotes ISNR (dB) and the right of the slash denotes FSIM.

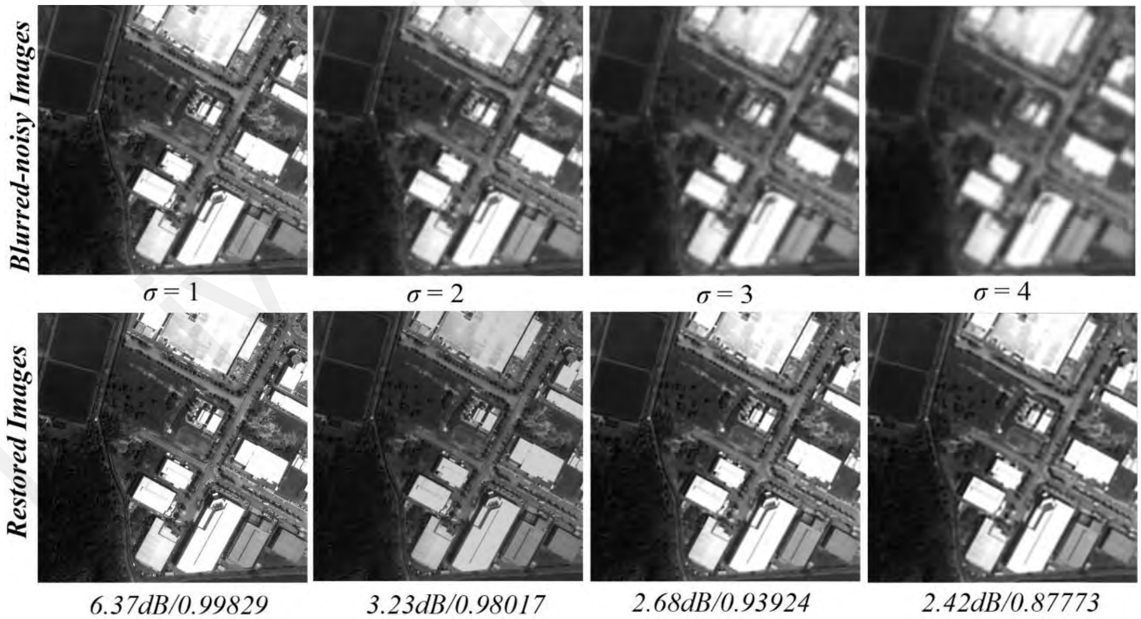

Figure 6.16: Experiment results of S7. The top row shows the blurred-noisy image with different amounts of blur, whereas the bottom row presents the respective image after the image restoration process. The quantitative measurement value at the left of the slash denotes ISNR (dB) and the right of the slash denotes FSIM.

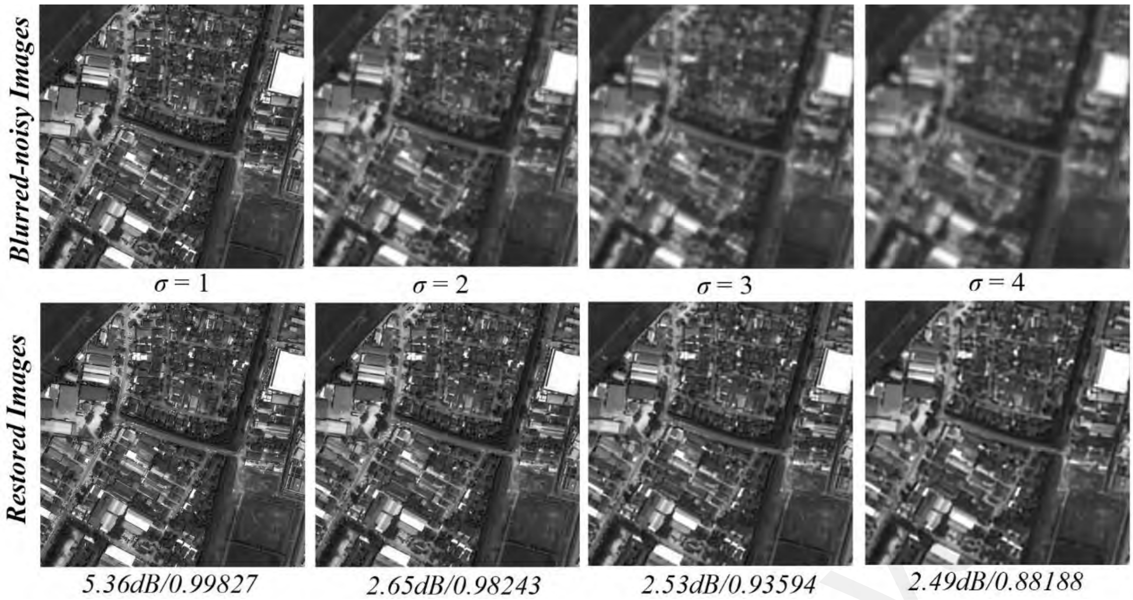

Figure 6.17: Experiment results of S8. The top row shows the blurred-noisy image with different amounts of blur, whereas the bottom row presents the respective image after the image restoration process. The quantitative measurement value at the left of the slash denotes ISNR (dB) and the right of the slash denotes FSIM.

6.4.2 Comparison with competing methods

This sub-section presents experimental evaluations for spatial quality improvement by the proposed regularization-based MTFC method against five competing methods which have been described briefly at the beginning of this section. All FSIM and ISNR results among competing methods on Dataset-1, Dataset-2, Dataset-3, and Dataset-4 are presented in Table 6.2, Table 6.3, Table 6.4, and Table6. 5. These results are generated using the same input blurry images and PSF kernel, hence they are directly comparable. The next section will first present the quantitative experiments and followed by qualitative evaluation.

6.4.2.1 Quantitative evaluation

For a more effective evaluation, the numerical experiment results will be discussed according to the group of datasets in a bar graph representation.

Dataset-1: Table 6.2 tabulates the FSIM and ISNR of Dataset-1 by the proposed method and the five competing methods.

Table 6.2: Numerical image restoration results of various regularisation methods for Dataset-1. The bold numbers are either the highest FSIM or ISNR, which indicate the best performance.

Dataset-1: Gaussian blur, $\sigma = 1$							
Data	**IQA Metric**	**MTF-based Filtering**	**Single prior-based Regularisation Method**		**Hybrid / Joint Statistical Regularisation Method**		
		Lee et al. (2016)	**Krishnan and Fergus (2009)**	**Pan et al. (2017)**	**Zhang, X. et al. (2015)**	**Zhang, J. et al. (2014)**	**Proposed Method**
S1	FSIM	0.99772	0.99751	0.99604	0.99652	0.99755	**0.99801**
	ISNR	1.55	3.57	2.69	4.31	**7.56**	6.96
S2	FSIM	0.99016	0.98793	0.98734	0.98985	0.99128	**0.99165**
	ISNR	0.62	2.4	2.02	3.65	**5.49**	4.26
S3	FSIM	0.99544	0.99587	0.99455	0.998	0.99811	**0.99818**
	ISNR	1.15	5.89	3.35	6.17	**7.58**	6.27
S4	FSIM	0.99487	0.99382	0.99395	0.99614	0.99684	**0.99785**
	ISNR	2.26	3.2	3.2	3.86	**7.05**	6.68
S5	FSIM	0.99472	0.992974	0.99181	0.99218	0.99298	**0.99369**
	ISNR	2.78	2.92	3.33	4.89	**7.81**	6.92
S6	FSIM	0.99508	0.99434	0.99414	0.99511	0.99551	**0.99553**
	ISNR	4.09	2.4	3.63	4.65	**5.91**	5.36
S7	FSIM	0.99814	0.99787	0.99735	0.99687	0.99787	**0.99829**
	ISNR	5.63	3.2	2.92	4.89	**7.51**	6.37
S8	FSIM	0.99516	0.99754	0.99621	0.99757	0.99764	**0.99827**
	ISNR	0.52	5.05	2.22	5.05	**6.84**	5.65

Accordingly, the restoration results are presented in a bar graph in Figure 6.18 for better visualization. From the figure, it can be noticed that all methods achieve a good performance in terms of FSIM, with a minimum FSIM value of 0.98734 and a maximum FSIM value as high as 0.99829. This makes sense since this dataset is with a small amount of blur (i.e., Gaussian blur, σ =1), therefore most of the information in the image is still intact and can be recovered based on the prior knowledge of the data.

In Figure 6.18, it is can be noticed the hybrid or joint statistical regularisation methods obtain a higher FSIM and ISNR value for most of the data compared to MTF-filtering based and single prior-based regularisation. Among them, in terms of FSIM, the proposed method (i.e., green bar) obtain the highest value for the whole dataset. Whereas, in terms of ISNR, the method of Zhang, J. et al. (2014) obtain the highest value for the whole dataset. The method of Zhang, X. et al. (2015) is in third place in both IQA metrics in most of the cases. Achievement of the proposed method in terms of FSIM shows that the proposed combined priors are effective in restoring the features component and preserving the structural component of the image better than other methods. In comparison, the method of (Pan et al., 2017) has the lowest FSIM in most cases. The Wiener filter of Lee et al. (2016) achieve a relatively high FSIM compared to (Pan et al.,2017) and (Krishan &Fergus, 2009), however, it achieved a relatively low ISNR compared to other methods in most cases, especially for Data S8 that have abundant detail.

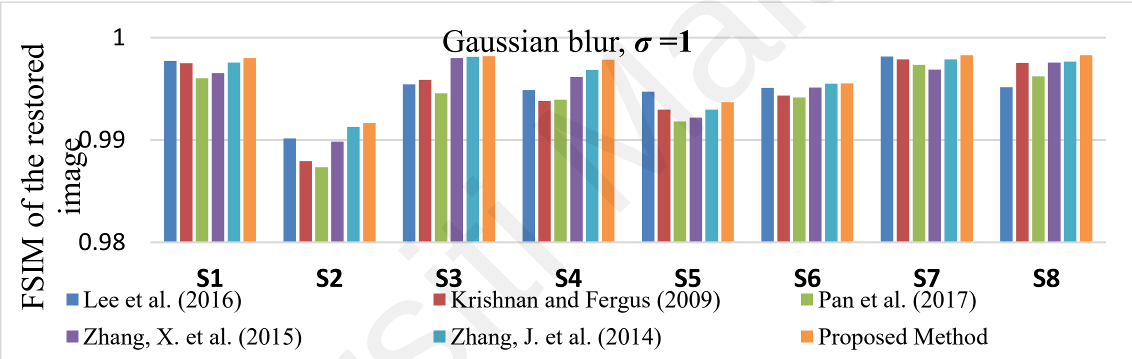

(a)

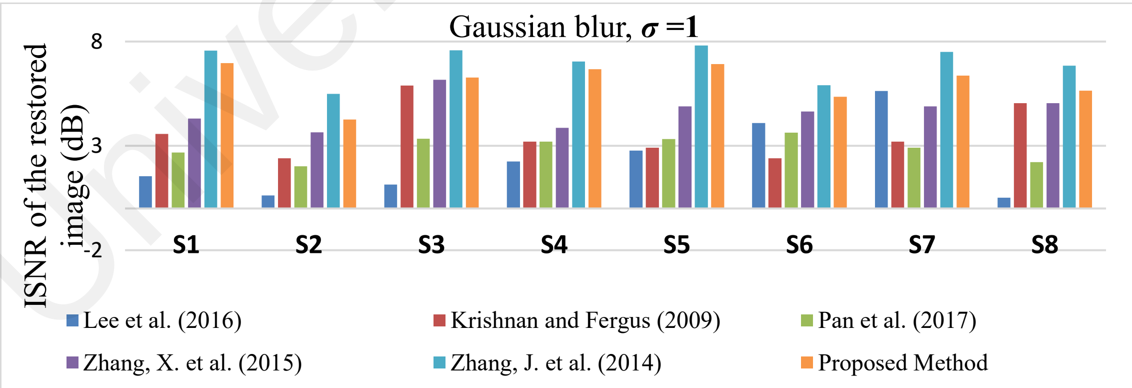

(b)

Figure 6.18: Numerical experiment results for Dataset-1. Graphs show (a) FSIM value and (b) ISNR value of the restored image.

Dataset-2: Figure 6.19 presents the FSIM and ISNR results of Dataset-2 by all competing methods. The numerical results of FSIM and ISNR of this dataset are tabulated in Table 6.3.

Table 6.3: Numerical image restoration results of various regularisation methods for Dataset-2. The bold numbers are either the highest FSIM or ISNR, which indicate the best performance.

Dataset-2: Gaussian blur, $\sigma = 2$							
Data	**IQA Metric**	**MTF-based Filtering**	**Single prior-based Regularisation Method**		**Hybrid / Joint Statistical Regularisation Method**		
		Lee et al. (2016)	**Krishnan and Fergus (2009)**	**Pan et al. (2017)**	**Zhang, X. et al. (2015)**	**Zhang, J. et al. (2014)**	**Proposed Method**
S1	FSIM	0.97957	0.97536	0.96957	0.97855	0.97957	**0.97961**
	ISNR	3.34	2.66	2.72	2.65	**3.97**	3.57
S2	FSIM	0.96172	0.95974	0.95891	0.96548	0.9685	**0.9692**
	ISNR	1.86	1.3	1.48	1.85	**2.26**	2.19
S3	FSIM	0.97911	0.97299	0.97746	0.97945	0.98192	**0.98292**
	ISNR	2.25	2.64	1.77	2.64	**3.09**	2.65
S4	FSIM	0.97182	0.96381	0.96718	0.98178	0.98279	**0.98379**
	ISNR	2.63	1.67	1.89	2.33	**3.04**	2.72
S5	FSIM	0.97308	0.9714	0.96974	0.97241	0.97751	**0.97851**
	ISNR	2.81	1.67	1.27	2.44	**3.03**	2.9
S6	FSIM	0.97516	0.96479	0.97314	0.97685	0.97983	**0.98009**
	ISNR	1.97	1.32	1.30	1.72	**3.09**	2.88
S7	FSIM	0.97609	0.96983	0.97033	0.97485	0.97885	**0.98017**
	ISNR	3.12	1.91	2.12	2.68	**3.60**	3.23
S8	FSIM	0.97462	0.97293	0.97505	0.97892	0.98199	**0.98243**
	ISNR	2.25	2.64	1.77	2.64	**3.09**	2.65

Based on the results in Table 6.3 and Figure 6.19, it can be observed that there is a slight decrement in the FSIM value for Dataset-2 due to a larger amount of blur compared to Dataset-1. The FSIM is within the range of 0.95891 to 0.98379. From the figure, the same trend of results can be observed, where the proposed method shows the highest FSIM value for datasets. Unfortunately, it is outperformed by Zhang, J. et al. (2014) in terms of ISNR with the second-highest ISNR in all cases. From the figure, generally, the method of Pan et al. (2017) that uses TV-based prior performs the worse in terms of FSIM and ISNR, followed by the method of Krishnan and Fergus, (2009), then the Wiener filter.

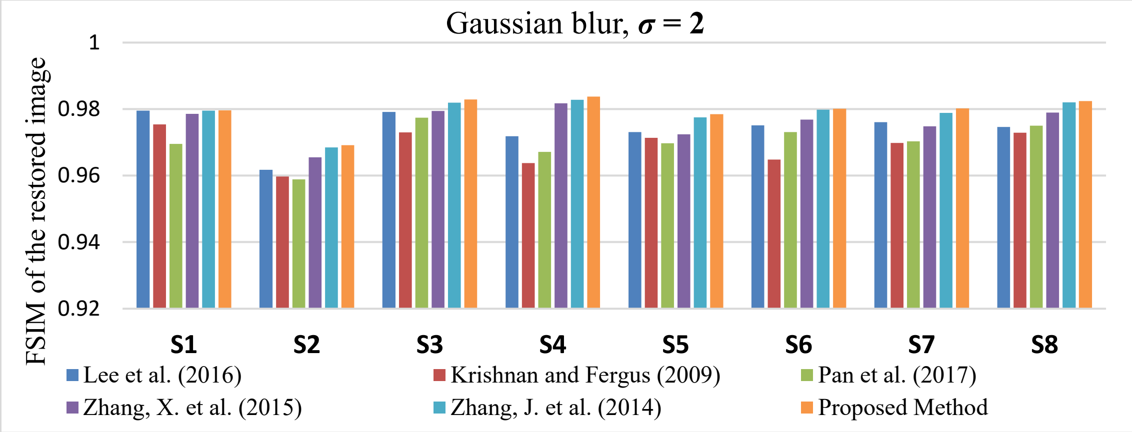

(a)

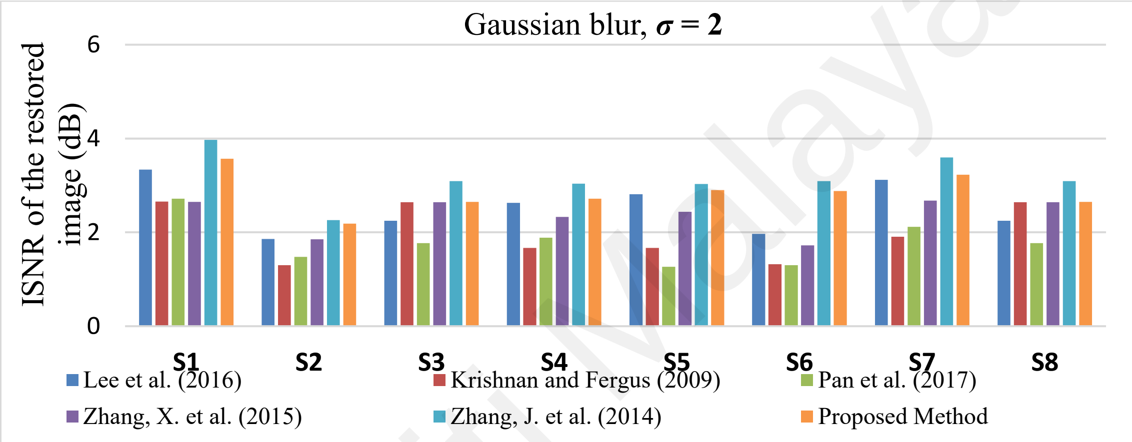

(b)

Figure 6.19: Numerical experiment results for Dataset-2. Graphs show (a) FSIM value and (b) ISNR value of the restored image.

Dataset-3: Table 6.4 and Figure 6.20 show the numerical results and the bar graph of FSIM and ISNR of Dataset-3, respectively. The FSIM value for this dataset is within the range of 0.91718 to 0.94258, as expected, it is lower than those in Dataset-1 and Dataset-2 since the blur is higher. In this dataset, the proposed method again achieves the highest FSIM for most of the data except for data S3, where the method by Zhang, J. et al. (2014) that uses a patch-based regulariser achieves a better FSIM than the proposed method. Data S3 (see Figure 6.11) depicts an airport runway image, this result demonstrates that the patch-based regularisation method is more effective in preserving the structure of images with less detail in large blur conditions. Moreover, it again achieves the highest ISNR for all cases. The proposed method achieves the second-highest ISNR in all cases, whereas the rest of the competing methods are almost comparable.

Table 6.4: Numerical image restoration results of various regularisation methods for Dataset-3. The bold numbers are either the highest FSIM or ISNR, which indicate the best performance.

Dataset-3: Gaussian blur, $\sigma = 3$							
Data	**IQA Metric**	**MTF-based Filtering**	**Single prior-based Regularisation Method**		**Hybrid / Joint Statistical Regularisation Method**		
		Lee et al. (2016)	**Krishnan and Fergus (2009)**	**Pan et al. (2017)**	**Zhang, X. et al. (2015)**	**Zhang, J. et al. (2014)**	**Proposed Method**
S1	FSIM	0.92723	0.92682	0.92551	0.92915	0.93426	**0.9343**
	ISNR	2.45	2.34	1.82	2.44	**2.72**	2.46
S2	FSIM	0.92057	0.92645	0.92403	0.93202	0.93739	**0.93896**
	ISNR	1.55	1.56	1.40	1.69	**2.01**	1.91
S3	FSIM	0.92403	0.92925	0.92896	0.93132	**0.93349**	0.93156
	ISNR	2.45	2.19	1.95	2.45	**2.91**	2.63
S4	FSIM	0.93701	0.93122	0.91913	0.93624	0.94145	**0.94258**
	ISNR	2.46	2.43	1.75	2.42	**2.68**	2.67
S5	FSIM	0.92882	0.92841	0.91718	0.92828	0.92896	**0.92952**
	ISNR	0.98	0.84	0.53	0.80	**1.72**	1.60
S6	FSIM	0.92249	0.92239	0.92372	0.92571	0.92859	**0.93259**
	ISNR	2.39	2.30	1.72	2.38	**2.53**	2.39
S7	FSIM	0.93416	0.93526	0.93457	0.93813	0.93908	**0.93924**
	ISNR	2.54	1.65	1.79	2.25	**2.84**	2.68
S8	FSIM	0.93539	0.93075	0.93372	0.92901	0.93554	**0.93594**
	ISNR	2.39	1.55	1.64	1.96	**2.77**	2.53

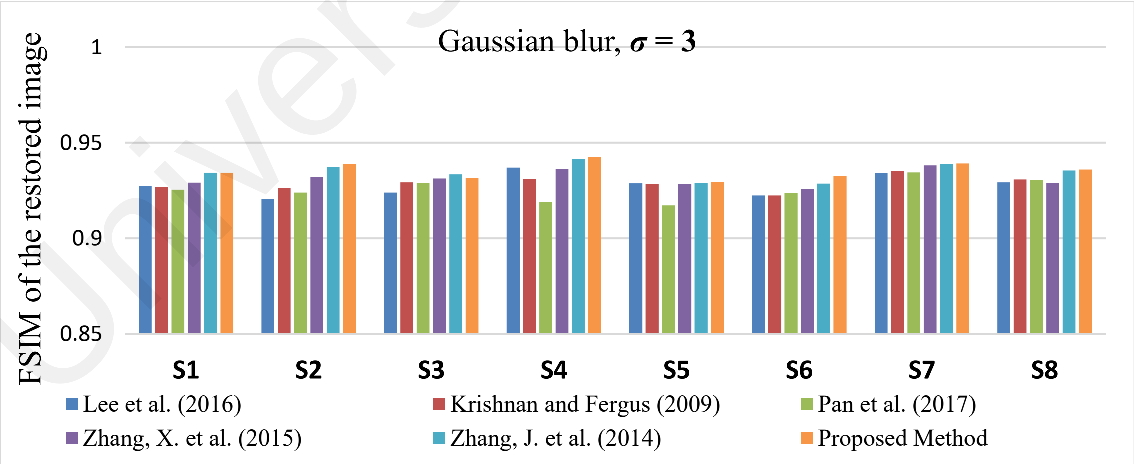

(a)

Figure 6.20: Numerical experiment results for Dataset-3. Graphs show (a) FSIM value and (b) ISNR value of the restored image.

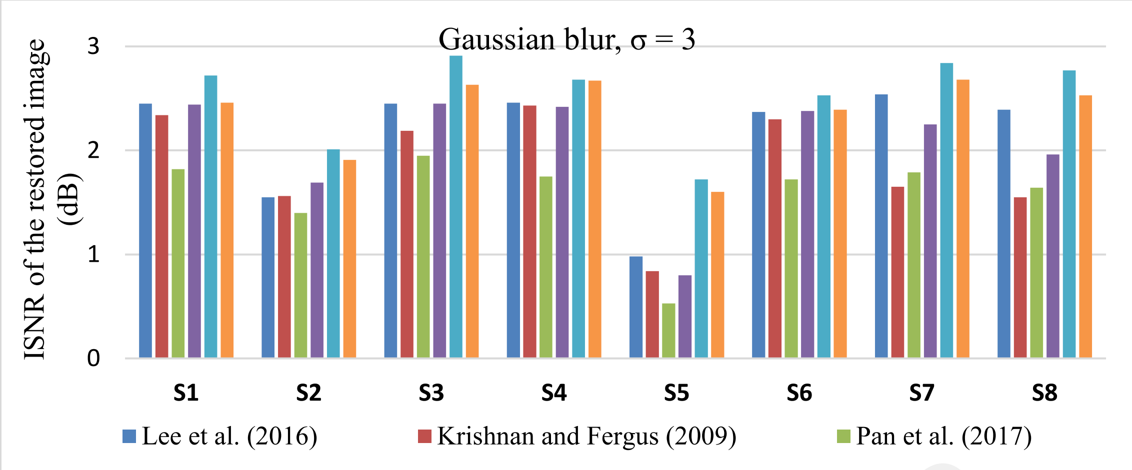

(b)

Figure 6.20, continued.

Dataset-4: Figure 6.21 presents the FSIM and ISNR results of Dataset-4 by all competing methods. The numerical results of FSIM and ISNR of this dataset are tabulated in Table 6.5.

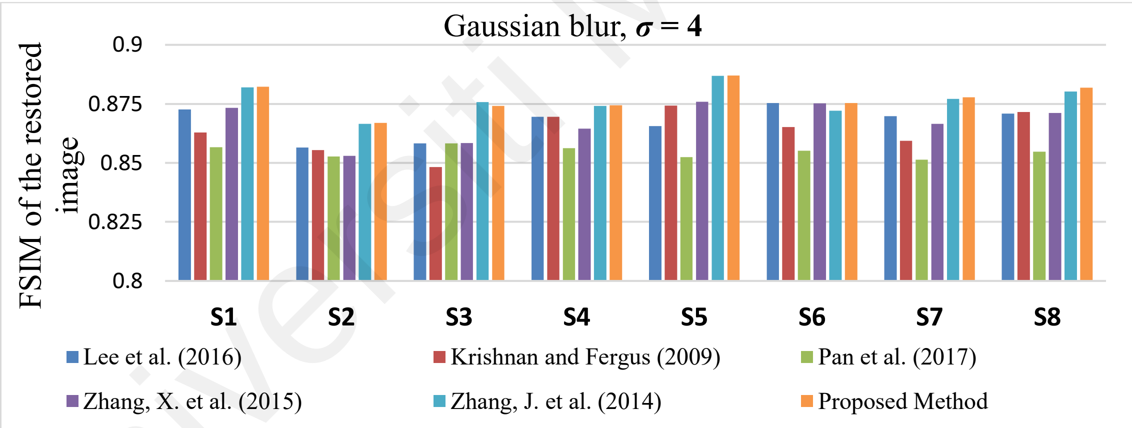

(a)

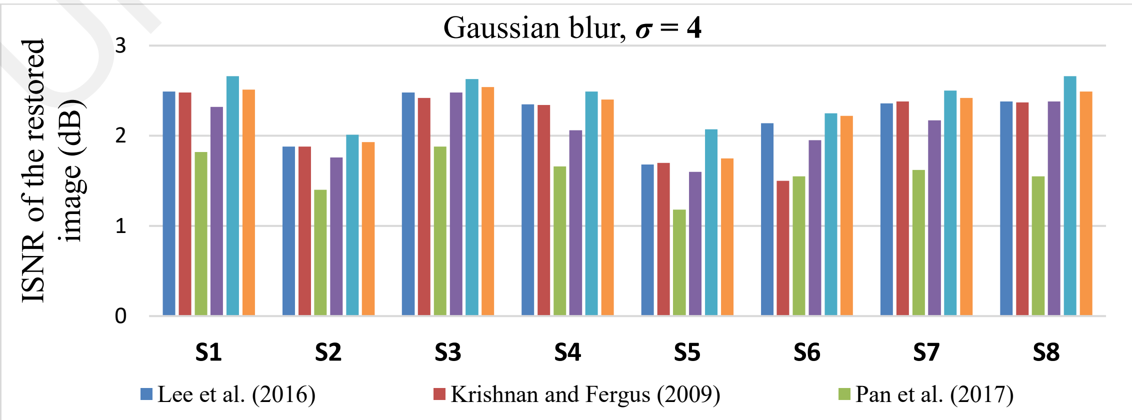

(b)

Figure 6.21: Numerical experiment results for Dataset-4. Graphs show (a) FSIM value and (b) ISNR value of the restored image.

For a dataset with blur ***σ* = 4,** the lowest range of FSIM is expected in this dataset since a lot of image content may be smoothened by the blur. The trend of the experiment results of Dataset-4 is similar to the previous datasets. From the table, the FSIM value within the range of 0.84823 to 0.88705 is obtained for this dataset. These values are the lowest among all.

Table 6.5: Numerical image restoration results of various regularisation methods for Dataset-4. The bold numbers are either the highest FSIM or ISNR, which indicate the best performance.

Dataset-4: Gaussian blur, $\sigma = 4$							
Data	**IQA Metric**	**MTF-based Filtering**	**Prior-based Regularization Method**		**Hybrid / Joint Statistical Regularization Method**		
		Lee et al. (2016)	**Krishnan and Fergus (2009)**	**Pan et al. (2017)**	**Zhang, X. et al. (2015)**	**Zhang, J. et al. (2014)**	**Proposed Method**
S1	FSIM	0.87259	0.86287	0.85666	0.8733	0.88196	**0.88227**
	ISNR	2.49	2.48	1.82	2.32	**2.66**	2.51
S2	FSIM	0.85651	0.85536	0.85267	0.85295	0.86651	**0.86693**
	ISNR	1.88	1.88	1.40	1.76	**2.01**	1.93
S3	FSIM	0.85833	0.84823	0.8583	0.8584	**0.87576**	0.87409
	ISNR	2.48	2.42	1.88	2.48	**2.63**	2.54
S4	FSIM	0.86953	0.86951	0.85619	0.86445	0.87415	**0.87434**
	ISNR	2.35	2.34	1.66	2.06	**2.49**	2.40
S5	FSIM	0.86557	0.87424	0.85248	0.87589	0.88684	**0.88705**
	ISNR	1.68	1.70	1.18	1.60	**2.07**	1.75
S6	FSIM	0.87531	0.86524	0.85518	0.87516	0.87216	**0.87539**
	ISNR	2.14	1.5	1.55	1.95	**2.25**	2.22
S7	FSIM	0.86981	0.85942	0.85142	0.86651	0.87709	**0.87773**
	ISNR	2.36	2.38	1.62	2.17	**2.5**	2.42
S8	FSIM	0.87088	0.8715	0.85471	0.87112	0.8802	**0.88188**
	ISNR	2.38	2.37	1.55	2.38	**2.66**	2.49

Discussion: There are several observations from the quantitative evaluation for all datasets; first, the hybrid or joint statistic regularisation methods are found to achieve higher FSIM and ISNR in all datasets, which means using a combined priors-based regulariser are more effective than a single prior-based regulariser for obtaining satisfying restoration results. Secondly, the proposed method considerably outperforms the other methods in terms of FSIM, with about 94% (i.e., 30 of 32 cases) the highest FSIM in all the cases. However, in terms of ISNR, the proposed MTFC method is outperformed by Zhang, J. et al. (2014), with the second-highest ISNR in all cases. The method by Zhang, J. et al., (2014) is a type of patch-based regularisation method. In their work, the authors exploit nonlocal statistical modeling to preserve the self-similarity property of an image. According to the authors, the advantage of nonlocal statistical modeling is that self-similarity among globally positioned image patches is exploited in a more effective statistical manner in a three-dimensional (3D) transform domain than nonlocal graphs incorporated in traditional nonlocal regularisations. Based on the experiments, it is noticed that the nonlocal statistical modeling for self-similarity is data-adaptive because of its content-aware search for similar patch within the nonlocal region, hence it is not only capable of preserving the common textures and details among all similar patches but also keep the distinguishing image intensities (i.e., prior based on image intensities) of each patch in a certain degree in the 3D transform domain. Different from (Zhang, J. et al., 2014), the proposed method utilizes the gradient-based type of priors and joint statistical modeling in the curve domain. As pointed out by Zhang, L. et al. (2011), the conventional metrics such as the ISNR operate directly on the intensity of the image and they do not correlate well with the subjective fidelity ratings. Besides, it is worth noting the FSIM can achieve much higher consistency with subjective evaluations than other IQA metrics. The FSIM is normalized in representation, and it is giving perception and saliency-based error, whereas ISNR is not normalized in representation, and from a semantic perspective, ISNR is giving only absolute error. From this point of view, since the proposed method considerably outperforms the other methods in terms of FSIM, second to Zhang, J. et al. (2014) in terms of ISNR, therefore, this work concludes that the proposed MTFC method is comparable to the Hybrid methods. The proposed method, thus, significantly outperformed the widely used Wiener filter and image prior-based regularisation methods (i.e., Krishnan & Fergus, 2009; Pan et al., 2017), with better ISNR and FSIM results in all cases.

6.4.2.2 Qualitative evaluation

This sub-section presents the qualitative evaluation of the image restoration results via visual observation. Figures 6.22 to 6.25 show visual quality restoration results for some of the datasets. Only four examples are shown, and each represents restoration for a different amount of blur. Note that these examples are selected based on their feature density in a scene.

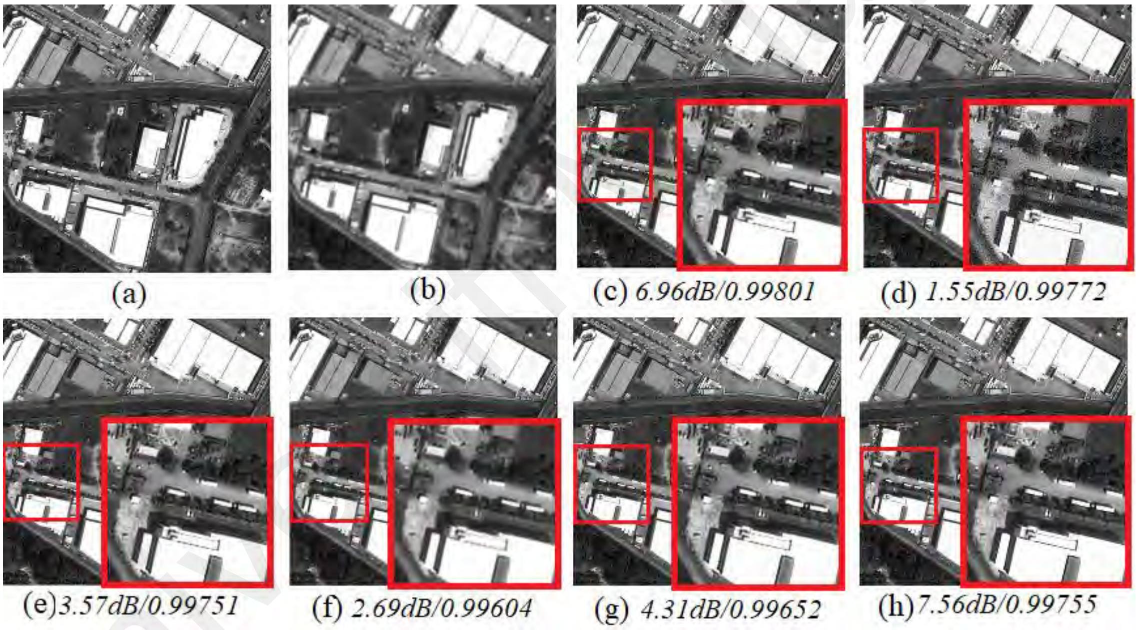

Figure 6.22: Visual quality comparison of image restoration in the case of blur σ =1, red box denotes cropped region; The quantitative measurement value at the left of the slash denotes ISNR (dB) and the right of the slash denotes FSIM. (a) Original image, (b) Blurred-noisy image, S1. Restoration results by (c) the proposed method, (d) Wiener filter (Lee et al., 2016), (e) Krishnan and Fergus (2009), (f) Pan et al (2017), (g) Zhang, X. et al. (2015), and (h) Zhang, J. et al. (2014).

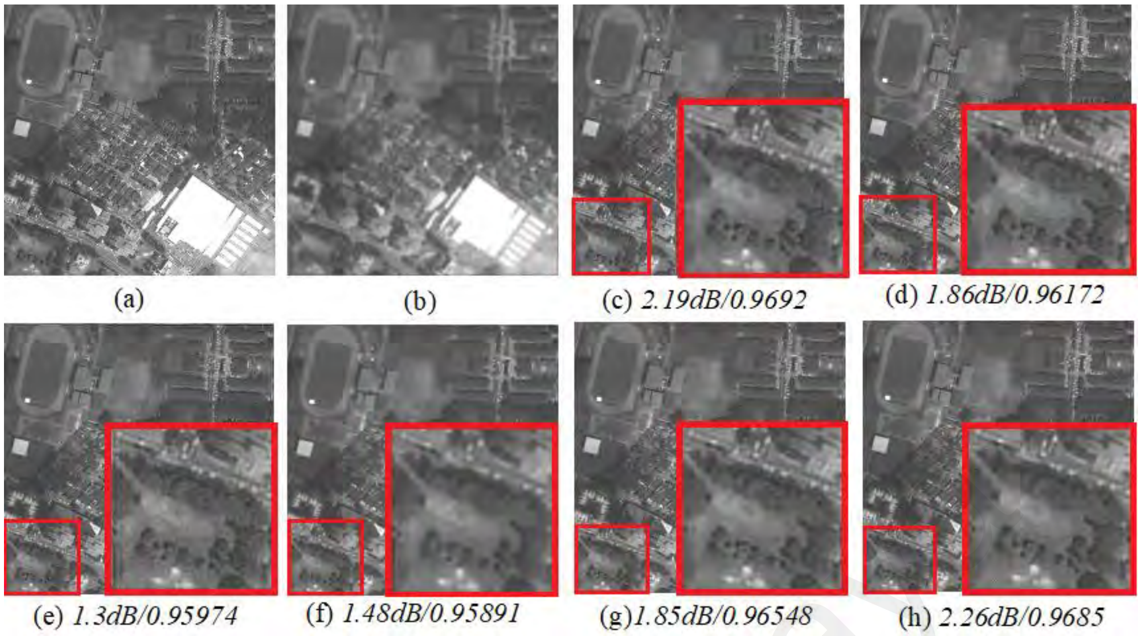

Figure 6.23: Visual quality comparison of image restoration in the case of blur σ =2, red box denotes cropped region; The quantitative measurement value at the left of the slash denotes ISNR (dB) and the right of the slash denotes FSIM. (a) Original image, (b) Blurred-noisy image, S2. Restoration results by (c) the proposed method, (d) Wiener filter (Lee et al., 2016), (e) Krishnan and Fergus(2009), (f) Pan et al (2017), (g) Zhang, X. et al. (2015), and (h) Zhang, J. et al. (2014).

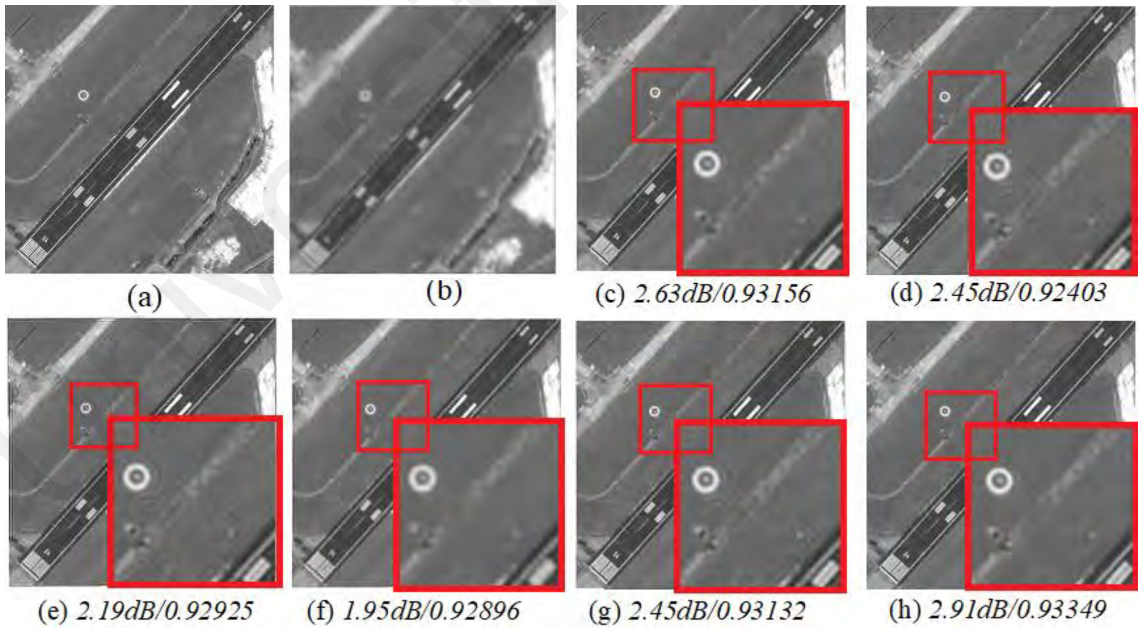

Figure 6.24: Visual quality comparison of image restoration in the case of blur σ =3, red box denotes cropped region; The quantitative measurement value at the left of the slash denotes ISNR (dB) and the right of the slash denotes FSIM. (a) Original image, (b) Blurred-noisy image, S3. Restoration results by (c) the proposed method, (d) Wiener filter (Lee et al., 2016), (e) Krishnan and Fergus(2009), (f) Pan et al (2017), (g) Zhang, X. et al. (2015), and (h) Zhang, J. et al. (2014).

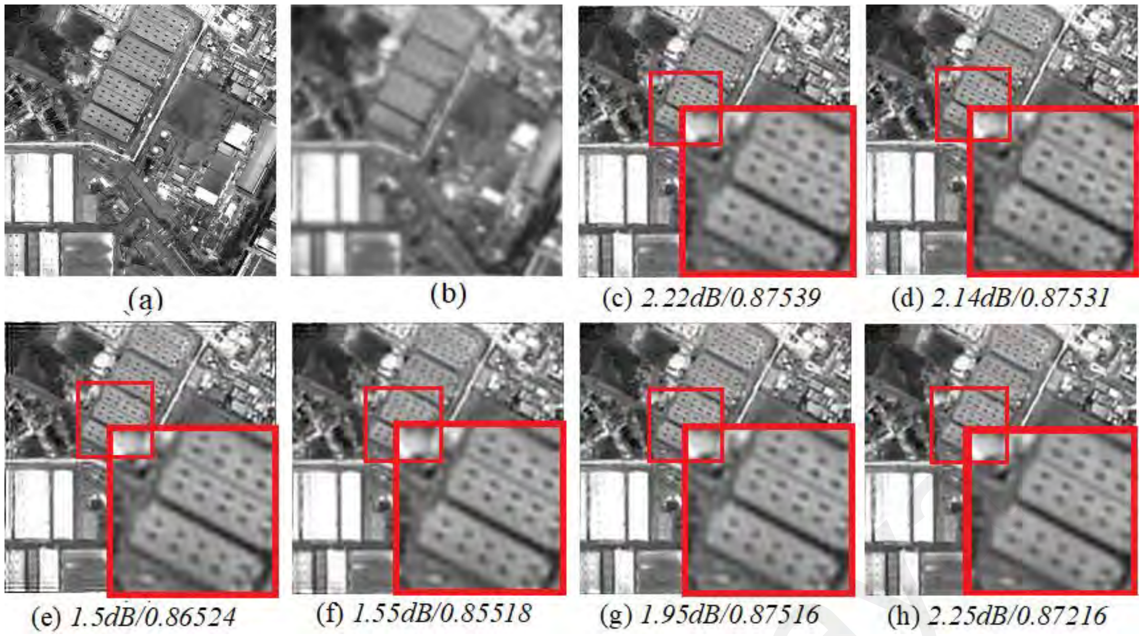

Figure 6.25: Visual quality comparison of image restoration in the case of blur σ =4, red box denotes cropped region; The quantitative measurement value at the left of the slash denotes ISNR (dB) and the right of the slash denotes FSIM. (a) Original image, (b) Blurred-noisy image, S6. Restoration results by c) the proposed method, (d) Wiener filter (Lee et al., 2016), (e) Krishnan and Fergus(2009), (f) Pan et al (2017), (g) Zhang, X. et al. (2015), and (h) Zhang, J. et al. (2014).

From visual observation, it is apparent that all the methods produce sharper images than the blurred-noisy image. From the close-up view, noise amplification can be observed in the restored results by Wiener filter (Lee et al., 2016); the method by Krishnan and Fergus (2009) is good at capturing contour structures but fails in recovering textures and produces over-smooth effects. Also, it can be observed that the method of (Krishnan & Fergus, 2009) can restore better texture than the method of (Pan et al, 2017) however it produces noticeable boundary artifacts. These artifacts can be overcome to some extent with edge tapering operations. Meanwhile, the hybrid method by Zhang, X. et al. (2015) can restore textures better than the method by Krishnan and Fergus (2009) and suppresses most of the noise-caused artifacts, however, it is exhibiting a lower contrast visual quality than other methods. In comparison, the hybrid method by Zhang, J. et al. (2014) produces a much cleaner image with sharper edges and textures, however, for large blur images, it tends to produce an unnatural appearance (i.e. cartoon effect) on the restored image.

Based on this experiment, the proposed regularisation-based MTFC method is found to be able to provide accurate restoration on both edges and textures with almost unnoticeable ringing artifacts. It is exhibiting good visual quality, which is consistent with FSIM. While it may not have to produce visual quality as clean as the method of Zhang, J. et al., 2014, but it exhibits a more natural effect than other methods and for large blurred images.

6.4.3 Experiments on Real Satellite Datasets

In a real-world application, the non-blind deconvolution performs as part of the blind image restoration, where the ground truth blur kernel is unknown, thus making it more challenging. Thus, experiments are conducted to study the practicability of the proposed method for spatial quality improvement of real satellite images.

The PSF kernel of the real satellite datasets is estimated using the proposed MTF measurement method in Chapter 4. As shown in Figure 6.26, even though the blur kernel is not precisely known, visually it can be observed the restored images are sharper images than the real unknown blur images. The visual quality implies that the proposed method can recover the details of the blurry image and suppress the ringing artifacts.

Figures 6.27 (a) to 6.27(d) depict the MTF plot with respect to the images in Figure 6.26. From Figure 6.27, it can be noticed that the MTFA under the MTF curve for the restored images is obviously larger than the real blur images. The MTFA ratio for images R1, R2, R3, and R4 is 1.53, 1.38, 1.26, and 1.37, respectively. The quantitative measurements indicate spatial image quality improvement by the proposed method. More of the experimental results can be found in Appendix E.

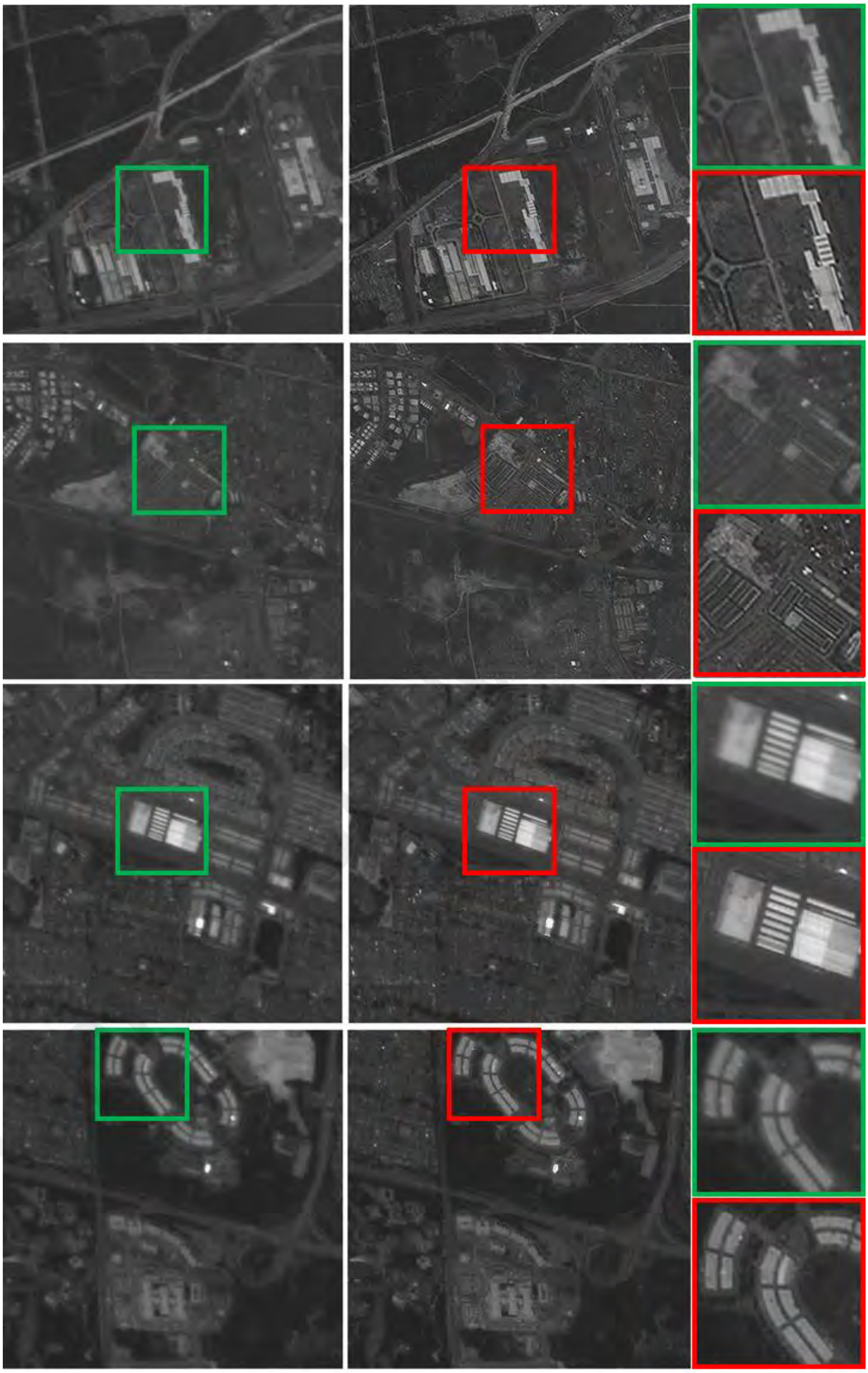

Figure 6.26: Visual quality comparison of image restoration on real satellite images. (a) Before image restoration, (b) After image restoration, and (c) The green and red box denotes cropped regions for (a) and (b), respectively.

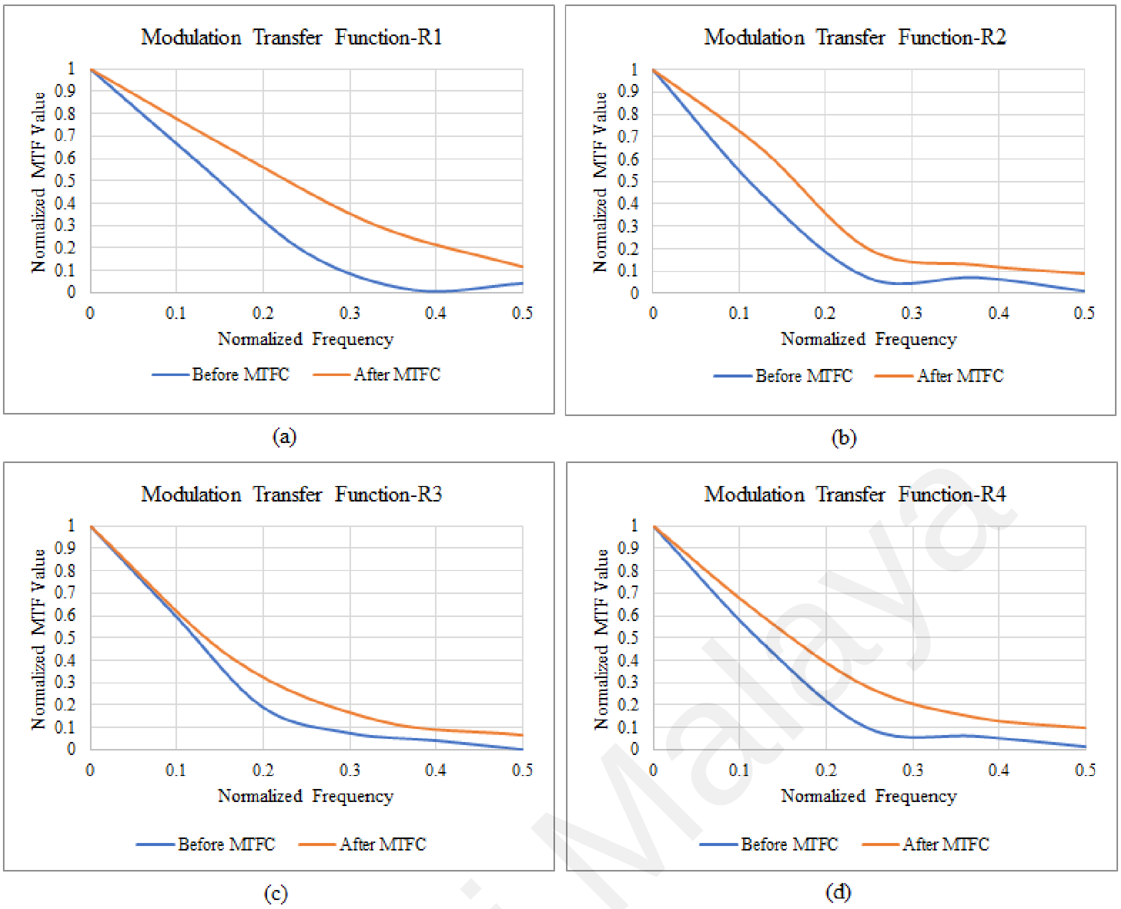

Figure 6.27: MTF profile for before and after MTFC correspond to figures 5.16(a) R1-first row (MTFA ratio= 1.53), (b) R1-second row (MTFA ratio: 1.38), (c) R3-third row (MTFA ratio = 1.26), and (d) R4-fourth row (MTFA ratio: 1.3).

6.4.4 Algorithm Complexity and Computational Time

The proposed method is implemented in MATLAB on an Intel Core i5 CPU with 8 GB of RAM. Comparing the u^L, u^U, f^L, f^U sub-problems in the bilevel programming, it is obvious to conclude that the main complexity of the proposed algorithm comes from the u^U sub-problem. However, as the primary computational task in both Upper-and Lower-level problems consists of FFT, therefore, overall it has a very low computational complexity. In the implementation, for an image of size 512×512, the bilevel optimization costs (9.53 ± 0.26) seconds. Table 6.6. presents the computational time of all competing methods on the test images. From the table, it is obvious that Wiener Filter (Lee et al, 2016) is the fastest method. The method by Krishnan and Fergus (2009) and Pan et al. (2017) come in second and third fastest, respectively. The proposed method being the fourth fastest. Although Zhang, J. et al. (2014) have the highest ISNR in most cases, it suffers from huge computational times due to the need for dictionary learning. It is about 120 times slower than the proposed method.

Table 6.6: Average processing time (seconds) of different methods on images of size 512×512.

Methods	Gaussian blur, σ			
	1	2	3	4
Lee et al. (2016)	0.15 ± 0.01	0.18 ± 0.02	0.21 ± 0.02	0.24 ± 0.02
Krishnan and Fergus (2009)	0.69 ± 0.02	0.79 ± 0.02	1.06 ± 0.05	1.25 ± 0.02
Pan et al. (2017)	4.80 ± 0.30	4.38 ± 0.43	4.79 ± 0.37	4.29 ± 0.34
Zhang, X. et al. (2015)	9.89 ± 0.39	10.79 ± 0.41	11.78 ± 0.80	12.64 ± 0.59
Zhang, J. et al. (2014)	1016.15 ± 86.22	1065.73 ± 83.53	1103.34 ± 94.48	1254.18 ± 103.93
Proposed Method	9.34 ± 0.21	9.35 ± 0.28	9.89 ± 0.33	9.56 ± 0.22

From Table 6.6, unlike methods by (Krishnan & Fergus, 2009; Zhang, X., et al. 2015; Zhang, J. et al., 2014), the computational complexity of the proposed method and Wiener filter (Lee et al., 2016) are independent of the amount of blur.

6.4.5 Algorithm Convergence and Robustness

In numerical optimization, the number of iterations for convergence, or convergence speed, is important. The proposed bilevel MTFC algorithm utilizes the alternating minimization method and least error minimization in solving the LLP and ULP, respectively. Both minimization methods ensure that each sub-problem has a closed-form solution. Thus, it has a fast convergence property. Figure 6.28 shows the improvement of SNR with respect to iterations. It is observed that with the growth of the iteration number, the ISNR curves increase monotonically and converge, which demonstrates the convergence of the proposed method. The algorithm convergence helps to determine the stopping criterion much easier by just pre-set the maximum iteration number.

Furthermore, from Figure 6.28(c), it is obvious that the initialization results in a higher quality of the intermediate latent image f_L from LLP require fewer iteration numbers to be convergent. The convergence analysis fully illustrates the robustness of the proposed method, that is, the proposed method can provide almost the same results when starting with various initializations in ULP.

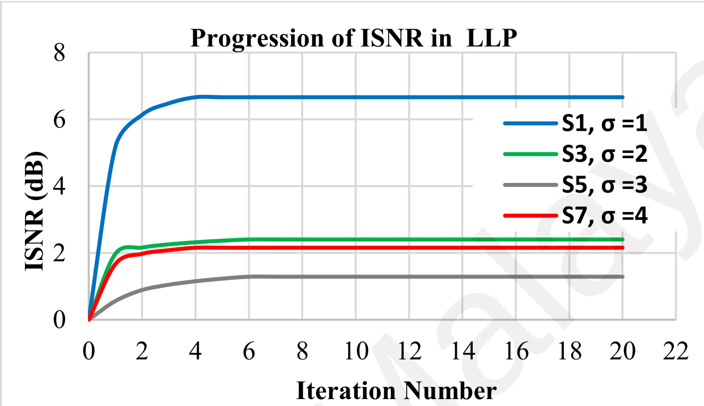

(a)

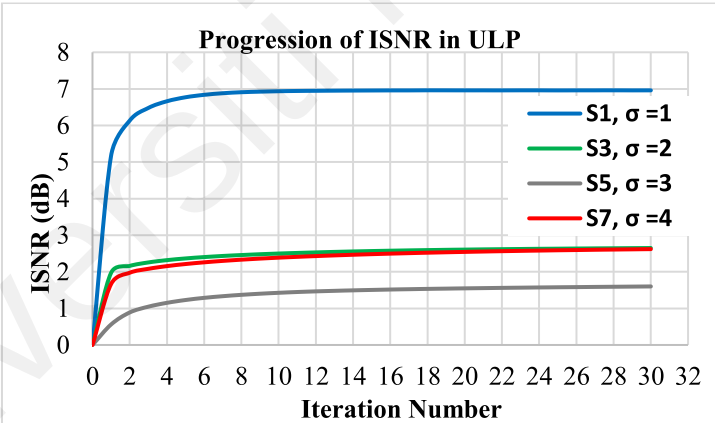

(b)

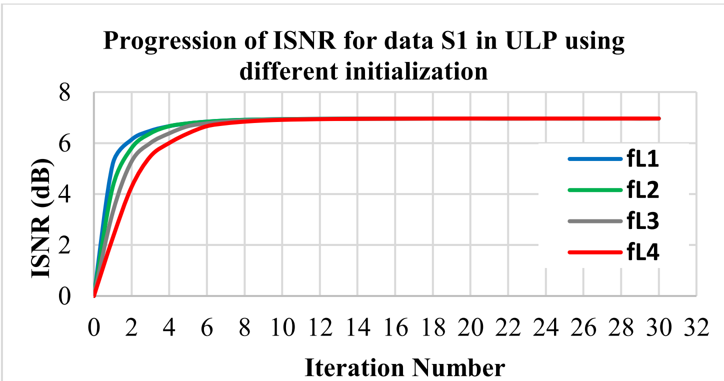

(c)

Figure 6.28: Verification of the convergence and robustness of the proposed algorithm.

6.5 Conclusion

This chapter describes a robust and efficient MTF compensation method for restoring optical satellite images with high fidelity using a joint statistical model in the Curvelet domain. This work exploited the merit of image prior characteristic in the local smooth and nonlocal self-similarity properties of an image, to design an effective regularization term to solve the underdetermined inverse problem of MTFC. In particular, this work shows that the regularization-based MTFC can be reformulated as a tractable optimization problem using the MBP. Extensive comparisons against leading methods in non-blind deconvolution are performed to evaluate the performance of the proposed method. The ISNR and FSIM, are used for image quality assessment in terms of effectiveness, whereas computation time is used for assessment in terms of efficiency. The evaluation results show that the proposed method achieves significant performance in preserving more image details and exhibits good convergence property with minimum computational complexity. This indicates the proposed regularization-based MTFC method found a compromise between solution accuracy and computational efficiency, which can be used to compensate for the degradation for optical satellite image spatial quality improvement before data dissemination.

CHAPTER 7: CONCLUSION

7.1 Research Summary

EOS data and its derived products shall have associated with quality assurance EOS data processing to enable users to assess their "fitness for purpose" (WGCV, 2019). As such, the research problem domain is in the field of optical EOS data Cal/Val that focused on spatial image characterisation and calibration. For on-orbit spatial characterisation, although there exist well-established methods in the current practice, these methods are generally constraint by stringent criteria, precision, and temporal issues, which created issues of reliability and flexibility. Whereas for spatial image calibration, due to the inherently ill-posed problem of image restoration methods that typically induce artifacts in the derived EOS products, the existing method has become an optional process for the user. Moreover, most studies in the field of image restoration have only focused on natural images, relatively only a few studies have attempted to restore optical satellite images. Furthermore, one of the most significant problems to existing image restoration methods is that they are usually suffered from computational complexity. With the aforementioned challenges, in this research work, new ideas are investigated to address the issues in the two research focus areas by introducing (1) a spatial characterisation framework for on-orbit optical EOS imaging and data assessment, and (2) solutions to image restoration problems for spatial image quality improvement. This thesis discussed their theory, design, development, and verified their performance by analyses and experiments using a wide range of datasets, consisting of synthetic and real satellite images.

The primary goal for this research work is to develop a consolidated framework that encompasses on-orbit spatial image characterisation and restoration methods, to facilitate spatial quality assurance of optical satellite data product processing in a reliable and flexible manner that is commensurate with the needs of the users (i.e., data processors, data providers, and end-users). By considering the primary goal of this research, different strategies with specific objectives are formulated. Specifically, there are four objectives for this research. The following briefly discussed how these objectives are achieved in their respective research focus area.

On-orbit spatial characterisation: The first objective of this research work is to develop a stochastic type of image-based MTF measurement framework for a convenient approach to conduct on-orbit characterisation and the second, is to evaluate the effectiveness and practicality of using stochastic characteristics targets for on-orbit spatial characterisation. In order to achieve these objectives, three strategies are established to guide the development of this framework. First, to ensure the efficiency of the algorithms, the image gradient is utilized to accelerate the numerical optimization process. Instead of the entire observed image, a segmentation method is developed to effectively select useful stochastic targets with a relative windowed TV as ideal candidates for PSF estimation. Second, to warrant reliable PSF estimation results, new TV-prior terms are introduced in structure extraction algorithms that adaptively select salient structures while mitigating detrimental structures. Third, to obtain a high fidelity PSF kernel, a new prior term is introduced in the minimization function to preserve the sparsity and continuity of the image gradient while suppressing the noises in the PSF kernel. The detailed research work for this framework was described in Chapter 4. This thesis divided the process of this framework into three phases, Selection of ideal candidates, Robust PSF estimation, and finally is the MTF calculation. Empirically, research work showed that the selection of an ideal candidate method can effectively select useful stochastic targets for PSF estimation. Experimental results demonstrated that the proposed framework is practical and effective. One of the strengths of this research work is that it represents a new norm for on-orbit spatial characterisation independent of the vicarious calibration target.

Spatial image restoration: The study in Chapter 5 is a continuation of the first framework in Chapter 4, which further study the proposed MTF measurement method as a degradation function; and evaluate it as the blur estimation in the blind deconvolution domain problem. The objective of the study, which also the third objective in research work is to conduct a comparative study for further understanding of image priors that appropriate to remove spatial blur in optical satellite images. To this end, this Work studies the significance of the most recently used state-of-art priors as a comparison. Since the proposed blur estimation method is a type of sparse representation method, hence, the graph-based prior (Bai et al. 2018) and low-rank priors (Ren et al., 2016) type of blur estimation methods are selected. This Work studied their motivations, mathematical representations, and developed the algorithms according to Bai et al. (2018) and Ren et al. (2016). The algorithms are experiments using datasets that are synthetically blurred with three groups of blurred cases, including defocus, Gaussian blur, and motion blur. The strengths of the study included an in-depth analysis of three different image priors on a different type of blur that may bring motivation and introduction to new insight into the research focus area.

The fourth objective is to develop a low computational regularized-based MTFC method that executes an optimal trade-off between noise regularization and detail preservation for high fidelity low-level vision processing of EOS data products. The details of the methods are discussed in Chapter 6. Specifically, new regularization functions are developed within a joint statistical model. The joint statistical model consists of (1) the local smoothness to suppress artifacts in the smooth region and along the edge, and (2) the nonlocal self-similarity image properties to preserve structure and image details. Empirically, this work showed that the joint statistical model can draw out the merit of a different image prior characteristic in different image properties. The effectiveness and efficiency of the proposed method have been demonstrated with five state-of-art methods. Although the findings show that the patch-based regularization method performs better, this study has several strengths. This study demonstrated that low computational optimization algorithms are possible with the use of MBP. With its ability for solving the disjunctive nature of the complementarity constraints, it is tractable and has shown good convergency properties. Besides, the minimization in MBP can be decoupled and solved separately in a single BP.

The section that follows discusses the findings from the research focus area. Based on the findings, comments on the strength and weaknesses of the research works will be presented. The significance of the findings will as the achievements, becomes the contribution of the study, where for all weaknesses, they will be the future works and direction of this research.

7.2 Research Findings

This section highlights the findings for the research work reported in this thesis based on the research focus area.

7.2.1 On-orbit Spatial Characterisation

From the research work in this focus area, there are several conclusive findings as follows:

i. On-orbit spatial calibration using the stochastic characteristic target in the observed image for MTF measurement was found practical. It is practical since image properties inherently containing nonlocal self-similarity characteristics, where its structure components can be extracted and used to estimate the PSF kernel (i.e., 2-D PSF) of the observed image. Based on Section 4.3.3., the FWHM of PSF value and the MTF values at Nyquist frequency can be calculated to characterize the spatial responsivity of the in-flight EOS imaging system. The experimental results demonstrate the effectiveness of the proposed method by achieving < 2.3% of relative SD at the Nyquist frequency as compared to the well-established edge method. Moreover, in this study, the proposed segmentation method that automatically identifies the ideal candidates for MTF measurement was found to be efficient, where it only takes about 3 min computation time for the MTF measurement of a real satellite image. This result further confirms the practicality of the stochastic characteristic-based target for on-orbit spatial calibration.

ii. This study confirmed that good region selection is critically important for ensuring the extraction of reliable structures for PSF kernel estimation. Consistent with the literature (Hu & Yang, 2015), using the *r*-map of the Equation (4.8), the study found that not all pixels of the input blurred image are informative, contrary, they could adversely affect the estimation results. For instance, regions with short length edges and regions with a large smooth area often contain many small-scale structures due to inevitable random noise, which usually causes large kernel estimation errors. This finding further supports the idea of using segmentation in the ideal candidate selection phase is useful to increase efficiency and effectiveness. This is because it is not usually beneficial to make full use of the input blurred image, with good region selection, ideal candidates can be found to wholly represent the observed image. Moreover, using ideal candidates not only improves effectiveness but also increases efficiency, as the algorithm runs faster on a sub-image than on the entire observed image.

iii. In this study, the incorporation of hyper-laplacian priors as an adaptive smoothness weight to the renowned TV-ℓ_2 model of Rudin et al. (1992) was found effective. As it ensures sparseness of gradient magnitudes that help mitigate the staircasing effect in the structure extraction steps. While this prior guarantees the sparseness of the PSF kernel, but it is also found to neglects the continuity which sometimes induced noisy

PSF kernel. Based on this finding, a new prior as defined in Equation (4.19) is proposed to maintain the non-zero gradients in the PSF kernel, which could simultaneously suppress noise in the kernel while ensuring sparsity and continuity of the kernel.

iv. In the kernel estimation phase, based on the results, it is confirmed that the kernel size did not have much influence on the accuracy of PSF kernel estimation if the size is large enough to contain the estimated kernel. However, oversized kernels are very likely to introduce estimation errors in images with rich details regions. Besides that, it required more computational time when using the multi-scale pyramid optimization process.

v. The proposed method can provide high precision data. However, the confidence level of the derived results can be influenced by the input data (i.e., the selected idea candidates). Recall that the ideal candidates for PSF estimation are selected based on a predefined threshold (i.e., > 90 % of the highest candidate *r*-map variance value), where they will be selected if their *r*-map variance value exceeds the threshold. As shown in Sub-section 4.4.3, a scene with the urban area typically has more salient edges than a scene that has more cloud coverage, therefore, the relative SD among candidates is lower. Hence, the heavy cloud cover scene should be excluded as datasets for spatial characterisation.

vi. For the proposed on-orbit spatial characterisation method, one unanticipated finding was that the algorithm is more effective for an observed image with a larger amount of blur. Results in Section 4.4.4 noted that the relative errors are relatively larger for smaller blur images. One possible explanation is that: in contrast to earlier findings of the effectiveness in a good region selection method for salient structure extraction, however, in this case, it required extensive parameter tuning to balance the trade-off between the data fidelity and prior function. Which may not always be the most optimum, thus compromise the estimation results.

7.2.2 Spatial Image Restoration

In this research focus area, the image restoration process is studied in two separate steps: the blur kernel estimation (i.e., the degradation function) and the final image restoration (i.e., non-blind deconvolution).

i. In the comparative studies of sparsity priors (i.e., the proposed method) to the state-of-art blur kernel estimation methods (i.e., graph-based priors and low-rank priors), it is somewhat surprising that the proposed sparsity priors method with much less complicated formulation than the foremost methods is proven to be the most robust where it can effectively estimate all groups of blurs, including defocus, Gaussian blur and motion blur. Between the other two methods, the graph-based priors type has been shown to perform better than the low-rank priors type. This study shows the robustness of sparsity-priors despite its simplicity, and it is suitable for blur removal in optical satellite images.

ii. In deblurring nonlinear motion, even though the proposed prior is better than low-rank priors, but the observed difference with graph-based priors was not significant. Nevertheless, it is found that that the proposed algorithms more capable than the graph-based prior algorithms to deblur images with both small and large blur kernels especially when the blurred images contain rich details.

iii. Among the three groups of blurs, the defocus type of blur was found the most complicated, as all representative algorithms achieve relatively higher SSDE on datasets. Among all, the graph-based priors type was found the weakest.

iv. In comparison to the low-rank and the proposed sparsity priors that also used the ℓ_1-regularized sparse representation-based type of image restoration methods, it is found that the graph-based prior has competitive restoration results with significantly low complexity. This outcome may be explained by the fact that the data fitting function was implemented as a locally graph filter, instead of matrix computation. The graph filter was implemented with a Lanczos method (Susnjara et al., 2015), which is faster than the conjugate gradient algorithm (Barrett et al. 1995) for this specific problem.

v. The most obvious finding to emerge from the comparative studies is that while the sparse prior in kernel estimation are helpful, the key component making blind deconvolution possible is not solely based on the choice of prior, but also requires the thoughtful choice of an estimator to produce a high-fidelity restored image.

vi. In the effort of developing a low computational and high fidelity regularized-based MTFC method, it is confirmed that utilizing only one image property in the regularization-based framework is not enough to obtain satisfying image restoration results. It is evident in this study that it was beneficial to combine multiple priors to improve restoration performance since different image priors characterize different and complementary aspects of natural image statistics. By solving the two complementary models in a closed-form solution using the bilevel programming, much faster convergence properties can be achieved which in turn lowers the computation time.

vii. In the regularized-based MTFC framework, in the aspect of effectiveness, the proposed method considerably outperforms the best among all other methods in terms of FSIM, with a minimum FSIM value of 0.86693 and maximum FSIM value as high as 0.99829 for gaussian blur SD of 4 and 1, respectively. However, one unexpected finding was that the proposed method was outperformed by the patch-based regularization method of Zhang, J. et al. (2014) in terms of ISNR. In visual comparison, Zhang, J. et al. (2014) produce a much cleaner image with sharper edges and textures. However, for large blur images, it tends to produce an unnatural appearance (i.e. cartoon effect) on the restored image. While the proposed method may not have to produce visual quality as clean as the method of Zhang, J. et al.,(2014) but it exhibits a more natural effect than other methods and for large blurred images. A possible explanation for these results might be that the conventional metrics such as the ISNR operate directly on the intensity of the image and they do not correlate well with the subjective fidelity ratings as pointed by Zhang, L. et al. (2011). Based on both quantitative and qualitative evaluation results, since the FSIM differences between the two methods are relatively small, therefore, these findings suggest that the patch-based regularization method is better than the proposed methods. Nevertheless, in the aspect of efficiency, despite its effectiveness, the patch-based regularization method of Zhang, J. et al. (2014) suffers from huge computational times due to the need for dictionary learning, where it required about 120 times more than the proposed method.

7.3 Research Achievements and Contributions

This section elaborates on the achievements in the respective research focus areas, and subsequently, draws together the contributions in this research.

7.3.1 On-orbit Spatial Characterisation

This thesis found an alternative to onboard calibration and vicarious calibration that attributes to post-launch Cal/Val of EOS data. The approach is versatile as it is not restricted to target selection criteria and temporal issues in vicarious calibration that require the use of a well-separated fixed characteristics target. Instead, this thesis proposes an approach to use a stochastic characteristic target in the observed scene as spatial data input to the MTF measurement method which was formulated as a constrained optimization problem to accurately estimate the PSF kernel. In the process, this thesis successfully develops a framework comprised of (1) a high precision and efficient segmentation method that can automatically select ideal candidates for PSF estimation; (2) an adaptive structure selection method to select reliable structures effectively for PSF estimation; and (3) a robust PSF estimation method that can simultaneously suppress noises while preserving the sparsity and continuity of the PSF kernels for MTF measurement. With the proposed on-orbit MTF measurement framework, this thesis has achieved the first objective of this research. In the experiments, the framework was found to be able to produce a high confidence level of MTF measurement results (i.e., relative SD of the Nyquist frequency between the well-established edge method and the proposed method is < 2.3%.). Moreover, it is also found to be efficient since it only takes about 3 min computation time to obtain the MTF measurement results for on-orbit spatial characterisation. Based on these evaluation results, this thesis has shown that using stochastic characteristics targets for on-orbit spatial characterisation is practical and effective, which, in turn, has shown the achievement of the second objective for this research.

7.3.2 Spatial Image Restoration

The studies under this research focus area extend knowledge of the ill-posed image restoration problem, particularly for optical satellite images. In the research work, two different prior-based (i.e., low-rank priors and graph-based priors) are developed according to the existing work in the literature and conducted a comparative study to the proposed MTF measurement method that was designed with sparsity priors. This study drew out insightful analysis and conclusive findings of the low-level vision processing, including the behavior and the importance of the image priors in different types of blur, the query whether complex formulation will warrant a more effective algorithm, and the importance of estimator for successful final image restoration. Based on the analyses and findings, the thesis has met the third research objective that aims to gain a better understanding of image priors that appropriate for the removal of spatially varying blur in optical satellite images.

Further to this research focus, a well-posed image restoration problem is created by exploiting the merit of image statistical properties, including its non-gaussianity and heavy tails property, and also its representation in multi-resolution. To this end, this thesis successfully developed a new framework MTFC encompasses (1) two regularization models with a new form of minimization function; one was used for characterizing the properties of image smoothness and image structure, whereas the other one was used for characterizing the properties of image texture; and (2) a joint statistic model that fused the two complementary models in curvelet domain. One significant achievement in this framework is that this thesis successfully developed a robust bilevel programming algorithm with a fast convergence property to solve the underdetermined inverse problems of MTF using the two complementary regularization models. From the numerical measurement in terms of effectiveness, although the proposed MTFC method is outperformed by one of the competing methods (i.e., the patch-based regularization method), it is significantly outperformed other competing methods, including the existing MTFC. Whereas, in terms of efficiency, it takes about (9.53 ± 0.26) seconds, which is significantly better than the patch-based regularization method that takes about (1109.85 ± 102.63). Moreover, in terms of visual evaluation, it is comparable to the patch-based regularization method. The evidence presented thus suggested this thesis met the fourth objective since the proposed algorithms are effective as it capable of finding an optimal trade-off between noise regularization and detailed preservation in the restored image, and they are practical to use in optical satellite images as they run with low computation time.

7.3.3 Contributions

Based on the research achievements, this Work suggests that the research works make important contributions to the field of EOS data Cal/Val by introducing

i. A new approach of on-orbit spatial characterisation using the stochastic characteristic targets, which offers an automated and flexible way to spatial characterisation. This is the first study that has evaluated the effectiveness and practicality of stochastic characteristics target for on-orbit spatial characterisation.

ii. A robust PSF estimation method was designed with an improved TV-ℓ_2 model and new sparse priors regularization for ensuring an accurate estimation of degradation function for blind image restoration.

iii. A practical and effective regularized-based MTFC method to improve the spatial quality of EOS data for reliable data dissemination. Notwithstanding the findings from Sub-section 7.2.2. (iv), this Work offers valuable insights into the use of image statistical properties in optical satellite image processing and analysis.

iv. A comparative study about the usefulness of image priors for spatially varying and invariant blur in optical satellite images; and comprehensive literature of spatial characterisation and restoration in optical satellite images. The study, therefore, will introduce new insight into the research focus area that may promote innovation and motivation to guide future research in this area.

7.4 Future Works and Directions

Despite the achievements and contributions presented in Section 7.3, there are weaknesses found in the findings and other important issues worth further research. Besides, based on the studies, the real-world image restoration problem is still a challenging task and needs future research for new solutions. The following section presents the direction for future works.

7.4.1 Deep prior learning

Deep Learning, and Deep Convolutional Neural Networks (DCNN) in particular, currently set the state-of-the-art performance in signal and data processing. Recently, in remote sensing, a considerable amount of research has adopted the application of deep learning for typical supervised learning tasks such as classification (e.g., Romero, Gatta, & Camps-Valls, 2016; Fotiadou, Tsagkatakis, & Tsakalides, 2017). As pointed in the findings, one critical aspect to ensure the availability of reliable structure for PSF estimation is through a good region selection. Even though the proposed Ideal Candidates Selection technique was found to be effective, it cannot differentiate the object of the scenes. In the experiments, it was found that a scene with a more urban area and lesser cloud cover provides a higher confidence level results since more salient edges can be found in the observed scene. As remote sensing data also bring chance and challenge for deep learning. Therefore, this thesis proposes to further the research work to investigate the potential of deep learning in on-orbit spatial characterisation, particularly in the selection of ideal candidates phase.

7.4.2 New image priors

Although new priors for image (and blur) modeling have been proposed in this Work, many competing models have been recently published, of particular interest here is the deep image prior. In the literature, most of the works emphasized that learning is necessary for building good image priors (Zhang, J. et al. 2015; Li et al., 2016; Zha et al. 2018), hence, a great deal of image statistics are captured by the structure of a convolutional image generator independent of learning, such as dictionary-based priors. Therefore, for the directions of this Work, it would be worth investigating the differences between deep images prior and the proposed models, as well as whether any of the features of this model can be adapted for use in the MTFC problem. Furthermore, a comparative study between dictionary-based priors and deep learning-based priors will also provide important insight into the development of approaches for remote sensing observation enhancement.

7.4.3 Determining Kernel Size in Blind Deconvolution

As presented in the findings, there is an issue in determining the ideal kernel size for blind deconvolution. On one hand, as discovered in Chapter 4, oversized kernels are very likely to introduce estimation errors for an observed image with rich details region (e.g., small scale edges) that leads to inaccurate results, moreover, it requires more computational time in a multi-scale pyramid optimization process. On the other hand, as discovered in Chapter 5, a smaller kernel size that the ground truth cannot provide sufficient support domain for the estimated kernel. In both cases, blur kernel estimation error is likely to be introduced, yielding severe artifacts in image restoration results. Currently, in most of the blind deconvolution methods, kernel size is treated as a hyper-parameter that is manually set. Ideally, the kernel size should be the same as the ground truth size so that it can completely constrain the PSF domain. However, in real practical application, it requires manual exhausted tuning. Therefore, in practice, users usually pre-defined a large value to guarantee the PSF domain. For further research, this thesis suggests a prediction step to exploit the structural information in degraded kernels and analyze a mechanism to estimation error in an oversized kernel, which subsequently formulates a regularization function as a stopping criterion in the optimization process to avoid oversized kernel issues.

7.4.4 Acceleration of algorithms

Many of the methods used rely on solving optimization problems, including the proposed methods that use CG algorithms and all competing methods in Chapter 6, or some of the other priors in the literature require nonlinear search procedures over sparse dictionaries. With computationally heavy algorithms of the kind described and scale necessary for processing the increasingly large images encountered in a real-world practical situation, and the change in the evolution of CPU designs, it is becoming a reality that signal processing methods cannot simply put off implementation details as a secondary step; again thought should be given during the algorithmic design stage. For instance, in Chapter 6, the successful results of patch-based regularization that exploits the nonlocal self-similarity properties of the image in preserving high fidelity images were inarguable, however, it was compromised with high computational complexity. Therefore, for future work, the author would like to study the feasibility of this regularization term in MTFC and explore ways to improve its efficiency by exploring the parallelization of algorithms, or deployment on new hardware in parallel computing.

7.5 Research Conclusion

This research set out with the ultimate aim of exploring a new approach or new methods for on-orbit spatial image characterisation and restoration. From the detailed discussion contained within this thesis, they have shown that all specific objectives of the Work have been fulfilled. In doing so, this thesis has contributed a consolidated framework to address the challenges of the optical EOS data Cal/Val particularly in spatial characterisation and calibration through the development of the MTF measurement and compensation method. This study should, therefore, be of value to engineers or researchers from the satellite development program as a validation process in assessing the quality of the acquired EOS data to ensure its "fitness for purpose" before data dissemination. The findings presented in this thesis add to the understanding of the ill-posed inverse problem in PSF estimation for spatial characterisation and calibration. Besides, they also provide insights and directions for future works. Furthermore, these findings contribute to the evidence that supports the achievements and contribution of the Work. Therefore, this thesis concluded that the primary goal for this research was fulfilled.

REFERENCES

Abdou, W. A., Helmlinger, M. C., Conel, J. E., Bruegge, C. J., Pilorz, S. H., Martonchik, J. V. & Gaitley, B. J., (2000). Ground measurements of surface BRF and HDRF using PARABOLA III. *Journal of Geophysical Research*, *106*(11), 976.

Afonso, M., Bioucas-Dias, J., & Figueiredo, M. (2010). Fast image recovery using variable splitting and constrained optimization. *IEEE Transactions on Image Processing*, *19*(9), 2345–2356.

Aghdasi, F., & Ward, R. K. (1996). Reduction of boundary artifacts in image restoration. *IEEE Transactions on Image Processing*, *5*(4), 611–618. https://doi.org/10.1109/83.491337

Agrawal, A., & Raskar, R. (2007). Gradient Domain Manipulation Techniques in Vision and Graphics. *Proceedings of the International Conference on Computer Vision*.

Aharon, M., Elad, M., & Bruckstein, A. (2006). K-SVD: An algorithm for designing overcomplete dictionaries for sparse representation. IEEE Transactions on Signal Processing, *54*(11), 4311–4322.

Al-Hamdan, M. Z., Cruise, J. F., Rickman, D. L., & Quattrochi, D. A. (2010). Effects of spatial and spectral resolutions on fractal dimensions in forested landscapes. *Remote Sensing*, *2*, 611–640.

Al-Hamdan, M. Z., Cruise, J. F., Rickman, D. L., & Quattrochi, D. A. (2012). Characterisation of forested landscapes from remotely sensed data using fractals and spatial autocorrelation. *Advances in Civil Engineering*, 1–15.

Ali, M. A., Eltohamy, F., & Salama, G. I. (1995). Estimation of NIIRS, for high resolution satellite images, using the simplified GIQE. *International Journal of Innovative Research in Computer and Communication Engineering*, *4*, 8403–8408.

Aljadaany, R., Pal, D. K., & Savvides, M. (2019). Douglas-Rachford Networks : Learning Both the Image Prior and Data Fidelity Terms for Blind Image Deconvolution. *In 2019 IEEE/CVF Conference on Computer Vision and Pattern Recognition*, 10227-10236.

Amizic, B., Babacan, S., Michael, K., Molina, R., & Katsaggelos, A. (2010). Fast total variation image restoration with parameter estimation using bayesian inference. *Proceedings of IEEE International Conference on Acoustics Speech and Signal Processing*, 770–773.

Amizic, B., Babacan, S., Michael, K., Molina, R., & Katsaggelos, A. (2010). Fast total variation image restoration with parameter estimation using bayesian inference. *IEEE International Conference on Acoustics Speech and Signal Processing*, 770–773.

Anam, C., Budi, W. S., Fujibuchi, T., Haryanto, F., & Dougherty, G. (2019). Validation of the tail replacement method in MTF calculations using the homogeneous and non-homogeneous edges of a phantom. *Journal of Physics: Conference Series*, *1248*(1). https://doi.org/10.1088/1742-6596/1248/1/012001

Andrews, H. C., & Hunt, B. R. (1977). *Digital Image Restoration*. Englewood Cliffs, NJ: Prentice-Hall, 238

Apostoloff, N., & Fitzgibbon, A. (2004). Bayesian video matting using learnt image priors. *Proceedings of the IEEE Computer Society Conference on Computer Vision and Pattern Recognition*, I-I.

ATSB (2010). RazakSAT - The High-Resolution Earth Observation Satellite – Specification 11 February 2010, Available at http://www.atsb.my/

Aubert, G., & Aujol, J. F. (2005). Modeling very oscillating signals. Application to image processing. *Applied Mathematics and Optimization*, *51*(2), 163– 182.

Aujol, J. F., & Chambolle. A. (2005). Dual norms and image decomposition models. *International Journal on Computer Vision*, *63*(1), 85–104

Aujol, J. F., Aubert, G., Blanc-F´eraud, L., & Chambolle. A. (2005). Image decomposition into abounded variation component and an oscillating component. *Journal of Mathematical Imaging and Vision*, *22*(1), 71–88.

Aujol, J.-F., Gilboa, G., Chan, T., & Osher, S. (2006). Structure-Texture Image Decomposition Modeling, Algorithms, and Parameter Selection. *International Journal of Computer Vision*, *67*(1), 111–136. doi:10.1007/s11263-006-4331-z

Ayers, G., & Dainty, J., Iterative blind deconvolution method and its applications, *Optics Letter*, 13(7), 547–549, 1988

Babacan, S., Molina, R., & Katsaggelos, A. (2008). Parameter estimation in TV image restoration using variational distribution approximation. *IEEE Transactions on Image Processing*, *17*(3), 326–339.

Backman, S. M., Makynen, A. J, Kolehmainen, T. T., & Ojala, K. M. (2004). Random target method for fast MTF inspection. *Optics Express*, *12*(12), 2610–2615.

Bahadir, K., & Xin, L. (2012). *Image Restoration, Fundamentals and Advances,* Digital Imaging and Computer Vision, Book 7, (1st ed.), Boca Raton, Florida: CRC Press,

Bai, Y., Cheung, G., Liu, X., & Gao, W. (2018). Blind image deblurring via reweighted graph total variation. *Proceedings of the IEEE International Conference on Acoustics, Speech and Signal Processing.*

Bai, Y., Cheung, G., Liu, X., & Gao, W. (2019). Graph-Based Blind Image Deblurring From a Single Photograph. *IEEE Transactions on Image Processing*, *28*(3), 1404–1418.

Banham, M. R., & Katsaggelos, A. K. (1997). Digital image restoration. *IEEE Signal Processing Magazine*, *14*(2), 24–41.

Bannari, A., Omari, K., Teillet, P. M., & Fedosejes, G. (2004). Multi-sensor and multi-scale survey and characterization for radiometric spatial uniformity and temporal stability of Railroad Valley Playa (Nevada) test site used for optical sensor calibration. *Proceedings of SPIE - The International Society for Optical Engineering 5234*, 590-604.

Barrett R., Berry, M. W., Chan, T. F., Demmel, J., Donato, J., Dongarra, J., …, Vorst, H. V. D. (1994). Templates for the Solution of Linear Systems Building Blocks for Iterative Methods. *SIAM*.

Bascle, B., Blake, A., & Zisserman, A. (1996). Motion deblurring and superresolution from an image sequence. *Proceedings of the European Conference on Computer Vision*, *2*, 573–582.

Beck A., & Teboulle, M. (2009). A fast iterative shrinkage-thresholding algorithm for linear inverse problems. *SIAM Journal on Imaging Sciences*, *2*(1), 183–202.

Beck, A., & Teboulle, M. (2009). Fast gradient-based algorithms for constrained total variation image denoising and deblurring problems. *IEEE Transactions on Image Processing*, *18*(11), 2419–2434.

Bect, J., Aubert, G., Blanc-F´eraud, L., & Chambolle, A. (2004). A L1 unified variational framwork for image restoration. *The 8th European Conference on Computer* Vision. 1-3.

Bellettini, G., Caselles, V., & Novaga, M. (2002). The total variation flow in RN . *Journal of Differential Equations*, *184*(2), 475–525.

Belward, A. S., & Skøien, J. O. (2015). Who launched what, when and why; trends in global land-cover observation capacity from civilian earth observation satellites. *ISPRS Journal of Photogrammetry and Remote Sensing*. https://doi.org/10.1016/j.isprsjprs.2014.03.009

Bensebaa, K., Banon, G. J. F, Fonseca, L. M. G., & Erthal, G.J., (2007). On-orbit spatial resolution estimation of CBERS-2 imaging system using ideal edge target. *Signal Processing for Image Enhancement and Multimedia Processing*, *31*, 37-48.

Berger, P., Hannak, G., & Matz, G. (2017). Graph signal recovery via primal dual algorithms for total variation minimization. *IEEE Journal of Selected Topics in Signal Processing*, *11*(6), 842–855.

Bhat P., Zitnick C. L., Cohen M., Curless B.: Gradientshop: (2010). A Gradient-Domain Optimization Framework For Image And Video Filtering. *ACM Transactions on Graphics*, *29*(2), 10.

Bhutada, G. G., Anand, R. S., & Saxena, S. C. (2011). Edge preserved image enhancement using adaptive fusion of images denoised by wavelet and curvelet transform. *Digital Signal Processing*, *21*(1), 118–130.

Bigdeli, S. A., Jin, M., Favaro, P., & Zwicker, M. (2017). Deep mean-shift priors for image restoration. *Advances in Neural Information Processing Systems*, *2017-Decem*(Nips), 764–773.

Bigdeli, S. A., Jin, M., Favaro, P., & Zwicker, M. (2017). Deep mean-shift priors for image restoration. *Advances in Neural Information Processing Systems*, 764–773.

Bioucas-Dias, J., & Figueiredo, M. (2007). A new TwIST: two-step iterative shrinkage/thresholding algorithms for image restoration. *IEEE Transactions on Image Processing*, *16*(12), 2992–3004.

Bioucas-Dias, J., Figueiredo, M., & Oliveira, J. (2006). Total variation-based image deconvolution: a majorization-minimization approach. *Proceedings of IEEE International Conference on Acoustics, Speech and Signal Processing*, *2*, 861–864.

Blanc, P. (2008). *Calibration Test Sites Selection and Characterisation-WP210* (No. TN-WP210-001-ARMINES). Toulouse, France.

Blanc, P., & Wald, L. (2008). Image Quality – WP224 (ARMINES). TN-WP224- 001-ARMINES, Issue 1.0, ESA/ESRIN

Blanc, P., & Wald, L. (2009). *A review of earth-viewing methods for in-flight assessment of modulation transfer function and noise of optical spaceborne sensors*. Working Paper. doi:10.3390/algor10x000x

Blonski, S., (2005). Spatial resolution characterization for QuickBird image products: 2003-2004 season. *Proceedings of the 2004 High Spatial Resolution Commercial Imagery Workshop*, USGS.

Boggione, G. A. & Fonseca, L. M. G., (2003). Restoration of Landsat-7 Images. *Proceedings of international of 30th Symposium on Remote Sensing of Environment: Information for Risk Management and Sustainable Development*. 10-14.

Bolz, J., Farmer, I., Grinspun, E., & Schröder, P. (2003). Sparse Matrix Solvers On The Gpu: Conjugate Gradients And Multigrid. *ACM Transactions on Graphics*. *22*(3), 917–924.

Bonneel N., Sunkavalli K., Tompkin J., Sun, D., Paris S., & Pfister H. (2014). Interactive Intrinsic Video Editing. *ACM Transactions on Graphics*, *33*(6), 197. doi:10.1145/2661229.2661253

Boreman, G. D. (2001). *Modulation Transfer Function in Optical and Electro-Optical Systems*, Bellingham, WA:SPIE Press.

Bovik, A. (2009). *The Essential Guide to the Image Processing*. New York, USA: Academic Press.

Bretschneider, T. (2002). Blur identification in satellite imagery using an image doublet. *Proceedings of 23rd Asian Conference on Remote Sensing*, 25-29.

Bretschneider, T. (2002). On the deconvolution of satellite imagery, *Proceedings of IEEE International Geoscience and Remote Sensing Symposium*, *4*, 2450–2452.

Bruckstein, A. M., Donoho, D. L., & Elad, M. (2009). From sparse solutions of systems of equations to sparse modeling of signals and images. *SIAM Review*, *51*(1). 34–81.

Bruckstein, A. M., Donoho, D. L., & Elad, M. (2017). Nonconvex and nonsmooth total generalized variation model for image restoration. *IEEE Transactions on Geoscience and Remote Sensing*, *7*(3), 1–13. https://doi.org/10.1016/j.eswa.2014.09.017

Bruckstein, A. M., Donoho, D. L., & Elad, M. (2017). Nonconvex and nonsmooth total generalized variation model for image restoration. *IEEE Transactions on Geoscience and Remote Sensing*, *7*(3), 1–13. doi:10.1016/j.eswa.2014.09.017

Buades, A., Coll, B., & Morel, J. M. (2005). A non-local algorithm for image denoising. *Proceedings of International Conference on Computer Vision and Pattern Recognition*, 60–65.

Burns, P. D., & Williams, D. (2002). Refined slanted-edge measurement practical camera and scanner testing. *in I&ST SPIE PICS*, 191–195.

Cai, J. F., Osher, S., & Shen, Z. W. (2009). Split Bregman methods and frame-based image restoration. *Journal of Multiscale Modeling and Simulation*, *8*, 5057–5071.

Cai, J., Dong, B., Osher, S., & Shen, Z. (2012). Image restorations: total variation, wavelet frames and beyond. *Journal of the American Mathematical Society*, *25*, 1033-1089.

Cai, J.-F., Candès, E. J., & Shen, Z. (2010). A singular value thresholding algorithm for matrix completion. *SIAM Journal on Optimization*, *20*(4), 1956–1982.

Cai, J.-F., Ji, H., Liu, C.,& Shen, Z. (2012). Framelet-based blind motion deblurring from a single image. IEEE Transactions on Image Processing, *21*(2), 562–572.

Campisi, P., & Egiazarian, K., (2017). Blind Image Deconvolution: Theory and Applications. New York: CRC Press.

Candès, E. J., & Donoho, D.L. (2000). Curvelets, multiresolution representation, and scaling laws. *Wavelet Applications in Signal and Image Processing VIII, SPIE*, *4119*, 1–12.

Candès, E. J., Demanet, L., Donoho, D., & Ying, L. (2006). Fast discrete curvelet transforms. *Journal of Multiscale Modeling and Simulation*, *5*(3), 861–899.

Candès, E. J., Li, X., Ma, Y., & Wright, J. (2011). Robust principal component analysis. *Journal of the ACM*, *58*(3), 11.

Candès, E. J., Romberg, J., & Tao, T. (2006). Robust uncertainty principles: Exact signal reconstruction from highly incomplete frequency information. *IEEE Transactions on Information Theory.* *52*(2), 489–509.

Cao, S., He, N., Zhao, S., Lu, K., & Zhou, X. (2018). Single image motion deblurring with reduced ringing effects using variational Bayesian estimation. *Signal Processing*, *148*, 260–271. https://doi.org/10.1016/j.sigpro.2018.02.015

Cao, S., He, N., Zhao, S., Lu, K., & Zhou, X. (2018). Single image motion deblurring with reduced ringing effects using variational Bayesian estimation. *Signal Processing*, *148*, 260–271. https://doi.org/10.1016/j.sigpro.2018.02.015

Cao, S., He, N., Zhao, S., Lu, K., & Zhou, X. (2018). Single image motion deblurring with reduced ringing effects using variational Bayesian estimation. *Signal Processing*, *148*, 260–271. https://doi.org/10.1016/j.sigpro.2018.02.015

Cao, S., Tan, W., Xing, K., He, H., & Jiang, J. (2018). Dark channel inspired deblurring method for remote sensing image. *Journal of Applied Remote Sensing*, *12*(1), 1–13. https://doi.org/10.1117/1.JRS.12.015012

Cao, S., Zhang, Q., He, N., & Lu, K. (2016). Ringing reduction in image restoration using cyclic boundary. *ACM International Conference Proceeding Series*, *19-21-August-2016*, 197–200. https://doi.org/10.1145/3007669.3008271

Cao, X., Ren, W., Zuo, W., Guo, X., & Foroosh, H. (2015). Scene text deblurring using text-specific multiscale dictionaries. *IEEE Transactions on Image Processing*, *22*(4), 1302–1314.

Chambolle, A. (2004). An algorithm for total variation minimization and applications. *Journal of Mathematical Imaging and Vision*. *20*(1), 89–97.

Chambolle, A., & Lions, L.O. (1997). Image recovery via total variation minimization and related problems. *Numerische Mathematik*, *76*(3):167–188.

Chan, T. F. & Shen. J. (2005). Image Processing and Analysis: Variational, PDE, wavelet, and Stochastic Methods. *SIAM*, ISBN: 089871589X

Chan, T., & Esedoglu. S. (2004). Aspects of total variation regularized L1 function approximation. *SIAM Journal on Applied Mathematics*, *65*(5), 1817–1837.

Chan, T., & Zhou, H. M. (2007). Total variation wavelet thresholding. *Journal of Science Computer*, *32*, 315–341.

Chang, C., & Wu, J. (2015). A New Hyper-Laplacian Prior-Based Deconvolution Method for Single Image Deblurring, *International Journal of Computer, Consumer and Control*, *4*(1), 9–18.

Chang, C., & Wu, J. (2015). A New Hyper-Laplacian Prior-Based Deconvolution Method for Single Image Deblurring. *International Journal of Computer, Consumer and Control (IJ3C)*, *4*(1), 9–18

Chang, Y., Yan, L., Fang, H., Zhong S., & Liao, W. (2019). HSI-DeNet: Hyperspectral Image Restoration via Convolutional Neural Network. *IEEE Transactions on Geoscience and Remote Sensing*, 57(2), 667-682.

Chang, Y., Yan, L., Fang, H., Zhong, S., & Liao, W. (2019). HSI-DeNet: Hyperspectral Image Restoration via Convolutional Neural Network. *IEEE Transactions on Geoscience and Remote Sensing*, *57*(2), 667–682. https://doi.org/10.1109/TGRS.2018.2859203

Chen SS, Donoho DL, Saunders MA (1998) Atomic decomposition by basis pursuit. SIAM journal on scientific computing 20(1):33–61

Chen, H. S. (1997). *Remote sensing calibration systems : an introduction*. *Studies in Geophysical Optics and Remote Sensing*. Hampton, Virginia: A. Deepak Publishing.

Chen, H., Wang, C., Song, Y., & Li, Z. (2015). Split Bregmanized anisotropic total variation model for image deblurring. *Journal of Visual Communication and Image Representation*, *31*, 282–293.

Chen, S., Donoho, D., & Saunders, M. (2001). Atomic decompositions by basis pursuit, *SIAM Review*, *43*, 129–159.

Chen, X. W., & Lin, X. (2014). Big data deep learning: Challenges and perspectives. *IEEE Access*, *2*, 514–525. https://doi.org/10.1109/ACCESS.2014.2325029

Chen, X., & Zhu, Q. (2018). A Fast FFT-Based Iterative Algorithm for Image Deblurring With Anti-Reflective Boundary Conditions, *147*(Ncce), 431–441. https://doi.org/10.2991/ncce-18.2018.68

Chen, Y., & Liu, K. (2013). Image Denoising Games. *IEEE Transactions on Circuits and Systems for Video Technology*, *23*(10), 1704–1716.

Cheng, M. H., Huang, T. Z., Zhao, X. Le, Ma, T. H., & Huang, J. (2019). A variational model with hybrid Hyper-Laplacian priors for Retinex. *Applied Mathematical Modelling*, *66*, 305–321. https://doi.org/10.1016/j.apm.2018.09.022

Cheng, M. H., Huang, T. Z., Zhao, X. Le, Ma, T. H., & Huang, J. (2019). A variational model with hybrid Hyper-Laplacian priors for Retinex. *Applied Mathematical Modelling*. https://doi.org/10.1016/j.apm.2018.09.022

Cheng, M. H., Huang, T. Z., Zhao, X., Ma, T. H., & Huang, J. A. (2019). A variational model with hybrid Hyper-Laplacian priors for Retinex. *Applied Mathematical Modelling*, *66*, 305–321.

Cheong, H., Chae, E., Lee, E., Jo, G., & Paik, J. (2015). Fast image restoration for spatially varying defocus blur of imaging sensor. *Sensors (Switzerland)*, *15*(1), 880–898. https://doi.org/10.3390/s150100880

Cheong, H., Chae, E., Lee, E., Jo, G., & Paik, J. (2015). Fast image restoration for spatially varying defocus blur of imaging sensor. *Sensors (Switzerland)*, *15*(1), 880–898. doi:.0.3390/s150100880

Cho, H., Lee, H., Kang, H., & Lee, S. (2014). Bilateral Texture Filtering. *ACM Transactions on Graphics*, *33*(4).

Cho, H., Wang, J., & Lee, S. (2012). Text image deblurring using text-specific properties. *Proceedings of the 12th European Conference on Computer Vision*, 524–537.

Cho, S., & Lee, S. (2009). Fast motion deblurring. *ACM Transactions on Graphics*, *28*(5).

Cho, S., Cho, H., Tai, Y. W., & Lee, S. (2012b). Registration based non-uniform motion deblurring. *Computer Graphics Forum*, *31*(7), 2183–2192.

Cho, T. S., Joshi, N., Zitnick, C. L., Kang, S. B., Szeliski, R., & Freeman, W. T. (2010). A content-aware image prior. *Proceedings of the IEEE Computer Society Conference on Computer Vision and Pattern Recognition*, 169–176. doi:10.1109/CVPR.2010.5540214

Choi, T., Xiong, X., & Wang, Z. (2014).On-Orbit Lunar Modulation Transfer Function Measurements for the Moderate Resolution Imaging Spectroradiometer. *IEEE Transactions on Geoscience and Remote Sensing*, 52(1), 2014, 270–277

Choksi, R., Gennip, Y. V., & Oberman, A. (2011). Anisotropic total variation regularized l1-approximation and denoising/deblurring of 2d bar codes. *Inverse Problem and Imaging*, *3*, 591–617.

Cleveland, W., (1985). The Elements of Graphing Data. Wadsworth, Belmont, CA, USA.

Coltman J. W. (1954). The Specification of Imaging Properties by Response to a Sine Wave Input. *Journal of the optical society of America*, 44(6), 468–469.

Constantinos, B., & Sheldon. J. (1990). Surface fitting method for three dimensional scattered data. *International Journal for Numerical Methods in Engineering*. *29*, 633 - 645. doi:10.1002/nme.1620290311.

Cook, M. K., Peterson, B. A., Dial, G., Gibson, L. Gerlach, F. W., Hutchins, K., …, & Bowen, H. S. (2001). IKONOS technical performance assessment. *Proceedings of SPIE 4381*, 94–108.

Couprie, C., & Grady, L., & Najman, L., Pesquet, J.-C., & Talbot, H. (2013). Dual constrained TV-based regularization on graphs. *SIAM Journal on Imaging Sciences*, *6*(3), 1246–1273.

Couzinie-Devy, F., Mairal, J., Bach, F., & Ponce. J. (2011). Dictionary learning for deblurring and digital zoom. [Online]. Available: http://arxiv.org/abs/1110.0957

Crespi, M., & Vendictis, L. De. (2009). A Procedure for High Resolution Satellite Imagery Quality Assessment. *Sensors*, *9*(5), 3289–3313. doi:10.3390/s90503289

Crochiere, R. E., & Rabiner, L. R., (1983). *Multirate Digital Signal Processing*, Englewood Cliffs, N.J.: Prentice Hall.

Csisz´ar, I. and Tusn´ady, G. (1984) “Information geometry and alternating minimization procedures.” Statistics and Decisions Supp. 1, pp. 205–237

Dabov, K., Foi, A., Katkovnik, V., & Egiazarian, K. (2007). Image denoising by sparse 3-D transform-domain collaborative filtering. *IEEE Transactions on image processing*, *16*(8), 2080–2095.

Daniels, A., Boreman, G. D., Ducharme, A. D., & Sapi, E. (1995). Random transparency targets for modulation transfer function measurement in the visible and infrared regions. *Optical Engineering*, *34*(3), 860–868. doi:10.1117/12.190433

Daubechies, I., & Teschkeb, G. (2005). Variational image restoration by means of wavelets: simultaneous decomposition, deblurring, and denoising. *Applied and Computational Harmonic Analysis*, *19*, 1–16.

Deans. S. R. (1992), *The Radon Transform And Some of Its Applications*. Krieger Publishing Company, 1992.

Dherete, P., & Rouge, B. (2003). Image de-blurring and application to SPOT5 THR satellite imaging. *IEEE International Geoscience and Remote Sensing Symposium, 1*, *3*18-320. doi:10.1109/IGARSS.2003.1293762

Dial, G., Bowen, H., Gerlach, F., Grodecki, J., & Oleszczuk, R. (2003). IKONOS satellite, imagery, and products. *Remote Sensing of Environment*, *88*(1-2), 23–36.

Do M. N., & Vetterli, M. (2005). The contourlet transform: An efficient directional multiresolution image representation. *IEEE Transactions on Image Processing*, *14*(12), 2091–2106.

Donatelli, M., Estatico, C., Martinelli, A., & Serra-Capizzano, S., (2006). Improved image deblurring with anti-reflective boundary conditions and re-blurring. *Inverse Problems*, *22*, 2035–2053.

Dong, J., Pan, J., & Su, Z. (2017). Blur kernel estimation via salient edges and low rank prior for blind image deblurring. *Signal Processing: Image Communication*, *58*, 134-145. doi:10.1016/j.image.2017.07.004

Dong, J., Pan, J., Su, Z., & Yang, M. H. (2017). Blind Image Deblurring with Outlier Handling. *Proceedings of the IEEE International Conference on Computer Vision*, *2017-October*, 2497–2505. https://doi.org/10.1109/ICCV.2017.271

Dong, W., Shi, G., & Li, X. (2013). Nonlocal image restoration with bilateral variance estimation: A low-rank approach. *IEEE Transactions on Image Processing*, *22*(2), 700–711. doi:10.1109/TIP.2012.2221729

Dong, W., Shi, G., Ma, Y., & Li, X. (2015). Image Restoration via Simultaneous Sparse Coding: Where Structured Sparsity Meets Gaussian Scale Mixture. *International Journal of Computer Vision*, *114*(2–3), 217–232. https://doi.org/10.1007/s11263-015-0808-y

Dong, W., Shi, G., Ma, Y., & Li, X. (2015). Image Restoration via Simultaneous Sparse Coding: Where Structured Sparsity Meets Gaussian Scale Mixture. *International Journal of Computer Vision*, *114*(2–3), 217–232. doi:10.1007/s11263-015-0808-y

Dong, W., Zhang, L., & Shi, G. (2011). Centralized sparse representation for image restoration. *International Conference on Computer Vision*, 259–1266.

Dong, W., Zhang, L., Shi, G., & Li, X. (2013). Nonlocally centralized sparse representation for image restoration. *IEEE Transactions on Image Processing*, *22*(4), 1620–1630. doi: 10.1109/TIP.2012.2235847

Dong, W., Zhang, L., Shi, G., & Wu, X. (2011). Image deblurring and super-resolution by adaptive sparse domain selection and adaptive regularization. *IEEE Transactions on Image Processing*, *20*(7), 1838–1857. doi:10.1109/TIP.2011.2108306

Donoho, D. L. (2006). Compressed sensing. *IEEE Transactions on Information Theory*, *52*(4), 1289–1306.

Donoho, D. L., Gavish, M., & Montanari, A. (2013). The phase transition of matrix recovery from Gaussian measurements matches the minimax MSE of matrix denoising. *Proceedings of the National Academy of Sciences*, *110*(21), 8405–8410.

Duan, Y., Xu, S., Yuan, S., Chen, Y., Li, H., Da, Z, & Gao, L. (2018). Modified slanted-edge method for camera modulation transfer function measurement using nonuniform fast Fourier transform technique. *Optical Engineering*, *57*(1), 014103.

Dupe, F.-X,. Fadili, J. M., & Starck, J.-L. (2009). A proximal iteration for deconvolving poisson noisy images using sparse representations. *IEEE Transactions on Image Processing*, *18*(2), 310–321.

Durand, F., & Dorsey, J. (2002). Fast Bilateral Filtering for the Display of High-Dynamic-Range Images. *ACM Transactions on Graphics*, *21*(3). doi:10.1145/566654.566574

Eastman, J. R. (2001). Introduction to Remote Sensing and Image Processing. *Guide to GIS and Image Processing*, *1*, 17–34).

Efros, A., & Leung, T. (1999). Texture synthesis by non parametric sampling. *Proceedings of International Conference on Computer Vision*, *2*, 1033–1038.

Elad, M. & Aharon, M. (2006). Image denoising via sparse and redundant representations over learned dictionaries. *IEEE Transactions on Image Processing*, *15*(12), 3736–3745

Elad, M., & Aharon, M. (2006). Image denoising via sparse and redundant representations over learned dictionaries. *IEEE Transactions on Image Processing*, *15*(12), 3736–3745.

Elmoataz, A. Lezoray, O. and Bougleux, S. (2008). Nonlocal discrete regularization on weighted graphs: A framework for image and manifold processing. *IEEE Transactions on Image Processing*, *17*(7), 1047–1060.

Engan, K. Aase, S. O., & Hakon-Husoy, J. H. (1999). Method of optimal directions for frame design. *Proceedings of IEEE International Conferemce on Acoustic, Speech, Signal Processing*, *5*, 2443–2446.

Esedoglu, S., & Osher, S. J. (2004). Decomposition of images by the anisotropic Rudin-Osher-Fatemi model. *Communications on Pure and Applied Mathematics*, *57*(12), 1609–1626.

Estribeau M., & Magnan, P. (2004). Fast MTF measurement of CMOS imagers using ISO 12233 slanted-edge methodology. *Proceedings of SPIE 5251, Detectors and Associated Signal Processing*, 243–253.

Evtikhiev, N. N., Krasnov, V. V., & Starikov, S. N. (2013). A method of generating amplitude masks with a constant power spectra and using them to measure the two-dimensional modulation-transfer functions of optical systems. *Journal of Optical Technology*, *80*(5), 294–300.

"Falcon 1 Flight 5". Archived from the original on 2011-01-04.

Fang, H., & Yan, L. (2014). Parametric blind deconvolution for passive millimeter wave images with framelet regularization. *Optik*, *125*(3), 1454–1460.

Farbman, Z., Fattal, R., Lischinski, D., & Szeliski R. (2008). Edge-Preserving Decompositions For Multi-Scale Tone And Detail Manipulation. *ACM Transactions on Graphics*, *27*(3). doi:10.1145/1360612.1360666

Farbman, Z., Hoffer, G., Lipman, Y., Cohenor, D., & Lischinski D. (2009). Coordinates For Instant Image Cloning. *ACM Transactions on Graphics*, *28*(3).

Farsiu, S., M. D. Robinson, M. D., Elad, M., & Milanfar, P. (2004). Fast and robust multiframe super resolution. *IEEE Transactions on Image Processing*, *13*(10), 1327–1344.

Fattal, R., Lischinski, D., & Werman, M. (2002). Gradient Domain High Dynamic Range Compression. *ACM Transactions on Graphics*, *21*(3), 249 – 256.

Feichtinger, H. G. (1989). Atomic characterizations of modulation spaces through Gabor-type representations. *The Rocky Mountain Journal of Mathematics, 19*(1), 113–125.

Fergus, R., Singh, B., Hertzmann, A., Rowels, S. T., & Freeman, W. T. (2006). Removing camera shake from a single photograph. *ACM Transactions on Graphics*, *25*(3), 3787–794

Field, D. (1994). What is the goal of sensory coding? *Neural Computation*, *6*, 559–601.

Figueiredo, M. A. T., & Nowak, R. D. (2003). An EM algorithm for wavelet- based image restoration. *IEEE Transactions on Image Processing*, *12*(8), 906–916.

Figueiredo, M., Nowak, R., & Wright, S. (2007). Gradient projection for sparse reconstruction: Application to compressed sensing and other inverse problems. *IEEE Journal of Selected Topics in Signal Processing*, *1*(4), 586–597.

Foi, A., & Boracchi, G. (2016). Foveated Nonlocal Self-Similarity. *International Journal of Computer Vision*, *120*(1), 78–110. doi:10.1007/s11263-016-0898-1

Fonseca, L. M. G., Prasad, G. S. S. D., & Mascarenhas, N. D. A. (1993). Combined Interpolation-Restoration of Landsat Images through FIR Filter Design Techniques. *International Journal of Remote Sensing*, *14*(13), 2547–2561. doi: 10.1080/01431169308904292

Fotiadou, K.; Tsagkatakis, G.; Tsakalides, P. Deep convolutional neural networks for the classification of snapshot mosaic hyperspectral imagery. Electron. Imaging 2017, 2017, 185–190.

Fox, N. (2010a). *QA4EO: A guide to "reference standards " in support of Quality Assurance requirements of GEO: (QA4EO-QAEO-GEN-DQK-003)*.

Fox, N. (2010b). A guide to establish a Quality Indicator on a satellite sensor derived data product (No. QA4EO-QAEO-GEN-DQK-001). United Kingdom (UK).

Francesconi, B., Lonjou, V., & Lafrance, B. (2017). Copernicus Sentinel-2A Calibration and Products Validation Status. *Remote Sensing*, *9*(6). doi: 10.3390/rs9060584

Gascon, F., Bouzinac, C., Thépaut, O., Jung, M., Francesconi, B., Louis, J., … Fernandez, V. (2017). Copernicus Sentinel-2A Calibration and Products Validation Status. *Remote Sensing*, *9*(6), 584. https://doi.org/10.3390/rs9060584

Gastal, E. S. L., & Oliveira, M. M. (2011). Domain Transform For Edge-Aware Image And Video Processing. *ACM Transactions on Graphics*, *30*.

Geman D., & Yang, C. (1995). Nonlinear image recovery with half-quadratic regularization. *IEEE Transactions on Image Processing*, *4*(7), 932– 946.

Geman, D., & Reynolds, G. (1992). Constrained restoration and the recovery of discontinuities. *IEEE Transactions on Pattern Analysis and Machine Intelligence*, *14*(3), 367–383.

George, C. F., & Smith, H. W. (1962). The application of inverse convolution techniques to improve signal response of recorded geophysical data. *Proceedings of The IRE*, *50*(11), 2313-2319

Ghosh, J. K., & Somvanshi, A. (2008). Fractal-based dimensionality reduction of hyperspectral images. *Journal of the Indian Society of Remote Sensing*, *36*, 235–241.

Gilles, J. (2007). Noisy Image Decomposition : A New Structure , Texture and Noise Model based on Local Adaptivity. *Journal of Mathematical Imaging and Vision*, *28*(3). doi:10.1007/s10851-007-0020-y

Goldstein, T., & Osher, S. (2009). The split Bregman algorithm for L1 regularized problems. *SIAM Journal on Imaging Sciences*, *2*, 323–343.

Gong, D., Zhang, Z., Shi, Q., Hengel, A. van den, Shen, C., & Zhang, Y. (2018). *Learning an Optimizer for Image Deconvolution*. 1–17. http://arxiv.org/abs/1804.03368

Gonzalez, R. C., & Woods, R. E. (2018). *Digital Image Processing*. (4th ed.). Harlow, United Kingdom: Pearson Education Limited.

Goodnight, N., Woolley, C., Lewin, G., Lue-Bke D., & Humphreys G. (2003). A Multigrid Solver For Boundary Value Problems Using Programmable Graphics Hardware. *Proceedings of Graphics Hardware*, 102–111.

Gribok, A. V., Paik, J., & Abidi, M. A. (2016). *Optimization Techniques in Computer Vision: Ill-Posed Problems and Regularization*. (1st ed.), Advances in Computer Vision and Pattern Recognition, Springer.

Grosse, R., Johnson, M. K., Adelson, E. H., & Freeman W. T. (2009). Ground Truth Dataset And Baseline Evaluations for Intrinsic Image Algorithms. *Proceedings of the International Conference on Computer Vision*, 2335–2342.

Gu J., Liu L., Hu H. (2015). Patch-based Sparse Dictionary Representation for Face Recognition with Single Sample per Person. In: Yang J., Yang J., Sun Z., Shan S., Zheng W., Feng J. (eds) *Biometric Recognition*. Lecture Notes in Computer Science, 9428, Springer.

Gu, S., Zhang, L., Zuo, W., & Feng, X. (2014). Weighted nuclear norm minimization with application to image denoising. *Proceedings of the IEEE Conference On Computer Vision and Pattern Recognition*, 2862–2869.

Guo, H. (2011). A simple algorithm for fitting a gaussian function. *IEEE Signal Processing Magazine*, *28*(5), 134–137. doi:10.1109/MSP.2011.941846

Gupta, A., Joshi, N., Zitnick, C. L., Cohen, M., & Curless, B. (2010). Single image deblurring using motion density functions. *Proceedings of the European Conference on Computer Vision*, 171–184

Hacohen, Y., Shechtman, E., & Lischinski, D. (2013). Deblurring by example using dense correspondence. *Proceedings of The IEEE International Conference on Computer Vision*, 2384–2391.

Hadamard, J. (1952). Lectures on Cauchy's problem in linear partial differential equations. Dover, reprint.

Haghshenas, J. (2017). Vibration effects on remote sensing satellite images. *Advances in Aircraft and Spacecraft Science*, *4*(5), 543–553. doi:10.12989/aas.2017.4.5.543

Han, B. (2019). Gibbs Phenomenon of Framelet Expansions and Quasi-projection Approximation. *Journal of Fourier Analysis and Applications*, *25*(6), 2923–2956. https://doi.org/10.1007/s00041-019-09687-9

Hansen, P. C., Nagy, J. G., & O'Leary, D. (2006). Deblurring Images: Matrices, Spectra, and Filtering, *SIAM*, Philadelphia, Pa, USA.

He, K., Sun, J., & Tang X. (2013). Guided Image Filtering. *IEEE Transactions on Pattern Analysis and Machine Intelligence*, *35*, 1397-1409.

Hearn, D. R. (2002). Earth Observing-1 Advanced Land Imager: Imaging performance on-orbit. Project report F19628-00-C-0002, NASA under US Air Force contract.

Helder, D. L., Choi, T., & Rangaswamy M. (2004). In-flight characterization of spatial quality using point spread function. *in Post-Launch Calibration Satellite Sensors, ISPRS Book Series - Volume 2.* 151–170.

Helder, D., Choi, J., & Anderson, C. (2006). On-orbit modulation transfer function (MTF) measurements for IKONOS and QuickBird. *Proceedings of the JACIE 2006 Civil Commercial Imagery Evaluation Workshop*,14–16.

Hidane, M., Lzoray, O., & Elmoataz, A. (2013). Nonlinear multilayered representation of graph-signals. *Journal of Mathematical Imaging and Vision*, *45*(2), 114–137.

Hillery, A. D., & Chin, R. T. (1991). Iterative Wiener filters for image restoration. *IEEE Transactions on Signal Processing*, *39*(8), 1892–1899.

Holst, G. C., (2017). *Electro-optical imaging system performance*. (6th ed). Washington: JCD Publishing and SPIE Optical Engineering Press.

Hu, W., Cheung, G., & Kazui, M. (2016). Graph-based dequantization of block-compressed piecewise smooth images. *IEEE Signal Processing Letters*, *23*(2), 242–246.

Hu, W., Cheung, G., Li, X., & Au, O. C. (2014). Graph-based joint denoisinzg and super-resolution of generalized piecewise smooth images. *Proceedings of the IEEE International Conference on Image Processing*, 2056–2060.

Hu, W., Li, X., Cheung, G., & Au, O. C. (2013). Depth map denoising using graph-based transform and group sparsity. *IEEE International Workshop on Multimedia Signal Processing*, 001–006.

Hu, Z., & Yang, M.-H. (2015). Learning Good Regions to Deblur Images. *International Journal of Computer Vision*, *115*(3), 345–362. http://link.springer.com/chapter/10.1007/978-3-642-33715-4_5

Hu, Z., Cho, S., Wang, J., & Yang, M. (2018). Deblurring Low-Light Images with Light Streaks. *IEEE Transactions on Pattern Analysis and Machine Intelligence*, *40*(10), 2329–2341. doi.:10.1109/TPAMI.2017.2768365

Hu, Z., Huang, J.-B., & Yang, M.-H. (2010). Single image deblurring with adaptive dictionary learning. *Proceedings of The IEEE International Conference on Image Processing*, 1169–1172.

Hua, M., Bie, X., Zhang, M., & Wang, W. (2014). Edge-Aware Gradient Domain Optimization Framework For Image Filtering By Local Propagation. *IEEE Conference on Computer Vision and Pattern Recognition*, 2838–2845.

Huang, J., Huang, T., Zhao, X., & Xu, Z. (2013). Image restoration with shifting reflective boundary conditions. *Science China Information Sciences*, *56*(6), 1–15. doi:10.1007/s11432-011-4425-2

Huang, Z., Fang, H., Li, Q., Li, Z., Zhang, T., Sang, N., & Li, Y. (2018). Optical remote sensing image enhancement with weak structure preservation via spatially adaptive gamma correction. *Infrared Physics and Technology*, *94*, 38–47.

Hwang, H., Choi. Y.-W., Kwak, S., Kim, M., & Park., W. (2008). MTF assessment of high resolution satellite images using ISO 12233 slanted-edge method. *Proceedings of SPIE 7109*, 710905.

Hwang, H., Park, W., & Kwak, S. (2011). MTF Assessment and Image Restoration Technique for Post-Launch Calibration of DubaiSat-1. *Korean Journal of Remote Sensing*, *27*(5), 573–586.

I2R, (2018). *Guide to Spatial Imagery Digital Imagery Spatial Resolution*. Innovative Imaging and Research Corporation, United States Geological Survey

Infrared and Visible Optical Sensors Subgroup. (2019, October 19), Retrieve from: http://calvalportal.ceos.org/ceos-wgcv/ivos

Irons, J. R., Markham, B. L., Nelson, R. F., Toll, D. L., Williams, D. L., Latty, R. S., & Stauffer M. L. (1985). The effects of spatial resolution on the classification of Thematic Mapper data. *International Journal of Remote Sensing 6*(8): 1385-1403

ISO 12233:2017(E), (2017). Photography–Electronic still picture imaging–Resolution and spatial frequency responses. International Organization for Standardization, Geneva.

Jalobeanu, A., Zerubia, J., & Blanc-Féraud, L. (2007). Bayesian estimation fo blur and noise in remote sensing imaging. *in Blind image deconvolution: Theory and Applications*, P. Campisi and K. Egiazarian, Eds. CRC.

Javaran, T. A., Hassanpour, H., & Abolghasemi, V. (2017). Non-blind image deconvolution using a regularization based on re-blurring process. *Computer Vision and Image Understanding*, *154*, 16–34. doi:10.1016/j.cviu.2016.09.013

JCGM. (2012). *JCGM 200: 2008 International vocabulary of metrology — Basic and general concepts and associated terms (VIM). International Organization for Standardization Geneva ISBN* (Vol. 3). Retrieved from http://www.bipm.org/utils/common/documents/jcgm/JCGM_200_2008.pdf

Jensen, J. R., (1983). Review Article: Biophysical Remote Sensing. *Annals of the Association of American Geographers*, *73*(1), 111-132.

Ji, H., C. Liu, C., Shen, Z., and Xu, Y. (2010). Robust video denoising using low rank matrix completion, *Proceedings of the IEEE Conference on Computer Vision and Pattern Recognition*, 1791–1798.

Ji, H., Huang, S., Shen, Z., & Xu, Y. (2011). Robust video restoration by joint sparse and low rank matrix approximation, *SIAM Journal on Imaging Sciences*, *4*(4), 1122–1142.

Jiang M. –Y., Chen X. –N., & Yu X.-Q. (2012). A blind restoration method for defocus blurred remote sensing imagery. *Science of Surveying and Mapping*, *4*.

Jidesh, P., & K., S. H. (2018). Non-local total variation regularization models for image restoration. *Computers and Electrical Engineering*, *67*, 114–133. doi:10.1016/j.compeleceng.2018.03.014

Jordan, M. I., Ghahramani, Z., Jaakkola, T. S., & Saul, L. K. (1999). Introduction to variational methods for graphical models. *Machine Learning*, *37*(2), 183–233. https://doi.org/10.1023/A:1007665907178

Joseph, G. (2000). How well do we understand Earth observation electro-optical sensor parameters. *ISPRS Journal of Photogrammetry and Remote Sensing*, *55*(1), 9–12.

Joshi, N., Kang, S. B., Zitnick, C. L., & Szeliski, R. (2010). Image deblurring using inertial measurement sensors. *Proceedings of ACM SIGGRAPH*, *30*, 1-9.

Joshi, N., Szeliski, R., & Kriegman, D. J. (2008). PSF estimation using sharp edge prediction. *Proceedings of the IEEE Conference on Computer Vision and Pattern Recognition*, 1-8.

Jung, M., Bresson, X., Chan, T. F. & Vese, (2011). L. A. Nonlocal Mumford-Shah regularizers for color image restoration, *IEEE Transactions Image Processing*, *20*(6), 1583–1598.

Jung, M., Bresson, X., Chan, T. F., & Vese, L. A. (2011). Nonlocal Mumford-Shah regularizers for color image restoration. *IEEE Transactions on Image Processing*, *20*(6), 1583–1598.

Kaftandjian, V., Zhu Y. -M., Roziere, G., Peix, G., & Babot, D. (1996). A comparison of the ball, wire, edge, and bar/space pattern techniques for modulation transfer function measurements of linear x-ray detectors. *Journal of X-Ray Science and Technology, 6*(2), 205–221.

Kaiser, G. & Schneider, W. (2008), Estimation of sensor point spread function by spatial subpixel analysis, *International Journal of Remote Sensing*, *29*(7–8), 2137–2155.

Kameche, M., & Benmostefa, S. (2016). In-flight MTF stability assessment of ALSAT-2A Satellite. *Advances in Space Research*, *58*(1), 117–130.

Kang, C. H., Chung, J. H., & Kim, Y. H. (2015). On-orbit MTF estimation for the KOMPSAT-3 satellite using star images. *Remote Sensing Letters*, *6*(12), 1002–1011. doi:10.1080/2150704X.2015.1093189

Kang, J., Hao, Q., & Cheng, X. (2014). Measurement and comparison of one-and two-dimensional modulation transfer function of optical imaging systems based on the random target Method. *Optical Engineering*, *53*(10), 104105.

Karacan, L., Erdem, E., & Erdem, A. (2013). Structure-Preserving Image Smoothing Via Region Covariances. *ACM Transactions on Graphics*, *32*(6).

Kass, M., & Solomon, J. (2010). Smoothed Local Histogram Filters. *ACM Transactions on Graphics*, *29*(4), 100:1–100:10.

Katkovnik, V. D., Paliy, K. Egiazarian, and J. Astola (2006). Frequency Domain Blind Deconvolution in Multiframe Imaging using Anisotropic Spatially-Adaptive Denoising. *Proceedings of the 14th European Signal Processing Conference*. 1-5.

Keller, G., Chang, T., & Xiong, X. (2017). MTF analysis using lunar observations for Himawari-8/AHI. *Proceedings of SPIE, 10402*, *in Earth Observing Systems XXII*, *104022I*. doi:10.1117/12.2274091

Kheradmand, A., & Milanfar, P. (2014). A general framework for regularized, similarity-based image restoration. *IEEE Transactions on Image Processing*, *23*(12), 5136–5151.

Khetkeeree, S., & Liangrocapart, S. (2018). On-orbit point spread function estimation for THEOS imaging system. *Proceedings of SPIE*, 10714.

Khristenko, U., Scarabosio, L., Swierczynski, P., Ullmann, E., & Wohlmuth, B. (2019). Analysis of boundary effects on PDE-based sampling of whittle-matern random fields. *SIAM-ASA Journal on Uncertainty Quantification*, *7*(3), 948–974. https://doi.org/10.1137/18M1215700

Kim, H. H., Seo, D. C., Jeong, J. H., Park, D. S., & Lee, D. H. (2020). An analysis of the effect of tilt angle on MTF of KompsAT-3A. *40th Asian Conference on Remote Sensing, ACRS 2019*, (ACRS), 3–5.

Kim, T. H., Ahn, B. & Lee, K. M. (2013). Dynamic scene deblurring. *Proceedings of IEEE International Conference on Computer Vision*, 3160–3167.

Kindermann, S., Osher, S., & Jones, P.W. (2005). Deblurring and denoising of images by nonlocal functionals, *Multiscale Model. Simulations,* 4(4), 1091–1115

Kohm, K. (2004). Modulation transfer function measurement method and results for the orbview-3 high resolution imaging satellite. *International Archives of the Photogrammetry, Remote Sensing and Spatial Information Sciences*, *35*.

Krishnan, D. & Fergus, R. (2009). Fast image deconvolution using hyper-Laplacian priors. *Proceedings of in Advances in Neural Information Processing Systems*, *22*, 1–9.

Krishnan, D., Tay, T., & Fergus, R. (2011). Blind deconvolution using a normalized sparsity measure. *Proceedings of IEEE Conference on Computer Vision and Pattern Recognition*, 233–240.

Kuhls-Gilcrist, A., Bednarek, D. R., & Rudin, S. (2010). A method for the determination of the two-dimensional MTF of digital radiography systems using only the noise response. *Medical Imaging 2010: Physics of Medical Imaging*, *7622*. https://doi.org/10.1117/12.843918

Kumari, K., Das, D., Suresh, S. Lal, S., & Narasimhadhan, A. V. (2018). A robust framework for quality enhancement of aerial remote sensing images. *Infrared Physics and Technology*, *93*, 362–374.

Kundur D., & Hatzinakos, D. (1996). Blind image deconvolution: an algorithmic approach to practical image restoration. *IEEE Signal Processing Magazine*, *13*(3), 43–64.

Kundur, D., & Hatzinakos, D. (1996). Blind Image Deconvolution. *IEEE Signal Processing Magazine*, *13*(3), 97–121. doi:10.1002/9781118603864.ch3

Kunisch, K., & Pock, T. (2013). A Bilevel Optimization Approach for Parameter Learning in Variational Models. *SIAM Journal on Imaging Sciences*, *6*(2). 938–983.

Kwon, J. Y., & Kang, M. G. (2018). Restoration for Out-of-Focus Color Image Based on Gradient Profile Sharpness. *Circuits, Systems, and Signal Processing*, *37*(1), 178–202. https://doi.org/10.1007/s00034-017-0542-5

La Camera, A., Schreiber, L., Diolaiti, E., Boccacci, P., Bertero, M., Bellazzini, M., & Ciliegi, P. (2015). A method for space-variant deblurring with application to adaptive optics imaging in astronomy. *Astronomy & Astrophysics*, *579*(May), A1. https://doi.org/10.1051/0004-6361/201525610

Lagendijk, R. L., Biemond, J., & D. E. Boekee, (1990). Identification and restoration of noisy blurred images using the expectation-maximization algorithm. *IEEE Transactions on Acoustics, Speech, and Signal Processing*, *38*(7), 1180-1191.

Lai, W. S., Huang, J. Bin, Hu, Z., Ahuja, N., & Yang, M. H. (2016). A Comparative Study for Single Image Blind Deblurring. *Proceedings of the IEEE Computer Society Conference on Computer Vision and Pattern Recognition*, 1701–1709. doi:10.1109/CVPR.2016.188

Lam, E. & Goodman, J. (2000). A mathematical analysis of the DCT coefficient distributions for images. *IEEE Transactions on Image Processing*, *9*(10), 1661–1666.

Lam, N. S-N., Qiu, H. L., Quattrochi, D. A., & Emerson, C.W. (2002). An Evaluation of Fractal Methods for Characterizing Image Complexity. *Cartography and Geographic Information Science*, *29*, 25-35.

Land, E. H., & Mccann, J. J. (1971). Lightness And Retinex Theory. *Journal of The Optical Society Of America*, *61*(1), 1–11.

Le´ger, D., Viallefont, F., Deliot, P., & Valorge, C., (2004). *On-orbit MTF Assessment of Satellite Cameras. Post-launch Calibration of Satellite Sensors*. Taylor and Francis Group, London, 67– 75.

Le´ger, D., Viallefont, F., Hillairet, E., & Meygret, A., (2002). In-flight refocusing and MTF assessment of SPOT5 HRG and HRS cameras. *Proceedings of SPIE of Sensors, Systems, and Next-Generation Satellites VI*, *4881*, 224–231.

Leachtenauer, J. C. (1996). National Imagery Interpretability Rating Scales: Overview and Product Description. *Proceedings of the American Society of Photogrammetry and Remote Sensing Annual Meetings*.

Lee, D., Helder, D. Jeong, J., Park, D., Seo, D., & Choi, H. (2016). Spatial Quality by Edge target with KOMPSAT-3 & KOMPSAT-3A. *Proceedings of The Imaging & Geospatial Technology Forum* (IGTF 2016).

Lee, D., Helder, D., Christopherson, J., & Stensaas, G. (2014). *Spatial Quality for Satellite Image data and Landsat8 OLI Lunar data*. http://ceos.org/document_management/Working_Groups/WGCV/Meetings/WGCV-38/WGCV_38_DongHan_1002.pdf

Lee, D.-H., Seo, D. C., Song, J. H., Chung, J. H., Park, S. Y., Choi, M. J., & Lim, H. S. (2008). Image restoration of calibration and validation for KOMPSAT-2. *The International Archives of the Photogrammetry, Remote Sensing and Spatial Information Sciences*, *37*(B1), 57–62.

Lee, H., Jeon, J., Kim, J., & Lee, S. (2017). Structure-Texture Decomposition of Images with Interval Gradient. *Computer Graphics Forum*, *36*(6), 262–274. doi:10.1111/cgf.12875

Lee, J. H., & Ho, Y. S. (2011). High-quality non-blind image deconvolution with adaptive regularization. *Journal of Visual Communication and Image Representation*, *22*(7), 653–663.

Léger, D., Duffaut, J., & Robinet, F. (1994). MTF measurement using spotlight. *Proceedings of IEEE Geoscience and Remote Sensing Symposium, 4*, 2010–2012.

Léger, D., Viallefont, F., Deliot, P., & Valorge, C. (2004). On-orbit MTF assessment of satellite cameras. In Morain & Budge (Eds), *Post-Launch Calibration of Satellite Sensors* (pp. 67-75). Taylor and Francis Group.

Léger, D., Viallefont, F., Deliot, P., & Valorge, C. (2004). *Post-Launch Calibration of Satellite Sensors, On-orbit MTF assessment of satellite cameras*, Morain & Budge Eds, Taylor and Francis Group, 4, 67–75.

Leger, D., Viallefont, F., Hillairet E., & Meygret A. (2003). In-flight refocusing and MTF assessment of Spot5 HRG and HRS cameras. *Proceedings of Sensors, Systems, and Next-Generation Satellites VI*, *SPIE*, *4881*, 224-231.

Leloğlu, U., Gürbüz, S., Özen, H., & Gürol, S. (2008). Characterization of the spatial uniformity of the Tuz Gölü calibration test site. *Proceedings of XXIst International Society for Photogrammetry and Remote Sensing Congress*, *XXXVII*, *Pa*, 11–14.

Levin, A. (2006). Blind motion deblurring using image statistics. *Proceedings of Advances in Neural Information Processing Systems*, 841–848

Levin, A. (2006). Blind motion deblurring using image statistics. *Proceedings of the 19th International Conference on Neural Information Processing Systems*, 841–848.

Levin, A., Fergus, R., Durand, F., & Freeman, W. (2007). Image and depth from a conventional camera with a coded aperture. *ACM Transactions on Graphics*, *26*(3), 70. doi:10.1145/1276377.1276464

Levin, A., Weiss, Y., Durand, F., & Freeman, W. T. (2009). Understanding and evaluating blind deconvolution algorithms, *Proceedings of IEEE conference on Computer Vision and Pattern Recognition*, 964–1971.

Levin, A., Weiss, Y., Durand, F., & Freeman, W. T. (2011). Efficient marginal likelihood optimization in blind deconvolution. *Proceedings of IEEE conference on Computer Vision and Pattern Recognition*, 2657–2664.

Levin, A., Weiss, Y., Durand, F., & Freeman, W. T. (2011). Understanding blind deconvolution algorithms(Extend). *IEEE Transactions on Pattern Analysis and Machine Intelligence*, *33*(12), 2354–2367. doi:10.1109/TPAMI.2011.148

Levy, E., Peles, D., Opher-Lipson M., & Lipson, S. G. (1999). Modulation transfer function of a lens with a random target method. *Applied Optics*, *38*(4), 679-683.

Li, B., Lin, G., Chen, Q., & Wang, H. (2014). Image denoising with patch estimation and low patch-rank regularization. *Multimedia Tools and Applications*, *71*(2), 485–495.

Li, D., & Simske, S. (2009). Atmospheric turbulence degraded-image restoration by kurtosis minimization. *IEEE Geoscience and Remote Sensing Letters*, *6*(2), 244–247. doi: 10.1109/ICMA.2009.5245072

Li, J., & Liu, Z. (2017). Image quality enhancement method for on-orbit remote sensing cameras using invariable modulation transfer function. *Opt. Express*, *25*(15), 17134–17149. doi:10.1364/OE.25.017134

Li, J., Liu, Z., & Liu, F. (2017). Using sub-resolution features for self-compensation of the modulation transfer function in remote sensing. *Optics Express*, *25*(4), 4018.

Li, J., Wattanachote, K., & Wu, Y. (2019). Maximizing nonlocal self-similarity prior for single image super-resolution. *Mathematical Problems in Engineering*, doi:10.1155/2019/3840285

Li, J., Xing, F., Sun, T., & You, Z. (2015). Efficient assessment method of on-board modulation transfer function of optical remote sensing sensors. *Optics Express*, *23*(5), 6187. doi:10.1364/OE.23.006187

Li, J., Xue, F., & Blu, T. (2018). Accurate 3D PSF estimation from a wide-field microscopy image. *The IEEE 15th International Symposium on Biomedical Imaging (ISBI 2018), Washington, DC.* 501-504. doi:10.1109/ISBI.2018.8363625

Li, K., Zhang, Y., Zhang, Z., & Yu, Y. (2018). An Automatic Recognition and Positioning Method for Point Source Targets on Satellite Images. *ISPRS International Journal of Geo-Information*, *7*(11), 434. doi.10.3390/ijgi7110434

Li, L., Si, Y., Jia, Z. (2017). Remote sensing image enhancement based on non-local means filter in NSCT domain. *Algorithms*, *10*(4), 1–13.

Li, S., Wang, H., Wang, L., Yu, X., & Yang, L. (2018). Variational method based on Retinex with double-norm hybrid constraints for uneven illumination correction. *Journal of Applied Remote Sensing*, *12*(1), 1–15. https://doi.org/10.1117/1.JRS.12.015017

Li, X. Gu, X., Fu, Q., Yu, T., Gao, H., Li, J., & Liu, L. (2013). Removing atmospheric MTF and establishing an MTF compensation filter for the HJ-1A CCD camera. *International Journal of Remote Sensing*. *34*(4), 1413–1427

Li, Y., & Clarke, K. C. (2013). Image deblurring for satellite imagery using small-support-regularized deconvolution. *ISPRS Journal of Photogrammetry and Remote Sensing*, *85*, 148–155. doi:10.1016/j.isprsjprs.2013.08.002

Li, Y., Tofighi, M., Monga, V., & Eldar, Y. C. (2019). An Algorithm Unrolling Approach to Deep Image Deblurring, 1–14. http://arxiv.org/abs/1902.05399

Liang, S., Li, X., & Wang, J. (2012). *Advanced Remote Sensing: A Systematic View of Remote Sensing*. Academic Press.

Lin, F.-R.; Ng, M.K.; Ching, W.-K. (2005). Factorized banded inverse preconditioners for matrices with Toeplitz structure. *SIAM Journal on Scientific Computing*, *26*, 1852–1870.

Lisani, J. L., Michel, J., Morel, J. M., Petro, A. B., & Sbert, C. (2016). An Inquiry on Contrast Enhancement Methods for Satellite Images. *IEEE Transactions on Geoscience and Remote Sensing*, *54*(12), 7044–7054. https://doi.org/10.1109/TGRS.2016.2594339

Liu, H, Liu, S., Huang, T., Zhang, Z., Hu, Y., & Zhang, T. (2016). Infrared spectrum blind deconvolution algorithm via learned dictionaries and sparse representation. *Applied Optics*, *55*(10), 2813–2818

Liu, J., & Osher, S. (2019). Block Matching Local SVD Operator Based Sparsity and TV Regularization for Image Denoising. *Journal of Scientific Computing*, *78*(1), 607–624. doi:10.1007/s10915-018-0785-8

Liu, R. W., Wu, D., Wu, C. S., Xu, T., & Xiong, N. (2016). Constrained Nonconvex Hybrid Variational Model for Edge-Preserving Image Restoration. *Proceedings of 2015 IEEE International Conference on Systems, Man, and Cybernetics*, 1809–1814. doi:10.1109/SMC.2015.317

Liu, R., & Jia, J. (2008). Reducing boundary artifacts in image deconvolution. *Proceedings of the International Conference on Image Processing*, 505–508. doi:10.1109/ICIP.2008.4711802

Liu, R., & Jia, J. Y. (2008). Reducing boundary artifacts in image deconvolution. *Proceedings of IEEE International Conference on Image Processing*.

Liu, T., Chen, Z., Liu, S., Zhang, Z., & Shu, J. (2016). Blind image restoration with sparse priori regularization for passive millimeter-wave images. *Journal of Visual Communication and Image Representation*, *40*, 58–66. https://doi.org/10.1016/j.jvcir.2016.06.007

Liu, X., & Huang, L. (2014). An efficient algorithm for adaptive total variation based image decomposition and restoration. *International Journal of Applied Mathematics and Computer Science*, *24*(2), 405–415. doi:10.2478/amcs-2014-0031

Liu, X., Cheung, G., Wu, X., & Zhao, D. (2015). Inter-block soft decoding of JPEG images with sparsity and graph-signal smoothness priors. *Proceedings of the IEEE International Conference on Image Processing*, 1628–1632.

Liu, X., Cheung, G., Wu, X., & Zhao, D. (2017). Random walk graph laplacian-based smoothness prior for soft decoding of jpeg images. *IEEE Transactions on Image Processing*, *26*(2), 509–524.

Liu, X., Tanaka, M., & Okutomi, M. (2013). Single-image noise level estimation for blind denoising. *IEEE Transactions on Image Processing*, *22*(12), 5226–5237.

Liu, X., Zhai, D., Zhao, D., Zhai, G., & W. Gao, (2014). Progressive image denoising through hybrid graph Laplacian regularization: A unified framework. *IEEE Transactions on Image Processing*. *23*(4), 1491–1503.

Loew, A., Bell, W., Brocca, L., Bulgin, C. E., Burdanowitz, J., Calbet, X., … Verhoelst, T. (2017). Validation practices for satellite-based Earth observation data across communities. *Reviews of Geophysics*, *55*(3), 779–817. doi:10.1002/2017RG000562

Ma, J., & Plonka, G. (2010). A Review of Curvelets and Recent Applications. *IEEE Signal Processing Magazine*, *27*(2), 118–133.

Ma, J., Zhou, H., Zhao, J., Gao, Y., Jiang, J., & Tian, J. (2015). Robust feature matching for remote sensing image registration via locally linear transforming. *IEEE Transactions on Geoscience and Remote Sensing*, *53*, 6469–6481.

Ma, L., Xu, L., & Zeng, T. (2017). Low Rank Prior and Total Variation Regularization for Image Deblurring. *Journal of Scientific Computing*, *70*(3), 1336–1357. doi:10.1007/s10915-016-0282-x

Ma, T.-H. Lou, Y., & Huang, T.-Z. (2017). Truncated L1-2 models for sparse recovery and rank minimization. *SIAM Journal of Imaging Sciences*, *10*(3), 1346-1380. doi:10.1137/16M1098929.

Ma, Z., He, K., Wei, Y., Sun, J., & Wu, E. (2013). Constant Time Weighted Median Filtering For Stereo Matching And Beyond. *IEEE International Conference on Computer Vision*, 49–56.

Maheshwari, S., & Krishnapriya, P. (2016). Satellite Image Enhancement and Restoration – A Review, *6*(September), 198–204.

Mairal, J., Bach, F., Ponce, J., & Sapiro, G. (2009). Online dictionary learning for sparse coding. *Proceedings of the 26th annual international conference on machine learning*, 689–696.

Mairal, J., Bach, F., Ponce, J., Sapiro, G., & Zisserman, A. (2009). Non-local sparse models for image restoration. *Proceedings of the IEEE International Conference on Computer Vision*, 2272–2279.

Mallat S., & Yu, G. (2010). Super-resolution with sparse mixing estimators. *IEEE Transactions on Image Processing*, *19*(11), 2889–2900.

Mallat, S. (2009). *A wavelet tour of signal processing: the sparse way*. (3rd ed.) San Diego, USA: Elsevier Science Publishing.

Mallat, S. G. (1989). A theory for multiresolution signal decomposition: the wavelet representation. *IEEE Transactions on Pattern Analysis and Machine Intelligence*, *11*(7), 674–693.

Mallat, S., & Yu, G. (2010). Super-resolution with sparse mixing estimators. *IEEE Transactions on Image Processing*, *19*(11), 2889–2900.

Markham, B. L. (1985). The Landsat sensors' spatial responses. *IEEE Transactions on Geoscience and Remote Sensing*, *23*(6), 864-875.

Masaoka, K., Yamashita, T., Nishida, Y., & Sugawara, M. (2014). Modified slanted-edge method and multidirectional modulation transfer function estimation. *Optics Express*, 22(5), 6040–6046.

McGillem, C. D., Anuta, P. E., Malaret E., & Yu, K. B. (1983). Estimation of a remote sensing system point-spread function from measured imagery. *Proceedings of Machine processing of remotely sensed data symposium*, 62-68.

McNeill, S.J., & Pairman, D., (1998). Estimation of the SPOT multispectral sensor point spread function. *Proceedings of the 9th Australasian Remote Sensing and Photogrammetry Conference*.

Mesarovi, V. Z., Galatsanos, N. P., & Katsaggelos, A. K. (1995). Regularized constrained total leas1 squares image restoration. *IEEE Transactions on Image Processing*, *4*(8), 1096-1108.

Meyer, Y. (2001). *Oscillating Patterns in Image Processing and Nonlinear Evolution Equations*. The Fifteenth Dean Jacqueline B. Lewis Memorial Lectures, American Mathematical Society, Boston, Massachusetts.

Michaeli, T, & Irani, M. (2013). Blind deblurring using internal patch recurrence. *Proceedings of the 13th European Conference on Computer Vision*, 783–798.

Miller, K. (1970). Least-squares method for ill-posed problems with a prescribed bound. *SIAM Journal on Mathematical Analysis*, *1*, 52–74.

Min, D., Choi, S., Lu, J., Ham, B., Sohn, K., & Do M. N. (2014). Fast Global Image Smoothing Based On Weighted Least Squares. *IEEE Transactions. Image Processing*, *23*(12), 5638– 5653.

Min, M., Cao, G., Xu, N., Bai, Y., Jiang, S., Hu, X., … Zhang, P. (2016). On-Orbit Spatial Quality Evaluation and Image Restoration of FengYun-3C/MERSI. *IEEE Transactions On Geoscience And Remote Sensing*, *54*(12), 6847–6858. doi:10.1109/TGRS.2016.2569038

Mittal, S., & Garg, A. (2013). Blind Restoration Of Remote Sensing. In IEEE *conference Multimedia, Signal Processing and Communication Technologies.* 75–79.

Mizutani, R., Saiga, R., Takekoshi, S., Inomoto, C., Nakamura, N., Itokawa, M.,...Suzuki, Y. (2016). A method for estimating spatial resolution of real image in the Fourier domain. *Journal of Microscopy*, *261*(1), 57–66.

Molina, R., Mateos, J., & Katsaggelos, A. (2006). Blind deconvolution using a variational approach to parameter, image, and blur estimation. *IEEE Transactions on Image Processing*, *15*(12), 3715–3727.

Morain S.A., & Budge A. M. (2004). Post-Launch Calibration of Satellite Sensors: *Proceedings of the International Workshop on Radiometric and Geometric Calibration*, 1st edn. ISPRS Book Series, CRC Press

Mu, X. Xu, S., Li, G., & Hu, J. (2013). Remote sensing image restoration with modulation transfer function compensation technology in-orbit. *Proceedings of SPIE 8768,* *International Conference on Graphic and Image Processing (ICGIP 2012), 87681K (2013)*. doi:10.1117/12.2010775

Mumford, D., & Shah, J. (1989). Optimal approximation by piecewise smooth functions and associated variational problems. *Communications on Pure and Applied Mathematics*, *42*, 577–685.

Nan, Y. B., Tang, Y., Zhang, L. J., Zheng, C., & Wang, J. (2015). Evaluation of influences of frequency and amplitude on image degradation caused by satellite vibrations. *Chinese Physics B*, *24*(5), 3–11. doi:10.1088/1674-1056/24/5/058702

Neelamani, R., Choi, H., & Baraniuk, R. (2004). ForWaRD: Fourier-Wavelet Regularized Deconvolution for Ill-Conditioned Systems. *IEEE Transactions on Signal Processing*, *52*(2), 418–433.

Ng, M., Chan, R., & Tang, W. (1999). A fast algorithm for deblurring models with Neumann boundary conditions. *SIAM Journal on Scientific Computing*, *21*, 851–866

Niesen, U., Shah, D., & Wornell, G. W. (2009). Adaptive alternating minimization algorithms. *IEEE Transactions on Information Theory*, *55*(3), 1423–1429. https://doi.org/10.1109/TIT.2008.2011442

Nikolova, M. Steidl, G. & Weiss, P. (2015). Bilevel Image Denoising using Gaussianity Tests. *in: Scale Space and Variational Methods in Computer Vision*. Lecture Notes in Computer Science, 9087, Springer International Publishing, 117–128

Nutpramoon R., Weerawong K,. & Apaphant P. (2007). In-Orbit MTF Measurement for Theos Imaging System. *Proceedings of Asian Conference on Remote Sensing (ACRS) 2007*.

Oh, E., & Choi, J. K. (2014). GOCI image enhancement using an MTF compensation technique for coastal water applications. *Optics Express*, *22*(22), 26908–26918.

Oh, T. -H., Kim, H., Tai, Y.-W., Bazin, J.-C., & Kweon, I. S. (2013). Partial sum minimization of singular values in RPCA for low-level vision. *Proceeding of the IEEE International Conference of Computer Vision*, 145–152.

Oh, T.-H., Kim, H., Tai, Y.-W., Bazin, J.-C., & Kweon, I. S. (2013). Partial sum minimization of singular values in RPCA for low-level vision. *Proceedings of the IEEE International Conference on Computer Vision*, 145–152.

Oliveira, J. P., Figueiredo, M. T., & Bioucas-Dias, J. M. (2014). Parametric blur estimation for blind restoration of natural images: linear motion and out-of-focus. *IEEE Transactions on Image Processing*, *23*(1), 466–477. doi:10.1109/TIP.2013.2286328

Osher, J., & Esedoglu, S. (2003). Decomposition of images by the anisotropic rudin-osher-fatemi model. *Communications on Pure and Applied Mathematics*, *57*, 1609–1626.

Osher, S. J., Sole, A., & Vese, L. A. (2003). Image decomposition and restoration using total variation minimization and the H−1 norm. *Multiscale Modeling and Simulation: A SIAM Interdisciplinary Journal*, *1*(3), 349–370.

Osher, S., & Rudin, L. I. (1990). Feature-oriented image enhancement using Shock filters. *SIAM Journal on Numerical Analysis*, *27*, 919–940.

Pagnutti, M., Blonski, S., Cramer, M., Helder, D., Holekamp, K., Honkavaara, E., & Ryan R. (2010). Targets, Methods, and Sites for assessing the in-flight spatial resolution of electro-optical data products, *Canadian Journal of Remote Sensing*, *36*(5), 583-601

Pagnutti, M., Ryan, R., Burch, K., Leggett, J., Ickes, J., & Graham, L. (2017). Automated on-orbit characterization of the DLR DESIS sensor on the international space station. in *16th Annual JACIE Workshop.*

Pan, J., Hu, Z., Su, Z., & Yang, M. (2014). Deblurring text images via L0-regularized intensity and gradient prior. *Proceedings of IEEE Conference on Computer Vision and Pattern Recognition*, 2901–2908.

Pan, J., Hu, Z., Su, Z., & Yang, M. H. (2017). L0-Regularized Intensity and Gradient Prior for Deblurring Text Images and beyond. *IEEE Transactions on Pattern Analysis and Machine Intelligence*, *39*(2), 342–355. https://doi.org/10.1109/TPAMI.2016.2551244

Pan, J., Hu, Z., Su, Z., & Yang, M. H. (2017). L0-Regularized Intensity and Gradient Prior for Deblurring Text Images and beyond. *IEEE Transactions on Pattern Analysis and Machine Intelligence*, *39*(2), 342–355. doi:10.1109/TPAMI.2016.2551244

Pan, J., Hu, Z., Su, Z., & Yang, M.-H. (2014). Deblurring face images with exemplars. *Proceedings of the European Conference on Computer Vision*, 47–62.

Pan, J., Hu, Z., Su, Z., & Yang, M.-H. (2014). Deblurring text images via L0-regularized intensity and gradient prior. *Proceedings of IEEE Conference on Computer Vision and Pattern Recognition*, 2901–2908.

Pan, J., Liu, R., Su, Z., & G. Liu, G. (2014). Motion blur kernel estimation via salient edges and low rank prior. *IEEE International Conference on Multimedia and Expo*, 1-6. doi:10.1109/ICME.2014.6890182

Pan, J., Liu, R., Su, Z., & Liu, and G. (2016). Robust Kernel Estimation with Outliers Handling for Image Deblurring. *Cvpr 2016*, 2800–2808. https://doi.org/10.1109/CVPR.2016.306

Pan, J., Sun, D., Pfister, H., & Yang, M.-H. (2016). Blind Image Deblurring using Dark Channel Prior. *IEEE Conference on Computer Vision and Pattern Recognition*. doi:10.1109/CVPR.2016.180

Pang, J., & Cheung, G. (2017). Graph Laplacian regularization for inverse imaging: Analysis in the continuous domain. *IEEE Transactions on Image Processing*, *26*(4), 1770–1785.

Pan, J. Sun, D., Pfister, H. and Yang M.-H. (2016). Blind image deblurring using dark channel prior. In *Computer Vision and Pattern Recognition*, 1628– 1636.

Papafitsoros K, Sch¨onlieb CB (2014) A combined first and second order variational approach for image reconstruction. *Journal of mathematical imaging and vision* 48(2):308–338

Parikh, N., & Boyd, S. (2014). Proximal algorithms. *Foundations and Trends in Optimization*, *1*(3), 127–239.

Paris, S., Hasinoff, S. W., & Kautz, J. (2011). Local laplacian filters: Edge-aware image processing with a laplacian pyramid. *ACM Transactions on Graphics, 30*(4), 1-12.

Park, D., H. Kim, H., Seo, Y., Jung, J., Seo, D., & LEE, D. (2018). Analysis of Aging Trends on KOMPSAT-3 using RER. The Korean Society of Remote Sensing Fall Conference, 2018.

Park, S. C., Park, M. K., & Kang, M. G. (2003). Super-resolution image reconstruction: a technical overview. *IEEE Signal Processing Magazine*, *20*(3), 21–36.

Park, S. K., Schowengerdt, R., & Kaczynski, M.-A. (1984). Modulation-transfer-function analysis for sampled imaging systems. *Applied Optics*, *23*(15), 2572-2582.

Pentland, A. P. (1984). Fractal-based description of natural scenes, *IEEE Transactions on Pattern Analysis and Machine Intelligence*, *PAMI-6*(6), 661–674.

Pérez, P., Gangnet, M., & Blak, A. (2003). Poisson Image Editing. *ACM Transaction on Graphics*, *22*(3), 313 – 318.

Peyré, G., (2008). Image processing with nonlocal spectral bases, *Multiscale Modeling and* Simulation, *7*(2), 703–730.

Peyré, G., Bougleux, S., & Cohen, L. (2008). Non-local regularization of inverse problems. *Proceedings of the 10th European Conference on Computer Vision*: *Part IIIO*, 57–68. doi:10.1007/978-3-540-88690-7_5.

Pitkow, X. (2010). Exact feature probabilities in images with occlusion. *Journal of Vision*, *10*(14), 2010.

Poli, D., Remondino, F., Angiuli, E., & Agugiaro, G. (2015). Radiometric and geometric evaluation of GeoEye-1, WorldView-2 and Pléiades-1A stereo images for 3D information extraction. *ISPRS Journal of Photogrammetry and Remote Sensing*, *100*, 35–47. doi:10.1016/j.isprsjprs.2014.04.007

Portilla, J., Strela, V., Wainwright, M. J., & Simoncelli, E. P. (2003). Image denoising using scale mixtures of gaussians in the wavelet domain. *IEEE Transactions on Image processing*, *12*(11), 1338–1351.

Pratt, J. W., Edgeworth, F.Y., & Fisher, R.A. (1976). On the efficiency of maximum likelihood estimation. *The Annals of Statistics*, *4* (3), 501–514.

QA4EO task team. (2010). *A Quality Assurance Framework for Earth Observation: Principles version 4.0*. http://qa4eo.org/docs/QA4EO_Principles_v4.0.pdf

Qian, Y., Wang, N., Ma, L., & Liu, Y. (2017). Vicarious radiometric calibration/validation of Landsat-8 operational land imager using a ground reflected radiance-based approach with Baotou site in China. *Journal of Applied Remote Sensing*

Rangaswamy, M. K. (2003). *Two-dimensional On-orbit Modulation Transfer Function Analysis Using Convex Mirror Array*. South Dakota State University. doi:10.16309/j.cnki.issn.1007-1776.2003.03.004

Rauchmiller, R. F. & Schowengerdt, R. A. (1988). Measurement of the landsat thematic mapper modulation transfer function using an array of point sources. *Optical Engineering*, *27*(4), 334–343.

RazakSat.eoPortal Directory.(2019). Available at: https://earth.esa.int/web/eoportal/satellite-missions/r/razaksat

Ren, W., Cao, X., Pan, J., Guo, X., Zuo, W., & Yang, M. H. (2016). Image Deblurring via Enhanced Low-Rank Prior. *IEEE Transactions on Image Processing*, *25*(7), 3426–3437. doi:10.1109/TIP.2016.2571062

Reulke, R., Becker, S., Haala, N., & Tempelmann, U. (2006). Determination and improvement of spatial resolution of the CCD-line-scanner system ADS40. *Journal of Photogrammetry & Remote Sensing*, 60, 81–90.

"RM142m RazakSAT faulty after just one year, says federal auditor - The Malaysian Insider". themalaysianinsider.com. Archived from the original on 2014-10-14. Retrieved 2014-09-13.

Rodin, C. D., Andrade, F. A. de A., Hovenburg, A. R., & Johansen, T. A. (2019). A survey of practical design considerations of optical imaging stabilization systems for small unmanned aerial systems. *Sensors (Switzerland)*, *19*(21). doi:10.3390/s19214800

Roland, J. K. M. (2015). A study of slanted-edge MTF stability and repeatability. *Proceedings of SPIE- Image Quality and System Performance XII*, 9396.

Romero, A.; Gatta, C.; Camps-Valls, G. Unsupervised deep feature extraction for remote sensing image classification. IEEE Trans. Geosci. Remote Sens. 2016, 54, 1349–1362.

Rondeaux, G., Steven, M. D., Clark, J. A. and Mackay, G., 1998. La Crau: A European test site for remote sensing validation. *International Journal of Remote Sensing*, *19*, 2775-2788.

Roth S., & Black. M. J. (2005). Fields of experts: A framework for learning image priors. *IEEE Computer Society Conference on Computer Vision and Pattern Recognition*, *2*, 860-867.

Roth, S., & Black, M. J. (2009). Fields of experts. *International Journal of Computer Vision*, *82*(2), 205–229.

Roth, S., & Black, M. J. (2005). Fields of experts: A framework for learning image priors. *Proceedings of the IEEE Computer Society Conference on Computer Vision and Pattern Recognition*, *II*, 860–867. doi:10.1109/CVPR.2005.160

Ruderman, D. L. (1996). Origins of Scaling in Natural Images, *Vision Research*, *37*(23), 3385–3398.

Rudin, L. I., Osher, S., & Fatemi, E. (1992). Nonlinear total variation-based noise removal algorithms. *Journal of Physics D*, *60*(1), 259–268.

Rudin, L., & Osher, S. (1990). Feature-oriented image enhancement using shock filters," *SIAM Journal on numerical analysis*, *27*(4), 919–940.

Ruiz, C. P. & Lopez, F. J. A. (2002). Restoring SPOT images using PSF-derived deconvolution filters. *International Journal of Remote Sensing*, *23*(12), 2379–2391.

Ryan, R., Braxton, B., Schowengerdt, R. A., Choi, T. Helder, D., Bronski, S. (2003). IKONOS spatial resolution and image interpretability characterization. *Remote Sensing of Environment*, *88*(1-2), 37–52.

Saerom, H., Sojin, O., Jonghee, B., Sung-Eui, Y., & Bochang, M. (2019). Gradient Outlier Removal for Gradient-Domain Path Tracing. *Computer Graphics Forum*, *38*(2), 245–253. https://doi.org/https://doi.org/10.1111/cgf.13634

Saerom, H., Sojin, O., Jonghee, B., Sung-Eui, Y., & Bochang, M. (2019). Gradient Outlier Removal for Gradient-Domain Path Tracing. *Computer Graphics Forum*, *38*(2), 245–253. Doi: 10.1111/cgf.13634

Santer, R., Schmechtig, C., & Thome K. (2013). Uncertainties in the calibration of SPOT sensors with reference to test-sites White Sands and La Crau. Journal of Chemical Information and Modeling, 53(9), 1689–1699. Doi: 10.1017/CBO9781107415324.004

Saiga, R., Takeuchi, A., KentaroUesugib, Yasuko, T., Suzuki, Y., & Mizutania, R. (2018). Method for estimating modulation transfer function from sample images *Micron,* 105, 64–69.

Sajid, M., & Khurshid, K., (2015). Satellite Image Restoration Using RLS Adaptive Filter and Enhancement by Image Processing Techniques. *Symposium on Recent Advances in Electrical Engineering*, 1–7.

Sánchez, J., Meinhardt-Llopis, E., & Facciolo, G. (2013). TV-L1 Optical Flow Estimation. *Image Processing On Line*, *1*(1), 137–150. doi:10.5201/ipol.2013.26

"Spacex Successfully Launches Satellite Into Earth Orbit," July 14, 2009, Space Travel, Url: Http://Www.Space-Travel.Com/Reports/Spacex_Successfully_Launches_Satellite Into_Earth_Orbit_999.Html

Savitzky, A. (1964). Smoothing and Differentiation of Data by Simplified Least Squares Procedures. *Analytical Chemistry*, *36,* 1627–1639.

Schiller, S. Silny, J., & Taylor, M., (2012). In-flight performance assessment of imaging systems using the specular array radiometric calibration (SPARC) method. Proceedings of Joint Agency Commercial Imagery Evaluation Workshop, Fairfax, VA, USA, 1–26.

Schiller, S. Teter, M., & Silny, J. (2017). Comprehensive Vicarious Calibration and Characterization of a Small Satellite Constellation Using Specular Array Calibration (SPARC) Method. In *31st Annual AIAA/USU Conference on Small Satellites*.

Schmidt, U., Gao, Q., & Roth, S. (2010). A generative perspective on MRFs in low-level vision. *Proceedings of IEEE Conference on Computer Vision and Pattern Recognition*, 1751–1758.

Schott, J. R. (2007). *Remote Sensing: The Image Chain Approach*, (2nd ed.), New York: Oxford University Press.

Schowengerdt, R. A. (1976). A method for determining the operational imaging performance of orbital earth resources sensors. *Proceedings Annual American Society of Photogrammetry Concention -1*. 25-62.

Schowengerdt, R. A. (2007). *Remote sensing: Models and methods for image processing*. Elsevier (3rd ed.). Academic Press.

Schowengerdt, R. A. and P. N. Slater (1972). Determination of inflight MTF of orbital earth resources sensors. *ICO IX Congress on Space Optics*, Santa Monica, CA, 693-703.

Schowengerdt, R. A., Archwamety, C., & Wrigley, R. C. (1985). Landsat Thematic Mapper image-derived MTF. *Photogrammetric Engineering and Remote Sensing*, *51*(9), 1395–1406.

Seghouane, A.-K. (2010). Maximum likelihood blind image restoration via alternating minimization. In *2010 IEEE International Conference on Image Processing* (pp. 3581–3584). doi:10.1109/ICIP.2010.5650975

Semenov, A. A., Moshkov, A. V., Pozhidayev, V. N., Barducci, A., Marcoionni, P., & Pippi, I. (2011). Estimation of normalized atmospheric point spread function and restoration of remotely sensed images. *IEEE Transactions on Geoscience and Remote Sensing*, *49*(7), 2623–2634. doi:10.1109/TGRS.2011.2114351

Sendur, I., & Selesnick, L., (2002). Bivariate shrinkage with local variance estimation, *IEEE Transactions on Signal Processing*, *9*(12) , 438–441.

Seo, D., Hong, G., Jin, C., Park, D., Ji, S., & Lee, D. (2015). Overview of KOMPSAT-3A calibration and validation. *ACRS 2015 - 36th Asian Conference on Remote Sensing: Fostering Resilient Growth in Asia, Proceedings*, 2–7.

Serra-Capizzano, S. (2003). A note on antireflective boundary conditions and fast deblurring models. *SIAM Journal on Scientific Computing*, *25*, 1307–1325.

Sha, L., Schonfeld, D. & Wang,L. (2019). Graph Laplacian Regularization with Sparse Coding for Image Restoration and Representation. *IEEE Transactions on Circuits and Systems for Video Technology.* doi:10.1109/TCSVT.2019.2913411

Shaham, T. R., & Michaeli, T. (2016). Visualizing image priors. *European Conference on Computer Vision*, 136–153.

Shan, Q., J. Jia, J. & Agarwala, A. (2008). High-quality motion deblurring from a single image. *ACM Transactions on Graphics*, *27*, 73:1–73:10.

Shen, H., Du, L., Zhang, L., & Gong, W. (2012). A Blind Restoration Method for Remote Sensing Images. *IEEE Geoscience And Remote Sensing Letters*, *9*(6), 1137–1141.

Shen, H., Zhao, W., Yuan, Q., & Zhang, L. (2014). Blind restoration of remote sensing images by a combination of automatic knife-edge detection and alternating minimization. *Remote Sensing*, *6*(8), 7491–7521. https://doi.org/10.3390/rs6087491

Shen, H., Zhao, W., Yuan, Q., & Zhang, L. (2014). Blind Restoration of Remote Sensing Images by a Combination of Automatic Knife-Edge Detection and Alternating Minimization. *Remote Sensing*, *6*(8), 7491–7521. doi:10.3390/rs6087491

Sheskin, D. J. (2011). *Handbook of Parametric and nonparametric statistical procedures: Fifth edition* (5th ed.). Florida, USA: Chapman & Hall/CRC.

Shi, X., Wang, L., Shao,X., Wang, H., & Tao. Z, (2015). Accurate estimation of motion blur parameters in noisy remote sensing image, *Proceedings of SPIE 9501, Satellite Data Compression, Communications, and Processing XI, 95010X*

Shuman, D. I., Narang, S. K., Frossard, P., Ortega, A., & Van-dergheynst, P. (2013). The emerging field of signal processing on graphs: Extending high-dimensional data analysis to networks and other irregular domains. *IEEE Signal Processing Magazine*, *30*(3), 83–98.

Simoncelli, E. P., & Freeman, W. T. (1995). Steerable pyramid: a flexible architecture for multi-scale derivative computation. *IEEE International Conference on Image Processing*, *3*, 444–447. doi:10.1109/icip.1995.537667

Six, D., Fily, M., Alvain, S., Henry, P., & Benoist, J.-P., (2004). Surface characterisation of the Dome Concordia area (Antarctica) as a potential satellite calibration site, using Spot 4/Vegetation instrument. *Remote Sensing of Environment*, *89*, 83-94.

Si-Yao, L., Ren, D., & Yin, Q. (2019). Understanding kernel size in blind deconvolution. *Proceedings of 2019 IEEE Winter Conference on Applications of Computer Vision, WACV 2019,* (3), 2068–2076. doi:10.1109/WACV.2019.00224.

Slater, P. N. (1980). *Remote Sensing–Optics and Optical Systems*. MA: Addison-Wesley.

Smith, L. N. (2012). Estimating an Image's Blur Kernel from Edge Intensity Profiles, *Mathematics*. 1–39.

Squara, P., Scheeren, T. W. L., Aya, H. D., Bakker, J., Cecconi, M., Einav, S., … Saugel, B. (2020). Metrology part 1: definition of quality criteria. *Journal of Clinical Monitoring and Computing*, *35*(1), 17–25. https://doi.org/10.1007/s10877-020-00494-y

Sroubek, F., & Flusser, J. (2005). Multichannel Blind Deconvolution of Spatially Misaligned Images. *IEEE Transactions On Image Processing*, *14*(7), 874-883.

Šroubek, F., & Milanfar, P. (2012). Robust multichannel blind deconvolution via fast alternating minimization. *IEEE Transactions on Image Processing*, *21*(4), 1687–1700. https://doi.org/10.1109/TIP.2011.2175740
Šroubek, F., & Milanfar, P. (2012). Robust multichannel blind deconvolution via fast alternating minimization. *IEEE Transactions on Image Processing*, *21*(4), 1687–1700. https://doi.org/10.1109/TIP.2011.2175740
Stanimirović, P. S., Stojanović, I., Katsikis, V. N., Pappas, D., & Zdravev, Z. (2015). Application of the least squares solutions in image deblurring. *Mathematical Problems in Engineering*. doi:10.1155/2015/298689

Starck, J. L., Elad, M., & Donoho, D. L. (2003). Image decomposition: separation of texture from piece-wise smooth content. *IEEE Transactions on Image Processing*, *14*(10), 1570-1582.

Steidl, G., & Weickert, J. (2002). Relations between soft wavelet shrinkage and total variation denoising. *Pattern Recognition*, 198–205,

Stensaas, G. (2014). USGS Report to the CEOS WGCV: 41 + Years of Continuous Landsat Global Observation.

Steriti, R. J., & Fiddy, M. A. (1994). Blind deconvolution of images by use of neural networks. *Optics Letter*, *19*(8), 575–577.

Storey, J. C. (2001). Landsat 7 on-orbit modulation transfer function estimation. *Proceedings of Joint Agency Commercial Imagery Evaluation*, *4540*, 50–61.

Subari, M. D., & Hassan, A. (2014). Building EOS capability for Malaysia - The options. *IOP Conference Series: Earth and Environmental Science*, *20*(1), 1–10. doi:10.1088/1755-1315/20/1/012034

Subr, K., Soler, C., & Durand, F. (2009). Edge-Preserving Multiscale Image Decomposition based on Local Extrema. *ACM SIGGRAPH Asia*, *147*, 1-9

Sun, L., Cho, S., Wang, J., & Hays, J. (2013). Edge-based blur kernel estimation using patch priors. *IEEE International Conference on Computational Photography*. 1–8.

Suresh, S., Das, D., Lal, S., & Gupta, D. (2018). Image quality restoration framework for contrast enhancement of satellite remote sensing images. *Remote Sensing Applications: Society and Environment*, *10*, 104–119.

Susnjara, A., Perraudin, N., Kressner, D., & Vandergheynst, P. (2015). Accelerated filtering on graphs using lanczos method. arXiv:1509.04537v3.

Takeda, H., Farsiu, S., & Milanfar, P. (2007). Kernel regression for image processing and reconstruction. *IEEE Transactions on Image Processing*, *16*(2), 349–366.

Tan, H.C., Lim, H., & Tan, B.T.G. (1991). Windowing techniques for image restoration. *CVGIP: Graphical Models Image Processing*, *53*(5), 491- 500.

Tan, S., & Jiao, L-C. (2007). Multishrinkage: analytical form for a Bayesian wavelet estimator based on the multivariate Laplacian model. *Optics Letter*, *32*(17) 2583–2585

Tang, S., Xie, X., Xia, M., Luo, L., Liu, P., & Li, Z. (2018). Spatial-scale-regularized blur kernel estimation for blind image deblurring. *Signal Processing: Image Communication*, *68*(August), 138–154. https://doi.org/10.1016/j.image.2018.07.010

Tang, Y., Xue, Y., Chen, Y., & Zhou, L. (2018). Blind deblurring with sparse representation via external patch priors. *Digital Signal Processing: A Review Journal*, *78*, 322–331. https://doi.org/10.1016/j.dsp.2018.03.017

Tansock, J., Bancroft, D., Butler, J., Cao, C., Datla, R., Hansen, S., … Xiong, X. (2015). Guidelines for Radiometric Calibration of Electro-Optical Instruments for Remote Sensing. *National Institute of Standards and Technology*, *HB 157*(April). doi:10.6028/NIST.HB.157

Tappen, M. F., Freeman, W. T., & Adelson, E. H. (2005). Recovering Intrinsic Images From A Single Image. *IEEE Transactions on Pattern Analysis and Machine Intelligence*, *27*(9).

Tappen, M. F., Liu, C., Adelson, E. H., & Freeman, W. T. (2007). Learning Gaussian Conditional Random Fields for Low-Level Vision, *Proceedings of the IEEE Conference on Computer Vision and Pattern Recognition*, 1-8

Techawatcharapaikul, C., Mittrapiyanurak, P., & Chiracharit, W. (2018). Improved Weighted Least Square Radiometric Calibration Based Noise and Outlier Rejection by Adjacent Comparagraph and Brightness Transfer Function. *Advances in Intelligent Systems and Computing*, *E101–D*(8), 46–55. https://doi.org/10.1007/978-3-030-19861-9_5

Teillet, P. M., Horler, D. N. H., & O'Neill, N. T. (1997). Calibration, validation, and quality assurance in remote sensing: a new paradigm. *Canadian Journal of Remote Sensing*, *23*(4), 401 – 414.

Thenkabail, P. S. (2015). *Remotely Sensed Data Characterization, Classification, and Accuracies*. (1st ed.). CRC Press.

Thome, K. J., Schiller, S., Conel, J. E., Arai, K., & Tsuchida, S., (1998). Results of the 1996 Earth Observing System vicarious calibration joint campaign at Lunar Lake Playa, Nevada (USA). *Metrologia, 35*, 631-638.

Thome, K. J., (2004). In-flight intersensor radiometric calibration using vicarious approaches. *Post-launch calibration of satellite sensors*. Morain, S. A. and Budge, A. M. London, Taylor and Francis, 95-102.

Thome, K., Gellman, D., Parada, R., Biggar, S., Slater, P. and Moran, M., (1993). In-flight radiometric calibration of Landsat-5 Thematic Mapper from 1984 to present.

Proceedings of the Society of Photo-Optical Instrumentation Engineers (SPIE), 47-59.

Tirer, T., & Giryes, R. (2019). Image Restoration by Iterative Denoising and Backward Projections. *IEEE Transactions on Image Processing*, *28*(3), 1220–1234. doi:10.1109/TIP.2018.2875569

Tomasi, C., & Manduchi, R. (1998). Bilateral Filtering For Gray And Color Images. *Proceedings of IEEE Conference on Computer Vision and Pattern Recognition*, 839–846.

Tropp, J. A., & Gilbert, A. C. (2007). Signal recovery from random measurements via orthogonal matching pursuit. *IEEE Transactions on Information Theory*, *53*(12), 655–4666

Tsagkatakis, G., Aidini, A., Fotiadou, K., Giannopoulos, M., Pentari, A., & Tsakalides, P. (2019). Survey of deep-learning approaches for remote sensing observation enhancement. *Sensors (Switzerland)*, *19*(18), 1–39. https://doi.org/10.3390/s19183929

Tu, Z., Xie, W., Cao, J., van Gemeren, C., Poppe, R., & Veltkamp, R. C. (2017). Variational method for joint optical flow estimation and edge-aware image restoration. *Pattern Recognition*, *65*(April 2016), 11–25. https://doi.org/10.1016/j.patcog.2016.10.027

Tzannes A. P., & Mooney J. M. (1995). Measurement of the modulation transfer function of infrared cameras. *Opt. Eng.*, *34*(6), 1808–1817.

Vanhamel, I., Pratikakis, I., & Sahli, H. (2003). Multiscale Gradient Watersheds Of Color Images. *IEEE Transactions on Image Processing*, *12*(6), 617–626.

Varanasi, M. K., Aazhang, B,. (1989). Parametric generalized Gaussian density estimation. *The Journal of the Acoustical Society of America*, *86*(4), 1404–1415.

Vese, L.A., & Osher, S.J. (2003). Modeling textures with total variation minimization and oscillating patterns in image processing. *Journal of Scientific Computing*, *19*, 553–572.

Viallefont-Robinet, F., & Léger, D. (2010). Improvement of the edge method for on-orbit MTF Measurement. *Opt. Express*, *18*, 3531–3545.

Viallefont-robinet, F., Helder, D., Fraisse, R., Newbury, A., Bergh, F., Van Den, Lee, D., & Saunier, S. (2018). Comparison of MTF measurements using edge method: towards reference data set. *Optics Express*, *26*(26), 33625–33648.

Vicarious Calibration. (2013. August 26), Available at: http://calvalportal.ceos.org/cal/val-wiki/-/wiki/CalVal+Wiki/Vicarious+Calibration

Villmann, T., Schleif, F. M., & Hammer, B. (2010). Sparse representation of data. *Proceedings of the 18th European Symposium on Artificial Neural Networks - Computational Intelligence and Machine Learning, ESANN 2010*, 225–234.

Vogel CR, Oman ME. Fast, (1998). Robust total variation-based reconstruction of noisy, blurred images. *IEEE Transaction on Image Processing*, *7*, 813–824.

Wainwright, M. J., & Simoncelli, E. P. (1999). Scale mixtures of gaussians and the statistics of natural images. *Proceedings of the 12th International Conference on Neural Information Processing Systems*, 855–861.

Wang, M., Yu, J., & Sun, W. (2015). Group-based hyperspectral image denoising using low rank representation. *IEEE International Conference on Image Processing*,1623–1627.

Wang, R., & Tao, D. (2014). Recent Progress in Image Deblurring. *Computer Vision and Pattern Recognition*, 1–53. http://arxiv.org/abs/1409.6838

Wang, S., Zhang, L., & Liang, Y. (2013). Nonlocal spectral prior model for low-level vision. *Proceedings of the 11th Asian conference on computer vision*, 231–244.

Wang, T., Li., S., & Li. X. (2009). An automatic MTF measurement method for remote sensing cameras. *IEEE International Conference of Computer Science and Information Technology*, *3*, 245–248.

Wang, Y., Ortega, A., Tian, D., & Vetro, A. (2014). A graph-based joint bilateral approach for depth enhancement. *Proceedings of the IEEE International Conference on Acoustics, Speech and Signal Processing*, 885–889.

Wang, Z., & Xiong, X. J. (2013). On-orbit spatial characterization of VIIRS using the Moon. *Proceedings of SPIE 8866*, 88661W.

Wang, Z., Bovik, A. C., Sheikh, H. R., & Simoncelli, E. P. (2004). Image quality assessment: from error visibility to structural similarity, *IEEE Transactions on Image Processing*, *13*(4), 600–612.

Wang, Z., Bovik, A.C., Sheikh, H.R., & Simoncelli, E.P. (2004). Image quality assessment: from error visibility to structural similarity. *IEEE Transactions on Image Processing*, *13*(4), 600-612.

Wang, Z., Choi, T., & Xiong, X. (2011). On-orbit modulation transfer function characterization of Terra MODIS using the Moon. *Proceeding of SPIE 8153*, 81531N.

Wang, Z., Xiong, X, Choi, T, & Link, D. (2014). On-orbit characterization of MODIS modulation transfer function using the Moon. *IEEE Transactions on Geoscience and Remote Sensing*, *52*(7), 4112–4121.

Wang, N., Li, C., Ma, L., Liu, Y., Meng, F., Zhao, Y., Wang, D. (2017). Ground-based automated radiometric calibration system in Baotou site, China. *Proceedings of SPIE, Image and Signal Processing for Remote Sensing XXIII*.

Wedel, A., Pock, T., Zach, C., *Bischof, H.* (2009). An improved algorithm for TV-L1 optical flow. *Lecture Notes Computer Science*, 5604, 23–45.

Wei, L., Lefebvre, S., Kwatra, V., & Turk, G. (2009). State of The Art In Example-Based Texture Synthesis. *In Euro-Graphics' 09 State of the Art Report*.

Wei, Q., & Weina, Z. (2011). Restoration of Motion-blurred Star Image Based on Wiener Filter. *The Fourth International Conference on Intelligent Computation Technology and Automation*, 691-694. doi:10.1109/ICICTA.2011.458

Weickert, J. (1998). *Anisotropic Diffusion in Image Processing*, 1 Teubner Stuttgart.

Weiss, B. (2006). Fast Median and Bilateral Filtering. *ACM Transactions on Graphics*, 25(3), 519–526.

Wen, B., Li, Y., & Bresler, Y. (2017). Non-Local Low-Rank Constraint for Image Restoration. *IEEE International Conference on Acoustics, Speech, and Signal Processing*, 2297–2301.

Wenny, B. N., Helder, D., Hong, J., Leigh, L., Thome, K. J., & Reuter, D. (2015). Pre- and Post-Launch Spatial Quality of the Landsat 8 Thermal Infrared. *Sensor Remote Sensing*, *7*(2), 1962-1980.

WGCV. (2019, September 20). http://ceos.org/ourwork/workinggroups/wgcv/

Whyte, O., Sivic, J., & Zisserman, A. (2014). Deblurring Shaken and Partially Saturated Images. *International Journal of Computer Vision*, *110*(2), 185–201. https://doi.org/10.1007/s11263-014-0727-3

Wiener, N. (1964). Extrapolation, Interpolation, and Smoothing of Stationary Time Series, MIT Press.

Wong, J. S. M. (2012). On-orbit Spatial Quality Assessment of RazakSAT^{TM} Images. In *Symposium Penyelidikan Angkasa*.

Wong, J. S. M., & Chan, C. S. (2015). Restoration of Blurred-Noisy Images Through the Concept of Bilevel Programming. In G. Bebis, R. Boyle, B. Parvin, D. Koracin, I. Pavlidis, R. Feris, … G. Weber (Eds.), *Advances in Visual Computing: 11th International Symposium, ISVC 2015, Las Vegas, NV, USA, December 14-16, 2015, Proceedings, Part II* (pp. 776–786). Cham: Springer International Publishing. https://doi.org/10.1007/978-3-319-27863-6_73

Wong, J., S. M. (2010). Modulation Transfer Function Compensation through a modified Wiener Filter for spatial image quality improvement. *WSEA, selected topics in power systems and remote sensing*, 177–182.

Wong, S. M., Ong, S., & Chan, C. S. (2019). On-orbit spatial characterization based on satellite image structure. *Journal of Applied Remote Sensing*, *13*(1), 157– 170.

Wood, L., Schowengerdt, R. A., & Meyer, D. (1986). Restoration for Sampled Imaging Systems. *Proceedings of SPIE, Applications of Digital Image Processing IX*, 697, 333-340.

Woods, J., Biemond, J., & Tekalp, A. (1985). Boundary value problem in image restoration. In *ICASSP '85. IEEE International Conference on Acoustics, Speech,* *and Signal Processing* (Vol. 10, pp. 692–695). https://doi.org/10.1109/ICASSP.1985.1168354

Wu, D., Yin, Y., Wang, Z., Gu, X., Verbrugghe, M., & Guyot, G., (1997). Radiometric characterisation of Dunhuang satellite calibration test site (China). *Physical measurements and signatures in remote sensing*. *1*, 151-160.

Wu, F., Dong, W., Shi, G., & Li, X. (2018). *Learning Hybrid Sparsity Prior for Image Restoration: Where Deep Learning Meets Sparse Coding*. 1–11. http://arxiv.org/abs/1807.06920

Wu, H.-H. P., & Schowengerdt, R. A. (1993). Improved fraction image estimation using image restoration. *IEEE Transactions on Geoscience and Remote Sensing*, *31*(4), 771-778.

Wu, Q., Wang, S., Kong, D., & Yin, B. (2016). Depth maps enhancement using nonlocal self-similarity based on the sparse representation. *International Journal of Simulation: Systems, Science and Technology*, *17*(25), 1–6. doi:10.5013/IJSSST.a.17.25.19

Wu, Z., Luo, Z., Zhang, Y., Guo, F., & He, L. (2018). Image quality assessment of high-resolution satellite images with MTF-based fuzzy comprehensive evaluation method. *International Archives of the Photogrammetry, Remote Sensing and Spatial Information Sciences*, *42*(3), 1907–1914. doi:10.5194/isprs-archives-XLII-3-1907-2018

Wu, Z., Luo, Z., Zhang, Y., Guo, F., & He, L. (2018). Image quality assessment of high-resolution satellite images with mtf-based fuzzy comprehensive evaluation method. *International Archives of the Photogrammetry, Remote Sensing and Spatial Information Sciences - ISPRS Archives*, *42*(3), 1907–1914. doi: 10.5194/isprs-archives-XLII-3-1907-2018

Xie, Q., Meng, D., Gu, S., Zhang, L., Zuo, W., Feng, X., & Xu, Z. (2014). On the Optimal Solution of Weighted Nuclear Norm Minimization. http://arxiv.org/abs/1405.6012

Xie, X., Wang, H., & Zhang, W. (2015). Statistic estimation and validation of in-orbit modulation transfer function based on fractal characteristics of remote sensing images. *Optics Communications*, *354*, 202–208.

Xu, M., Ming, M., Cong, M., & Huijie, Li, (2014). Research of on-orbit MTF measurement for the satellite sensors,. *Proceeding of SPIE 9158, Remote Sensing of the Environment: 18th National Symposium on Remote Sensing of China*, 915809

Xu, J., Zhang, L., Zhang, D., & Feng, X. (2017). Multi-channel Weighted Nuclear Norm Minimization for Real Color Image Denoising. *Proceedings of the IEEE International Conference on Computer Vision*, *2017-Octob*(61672446), 1105–1113. doi:10.1109/ICCV.2017.125

Xu, J., Zhang, L., Zuo, W., Zhang, D., & Feng, X. (2015). Patch Group Based Nonlocal Self-Similarity Prior Learning for Image Denoising. *Proceedings of the IEEE International Conference on Computer Vision*, 244–252. doi:10.1109/ICCV.2015.36

Xu, L., & Jia, J. (2010). Two-phase kernel estimation for robust motion deblurring. *Proceedings of the 11th European conference on Computer vision: Part I*, 157–170.

Xu, L., Lu, C., Xu, Y., & Jia, J. (2011). Image Smoothing Via L0 Gradient Minimization. *ACM Transactions Graphics*, *30*(6), 174:1–174:12.

Xu, L., Yan, Q., Xia, Y., Jia, J. (2012). Structure Extraction From Texture Via Relative Total Variation. *ACM Transactions on Graphics*, *31*(6), 139:1–139:10.

Xu, L., Zheng, S., & Jia, J. (2013). Unnatural L0 sparse representation for natural image deblurring. *Proceedings of IEEE Conference on Computer Vision and Pattern Recognition*, 1107–1114.

Xu, W., Xu, G., Wang, Y., Sun, X., Lin, D., & Wu, Y. (2018). Deep Memory Connected Neural Network for Optical Remote Sensing Image Restoration. *Remote Sensing*, *10*(12), 1893. https://doi.org/10.3390/rs10121893

Xu, W., Zhang, L., Yang, B., & Chen, H. (2011). On-orbit mtf measurement of high resolution satellite optical camera using periodic targets. *Acta Optica Sinica*, *31*(7). doi:10.3788/AOS201131.0711001

Xu, Y., Hu, X., & Peng, S. (2013). Robust image deblurring using hyper Laplacian model. *Lecture Notes in Computer Science (Including Subseries Lecture Notes in Artificial Intelligence and Lecture Notes in Bioinformatics)*, *7729 LNCS*(PART 2), 49–60. doi:10.1007/978-3-642-37484-5_5

Xue, F., & Blu, T. (2015). A Novel SURE-Based Criterion for Parametric PSF Estimation. *IEEE Transactions on Image Processing*, *24*(2), 595–607. https://doi.org/10.1109/TIP.2014.2380174

Yan, R., & Shao, L. (2016). Blind Image Blur Estimation via Deep Learning. *IEEE Transactions on Image Processing*, *25*(4), 1910–1921.

Yang, H., Zhang, Z. B., Wu, D. Y,. & Huang, H. Y. (2014). Image deblurring using empirical Wiener filter in the curvelet domain and joint non-local means filter in the spatial domain. *Journal on Imaging Sciences*, *62*(3), 178–185.

Yang, H., Zhu, M., Zhang, Z., & Huang, H. (2016). Guided Filter based Edge-preserving Image Non-blind Deconvolution, 12–15. http://arxiv.org/abs/1609.01839

Yang, J. Wright, J., Huang, T., & Ma, Y. (2010). Image super-resolution via sparse representation. *IEEE Transactions on Image Processing*, *19*(11), 2861–2873.

Yang, Q., Tan, K. H., & Ahuja, N. (2009). Real-Time O(1) Bilateral Filtering. *Proceedings Conference on Computer Vision and Pattern Recognition*, 557–564.

You, Y-L., & Kaveh M. (1996). A regularization approach to joint blur identification and image Restoration. *IEEE Transactions on Image Processing*, *5*, 416–428.

Yu, J., Chang, Z., & Xiao, C. (2019). Blur kernel estimation using sparse representation and cross-scale self-similarity. *Multimedia Tools and Applications*, *78*(13), 18549–18570. https://doi.org/10.1007/s11042-019-7237-9

Yu, J., Chang, Z., & Xiao, C. (2019). Blur kernel estimation using sparse representation and cross-scale self-similarity. *Multimedia Tools and Applications*, *78*(13), 18549–18570. doi.10.1007/s11042-019-7237-9

Zha, Z., Wen, B., Zhang, J., Zhou, J., & Zhu, C. (2019). A Comparative Study for the Nuclear Norms Minimization Methods, 2050–2054. https://doi.org/10.1109/icip.2019.8803145

Zha, Z-Y., Liu, X., Huang, X-H., Shi, H-L., Xu, Y-Y, Wang, Q., … Zhang, X. (2017). Analyzing the group sparsity based on the rank minimization methods. *Proceedings of 2017 IEEE International Conference on Multimedia and Expo*, 883–888.

Zhai G., & Yang, X. (2012). Image reconstruction from random sam- ples with multiscale hybrid parametric and nonparametric modelling. *IEEE Transactions on Circuits and Systems for Video Technology*, *22*(11), 1554–1563.

Zhang F., & Hancock, E. R. (2008). Graph spectral image smoothing using the heat kernel. *Pattern Recognition*, *41*, 3328–3342.

Zhang, C., Liu, W., Liu, J., Liu, C., Shi, C., (2018). Sparse representation and adaptive mixed samples regression for single image super-resolution. *Signal Processing: Image Communication,* 67, 79-89

Zhang, D., Hu, Y., Ye, J., Li, X., & He, X. (2012). Matrix completion by truncated nuclear norm regularization. *Proceedings of the IEEE conference on computer vision and pattern Recognition*, 2192–2199.

Zhang, H., Tang, L., Fang, Z., Xiang, C., & Li, C. (2018). Nonconvex and nonsmooth total generalized variation model for image restoration. *Signal Processing*, *143*, 69–85. doi:10.1016/j.sigpro.2017.08.021

Zhang, H., Wipf, D., & Zhang, Y. (2014). Multi-observation blind deconvolution with an adaptive sparse prior. *IEEE Transactions on Pattern Analysis and Machine Intelligence*, *36*(8), 1628–1643. https://doi.org/10.1109/TPAMI.2013.241

Zhang, H., Yang, J., Zhang, Y., & Huang, T. S. (2011). Sparse Representation Based Blind Image Deblurring. *IEEE International Conference on Multimedia and Expo*, 1–6.

Zhang, H., Yang, J., Zhang, Y., Nasrabadi, N. M., & Huang, T. S. (2011). Close the loop: Joint blind image restoration and recognition with sparse representation prior. *Proceedings of the IEEE International Conference on Computer Vision*, 770–777.

Zhang, J., Lin, G., Wu, G. L., Wang, C. & Cheng, Y. (2015). Wavelet and fast bilateral filter based de-speckling method for medical ultrasound images. *Biomedical Signal Processing and Control*, *18*, 1–10.

Zhang, J., Zhao, D., & Gao, W. (2014a). Group-based sparse representation for image restoration. *IEEE Transactions on Image Processing*, *23*(8), 3336–3351. doi:10.1109/TIP.2014.2323127

Zhang, J., Zhao, D., Jiang, F., & Gao, W. (2013). Structural group sparse representation for image compressive sensing recovery. *Proceedings of IEEE Data Compression Conference*, 331–340.

Zhang, J., Zhao, D., Xiong, R., Ma, S., & Gao, W. (2014b). Image restoration using joint statistical modeling in a space-Transform domain. *IEEE Transactions on Circuits and Systems for Video Technology*, *24*(6), 915–928.

Zhang, L., Mou, X., & Zhang, D. (2011). FSIM: A feature similarity index for image quality assessment. *IEEE Transactions on Image Processing*, *20*, 2378-2386

Zhang, L., Yuan, Q., Shen, H., & Li, P. (2011). Multiframe image super-resolution adapted with local spatial information. *Journal of the Optical Society of America A*, *28*, 381–390.

Zhang, Q., Xu, L., Jia, J. (2014). 100+ Times Faster Weighted Median Filter (WMF). *Proceedings of IEEE Conference on Computer Vision and Pattern Recognition*, 2830–2837.

Zhang, S., Wang, L., Shi, X., Wang, X., & Shao, X. (2014). High-resolution remote sensing image restoration based on double-knife-edge method. *Proceeding of SPIE 9124, Satellite Data Compression, Communications, and Processing X, 912405*.

Zhang, T., Ghanem, B., Liu, S., & Ahuja, N. (2010). Low-rank sparse learning for robust visual tracking. *Proceedings of 12th European Conference on Computer Vision*, 470–484.

Zhang, X. Wang, R., Tian, Y., & Wang, W. (2015). Image Deblurring Using Robust Sparsity Priors. *Proceedings of IEEE International Conference on Image Processing*, 138–142.

Zhang, X., Burger, X., Bresson X. M., & Osher, S., (2010). Bregmanized nonlocal regularization for deconvolution and sparse reconstruction, *SIAM Journal on Imaging Sciences*, *3*(3), 253–276.

Zhang, X., Shi, Y., Pang, Z. F., & Zhu, Y. (2017). Fast algorithm for image denoising with different boundary conditions. *Journal of the Franklin Institute*, *354*(11), 4595–4614. https://doi.org/10.1016/j.jfranklin.2017.04.011

Zhang, X., Wang, R., Jiang, X., Wang, W., & Gao, W. (2016). Spatially variant defocus blur map estimation and deblurring from a single image. *Journal of Visual Communication and Image Representation*, *35*, 257–264. doi:10.1016/j.jvcir.2016.01.002

Zheng S, Xu L, Jia J (2013) Forward motion deblurring. In: Proceedings of IEEE International Conference on Computer Vision, pp 1465–1472

Zhi, X., Jiang, S., Zhang, W., Wang, D., & Li, Y. (2017). Image degradation characteristics and restoration based on regularization for diffractive imaging. *Infrared Physics and Technology*, *86*, 226–238. https://doi.org/10.1016/j.infrared.2017.09.014

Zhi, Z., Hou, Q., Sun, X., Zhang, W., Li, L., & Wang, D. (2014). Degradation and restoration of high resolution TDICCD imagery due to satellite vibrations. *Proceedings of SPIE 9301, International Symposium on Optoelectronic Technology and Application: Image Processing and Pattern Recognition, 93012I.*

Zhong, W., Hong, D., Zhaowei, Sun Z., & Wu., X. (2009). Computation model of image motion velocity for space optical remote cameras. *International Conference on Mechatronics and Automation, Changchun*, 588-592.

Zhou, L., & Tang, J. (2017). Fraction-order total variation blind image restoration based on L1-norm. *Applied Mathematical Modelling*, *51*, 469–476. https://doi.org/10.1016/j.apm.2017.07.009

Zhou, X., Zhou, F., Bai, X., & Xue, B. (2014). A boundary condition based deconvolution framework for image deblurring. *Journal of Computational and Applied Mathematics*. https://doi.org/10.1016/j.cam.2013.10.028

Zhou, X., Zhou, F., Bai, X., & Xue, B. (2014). A boundary condition based deconvolution framework for image deblurring. *Journal of Computational and Applied Mathematics*, *261*(61233005), 14–29. doi:10.1016/j.cam.2013.10.028

Zhu, J., Li, K., & Hao, B. (2018). Image Restoration by a Mixed High-Order Total Variation and l1 Regularization Model. *Mathematical Problems in Engineering*, *2018*(3). doi:10.1155/2018/6538610

Zhu, J., Li, K., & Hao, B. (2019). Image Restoration by Second-Order Total Generalized Variation and Wavelet Frame Regularization. *Complexity*, *2019*(2). doi:10.1155/2019/3650128

Zhu, X., Cohen, S., Schiller, S., & Milanfar, P. (n.d.). Estimating Spatially Varying Defocus Blur from A Single Image. *IEEE Trans Image Processing*, *22*(12), 4879–4891. https://doi.org/10.1109/TIP.2013.2279316

Zhuo, S., & Sim, T. (2011). Defocus map estimation from a single image. *Pattern Recognition*, *44*(9), 1852–1858. doi:10.1016/j.patcog.2011.03.009

Zoran, D. (2013). Natural Image Statistics for Human and Computer Vision (Doctoral thesis, University of Jerusalem). https://people.csail.mit.edu/danielzoran/thesis.pdf

Zoran, D., & Weiss, Y. (2011). From learning models of natural image patches to whole image restoration. *Proceedings of IEEE Conference on Computer Vision and Pattern Recognition*, 479–486.